université de BORDEAUX

THÈSE PRÉSENTÉE

POUR OBTENIR LE GRADE DE

DOCTEUR DE

L'UNIVERSITÉ DE BORDEAUX

ÉCOLE DOCTORALE DES SCIENCES CHIMIQUES

SPÉCIALITÉ CHIMIE PHYSIQUE

Par Ruchao GAO

Synthèse de matériaux fonctionnels avancés par électrochimie bipolaire pour des applications catalytiques

Sous la direction de : Prof. Alexander KUHN
Co-directeur : Prof. Lin ZHANG

Soutenue le 04/12/2025

Membres du jury :

M. GIRAULT Hubert	Professeur, Ecole polytechnique fédérale de Lausanne, Suisse	Rapporteur
M. ETIENNE Mathieu	Directeur de Recherche, CNRS Nancy, France	Rapporteur
M. MANO Nicolas	Directeur de Recherche, CNRS Bordeaux, France	Examinateur
M. ZIGAH Dodzi	Professeur, Université de Poitiers, France	Président
Mme. ZHANG Lin	Professeur, Henan University, China	Co-directrice de thèse
M. KUHN Alexander	Professeur, Bordeaux INP, France	Directeur de thèse

Résumé

Synthèse de matériaux fonctionnels avancés par électrochimie bipolaire pour des applications catalytiques

L'électrochimie bipolaire permet la modification asymétrique sans fil d'objets conducteurs et semi-conducteurs, permettant ainsi la fabrication de particules Janus. Lorsqu'un tel objet est placé dans un champ électrique généré par deux électrodes d'alimentation en solution, une différence de potentiel s'établit à ses deux extrémités. Des réactions redox sont déclenchées simultanément aux extrémités opposées dès que la différence de potentiel est suffisante. En ajustant la direction et l'intensité du champ électrique, cette modification asymétrique peut être contrôlée avec précision.

L'objectif de cette thèse est de synthétiser des matériaux fonctionnels avancés par électrochimie bipolaire et d'explorer leur application catalytique. Dans un premier temps, une monocouche de graphène a été introduite comme matériau modèle 2D afin d'étudier la faisabilité de l'électrodéposition bipolaire. Des métaux, des composés de coordination métalliques et des polymères peuvent être déposés aux emplacements souhaités sur la monocouche de graphène, ce qui produit des objets hybrides multifonctionnels dotés de propriétés d'autopropulsion et de chimiluminescence. Ce graphène modifié peut également être utilisé pour fabriquer des nageurs enzymatiques à comportement dynamique contrôlé par l'application d'un champ magnétique externe. De plus, en couplant l'électrochimiluminescence bipolaire à un champ magnétique, un rotor 2D à base de graphène a été conçu afin de combiner l'électrochimie bipolaire à la dynamique rotationnelle. Le champ d'application de l'électrochimie bipolaire a ensuite été étendu aux microfeuillets de MXène afin d'évaluer l'applicabilité de cette approche à d'autres matériaux 2D.

Dans la dernière partie de cette thèse, l'électrochimie bipolaire assistée par la lumière a été introduite pour la modification de matériaux semi-conducteurs. Cette synergie entre lumière et champ électrique permet une modification sélective d'un côté des particules semi-conductrices. En ajustant l'intensité et la durée du champ électrique, la taille de la zone déposée a pu être ajustée avec précision. Enfin, les particules semi-conductrices modifiées sélectivement présente des performances photocatalytiques améliorées pour la remédiation environnementale.

Mots clés: Électrochimie bipolaire; Modification de surface; Particules Janus; Matériaux multifonctionnels; Catalyse

L'Institut des Sciences Moléculaires

ISM, UMR 5255, 16 Avenue Pey Berland, 33600 Pessac, France

Abstract

Synthesis of advanced functional materials via bipolar electrochemistry for catalytic applications

Bipolar electrochemistry enables wireless asymmetric modification of both conducting and semiconducting objects, thereby allowing the fabrication of Janus particles. When an object is placed in an electric field generated by two driving electrodes, a potential difference is established at its two ends. Redox reactions will be triggered simultaneously at opposite ends once the potential difference is sufficiently high. By adjusting the direction and intensity of the electric field, this modification can be precisely controlled.

The aim of this thesis is to synthesize advanced functional materials using bipolar electrochemistry and exploring their catalytic applications. First, graphene monolayers were introduced as a model 2D material to investigate the feasibility of bipolar electrodeposition. Metals, metal coordination compounds, and polymers can be deposited at desired positions of a graphene monolayer, resulting in multifunctional hybrid objects with self-propulsion and chemiluminescence properties. The modified graphene monolayer can also be used to fabricate enzymatic swimmers with controlled dynamic behavior by applying an external magnetic field. Furthermore, by coupling bipolar electrochemiluminescence with a magnetic field, a graphene-based 2D rotor is designed in order to combine bipolar electrochemistry with rotational dynamics. Then, the scope of bipolar electrochemistry was also extended to MXene microsheets to evaluate the applicability of this approach to other 2D materials.

In the last part of this thesis, light-assisted bipolar electrochemistry was introduced for the modification of semiconducting materials. This synergy of light and electric field enables selective modification of one side of semiconductor particles. By adjusting the electric field intensity and the duration of application, the size of the deposited area could be precisely tuned. Finally, the site-selective modified semiconductor particles show enhanced photocatalytic performance for environmental remediation.

Keywords: Bipolar electrochemistry; Surface modification; Janus particles; Multifunctional materials; Catalysis

Institute of Molecular Science

ISM, UMR 5255, 16 Avenue Pey Berland, 33600 Pessac, France

Acknowledgments

First and foremost, I would like to express my gratitude to my supervisor, Prof. Alexander Kuhn, and my co-supervisor, Prof. Lin Zhang, for their guidance, encouragement, and invaluable advice throughout my PhD studies. Their expertise, patience, and insightful feedback have been crucial for the completion of this thesis.

I am deeply grateful to all the members of my defence committee. My sincere thanks go to Prof. Hubert Girault and Dr. Mathieu Etienne for agreeing to be the referees of my thesis, and to Dr. Nicolas Mano and Prof. Dodzi Zigah for agreeing to be the jury members.

I would also like to thank Dr. Elisabeth Garanger and Prof. Mona Tréguer-Delapierre, members of my individual follow-up committee, for their valuable advice and continuous support over the past years.

I would like to thank all the current and former members of the Nsysa group. The collaborative atmosphere, seminars, annual lab days, and Christmas activities made my PhD journey enjoyable. Many thanks to Dr. Laurent Bouffier, Prof. Neso Sojic, Prof. Valérie Ravaine, Dr. Adeline Perro, Dr. Gabriel Loget, Dr. Guillaume Longatte, Dr. Mohsen Beladi-Mousavi, Dr. Gerardo Salinas, Patrick Garrigue, Dr. Stéphane Reculusa, Dr. Bertrand Goudeau, Véronique Lapeyre, and Olivier Fihey for their help with technology, equipment, and administrative matters, as well as for their kind support.

I would also like to thank all the friends and colleagues I met during these years: Miaoxia Liu, Dr. Wanmai Srisuwanno, Dr. Khaoula Mousavi, Dr. Zi Lin, Dr. Sifan Ji, Yupei Ma, Zirui Fan, Dr. Tianhua Sun, Leslie Rocio Arias Aranda, Guillaume Gimenez, Changlin Zhou, Xin Wu, Zikkawas Pasom, Dr. Youness Boukarkour, Dr. Sara Knezevic, Dr. Yuhan Huang, Marine Lavainne, Sorasak Klinyod, Fatima Mehri, Elisa D'Arrigo, Gaëtan Barth, Axelle Virepinte, Yuheng Fu, and Dr. Benjamin Lienard. Thank you all for your help and friendship, made this period memorable.

My deepest thank goes to my parents, grandfather, sister, and girlfriend for their unconditional love, patience, and constant encouragement. Their trust and support have always been my greatest motivation.

Finally, I gratefully acknowledge Henan University for providing my PhD scholarship. Without this generous support, this work would not have been possible.

Table of contents

Résumé ____ *i*
Abstract ____ *ii*
Acknowledgments ____ *iii*
Table of contents ____ *iv*
List of abbreviations ____ *vii*
Résumé de la thèse ____ *1*
Preface ____ *14*
Chapter 1 Introduction to bipolar electrochemistry ____ *15*

1.1 Principles of bipolar electrochemistry ____ **15**
1.1.1 Closed bipolar electrochemistry ____ 17
1.1.2 Open bipolar electrochemistry ____ 18
1.1.2.1 Open bipolar electrochemistry with conducting materials ____ 18
1.1.2.2 Open bipolar electrochemistry with semiconducting materials ____ 20
1.1.3 Indirect bipolar electrochemistry ____ 21

1.2 Applications of bipolar electrochemistry ____ **21**
1.2.1 Wireless synthesis of Janus objects ____ 21
1.2.1.1 Wireless synthesis of Janus objects with conducting materials ____ 22
1.2.1.2 Wireless synthesis of Janus objects with semiconducting materials ____ 27
1.2.2 Bipolar electrochemiluminescence ____ 29
1.2.3 Synthesis of gradient materials ____ 31
1.2.4 Bipolar electrochemistry driven motion ____ 34

1.3 Motivation and aims of the thesis ____ **37**
Chapter 2 Bipolar electrochemistry on graphene monolayers ____ *39*

2.1 Spatial precision tailoring the catalytic activity of graphene monolayers for designing Janus swimmers ____ **41**
2.1.1 Immobilization of freestanding graphene monolayers ____ 41
2.1.2 Site-selective deposition of Pt on graphene monolayers ____ 42
2.1.3 Precision deposition of Pt on graphene monolayers ____ 45
2.1.4 Dynamic behavior of Pt-graphene monolayers ____ 48
2.1.5 Highly controlled dynamic behavior of Pt-graphene monolayers ____ 52
2.1.6 Conclusion ____ 53

2.2 Synthesis of multi-functional graphene monolayers via bipolar electrochemistry ____ **55**
2.2.1 Multi-metal modification of graphene monolayers ____ 56
2.2.2 Multi-functionalized graphene monolayers and their applications ____ 59
2.2.2.1 Indirect deposition of Prussian blue on a graphene monolayer ____ 59
2.2.2.2 Indirect deposition of electrophoretic paints on graphene monolayer ____ 61
2.2.3 Conclusion ____ 64

2.3 Enzyme-modified graphene monolayers for the direct transformation of biochemical energy into motion ____ **65**
2.3.1 Fabrication of enzymatic Au-graphene ____ 66
2.3.2 Dynamic behavior of the enzymatic graphene swimmer ____ 68
2.3.3 Electrochemical analysis of the enzymatic graphene biofuel cell ____ 73
2.3.4 Energy conversion from electrical to mechanical energy ____ 74
2.3.5 Conclusion ____ 75

2.4 Bipolar Electrochemistry-Driven Rotation of Light-Emitting Graphene Monolayers 76
2.4.1 Design of 2D light-emitting magnetoelectrochemical rotor 77
2.4.2 ECL emission and the propulsion of a graphene monolayer rotor 78
2.4.3 Continuous rotation of the graphene monolayer rotor 83
2.4.4 Conclusion 85
2.5 Experimental section 86
2.5.1 Preparation of graphene monolayers 86
2.5.2 Fabrication of Pt-graphene-EP and luminol CL 86
2.5.2.1 Fabrication of Pt-graphene 86
2.5.2.2 Fabrication of Pt-graphene-EP 86
2.5.2.3 Luminol CL 87
2.5.3 Enzymatic graphene swimmer 87
2.5.3.1 Synthesis of Au-graphene 87
2.5.3.2 Modification of Au-graphene 87
2.5.3.3 Dynamic behavior of enzymatic graphene swimmers 88
2.5.3.4 Preparation of biofuel electrodes 88
2.5.3.5 Electrochemical measurements of an enzymatic graphene biofuel cell 89
2.5.4 ECL graphene monolayer rotor 89
2.6 Conclusion of Chapter 2 90
Chapter 3 Bipolar electrodeposition on alternative 2D material 91
3.1 Introduction to MXene 91
3.2 Modification of MXene via bipolar electrochemistry 92
3.2.1 In bulk solution 94
3.2.2 Optimization 96
3.2.3 On a glass substrate 98
3.3 Conclusion 100
Chapter 4 Bipolar electrodeposition on TiO_2 microspheres for environmental applications 101
4.1 Introduction to semiconductor photocatalyst 101
4.2 Bipolar electrodeposition on semiconducting materials 102
4.3 Modification of TiO_2 microspheres 103
4.3.1 Control experiments 105
4.3.2 Synergy of electric field and light 106
4.3.3 Precision control of light-assisted bipolar electrodeposition 107
4.3.4 Deposition of different metals 108
4.4 Application in photocatalysis 109
4.4.1 Photodegradation performance of RhB 110
4.4.1.1 The influence of modification on performance 110
4.4.1.2 Stability 112
4.4.2 Mechanism of the enhanced performance 112
4.5 Interferometric scattering microscopy of modified TiO_2 114
4.6 Experimental section 117
4.7 Conclusion 118
Chapter 5 Conclusion and perspectives 120
5.1 Conclusions 120

5.2 Perspectives 122
5.2.1 Perspective for the precise modification of microscale 2D objects 122
5.2.2 Perspective for the synthesis of multifunctional photocatalysts 123
Publications ***124***
References ***125***

List of abbreviations

Abbreviation	Meaning
1D	One dimensional
2D	Two dimensional
3D	Three dimensional
AFM	Atomic force microscopy
BOD	Bilirubin oxidase
BPE	Bipolar electrochemistry
CL	Chemiluminescence
CNT	Carbon nanotubes
CVD	Chemical vapor deposition
DBAE	2-(dibutylamino)ethanol
DC	Direct current
DNA	Deoxyribonucleic acid
DRA	Differential rolling average
ECL	Electrochemiluminescence
EDS	Energy dispersive spectroscopy
EP	Electrophoretic paints
Gox	Glucose oxidase
LED	Light emitting diode
MHD	Magnetohydrodynamic
NIPAM	Poly(N-isopropylacrylamide)
P3MT	Poly(3-methylthiophene)
PANI	Polyaniline
PB	Prussian blue
PBS	Phosphate buffered saline
PEDOT	Poly(3,4-ethylenedioxythiophene)
RhB	Rhodamine B
SDS	Sodium dodecyl sulfate
SEM	Scanning electron microscope
TEM	Transmission electron microscope
TEOS	Tetraethoxysilane
TPA	Tri-n-propylamine
UV	Ultraviolet

Résumé de la thèse

L'électrochimie bipolaire permet des réactions d'oxydation et de réduction simultanées aux extrémités opposées d'un objet, sans connexion directe. Cette approche sans fil permet la modification sélective d'un large éventail de matériaux, du conducteur au semi-conducteur. Ces caractéristiques la rendent particulièrement intéressante dans des domaines tels que l'électroanalyse, la génération de mouvement et, plus particulièrement, la synthèse de particules asymétriques.

L'électrochimie bipolaire a été utilisée avec succès pour construire des structures Janus avec de nombreux types d'objets. Cependant, son potentiel pour la synthèse de nouveaux matériaux multifonctionnels, notamment pour des applications catalytiques, reste insuffisamment exploré. Par conséquent, l'objectif de cette thèse est d'explorer plus en détail l'application de l'électrochimie bipolaire à la synthèse de matériaux fonctionnels avancés et d'étudier leur potentiel en catalyse.

Cette thèse présente d'abord les principes de l'électrochimie bipolaire et ses diverses applications. Les deux chapitres suivants se concentrent sur la manière dont l'électrochimie bipolaire peut être utilisée pour réaliser une modification précise de matériaux 2D en vue de la synthèse de matériaux multifonctionnels à fonctions catalytiques. Dans le dernier chapitre, nous présentons la modification spatialement contrôlée des matériaux semi-conducteurs via l'électrochimie bipolaire, et les performances photocatalytiques du semi-conducteur modifié sont étudiées.

1. L'électrochimie bipolaire

Le concept fondamental de l'électrochimie bipolaire repose sur la réalisation d'une « polarisation sans fil ». Lorsqu'un objet conducteur ou semi-conducteur est placé dans un champ électrique, une différence de potentiel est générée entre ses deux extrémités en raison du gradient de champ électrique, ce qui active des réactions d'oxydation et de réduction spontanées à ces extrémités. Contrairement aux systèmes électrochimiques conventionnels qui nécessitent une connexion à des électrodes de travail, l'électrochimie bipolaire fonctionne sans contact direct avec l'objet. Cette caractéristique accroît considérablement la compatibilité de l'électrochimie bipolaire avec des matériaux de tailles et de formes variées.

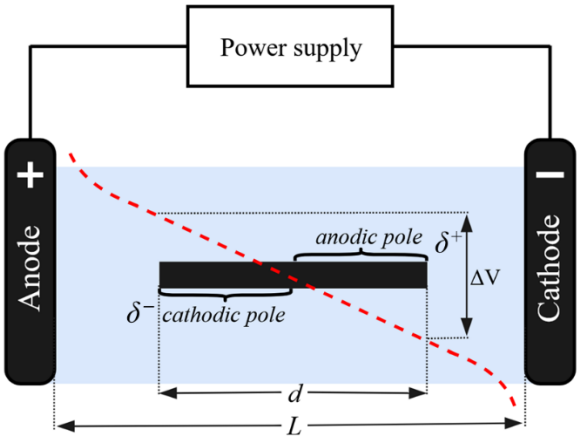

Figure 1 Schéma d'une cellule électrochimique bipolaire ouverte avec un matériau conducteur comme électrode bipolaire, la ligne pointillée rouge représente le potentiel dans la solution électrolytique.

Comme l'illustre la figure 1, lorsqu'une tension est appliquée entre deux électrodes de commande immergées dans une solution électrolytique, un champ électrique continu et uniforme s'établit entre elles. L'intensité du champ électrique (E) est directement proportionnelle à la tension appliquée (U) et inversement proportionnelle à la distance (L) entre les deux électrodes de commande. La relation entre ces paramètres est décrite par l'équation 1 :

$$E = \frac{U}{L} \tag{1}$$

L'électrode bipolaire étant conductrice, le potentiel en tout point de sa surface est égal, généralement considéré comme nul. Cependant, en raison de la présence d'un champ électrique dans la solution, la différence de potentiel interfaciale entre l'électrode bipolaire et l'électrolyte environnant varie sur sa longueur. Cette différence de potentiel (ΔV) atteint son maximum aux deux extrémités de l'électrode bipolaire et diminue progressivement vers le centre. La valeur de ΔV peut être calculée à l'aide de l'équation 2 :

$$\Delta V = E \times d \tag{2}$$

Ici, E représente l'intensité du champ électrique dans la solution et d la longueur de l'électrode bipolaire le long de la ligne de champ électrique. La valeur de ΔV dépend uniquement de l'intensité du champ électrique dans la solution et de la longueur de l'électrode bipolaire. Elle est indépendante de la position ou de l'orientation de l'électrode bipolaire dans l'électrolyte, ce qui permet de placer plusieurs électrodes bipolaires dans la même solution et de les faire fonctionner simultanément sous un même champ électrique.

Généralement, la réaction de réduction se produit à l'extrémité proche de l'électrode d'attaque de l'anode, appelée pôle cathodique (δ^-). Inversement, la réaction d'oxydation se produit à l'extrémité proche de l'électrode d'attaque de la cathode, appelée pôle anodique (δ^+). Pour déclencher les réactions d'oxydoréduction souhaitées, la différence de potentiel interfaciale (ΔV) doit être égale ou supérieure à la différence de potentiel standard (ΔE°) du couple redox cible. Ce seuil est essentiel pour garantir que les processus électrochimiques souhaités se produisent aux deux pôles de l'électrode bipolaire. Par exemple, les réactions qui se produisent aux extrémités cathodique et anodique de l'électrode bipolaire peuvent être représentées respectivement par les équations 3 et 4 :

$$Ox + ne^- \rightarrow Re \qquad E_1^\circ \tag{3}$$

$$Re' - ne^- \rightarrow Ox' \qquad E_2^\circ \tag{4}$$

La différence de potentiel standard entre ces deux réactions peut être exprimée comme suit :

D'un point de vue thermodynamique, ΔV ne doit pas être inférieur à ΔE° pour que les réactions redox souhaitées puissent être déclenchées. L'électrochimie bipolaire est largement utilisée dans de nombreux domaines de recherche, de la science des matériaux à l'électrochimie analytique en passant par la génération de mouvement. De plus, elle permet non seulement de modifier un objet unique avec plusieurs métaux, mais aussi d'incorporer différents matériaux sur une même cible. L'ajustement des paramètres expérimentaux permet de contrôler précisément l'ampleur et la position de ces modifications. Cette stratégie de modification flexible confère à l'électrochimie bipolaire la capacité de fabriquer des matériaux multifonctionnels avancés.

2. Électrochimie bipolaire sur monocouche de graphène

Le deuxième chapitre présente l'électrodéposition bipolaire de précision spatiale sur des monocouches de graphène pour la synthèse de matériaux 2D multifonctionnels et étudie leurs applications dans les nageurs autopropulsés, les hybrides de chimioluminescence, les dispositifs de conversion d'énergie enzymatique et les rotors électroluminescents.

Ce chapitre se compose de quatre parties. Tout d'abord, nous présentons une stratégie nouvelle et simple, basée sur le concept d'électrochimie bipolaire, réalisée à l'interface air-eau. L'électrodéposition sélective précise de métal sur une monocouche de graphène est réalisée, illustrée par le dépôt de platine sur les bords ou les coins du graphène dans une solution de H_2PtCl_6.

En raison de la nature hydrophobe du graphène, la monocouche de graphène flotte naturellement à l'interface air-eau, où sa position est très sensible aux perturbations externes telles que les courants d'air ou les vibrations mineures. Pour réaliser une modification bien contrôlée par électrochimie bipolaire, un dispositif de fixation est conçu et introduit dans le dispositif bipolaire. Ce dispositif est constitué d'une colonne inerte qui stabilise en douceur la feuille de graphène à l'interface air-eau.

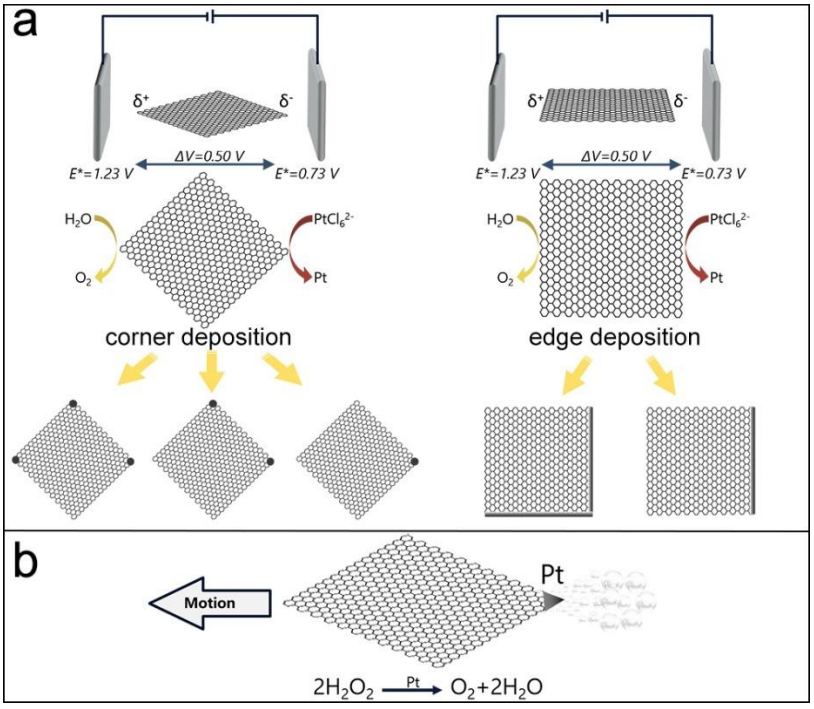

Figure 2 (a) Illustration du dépôt de Pt en coin ou en bord sur une monocouche de graphène. (b) Mécanisme de propulsion du nageur Janus Pt-graphène 2D.

Comme le montre la figure 2a, la monocouche de graphène, placée entre deux électrodes de commande, se polarise par rapport à l'électrolyte sous l'effet du champ électrique. Lorsque la différence de potentiel de polarisation générée entre les deux extrémités dépasse le potentiel seuil imposé par les réactions redox impliquées, le sel de platine peut être réduit du côté δ^- de la monocouche de graphène. L'ajustement de l'angle de l'objet 2D par rapport aux lignes de champ électrique permet un dépôt très sélectif à des emplacements prédéfinis, tels que différents coins ou bords. La taille du dépôt métallique peut également être contrôlée avec précision par l'intensité du champ électrique.

Par la suite, l'application potentielle des objets 2D hybrides ainsi obtenus a été étudiée en termes d'activité catalytique, visualisée par la décomposition site-spécifique du peroxyde d'hydrogène. Les bulles d'oxygène gazeux résultantes induisent un mouvement contrôlé, les qualifiant ainsi de nageurs 2D autopropulsés (figure 2b). En contrôlant précisément la taille de chaque cluster de platine déposé, il est possible d'affiner la formation des bulles et ainsi de créer intentionnellement une force motrice asymétrique, permettant aux nageurs Janus de se diriger dans une direction donnée. Plus précisément, le dépôt de platine est réalisé à deux coins voisins d'une monocouche de graphène, mais avec des temps de dépôt différents (5 minutes pour un coin et 10 minutes pour l'autre). La quantité de platine détermine l'intensité de la force motrice. Ainsi, le coin ayant subi un dépôt de platine de 10 minutes générera une force motrice plus élevée dans la solution combustible que le coin modifié pendant seulement 5 minutes. La force motrice globalement asymétrique entre les deux coins déplacera le nageur dans le sens horaire ou antihoraire pour la configuration opposée.

Deuxièmement, pour réaliser la synthèse de matériaux 2D multifonctionnels, nous introduisons des expériences de démonstration de principe sur la modification de monocouches de graphène avec divers matériaux à l'interface air-eau. Dans ce contexte, différents métaux, composés et polymères peuvent être déposés à n'importe quel endroit d'une feuille de monocouche de graphène.

Pour la préparation d'une monocouche de graphène modifiée multimétallique, le graphène a d'abord été placé à l'interface air/eau d'une solution de $HAuCl_4$, puis le bord de la monocouche de graphène carrée a été aligné à un angle de 45° par rapport à la direction du champ électrique appliqué. Dans ce cas, l'or se dépose à un angle du graphène lorsqu'un champ électrique suffisant est appliqué. Après le dépôt d'or, la solution de $HAuCl_4$ est remplacée par une solution saline de platine, puis la monocouche de graphène est tournée de 90°, puis un champ électrique approprié est appliqué pour la réduction du platine. En répétant ces étapes, des dépôts métalliques de Pd et de Cu ont été déposés avec succès à différents angles de la monocouche de graphène (figure 3a). De même, en plaçant la monocouche de graphène avec deux bords parallèles à la ligne de champ électrique, la modification multimétallique peut être réalisée aux bords de la monocouche de graphène.

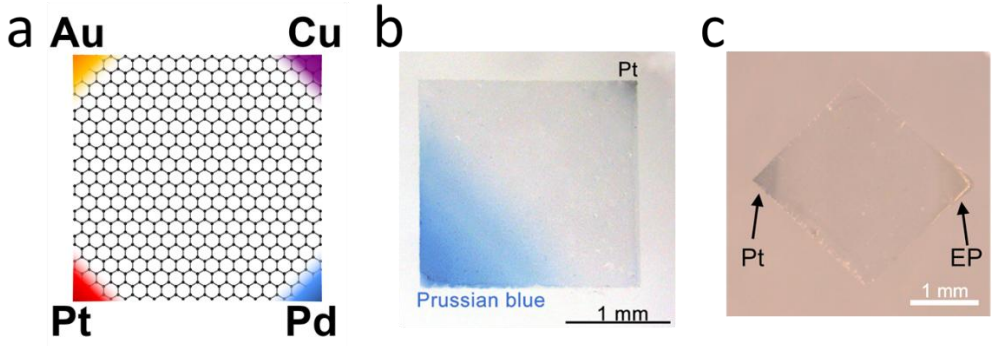

Figure 3 (a) Schéma de principe de la monocouche de graphène modifiée à plusieurs coins. (b) Micrographie d'une monocouche de graphène modifiée avec du bleu de Prusse et du Pt dans le coin opposé. (c) Micrographie d'une monocouche de graphène modifiée avec du Pt et de la peinture électrophorétique (EP).

Outre le simple dépôt métallique, l'électrochimie bipolaire permet également la modification de matériaux plus complexes sur l'objet cible, comme la modification du platine et du composé de

coordination métallique (bleu de Prusse, PB) à différentes positions d'une monocouche de graphène (figure 3b). Le principe du dépôt électrochimique bipolaire du bleu de Prusse repose sur des processus redox localisés se produisant aux pôles de la monocouche de graphène lorsqu'elle est polarisée dans un champ électrique. Au pôle δ^- de l'électrode bipolaire, les ions Fe^{3+} de la solution sont réduits en Fe^{2+} conformément à l'équation 6 :

$$Fe^{3+} + e^- \leftrightharpoons Fe^{2+} \quad (6)$$

Parallèlement, dans la solution principale, des ions hexacyanoferrates $[Fe(CN)_6]^{3-}$ sont déjà présents. Les ions Fe^{2+} fraîchement générés réagissent immédiatement avec $[Fe(CN)_6]^{3-}$ pour former le bleu de Prusse insoluble, $FeIII_4[FeII(CN)_6]_3$, qui précipite sélectivement à la surface du graphène autour du pôle δ^- (équation 7) :

$$4Fe^{2+} + 3[FeIII(CN)_6]^{3-} \leftrightharpoons FeIII_4[FeII(CN)_6]_3 \downarrow \quad (7)$$

Ce mécanisme de dépôt indirect est crucial car le graphène lui-même ne transfère pas directement d'électrons à $[Fe(CN)_6]^{3-}$.

Le bleu de Prusse est reconnu pour son comportement catalytique, notamment dans la médiation des processus de transfert d'électrons. Il peut favoriser efficacement l'oxydation du luminol en présence de peroxyde d'hydrogène. Lorsque les hybrides graphène-PB sont placés dans une solution de luminol/H_2O_2, une émission de chimioluminescence bleu vif a été observée à la position modifiée par le PB de la monocouche de graphène.

De plus, cette électrodéposition bipolaire indirecte peut également être utilisée pour modifier le polymère sur la monocouche de graphène 2D. Au cours du processus bipolaire, l'oxydation de l'eau au pôle anodique génère des protons, entraînant une diminution localisée du pH. Par conséquent, les groupes carboxyles des micelles de polymère chargées négativement sont protonés, ce qui diminue leur solubilité dans l'eau et déclenche la précipitation du polymère précisément du côté δ^+ de l'électrode bipolaire. Grâce à cette stratégie, nous avons pu co-déposer du platine et une peinture électrophorétique aux positions opposées d'une même feuille de graphène (figure 3c). La multifonctionnalité qui en résulte est illustrée dans une expérience de démonstration de principe par le mouvement autonome de la feuille de graphène modifiée. Ce mouvement est alimenté par la libération continue de bulles d'oxygène générées par la décomposition de H_2O_2 accélérée par le platine, couplée à une émission lumineuse simultanée. Cette dernière fonction est due à l'immobilisation de $K_3Fe(CN)_3$ dans le polymère poreux, réagissant avec le luminol pour générer une chimioluminescence localisée.

Dans la troisième partie, nous avons développé un nageur enzymatique de graphène en générant d'abord des couches d'or ultrafines aux deux extrémités d'une monocouche de graphène par électrodéposition bipolaire. Ensuite, la glucose oxydase (Gox) et la bilirubine oxydase (BOD) ont été immobilisées sur ces zones modifiées par l'or, situées de manière opposée. La présence de couches d'or assure un contact électrique efficace entre la feuille de graphène et le polymère redox contenant l'enzyme, facilitant ainsi le transfert d'électrons lors du processus de biocatalyse.

Ces objets hybrides enzymatiques 2D présentent un comportement dynamique intéressant en présence de glucose et d'oxygène. Comme le montre la figure 4a, en présence de glucose et d'oxygène, les réactions enzymatiques spatialement séparées établissent une biopile à

combustible court-circuitée. La Gox catalyse l'oxydation du glucose côté anodique, générant des électrons (e−, flèche rouge) qui traversent la monocouche de graphène pour être utilisés dans la réaction de réduction de l'oxygène médiée par la BOD côté cathodique. Simultanément, l'oxydation du glucose côté anodique génère continuellement des protons, tandis que la réduction de l'oxygène à la cathode en consomme. Par conséquent, les protons sont répartis de manière asymétrique le long de la couche de graphène et développent un champ électrique local. Ce champ auto-généré provoque un écoulement électroosmotique par migration des protons le long du nageur de graphène. Ceci induit une force (F_E, flèche orange) subie par le nageur de graphène, le propulsant dans la direction opposée au flux de protons. Plus important encore, l'application d'un champ magnétique externe permet de contrôler précisément leur comportement, permettant une rotation précise et une meilleure efficacité de conversion énergétique.

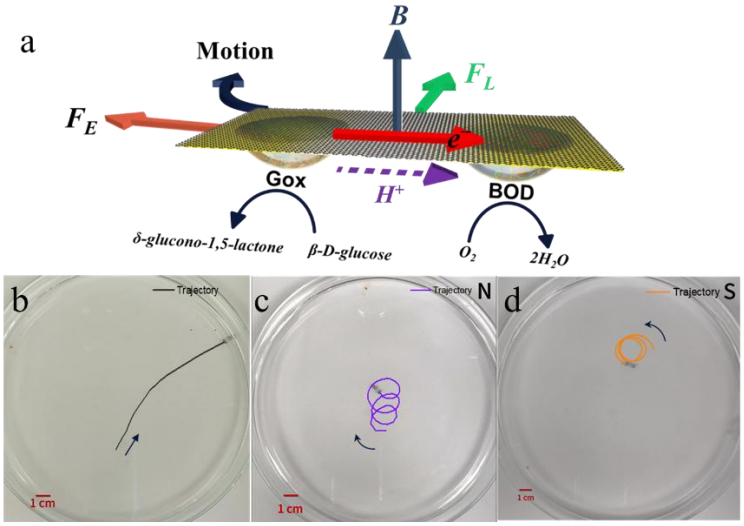

Figure 4 (a) Illustration du mécanisme du nageur enzymatique de graphène. Trajectoire d'un nageur enzymatique de graphène (DBO : Gox = 1: 1) se déplaçant à l'interface air/eau (b) en l'absence de champ magnétique et en présence d'un champ magnétique (c) pôle N vers le haut et (d) pôle S vers le haut. La solution combustible est composée de 0,1 M de PBS et de 20 mM de glucose à pH 7, à 37 °C et saturée en O_2.

Afin de valider ce mécanisme d'auto-électrophorèse, le comportement dynamique du nageur enzymatique de graphène a été systématiquement étudié dans diverses conditions. En l'absence de champ magnétique, le nageur enzymatique de graphène présente une propulsion linéaire en direction du bord modifié par Gox (Figure 4b). Lorsqu'un champ magnétique externe est appliqué à ce système, la force de Lorentz induite (F_L, flèche verte sur la Figure 4a), en synergie avec la force de Lorentz, entraîne un changement complet de trajectoire du nageur. Avec le pôle nord orienté vers le haut, on observe une rotation dans le sens horaire (Figure 4c). À l'inverse, avec le pôle sud orienté vers le haut, on observe une rotation dans le sens antihoraire (Figure 4c). Notamment, la présence d'un champ magnétique externe crée également un flux magnétohydrodynamique autour des deux spots enzymatiques. Cette convection peut également accélérer la réaction, et donc le rendement de conversion énergétique. Une vitesse accrue est observée à court terme en présence du champ magnétique avec le pôle nord orienté vers le haut. Cette amélioration peut être attribuée à la génération d'un flux magnétohydrodynamique local, facilitant le transport des molécules de substrat vers les deux points enzymatiques dès les premiers instants de l'expérience, lorsque le nageur commence à se déplacer. Après optimisation de la solution combustible et du rapport de charge entre les

enzymes, une vitesse extrêmement élevée, pouvant atteindre 6 cm/s, est atteinte. Plus important encore, nous démontrons pour la première fois que la trajectoire et la vitesse d'un tel nageur enzymatique peuvent être contrôlées et optimisées par un champ magnétique externe, permettant ainsi un transfert d'énergie optimisé.

Dans la dernière partie de ce chapitre, nous passons de l'électrodéposition bipolaire au mouvement électrochimique bipolaire et présentons un mécanisme de propulsion électrophorétique amplifié par champ magnétique pour concevoir un rotor magnétoélectrochimique électroluminescent (ECL) sans fil. Une monocouche de graphène sert de substrat à ce rotor en raison de son excellente transparence et de sa conductivité élevée, atouts majeurs pour le système électroluminescent.

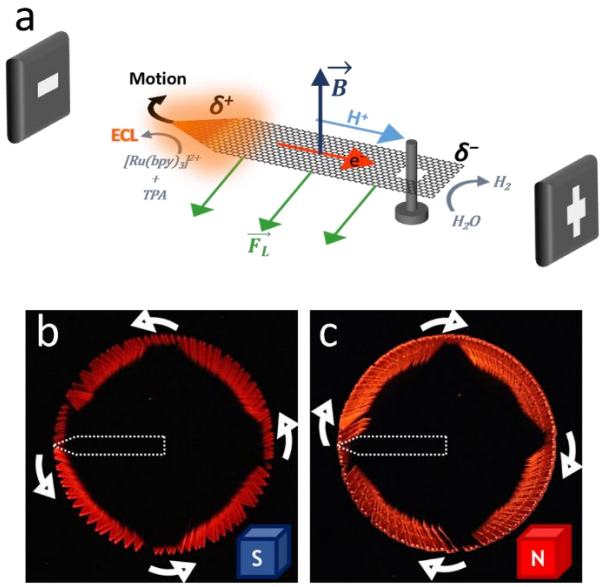

Figure 5 (a) Illustration du rotor monocouche de graphène électromagnétique émetteur de lumière sans fil en présence d'un champ magnétique externe orthogonal à la surface du BPE, avec une représentation des réactions électrochimiques associées, des électrodes motrices, de l'émission d'électrochimiluminescence, des extrémités polarisées anodiquement et cathodiquement (δ^+ et δ^-, respectivement), des courants ioniques électriques et de compensation de charge($\vec{J}$), dans ce cas des protons se déplaçant de l'anode à la cathode du BPE, du champ magnétique ($\vec{B}$) et de la force de Lorentz horizontale résultante ($\vec{F_L}$). Images optiques de l'émission ECL enregistrée pendant la réponse dynamique d'un rotor 2D en graphène de 1 cm de long se déplaçant à l'interface air/eau d'une solution de PBS 5 mM (pH 7,4), $[Ru(bpy)_3]^{2+}$ 2 mM, TPA 50 mM sous l'influence d'une configuration de champ électrique double alternatif (4 V/cm), en fonction de l'orientation du champ magnétique. (b) Pôle sud orienté vers le haut. (c) Pôle nord orienté vers le haut.

Le dispositif dynamique électroluminescent a été conçu en couplant l'oxydation du système ECL $[Ru(bpy)_3]^{2+}$/tri-n-propylamine (TPA) à des réactions de réduction de l'eau (Figure 5a). Ces processus génèrent un flux ionique compensant la charge le long de l'électrode bipolaire en graphène 2D. En présence d'un champ magnétique orienté orthogonalement au dispositif, les courants ioniques subissent une force de Lorentz, qui produit un couple supplémentaire sur l'objet (Figure 5a). Dans ces conditions, le graphène présente une rotation horaire ou antihoraire prévisible, dont le sens est déterminé par le champ magnétique externe. De plus, l'intensité et la vitesse angulaire de l'ECL étant directement liées à la cinétique des réactions électrochimiques, une corrélation claire a été établie entre les performances optiques et mécaniques du rotor et le champ électrique appliqué. Enfin, l'interaction entre l'orientation globale du champ électrique et la direction du champ magnétique permet des déplacements rotationnels complets contrôlés,

pouvant être surveillés par émission ECL. Cette rotation génère des flux hydrodynamiques supplémentaires et réduit les limitations du transport de masse, souvent des goulots d'étranglement critiques dans les processus redox hétérogènes.

Afin de vérifier la synergie entre les comportements optique et dynamique des monocouches de graphène sous champ électrique, nous avons d'abord étudié l'émission ECL et la propulsion du rotor sous un champ électrique de 4 V/cm seulement. Dans ce cas, l'émission ECL a été observée à l'extrémité anodique du rotor en graphène. Lorsqu'un champ magnétique était appliqué perpendiculairement à la cellule, une rotation horaire ou antihoraire prévisible était observée. Selon la règle de la main droite, lorsque le pôle nord de l'aimant était orienté vers le haut, une rotation électroluminescente dans le sens horaire était générée, tandis que l'orientation du pôle sud vers le haut entraînait une rotation antihoraire.

Cependant, en présence d'un seul champ électrique constant, le rotor en graphène ne peut atteindre qu'un faible angle de rotation. Pour obtenir une rotation continue, quatre électrodes d'entraînement ont été configurées de manière à ce que les champs appliqués soient mutuellement orthogonaux, générant un champ électrique global diagonal dans la cellule. Ce système a ensuite été combiné à un schéma de courant alternatif. Cette stratégie repose sur l'inversion séquentielle des directions de deux champs électriques tout en maintenant un champ magnétique externe constant. En inversant continuellement la direction du champ électrique adjacent, une rotation complète du rotor peut être obtenue. Dans ce cas, la trajectoire dépend également de l'orientation du champ magnétique externe : avec le pôle nord orienté vers le haut, le dispositif tourne dans le sens inverse des aiguilles d'une montre (Figure 5b), tandis qu'avec le pôle sud orienté vers le haut, une trajectoire inverse des aiguilles d'une montre est induite (Figure 5c). Ce mécanisme coopératif constitue ainsi une méthode fiable pour induire une rotation complète dans les rotors 2D émetteurs de lumière en couplant la polarisation électrochimique bipolaire au flux ionique induit par le champ magnétique.

3. Électrodéposition bipolaire sur un matériau 2D alternatif

Nous avons déjà réalisé la multifonctionnalisation de monocouches de graphène par électrochimie bipolaire. Cependant, la famille des matériaux 2D est remarquablement diversifiée, avec notamment les dichalcogénures de métaux de transition, le nitrure de bore hexagonal, le MXène et les oxydes feuilletés, chacun possédant des propriétés électroniques, catalytiques et interfaciales différentes. Par conséquent, la modification de ces matériaux 2D alternatifs par électrochimie bipolaire est cruciale pour évaluer la généralité de la stratégie sans fil, qui peut offrir de nouvelles perspectives pour la conception de matériaux 2D multifonctionnels avancés. Le Ti_3C_2-MXène a donc été sélectionné comme matériau 2D modèle afin d'explorer la faisabilité de la modification asymétrique d'autres matériaux 2D par électrochimie bipolaire.

Pour les objets 2D de taille micrométrique, le processus d'immobilisation devient plus complexe. À cette dimension, les particules individuelles ne peuvent plus être fixées avec des outils de fixation macroscopiques. Par conséquent, d'autres stratégies doivent être adaptées pour stabiliser les particules de MXène 2D lors de l'électrodéposition bipolaire. En raison du faible rapport d'aspect et de la surface sensible des microfeuillets de Ti_3C_2, l'électrochimie bipolaire assistée par capillarité et par gel ne se prête pas à cette étude. Dans ce contexte, nous adoptons

une stratégie simple en solution massive pour réaliser l'électrodéposition bipolaire, sans ajout de produits chimiques supplémentaires pour éviter l'oxydation des microfeuillets de Ti_3C_2. Cependant, en solution quasi neutre, la modification asymétrique de l'or sur Ti_3C_2 s'accompagne toujours d'une autoréduction spontanée à sa surface. Ce problème bloque la préparation de particules Janus complètes à base de Mxène.

Pour résoudre ce problème, nous avons mesuré le potentiel zêta de suspensions de Ti3C2 à différents pH afin d'évaluer l'influence de la charge de surface sur l'autoréduction spontanée des microfeuillets. Les résultats ont montré que le potentiel zêta de la suspension était d'environ -17,87 mV à pH ≈ 6, -9,23 mV à pH ≈ 4 et +7,17 mV à pH ≈ 2. Un potentiel zêta plus négatif signifie une plus grande capacité réductrice des particules de Ti_3C_2. Par conséquent, lorsque le MXène est dispersé sans ajustement du pH (par exemple, dans des conditions proches de la neutralité), il réduit spontanément les ions métalliques en solution, entraînant la formation d'agrégats métalliques à sa surface, même en l'absence d'agents électriques ou réducteurs. Par conséquent, une série d'expériences d'électrodéposition bipolaire a été réalisée dans des solutions à différents pH. Les résultats montrent qu'à pH = 2, des agrégats d'or se forment préférentiellement sur un bord de la microfeuille de Ti_3C_2, démontrant ainsi que l'autoréduction spontanée du Ti_3C_2 peut être efficacement inhibée en contrôlant les conditions électrolytiques.

Nous présentons ensuite une stratégie alternative consistant à immobiliser des microfeuilles de MXène sur un substrat solide. Comparée au système en solution massive, cette configuration permet de disperser uniformément des microfeuilles de Ti_3C_2 sur une lame de verre isolante (Figure 6a), ce qui fournit un substrat mécaniquement stable supprimant efficacement la rotation ou l'agrégation des particules individuelles pendant le dépôt. Dans ce cas, le sulfate de palladium a été choisi comme précurseur métallique afin d'évaluer plus en détail l'applicabilité des matériaux MXene au dépôt de différents métaux.

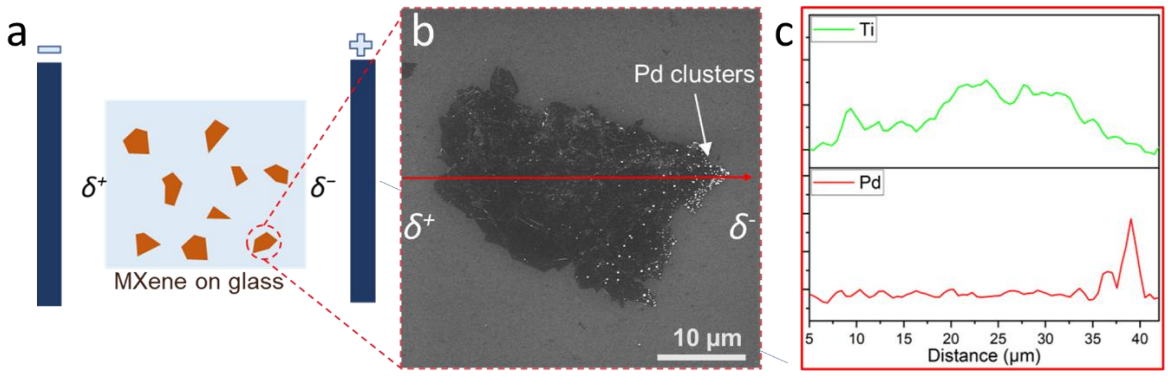

Figure 6 (a) Schéma du dépôt métallique asymétrique sur des microparticules de MXène par électrochimie bipolaire. Les microfeuilles de MXène sont dispersées sur une lame de verre par coulage en goutte. (b) Image MEB d'une microfeuille de MXène modifiée asymétriquement par un cluster de Pd. Le champ électrique appliqué est de 500 V/cm et le temps de dépôt est de 5 s. (c) Balayage EDS de la microfeuille de MXène, correspondant à la ligne rouge en (b).

Comme le montre la figure 6b, une microfeuille de Ti_3C_2 d'une longueur latérale d'environ 14,6 µm a été caractérisée après dépôt de Pd. Comme prévu, de nombreux amas de Pd ont été observés du côté δ^- de la microfeuille, tandis qu'aucun dépôt de Pd n'a été observé du côté δ^+. Pour fournir une preuve plus directe, une analyse par balayage linéaire EDS a été réalisée sur la microfeuille de Ti_3C_2 (Figure 6c). Le signal Ti était présent sur toute la microfeuille, et un pic

prononcé de Pd a été détecté à l'extrémité δ^-. Ce résultat démontre clairement que l'électrochimie bipolaire permet le dépôt sélectif de Pd sur les microfeuilles de Ti_3C_2.

Ces résultats démontrent que l'électrochimie bipolaire peut être appliquée à d'autres matériaux 2D comme méthode efficace de modification asymétrique. Ces résultats de preuve de concept élargissent la portée de l'électrochimie bipolaire au-delà du graphène et ouvrent de nouvelles opportunités pour la conception d'autres matériaux multifonctionnels à base de 2D pour la catalyse, la conversion d'énergie et les applications de détection.

4. Électrodéposition bipolaire sur microsphères de TiO_2 pour applications environnementales

Dans le quatrième chapitre, l'électrochimie bipolaire est combinée à l'excitation lumineuse pour étudier la modification asymétrique du TiO_2 sous l'effet d'un champ électrique externe. Cette approche permet non seulement d'étudier la modification de précision sur un matériau semi-conducteur, mais aussi d'évaluer systématiquement l'impact de ces modifications asymétriques sur les performances photocatalytiques.

Pour immobiliser les microsphères de TiO_2 pendant le dépôt, la stratégie assistée par gel est introduite dans cette étude. Les microsphères de TiO_2 sont d'abord dispersées dans un gel d'agarose contenant un précurseur métallique. Ensuite, lumière et champ électrique sont appliqués simultanément au mélange. Dans ce cas, les électrons du TiO_2 sont transférés de la bande de valence à la bande de conduction, ce qui entraîne la génération de paires électron-trou. En présence d'un champ électrique, un hémisphère devient polarisé positivement (δ^+), tandis que le côté opposé devient polarisé négativement (δ^-). Cette polarisation asymétrique génère un champ électrique interne à travers la microsphère de TiO_2, qui déplace les électrons vers le côté δ^+ et les trous vers le côté δ^- (Figure 7a). La synergie entre l'irradiation lumineuse et le champ électrique sépare les réactions redox du côté opposé, où les ions métalliques sont réduits du côté δ^+ et la réaction d'oxydation de l'eau se produit du côté δ^-. Un contrôle spatial aussi précis de la migration des porteurs de charge dans les semi-conducteurs n'est réalisable que par électrochimie bipolaire.

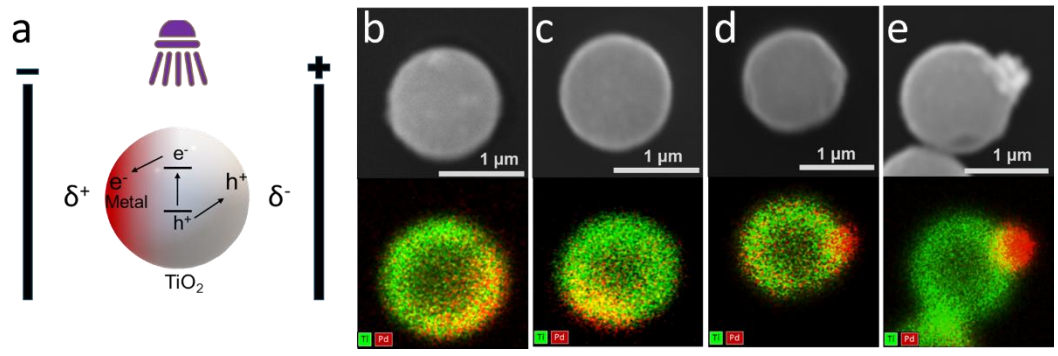

Figure 7 (a) Schéma de la modification du TiO_2 sous la seule application d'un champ électrique. Image MEB et cartographie EDS correspondante des microsphères Janus Pd-TiO_2 synthétisées sous différents champs électriques et durées d'irradiation, (b) 200 V/cm pendant 10 s, (c) 300 V/cm pendant 10 s, (d) 400 V/cm pendant 10 s, (e) 400 V/cm pendant 60 s.

Afin d'étudier le dépôt métallique de précision sur des microsphères de TiO_2, le sulfate de palladium a été choisi comme précurseur métallique et quelques expériences ont été réalisées sous différentes intensités de champ électrique et durées de dépôt. La figure 7b présente la morphologie et la distribution des éléments de la particule Janus Pd- TiO_2 synthétisée sous un

champ électrique de 200 V/cm. Les agrégats de Pd couvraient près de la moitié de la surface de la sphère, l'intensité du signal diminuant progressivement de l'extrémité de polarisation vers l'extrémité opposée. Lorsque le champ électrique augmentait à 300 V/cm, la zone de dépôt de Pd devenait plus localisée vers l'extrémité polarisée (Figure 7c). Avec une augmentation supplémentaire du champ électrique à 400 V/cm, les agrégats de Pd n'étaient observés que sur une petite zone (Figure 7d), indiquant qu'un champ électrique plus fort peut rapidement entraîner et confiner les électrons photogénérés dans une petite zone, où ils participent à la réaction de réduction du métal. La durée de dépôt est ensuite allongée de 10 à 60 s, comme le montre la Figure 7e. Des agrégats de Pd significativement agrandis ont été observés. Ces résultats démontrent qu'en électrochimie bipolaire à base de semi-conducteurs, un champ électrique plus élevé peut fournir une force motrice plus importante pour confiner les électrons et les trous dans une petite zone, tandis qu'un temps de dépôt plus long permet la croissance d'agrégats métalliques de taille plus importante.

L'influence de cette modification spatiale sur les performances photocatalytiques est ensuite étudiée. Théoriquement, le dépôt asymétrique de cocatalyseurs sur TiO_2 devrait améliorer l'efficacité photocatalytique en accélérant la séparation des porteurs de charge. Comme le montre la Figure 8a, les électrons photogénérés migrent principalement vers la zone modifiée par le Pd en raison du travail de sortie élevé du Pd, puis participent aux réactions de réduction. Cette voie de migration ordonnée minimise la recombinaison et améliore l'utilisation des porteurs de charge. Pour vérifier cela, des expériences de dégradation photocatalytique ont été réalisées en utilisant la rhodamine B (RhB) comme polluant organique modèle. Le photocatalyseur Janus Pd- TiO_2 et la solution de RhB obtenus ont été ajoutés dans un réacteur en verre placé sous lumière UV. L'activité photocatalytique a été quantifiée par le suivi de l'absorbance UV-vis de la solution de RhB, et l'efficacité de dégradation correspondante a été calculée à partir de cette absorbance en fonction du temps. La figure 8b présente les spectres d'absorption UV-vis de la solution de RhB en présence de photocatalyseurs Janus Pd- TiO_2 synthétisés sous un champ électrique de 200 V/cm. Le pic d'absorption caractéristique du RhB à environ 550 nm a progressivement diminué au fil du temps, confirmant la capacité de dégradation du photocatalyseur Janus Pd- TiO_2.

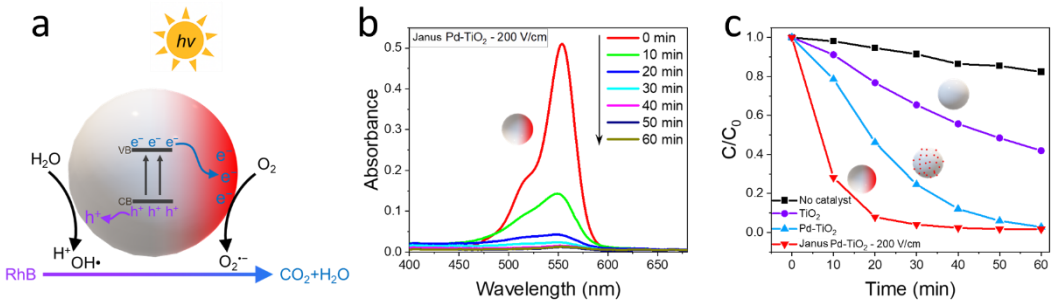

Figure 8 (a) Schéma du mécanisme de photodégradation de 5 ppm RhB par le photocatalyseur Janus Pd-TiO_2. (b) Spectres d'absorption UV-vis des solutions de RhB pendant l'expérience de photodégradation avec des microsphères de photocatalyseur Janus Pd-TiO_2 (synthétisées sous 200 V/cm et irradiées pendant 10 s) à différents temps d'irradiation. (c) Activité de photodégradation de RhB en fonction du temps d'irradiation lumineuse avec différents photocatalyseurs.

La figure 8c compare les performances de dégradation photocatalytique de différents échantillons. Sans catalyseur, seulement 18 % du RhB était dégradé après 60 minutes sous lumière UV, tandis que le TiO_2 pur atteignait 58 % en raison de la forte recombinaison électron-

trou. Le dépôt aléatoire de Pd à la surface du TiO_2 augmente le taux de dégradation à 97 % en 60 minutes. En revanche, le Janus Pd–TiO_2 a atteint environ 96 % de dégradation en seulement 30 minutes, soulignant l'avantage du dépôt asymétrique pour améliorer l'activité photocatalytique. Après trois cycles de tests de stabilité, aucune diminution notable de l'activité photocatalytique n'a été observée. Ces résultats démontrent que le dépôt spatial de cocatalyseurs à la surface d'un semi-conducteur peut améliorer significativement les performances photocatalytiques.

De plus, cette électrochimie bipolaire assistée par la lumière est également compatible avec d'autres métaux, tels que le dépôt asymétrique d'Ag et de Cu sur les microsphères de TiO_2. Cette compatibilité dans différents métaux suggère que cette approche peut être adaptée pour fabriquer une variété de matériaux fonctionnels avancés à base de semi-conducteurs, qui peuvent être appliqués dans la photocatalyse, la remédiation environnementale, la conversion/stockage d'énergie et d'autres domaines connexes.

5. Conclusion

Cette thèse a exploré systématiquement l'application de l'électrochimie bipolaire à la synthèse de matériaux multifonctionnels avancés. Dans un premier temps, une monocouche de graphène a été utilisée comme matériau modèle 2D afin de démontrer le potentiel de l'électrochimie bipolaire pour la fabrication de matériaux multifonctionnels à activité catalytique. Plusieurs résultats confirment ce potentiel : (i) Le comportement catalytique des hybrides Pt–graphène peut être contrôlé avec précision en ajustant la position de dépôt et la quantité d'agrégats métalliques sur la monocouche de graphène, comme le démontrent des nageurs de graphène autopropulsés à directions de mouvement réglables. (ii) La monocouche de graphène a été modifiée sélectivement avec de l'Au, du Pt, du Pd et du Cu. Outre les métaux, elle a également été co-modifiée avec du Pt et soit un composé de coordination, soit une peinture électrophorétique à différents endroits. La multifonctionnalité résultante a été démontrée par le mouvement autonome de la feuille de graphène couplé à une émission lumineuse simultanée. (iii) La monocouche de graphène a été intégrée à des enzymes après modification d'une fine couche d'Au par électrochimie bipolaire. Le rotor enzymatique de graphène obtenu présente un mouvement autonome, dont le comportement dynamique est contrôlé et amélioré sous champ magnétique. (iv) L'électrochimie bipolaire couplée à l'ECL et au champ magnétique a permis la conception de rotors en graphène émetteurs de lumière, où des réactions asymétriques déclenchent une émission ECL localisée, tandis que les forces de Lorentz induisent une dynamique rotationnelle contrôlée. Ces résultats soulignent la capacité de l'électrochimie bipolaire à combiner des comportements catalytiques, optiques et dynamiques au sein d'un même objet.

La stratégie d'électrodéposition bipolaire sélective de site a ensuite été étendue aux microfeuilles 2D de Ti_3C_2. Nous avons démontré que la réduction superficielle spontanée de Ti_3C_2 pouvait être supprimée en milieu acide, permettant ainsi une modification sélective de l'or dans la solution massive. L'immobilisation sur des substrats en verre a encore amélioré la sélectivité du dépôt métallique. Ces résultats de validation de principe ont confirmé la faisabilité de l'électrodéposition bipolaire d'autres matériaux 2D.

Enfin, l'électrochimie bipolaire assistée par la lumière a été appliquée aux microsphères semi-conductrices de TiO_2. En couplant l'excitation lumineuse au champ électrique, les porteurs de

charge photogénérés ont été séparés de part et d'autre, et des photocatalyseurs Janus Pd- TiO_2 à morphologie ajustable ont été synthétisés. Ces photocatalyseurs ont montré une activité photocatalytique nettement accrue, avec une dégradation du RhB plus de cinq fois supérieure à celle du TiO_2 pur.

Ces résultats ont démontré que l'électrochimie bipolaire permet d'intégrer plusieurs composants fonctionnels sur un même objet, permettant ainsi la fabrication de matériaux multifonctionnels avancés.

Preface

Bipolar electrochemistry is an established electrochemical technique that enables simultaneous oxidation and reduction reactions at the opposite extremities of an object without the need for a direct physical connection to a power supply. This wireless approach allows site-selective modification of a wide range of materials, from conductors to semiconductors. These features make it particularly attractive in areas such as electroanalysis, motion generation, and, especially the synthesis of asymmetric particles.

In recent years, bipolar electrochemistry has developed as a powerful strategy for the wireless functionalization of various materials. It has been successfully employed to construct Janus structures with numerous types of objects. However, the potential of bipolar electrochemistry for the controlled synthesis of novel multifunctional materials, particularly for catalytic applications, remains insufficiently explored. The objective of this thesis is to further explore the application of bipolar electrochemistry for the synthesis of advanced functional materials and to investigate their potential use in the field of catalysis.

The Chapter 1 introduces the fundamental principles of bipolar electrochemistry and its various applications, including the synthesis of Janus objects, bipolar electrochemiluminescence, the fabrication of gradient materials, and motion generation.

Chapter 2 presents bipolar electrodeposition with high spatial precision on two-dimensional (2D) graphene monolayers for the synthesis of functional graphene monolayers and highlights their applications in self-propelled swimmers, analytical chemistry, electrochemiluminescence, and enzymatic energy conversion systems.

Chapter 3 briefly presents the potential of bipolar electrochemistry in modifying alternative 2D materials.

This thesis also demonstrates the application of bipolar electrochemistry for the controlled modification of semiconductors. In Chapter 4, photochemistry is combined with bipolar electrochemistry to achieve precise modification of semiconductor materials and reveals the significant potential of the resulting photocatalysts for environmental remediation.

Finally, the manuscript ends with a conclusion and perspectives chapter to discuss further developments that can be envisioned for the more or less near future.

Chapter 1 Introduction to bipolar electrochemistry

Bipolar electrochemistry (BPE) is a unique wireless technique that utilizes conducting or semiconducting materials as bipolar electrodes to facilitate redox reactions to occur simultaneously at their different extremities. This wireless feature distinguishes bipolar electrochemistry from conventional electrochemical methods.

The concept of bipolar electrodes can be traced back to the early 20th century, when such configurations were first employed in industrial applications, such as in metal refining and extraction (Figure 1-1).[1] Later, in the 1960s, bipolar electrode systems were utilized in fluidized bed reactors, further confirming the possibility to induce redox reactions in dispersed conductive particles without direct connections. [2-4] But it was only during the mid-1980s that the possibility to carry out redox processes on micrometer scale conductive objects was first demonstrated experimentally.[5] Over the last two decades, BPE has attracted renewed interest due to its simplicity, versatility, and the ability to spatially control surface modifications.[6-9]

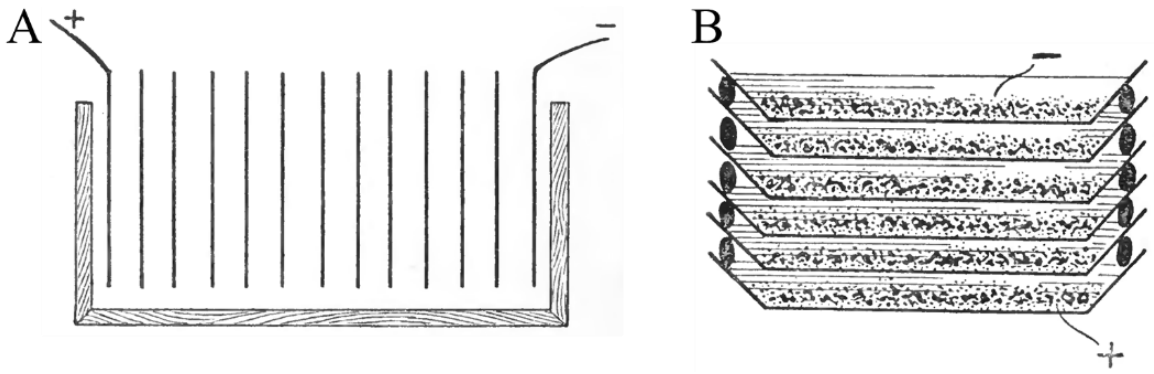

Figure 1-1 Schematic illustration of BPE for industrial applications. (A) Serial bipolar system used in industrial copper refining. In this system, the tank is filled with anode slabs acting as bipolar electrodes. Pure copper is deposited on one side of each slab, while crude copper is simultaneously dissolved from the opposite side. (B) Stacked bipolar electrochemical system for lead reduction. Powdered galena is packed on antimonial-lead trays separated by insulating rings and immersed in dilute sulfuric acid. Multiple trays are arranged in series, with only the top and bottom trays connected to the power supply, while the intermediate trays act as bipolar electrodes. Adapted from Ref. [1].

Today, bipolar electrochemistry is widely applied in fields such as materials science[10, 11], chemical synthesis[8, 12], sensing[6, 13], and energy conversion[14]. The wireless nature of bipolar electrochemistry enables novel reaction strategies, enhancing its relevance and potential for innovation in electrochemical research and technology development. This chapter aims to review the basic principles and various applications of bipolar electrochemistry.

1.1 Principles of bipolar electrochemistry

When it comes to electrochemistry, many people initially think of the classical three-electrode systems. Figure 1-2A presents the schematic diagram of a three-electrode system, the potential of the working electrode is controlled by a potentiostat with respect to a reference electrode. Theoretically, when the potential of the working electrode is set to be more negative than the formal redox potential of electroactive species in the electrolyte solution, electrons are transferred from the electrode to the electroactive substance, causing a reduction reaction. Conversely, when the electrode potential is set to be sufficiently positive, electrons are transferred from the electroactive substance to the electrode, resulting in an oxidation reaction.

Here the driving force for electron transfer arises from the interfacial potential difference between the electrode and the electrolyte solution.[15, 16]

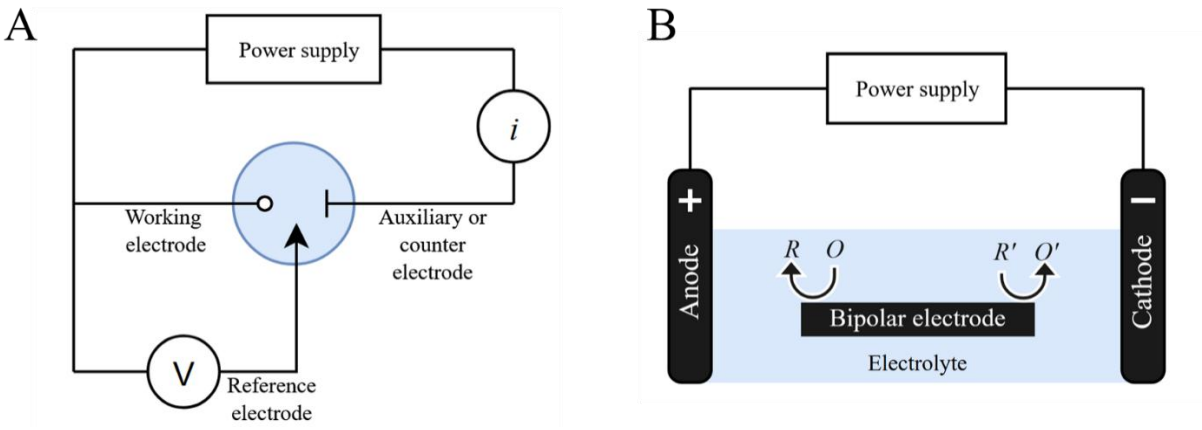

Figure 1-2 Schematic diagram of (A) a three-electrode electrochemical system and (B) a bipolar electrochemical system.

In contrast, in bipolar electrochemistry, the driving force of the reaction originates from an external electric field applied between two feeder electrodes (also called driving electrodes) positioned in the electrolyte solution. An object (the bipolar electrode) immersed in the electrolyte solution experiences an induced polarization without direct electrical contact to the external circuit. This feature defines the concept of BPE, enabling spatially separated oxidation and reduction reactions to occur simultaneously at the opposite extremities of a single object. The operational principle of BPE is based on the potential gradient in the electrolyte solution, where asymmetric redox reactions occur on bipolar electrodes[7]. As shown in Figure 1-2B, when a voltage is applied between the two driving electrodes (the anode and cathode of the power supply), an electric field is generated in the electrolyte solution. The bipolar electrode placed in this electric field experiences a potential difference along its length. The extremity of the bipolar electrode that is facing the cathode will be positively polarized, and oxidation reactions will take place at this polarized anode. Conversely, the opposite extremity of the bipolar electrode is negatively polarized, serves as the polarized cathode and facilitates reduction reactions. Such localized electrochemical activities, induced by the external electric field rather than via a direct connection with a wire, represents an intrinsic difference from traditional electrochemical methodologies.

The types and efficiency of electrochemical reactions occurring on the bipolar electrode depend on several factors, including the potential applied between the driving electrodes, the geometry and conductivity of the bipolar electrode, the conductivity of the electrolyte, and the distance between the two driving electrodes[17]. Adjusting these parameters allows precise control of reaction rates and selectivity, providing considerable flexibility in tailoring electrochemical processes to specific applications.

Bipolar electrochemistry can also be categorized into direct and indirect bipolar electrochemistry[18], based on the reaction mechanism. So far, most electrochemical reactions are direct reactions, meaning that redox reactions occur directly at the electrode/solution interface. In contrast, indirect bipolar electrochemistry does not rely on direct reactions between the targeted species and the electrode surface. Instead, the electrochemical reaction changes

the local environment (e.g. pH) near the electrode surface, which can activate more complex or coupled reactions.

Based on the configuration, bipolar electrochemistry can be divided into closed and open bipolar electrochemistry.[6] Closed bipolar electrochemistry allows oxidation and reduction reactions to occur independently in different electrolyte solutions by placing the two ends of the bipolar electrode in separate electrolyte compartments. Open bipolar electrochemistry enables simultaneous oxidation and reduction reactions at opposite ends of the bipolar electrode by placing it in one electrolyte solution. The majority of this thesis is dedicated to the synthesis of novel multifunctional materials using open bipolar electrochemistry.

The following content of this chapter will present a more detailed description of these distinct operational modes and review the applications of bipolar electrochemistry.

1.1.1 Closed bipolar electrochemistry

In closed bipolar electrochemistry, also referred to the stacked bipolar electrode systems[1], the cathodic pole (δ^-) and the anodic pole (δ^+) of the bipolar electrode are placed in two physically separated compartments, each one containing its own electrolyte solution and a driving electrode. As shown in Figure 1-3A, the anode driving electrode is placed in electrolyte 1, and the cathode driving electrode is placed in electrolyte 2. The two poles of the bipolar electrode extend into each electrolyte accordingly. When the bipolar electrochemical reactions are triggered, the current in this closed configuration flows from the anode driving electrode through electrolyte 1, across the bipolar electrode, and then through electrolyte 2 to the cathode driving electrode. The red dashed line in Figure 1-3A illustrates the distribution of the potential across the closed bipolar system, indicating how the potential distributes from the anode to the cathode. Due to the resistance of the electrolyte solution, the potential drop primarily occurs in the electrolyte between the driving electrodes and the ends of the bipolar electrode, as the resistance of the bipolar electrode itself is negligible in comparison.

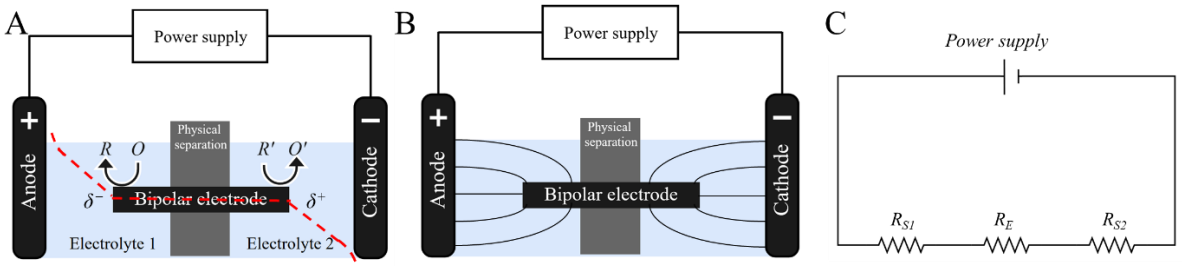

Figure 1-3 Simplified representation of (A) a closed bipolar electrochemistry cell, the red dashed line representing the potential drop across the system. (B) Schematic illustration of the electric field distribution in a closed bipolar system. (C) equivalent electrical circuit of a closed bipolar cell. R_{S1}, R_E and R_{S2} represent the resistance of electrolyte 1, the bipolar electrode (including its interfaces), and electrolyte 2, respectively. Reproduced from Ref. [7, 19].

Figure 1-3B shows a simplified schematic illustrating of the electric field distribution in a closed bipolar system. In this configuration, the two driving electrodes are physically separated, causing the electric field lines to be mainly concentrated around the bipolar electrode. As a result, the electric field lines bend toward the bipolar electrode, which is a consequence of the local variations in the potential across the electrolytes around the bipolar electrode.

Figure 1-3C illustrates the equivalent circuit of the closed bipolar setup, highlighting that the two electrolyte solutions and the bipolar electrode are electrically connected in series. Under ideal

conditions with very low solution resistance, the potential difference between the two ends of the bipolar electrode is approximately equal to the potential difference applied between the two driving electrodes. Therefore, a relatively low voltage is sufficient to trigger the redox reactions at the bipolar electrode.

This configuration has been widely used in analytical electrochemistry and microfluidic systems for sensing, electrocatalysis, and electroanalysis studies.[20, 21] Moreover, since all the current must pass through the bipolar electrode, the system provides the possibility to investigate the Faradaic processes on the bipolar electrode. By analyzing the overall current, one can gain insight into the reaction kinetics and mechanisms occurring at both the anodic and cathodic poles of the bipolar electrode[22, 23].

1.1.2 Open bipolar electrochemistry

In open bipolar electrochemical systems, the bipolar electrode is typically immersed in a single continuous electrolyte solution, with a sufficiently high voltage difference applied between the two driving electrodes. In this configuration, the bipolar electrode experiences a potential gradient along its length, inducing simultaneous oxidation and reduction reactions at its opposite ends. Unlike closed BPE setups, there is no physical separation between the δ^- pole and δ^+ pole of the bipolar electrode.

1.1.2.1 Open bipolar electrochemistry with conducting materials

Currently, most studies devoted to bipolar electrochemistry employ conductive materials as bipolar electrodes. As illustrated in Figure 1-4A, when a voltage difference is applied between the two driving electrodes immersed in the electrolyte, a continuous and, in a first-order approximation, a linear electric field is generated throughout the solution. This description assumes an idealized condition in which the influence of the bipolar electrode on the field distribution is neglected, and the electric field is considered to be uniform and linear throughout the electrolyte. The intensity of this electric field (*E*) is directly proportional to the applied voltage (*U*) and inversely proportional to the distance (*L*) between the driving electrodes. The relationship between these parameters can be described by equation 1.1:

$$E = U/L \tag{1.1}$$

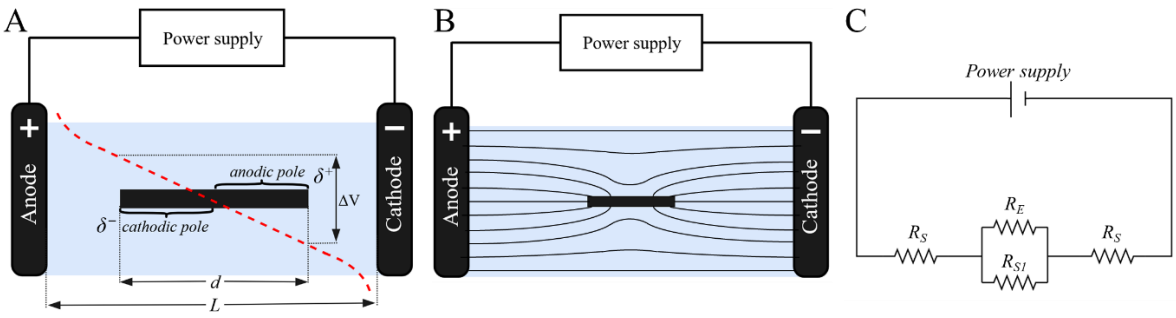

Figure 1-4 (A) Simplified representation of an open bipolar electrochemistry cell with a conducting material as the bipolar electrode, the red dashed line representing the ideal overall potential drop in the electrolyte solution. (B) Simplified schematic illustration of the electric field distribution in an open bipolar system, the electric field lines are represented by black lines. (C) Equivalent electrical circuit of an open bipolar cell. R_S, R_{S1}, and R_E represent the resistance of the electrolyte, of the electrolyte surrounding the bipolar electrode, and of the bipolar electrode, respectively. Reproduced from Ref. [7].

Since the bipolar electrode is a conductor, the potential at any position of its surface is equal. However, the interfacial potential difference between the bipolar electrode and the solution varies along its length due to the presence of the electric field in the solution. This potential difference (*ΔV*) reaches its maximum at the two extremities of the bipolar electrode and gradually decreases towards the center. The *ΔV* can be calculated as follows:

$$\Delta V = E \times d \tag{1.2}$$

where *d* is the length of the bipolar electrode.

Importantly, the value of *ΔV* depends only on two experimental parameters: the intensity of the electric field and the length of the bipolar electrode. It is not affected by the position of the bipolar electrode in the electrolyte, which allows multiple bipolar electrodes to be placed in the same solution and operate simultaneously under the same electric field[24].

Generally, the extremity of the bipolar electrode facing the anode driving electrode is the cathodic pole, while the extremity facing the cathode driving electrode is the anodic pole. To trigger the desired redox reactions, the voltage difference applied between the driving electrodes must be sufficient to produce a *ΔV* that is equal to or higher than the standard potential difference (*ΔE°*) of the target redox couples. This threshold condition is crucial to ensure that the intended electrochemical processes occur efficiently at the two poles of the bipolar electrode.

For the reduction half reaction,

$$Ox + ne^- \rightarrow Re \qquad E_1^\circ \tag{1.3}$$

For the oxidation half reaction,

$$Re' - ne^- \rightarrow Ox' \qquad E_2^\circ \tag{1.4}$$

Consequently, the *ΔE°* is:

$$\Delta E^\circ = E_2^\circ - E_1^\circ \tag{1.5}$$

As mentioned, ΔV_{min} must be not less than *ΔE°* for the two half reactions to be triggered.

In theory, when a voltage is applied to the driving electrodes immersed in an electrolyte, a uniform electric field is generated between them. While when a conductive object is introduced into this uniform field, the local electric field distribution is disrupted. Figure 1-4B illustrates the simplified electric field distribution in an open bipolar system. In contrast to the idealized case, the presence of the bipolar electrode in the electrolyte causes a non-uniform electric field distribution. The electric field lines bend towards the bipolar electrode due to local variations of the potential near the conducting surface, leading to a concentration of the electric field. Further away from the bipolar electrode its influence on the electric field decreases. As a result, the regions far from the bipolar electrode exhibit a relative uniform electric field, where the electric field lines are orthogonal to the driving electrodes.

Figure 1-4C shows the equivalent electrical circuit of an open bipolar cell. In this configuration, the resistance of the bipolar electrode and of the surrounding electrolyte solution are in a parallel configuration. The current can flow either through the bulk solution or through the bipolar electrode, depending on the local resistance. This illustrates that the bipolar electrode is not the only conducting path between the two driving electrodes, and consequently a higher voltage is

necessary to drive the desired electrochemical reactions, especially for objects with nano- and sub-micrometer dimensions.

1.1.2.2 Open bipolar electrochemistry with semiconducting materials

In addition to conducting materials, semiconducting materials can also be used as bipolar electrodes[25], enabling simultaneous oxidation and reduction reactions on a single object. It is well known that semiconducting materials can generate electron-hole pairs when they are exposed to light with a suitable wavelength. Normally, electrons and holes will randomly migrate to the object's surface sites and trigger redox reactions or recombine with each other during the migration process. With a bipolar electrochemistry set-up, it is possible to induce a separation between electrons and holes with the assistance of the present electric field[26-28]. Figure 1-5 illustrates the possible use of a bipolar electrochemistry system with semiconductors as the bipolar electrode. Due to the presence of the electric field in the electrolyte, one side of the object is positively polarized (δ^+) and another side is negatively polarized (δ^-). Then these charges may migrate in opposite directions. However, the situation is not exactly like the one with a conducting object, because in contrast to an electric conductor, a semiconducting object is not equipotential under the influence of an external electric field. This can lead in some cases to the generation of an internal electric field which drives the electrons and holes to opposite extremities in comparison to a conducting object.

These spatially separated charge carriers then participate in redox reactions at their respective ends. Notably, in this case, the driving force to trigger reactions is not directly provided by the electric field, but by the energy of the light. The redox capabilities of the charges is dominated by the bandgap of the semiconductor, while the role of the electric field is just to drive the charge separation.[27]

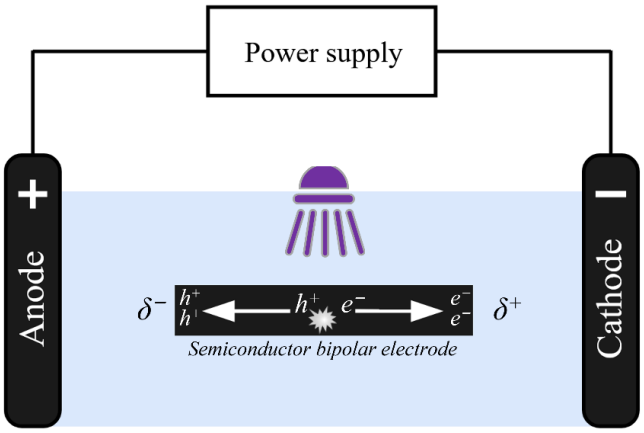

Figure 1-5 Schematic of an open bipolar electrochemistry cell with a semiconducting material as the bipolar electrode. The semiconductor generates electrons and holes under light irradiation, then electrons and holes are separated to different extremities under the influence of the external electric field.

A notable advantage of this light-assisted bipolar electrochemistry approach is its applicability to objects of virtually any size and shape. In particular, it enables the asymmetric modification of nanoscale objects[28], which is extremely challenging when bipolar systems only driven by the electric field.

1.1.3 Indirect bipolar electrochemistry

Indirect bipolar electrochemistry represents an extension of traditional bipolar systems, achieved by modulating the local environment around the bipolar electrode such as local pH or concentration changes.[18] Unlike direct bipolar electrochemistry, where electroactive species participate directly in the redox reactions at the bipolar electrode surface, indirect bipolar electrochemistry uses a first redox reaction to induce some local chemical changes which then in turn allow the non-redox transformation of a precursor into the target species. Figure 1-6A illustrates an example of such a local change, in this case the pH, induced for triggering indirect bipolar electrochemistry. When the applied electric field is sufficiently strong, the two ends of the bipolar electrode can simultaneously drive water oxidation and reduction reactions. The water oxidation generates protons at the anodic pole, leading to a local decrease in pH. Conversely, water reduction at the cathodic pole consumes protons resulting in a local increase in pH. This localized pH change can trigger reactions of pH-sensitive species around the electrode. As shown in Figure 1-6B, a U-shaped platinum wire acting as a bipolar electrode was placed in a solution containing universal pH indicator. A color change is visible after the application of an appropriate voltage. The solution near the anodic pole turns orange (acidic) and the cathodic end turns purple (alkaline).[29] This visual result exemplifies how bipolar electrochemistry can be used to induce indirect chemical reactions by locally modifying the solution environment without direct interaction between the electrode and the precursor of the target species.

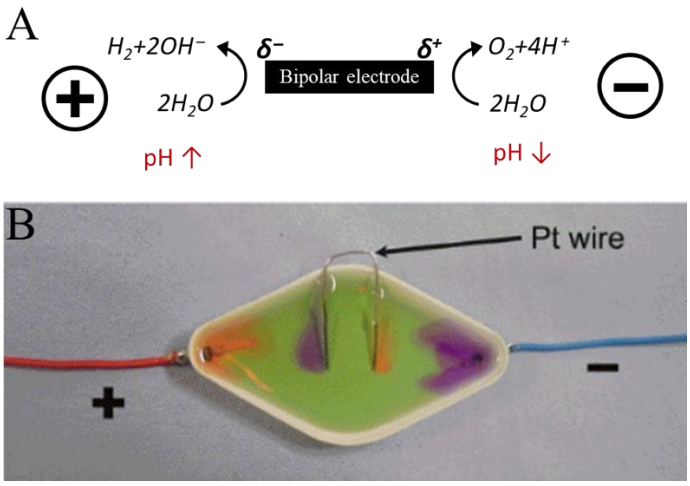

Figure 1-6 (A) Schematic illustration of the induced local pH changes in the electrolyte solution surrounding a bipolar electrode. (B) Bipolar electrochemistry cell filled with universal pH indicator solution with a U-shaped Pt wire as the bipolar electrode, adapted from Ref. [29].

1.2 Applications of bipolar electrochemistry

1.2.1 Wireless synthesis of Janus objects

The unique advantage of BPE is its wireless configuration, allowing redox reactions to occur without direct electrical connection to the object. This feature has been widely exploited for the synthesis of asymmetric macro- and microparticles, especially Janus particles[30], where different materials or surface properties can be introduced on opposite sides of an object.

Janus particles, named after the Roman god Janus, who is depicted with two faces looking in opposite directions, are asymmetric objects composed of two or more areas having different

chemical or physical properties. Janus materials have attracted significant attention due to their unique directional properties and multi-functionality, making them interesting for a wide range of applications, such as targeted delivery of molecules, self-assembly, catalysis, and self-propelled materials.[31, 32]

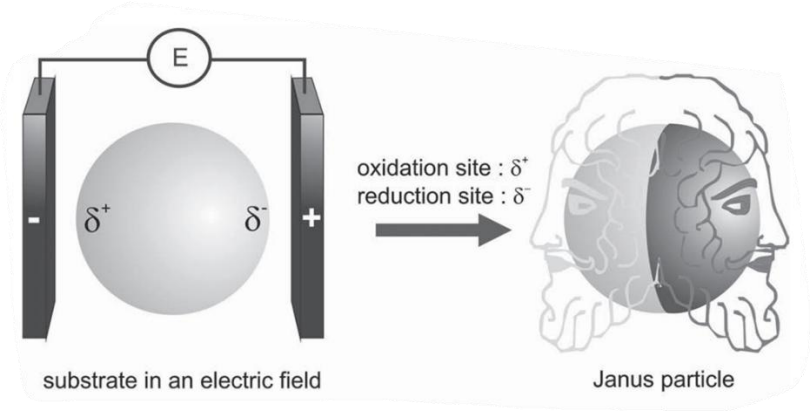

Figure 1-7 Bipolar electrochemistry for the bulk synthesis of Janus particles. Adapted from Ref. [24].

The key challenge in synthesizing Janus particles is the selective surface modification of an object, especially at the micro- or nanoscale. Traditional methods often require complex procedures or multi-step modifications, while bipolar electrochemistry offers a simple, wireless approach for synthesizing Janus particles. Figure 1-7 shows the schematic diagram of bipolar electrochemistry for the synthesis of Janus particles. By placing a conductive or semiconductive object in an electric field within an electrolyte solution, simultaneous oxidation and reduction reactions can be induced at opposite ends of the particle to trigger the site-selective surface modification.

1.2.1.1 Wireless synthesis of Janus objects with conducting materials

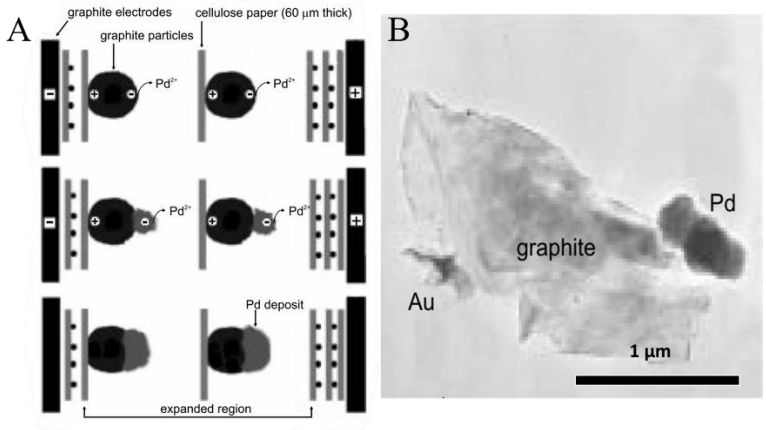

Figure 1-8 (A) Schematic representation of the preparation of a catalyst by bipolar electrodeposition. (B) Transmission electron microscope (TEM) image of a graphite particle modified with gold and palladium clusters at opposite ends. Adapt from Ref. [33].

To date, a wide range of Janus particles have been successfully synthesized via bipolar electrochemistry, utilizing various materials as bipolar electrodes. The earliest demonstrations of Janus particle synthesis via bipolar electrochemistry primarily focused on conducting materials, such as carbon-based materials and metal particles. In 1999, Bradley et al. reported the use of BPE for the contactless asymmetric electrodeposition of Pd clusters and Au clusters onto the opposite ends of graphite microparticles[33] (Figure 1-8). This work provided the fundamental

proof-of-concept for wireless bipolar electrochemical deposition and opened the door for the synthesis of asymmetric structures using simple experimental setups.

Among the diverse strategies developed since then, capillary-assisted bipolar electrodeposition is a particularly effective technique for achieving highly controlled Janus modification[34-37]. This technique is inspired by capillary electrophoresis, involving the placement of a conductive object, for example carbon fiber or nanotube, in a narrow capillary filled with electrolyte. When a voltage is applied across the capillary, a uniform electric field is generated along the axial direction, which can polarize the object and drives simultaneous redox reactions at its two ends. The major advantage of capillary-assisted bipolar system is that it allows the application of a high electric field, an important parameter for bipolar electrodeposition on objects of small dimensions.

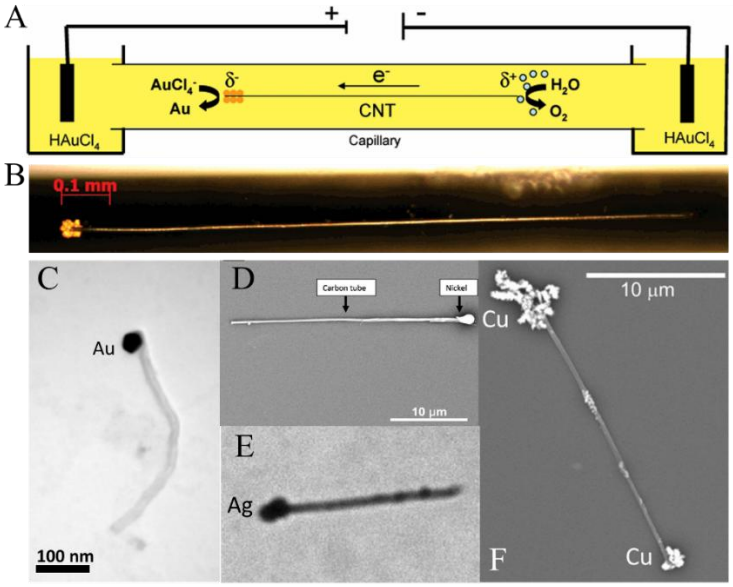

Figure 1-9 Capillary-assisted bipolar electrodeposition. (A) Capillary filled with an aqueous CNT/$AuCl_4^-$ suspension dipping into the two reservoirs of a capillary electrophoresis setup. (B) Optical micrographs of a carbon fiber inside a glass capillary with gold deposition by bipolar electrochemistry. (C) CNT modified on one end with a gold deposit. Adapted from Ref. [37]. (D) Carbon microtube modified at one end with nickel clusters. (E) Carbon microtube with silver clusters mofified at one end. (F) Carbon microtube modified at both ends with copper clusters of different size. Adapted from Ref. [34].

A representative example of this technique was reported by Warakulwit et al., who demonstrated the formation of Janus-type carbon nanotubes (CNT) via selective bipolar electrodeposition of gold nanoparticles[37] (Figures 1-9A-C). In their system, carbon nanotubes positioned in the capillary were subjected to an axial electric field, resulting in gold deposition at the cathodic pole of the carbon nanotubes. This system allows flexible replacement of the metal precursor to meet various application demands.[34] For instance, nickel, silver, or copper can be selectively deposited at one end of the carbon microtubes by simply changing the metal salt in the electrolyte solution, and both ends can be modified with metal clusters by changing the electric field direction in the capillary (Figures 1-9D-F). Moreover, the size of the deposited metal clusters can be fine-tuned by adjusting the deposition time. In addition to single-metal deposition, the method also enables the formation of bi-functional Janus structures. For example, when carbon nanotubes are placed in a mixed solution of a copper salt and pyrrole, bipolar electrodeposition results in the polymerization of pyrrole at the anodic end and the reduction of copper ions at the cathodic end.[34] This leads to carbon nanotubes asymmetrically

functionalized with entirely different materials on each side, further highlighting the versatility of this capillary-assisted BPE approach.

However, the capillary-assisted bipolar electrodeposition system is only suitable for particles with high aspect ratios, and the yield of the modification significantly declines for low aspect ratios or isotropic particles. This limitation partially arises from the fact that under the influence of high electric fields, Joule heating and electrophoretic effects induce convective flows that can cause particles to rotate, thus making it impossible to focus the bipolar reaction only at a specific area of the object. For larger low aspect ratios particles (e.g., millimeter and centimeter scale), one straightforward solution is to fix them on an insulating substrate and then place them in the bipolar cell. For sub-millimeter, micrometer, and nanometer scale particles, more refined strategies are required.

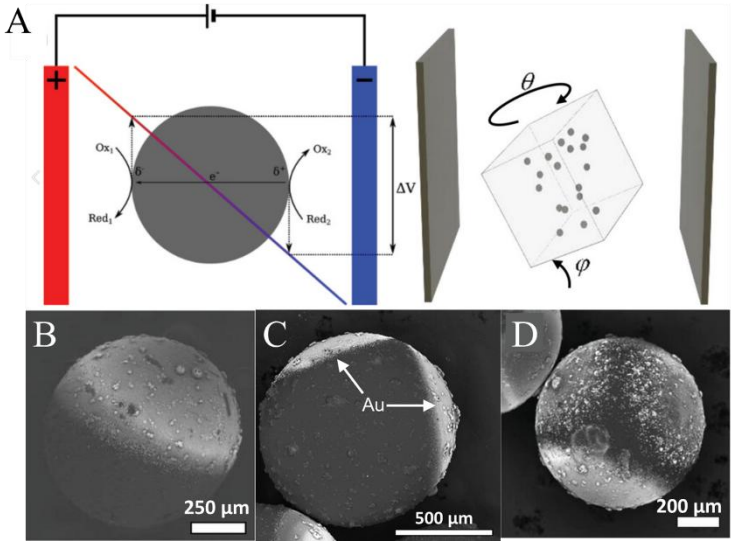

Figure 1-10 (A) Schematic representation of the principle of bipolar electrochemistry and setup for the deposition of patches at a controllable position on the surface of the glassy carbon beads. A gel, containing the glassy carbon beads and the metal precursor, is poured into a cubic mold. (B) Scanning electron microscope (SEM) image of glassy carbon beads with half-spherical surface modification with gold clusters. (C) SEM image of glassy carbon beads with two gold patches positioned at an angle of 90°. (D) SEM image of glassy carbon beads with three gold patches along three different axes forming 90° angles. Adapted from Ref. [38].

To address this challenge, the introduction of gelling agents into the reaction compartment of the bipolar cell allows suppressing the rotation of the suspended objects during the application of the electric field.[24] This approach enables precise control over metal deposition on both high aspect ratio objects such as carbon nanotubes and isotropic substrates like glassy carbon spheres. By increasing the viscosity of the electrolyte in the reaction component, the system becomes less sensitive to the size and shape of the object, and a high modification yield (up to 80%) can be achieved. In addition to improving modification yield, the use of gel in bipolar electrochemistry enables metal deposition on micro- and nano- scaled particles with high spatial precision. By tuning the experimental conditions, the shape of the deposits can be also controlled. Specifically, for moderate electric fields, metal clusters are confined to just a fraction of the hemisphere of the glassy carbon particles. Increasing the electric field intensity or particle size leads to a larger deposition area, while decreasing the electric field intensity allows the metal deposition to occur on a small surface fraction or even to form an isolated metal dot. These results clearly demonstrate that the deposit area can be fine-tuned from full hemispherical coverage down to

single point deposition with gel-assisted bipolar electrochemistry, offering a powerful control for synthesizing patchy surfaces.

In addition to hemispherical and patchy deposition, the gel-assisted bipolar electrochemistry can produce precise metallic rings on spherical particles[39]. This phenomenon arises when the migration rate of ions within the gel exceeds their reduction/oxidation rate, thereby restricting deposition to a narrow ring-shaped region. By adjusting the electric field intensity, the concentration of metal salt, and deposition time, the ring's position and width can be finely tuned. Multiple deposition steps with inversing the direction of the electric field or reorienting the particle further allows the formation of multi-ringed or orthogonal structures, enabling scalable fabrication of complex asymmetric particles.

Building on these results, recent work has proposed bipolar electrodeposition for generating particles with an increasing degree of complexity in terms of surface design. Instead of reversing or changing the direction of the electric field, this strategy introduces rotational control to define the exact number, position, and composition of metal patches on individual particles[38] (Figure 1-10). In this approach, the bipolar electrodes, made of glassy carbon beads, are immobilized in a solidified agarose gel block to suppress rotation, while the gel block is placed into a cubic mold, which can be easily rotated between sequential deposition steps. By carefully aligning the direction of the applied electric field relative to the particle orientation, metal patches can be selectively deposited at predefined surface locations. This enables not only the synthesis of simple Janus particles, but also multi-patch structures with precise angular separation, including two-patch configurations with 90° spacing, or even four distinct metal patches arranged in a chiral geometry.[38]

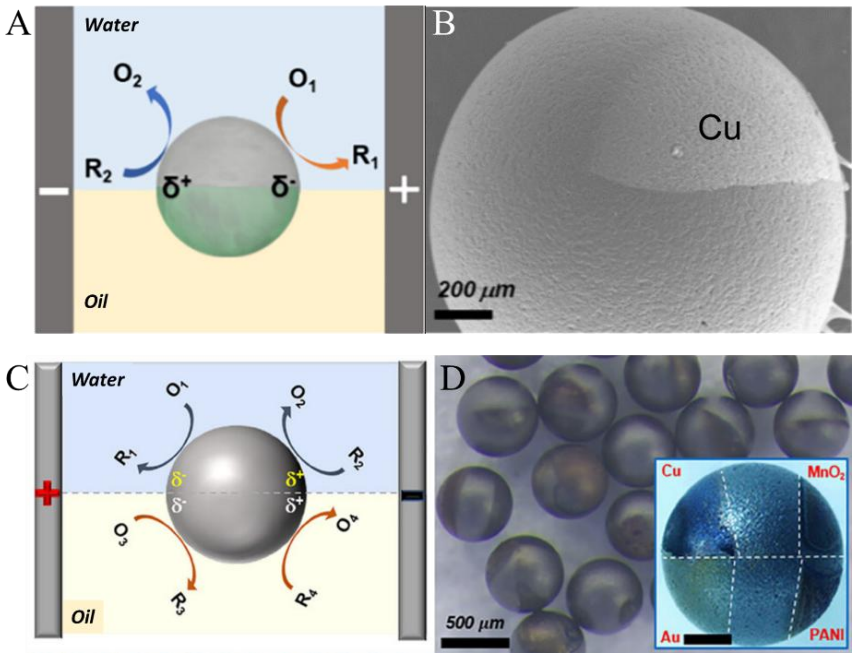

Figure 1-11 (A) Schematic illustration of surface-selective metal deposition on amphiphilic microparticles at the water/oil interface by bipolar electrochemistry. (B) SEM image of a Cu/glassy carbon Janus microbead with fractional hemispherical modification. (C) Schematic illustration of the synthesis of multicomponent patchy microparticles at the water/oil interface by bipolar electrochemistry. Adapted from Ref. [40]. (D) Multiple Cu/MnO_2/Au/PANI patchy microspheres after simultaneous Cu, MnO_2, and Au deposition, as well as aniline polymerization at the w/o interface by BPE. The inset shows a magnified view of a single modified microsphere. Adapted from Ref. [41].

Besides in aqueous bulk solutions, bipolar electrochemistry is also used to modify objects at liquid-liquid interfaces. Fu et al. proposed a method that utilizes a water–organic (water/oil) interface for bipolar modification (Figure 1-11A).[40] By using the immiscibility of the two phases, different redox reactions can be triggered independently on either side of an amphiphilic particle. First, this interfacial setup allows precise patch positioning, leading to high structural asymmetry and multifunctionality. Second, some electrochemical reactions usually require a special solvent environment to occur, and this water/oil system makes it possible to carry out simultaneous dual functionalization. Third, this strategy overcomes the limitation that the size of the modified area is limited to approximately half of the surface of the particle. For example, it is easy to achieve a quarter surface modification on a spherical bipolar electrode at the water/oil interface (Figure 1-11B).

Building on this concept, Xie et al. developed a one-pot approach that enables the simultaneous deposition of up to four different components on microspheres (Figure 1-11C).[41] By positioning amphiphilic glassy carbon beads at the water/oil interface and applying an electric field parallel to the interface, spatially controlled modifications were achieved through simultaneous redox reactions in both phases. The method allows for symmetric, diagonal, or even quadrant-based configurations. For example, in one step, Cu, MnO_2, Au, and polyaniline (PANI) can be deposited at different areas of one microbead (Figure 1-11D). Furthermore, by introducing sacrificial redox species, the size of each deposit can be precisely tuned. This strategy was extended beyond spherical beads to planar poly(3,4-ethylenedioxythiophene) (PEDOT) films, demonstrating the versatility of the method with respect to dimensions and materials.

Beyond direct redox-based modifications, indirect bipolar electrochemistry provides a versatile route to synthesize Janus particles from non-electroactive precursors. As discussed in Section 1.1.3, this strategy usually relies on electrochemically induced pH gradients around the bipolar electrode. Typically, water oxidation at the δ^+ side produces localized acidity, while water reduction at the δ^- side creates an alkaline environment (Figure 1-12A). These local pH changes can trigger the precipitation or polymerization of pH-sensitive compounds, enabling the spatially selective deposition of materials otherwise incompatible with direct electrochemistry.

Using this approach, a wide variety of complex materials can be deposited in an asymmetric way[18]. For instance, silica can be deposited through the sol–gel process, where hydroxide ions generated at the δ^- side catalyse the condensation of Tetraethoxysilane (TEOS) precursors to form polysiloxane layers (Figure 1-12B). Similarly, titanate layers can be formed anodically using preformed colloidal precursors, with the deposit thickness being controllable by tuning the intensity of the electric field (Figure 1-12C).

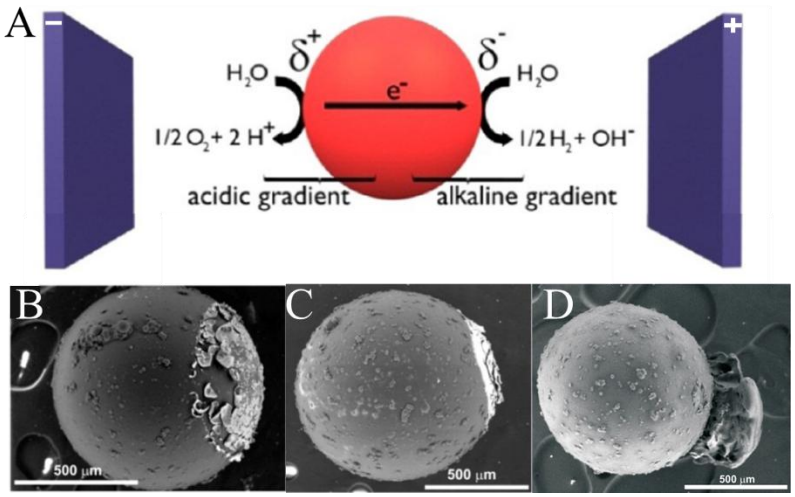

Figure 1-12 Selective surface functionalization via indirect bipolar electrodeposition (A) Scheme of the indirect bipolar electrodeposition principle. SEM images of glassy carbon beads modified with (B) silica, (C) titanate, and (D) electrophoretic deposition paints. Adapted from Ref. [18].

Electrophoretic paints (EP), commonly used as anticorrosion coatings, can also be selectively precipitated due to pH-triggered neutralization (Figure 1-12D). EP form porous polymers, which have great potential as carriers for fixing or delivering molecular compounds. In a similar manner, redox catalysts can trigger polymer formation, resulting in the deposition of polymers [35].

Closed bipolar electrochemical systems can also provide conditions in which the two ends of a single particle are placed in different electrolyte solutions to generate Janus structures. However, this approach is generally limited to relatively large particles, as smaller particles are difficult to use as bridges between the physically separated compartments. By applying an alternating voltage across the driving electrodes, it is possible to induce anodic oxidation on both sides of the bipolar electrode. Using this strategy, Macak's group successfully generated asymmetric TiO_2 nanotube layers on both sides of a titanium foil placed in a closed BPE cell[42]. The resulting nanotube layers exhibited significant differences in diameter and thickness. The method is also extendable to other metals. For example, similar alternating-polarity bipolar anodization has been used to produce asymmetric nano-porous WO_3 layers on both faces of a tungsten foil[43].

1.2.1.2 Wireless synthesis of Janus objects with semiconducting materials

The above discussed Janus particles were synthesized using conductive materials as bipolar electrodes. Since their conductivity is much higher than that of electrolytes, reactions at the two ends can be triggered, as long as the electric field is sufficient. However, the material of bipolar electrode can also be extended to semiconductors, for which reactions cannot be induced only by an electric field. To induce asymmetric modification with semiconducting materials, light-assisted bipolar electrochemistry[25-28] has been developed, where the external electric field is combined with ultraviolet (UV) or visible light to generate charge carriers within the semiconductor. The generated electrons and holes are then spatially separated by the electric field and driven to opposite ends of the particle, where they participate in redox reactions. Ongaro et al. first demonstrated this concept of using bipolar electrochemistry for synthesizing Janus particles from semiconductor materials[25]. Specifically, TiO_2 nanofibers are suspended in an electrolyte containing a gold salt, and an electric field and UV light are applied simultaneously. In this case, the electron-hole pairs generated by UV light are guided to different ends under the

influence of the external electric field. Gold ions are reduced at the end where electrons accumulate, leading to selective deposition of gold clusters on one end of the TiO_2 nanofibers. This work marked the first successful use of light-assisted bipolar electrochemistry for generating semiconductor Janus structures.

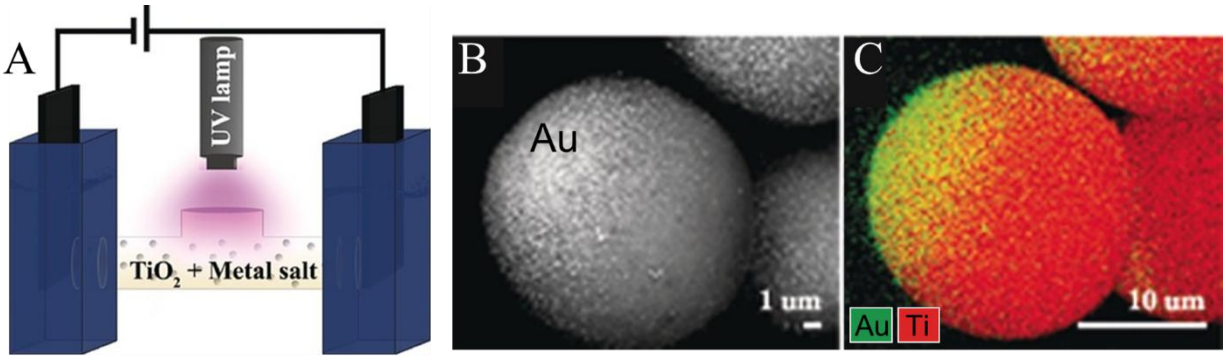

Figure 1-13 Metal deposition on semiconducting materials by light-assisted bipolar electrodeposition. (A) Schematic representation of the bipolar electrochemical cell allowing simultaneous UV irradiation. (B, C) SEM and energy dispersive spectroscopy (EDS) images of gold deposited on TiO_2 microspheres. Adapted from Ref. [28].

Tiewcharoen et al. extended this strategy to isotropic TiO_2 micro- and nanospheres (Figure 1-13).[28] To prevent the rotation under the electric field, TiO_2 particles were fixed in the agarose gel. Under UV light illumination and with an optimized electric field, Au was deposited asymmetrically on the TiO_2 particles. Remarkably, they observed that the reduction of metal ions occurred on the δ^+ side of the semiconducting bipolar electrode, which is contrary to classical BPE systems, suggesting that the charge transport mechanism in semiconductors under the influence of an external electric field is more complex and may involve localized accumulation of photogenerated electrons. This finding confirmed the adaptability of the method to isotropic substrates and revealed new fundamental aspects of semiconductor-based bipolar systems. Melvin et al. further investigated the mechanism of light-assisted bipolar electrochemistry with macroscale hybrid TiO_2-polyaniline objects.[27] Simultaneous exposure to light and electric field triggers large scale charge carrier separation in semiconductors. The photogenerated electrons and holes can be spatially separated over large distances (exceeding several millimeters), as evidenced by the reduction of gold ions. This phenomenon is the consequence of the synergy of the principles of bipolar electrochemistry and semiconductor physics.

Expanding the type of materials employable for light-assisted BPE beyond inorganic semiconductors, Missaoui and co-workers successfully generated Janus particles using fully organic semiconductors based on the conjugated polymer poly[*N*-9′-heptadecanyl-2,7-carbazole-*alt*-5,5-(4,7-di-2-thienyl-2′,1′,3′-benzothiadiazole)] (PCDTBT) as a donor with the fullerene derivative [6,6]-phenyl-C_{61}-butyric acid methyl ester ($PC_{61}BM$) as an electron acceptor.[26] Under light exposure and with a moderate electric field, charge carriers were generated and directed to opposite poles of the particles. Metal precursors such as $AuCl_4^-$ were reduced selectively at one end, forming metal–organic Janus structures. These Janus particles exhibited significantly enhanced photocatalytic hydrogen evolution compared to uniformly coated samples, due to the spatial separation of charge carriers.

1.2.2 Bipolar electrochemiluminescence

Electrochemiluminescence (ECL) is a light-emitting process triggered by electrochemical reactions, combining the high selectivity of electrochemistry with the high sensitivity of optical detection. The mechanism of ECL involves the generation of electroactive species at the electrode surface at a suitable potential. These species then undergo electron-transfer reactions to form excited states and light-emission occurs when these species return to their ground state.[44-46] Theoretically, ECL is essentially a chemiluminescent reaction initiated electrochemically, thus eliminating the need for an external light source. This feature simplifies the detection setup and minimizes background noise originating from the interference with excitation light, providing ECL with a unique advantage in analytical applications.

The integration of bipolar electrochemistry and ECL eliminates the need for a direct wire connection[47], which enables wireless control of the light-emitting reaction at the bipolar electrodes and further enhances its compatibility with many fields. Like conventional ECL, BPE-ECL relies on the interaction between the analyte and a luminescent reagent to generate a signal. The first report on this concept dates back to 2001 when Manz and co-workers developed a wireless BPE-ECL sensing system for bioanalysis[29]. In this design, a U-shaped platinum wire was positioned as a bipolar electrode within a microchannel containing $Ru(bpy)_3^{2+}$ and TPA. When a potential is applied across the channel, ECL emission occurs at the anodic end of the bipolar electrode. Notably, the presence of amino acids can cause a decrease in the intensity of the ECL signal, and the degree of attenuation varies as a function of the nature of the chemical species, illustrating the possibility to use BPE-ECL as an indirect detection scheme.

BPE-ECL has the unique advantage of combining wireless electrochemical activation with optical signal output in a single, simple setup. In typical BPE-ECL setups, one end of the bipolar electrode serves as the sensing site where the analyte reacts, while the other end ensures the ECL emission. This physical separation of functions, combined with the wireless feature, makes BPE-ECL systems exceptionally suitable for miniaturization, integration, and portability. Moreover, the light-emitting output can be easily captured by the naked eye or low-cost optical equipment, enabling non-contact, real-time signal readout. Recent advances have demonstrated the practical utility of this principle in closed bipolar configurations for bioanalysis. For example, Wang et al. developed a cathodic ECL biosensor for blood glucose detection using a closed BPE system.[48] The designed setup consisted of two physically separated cells, a sensing cell containing glucose oxidase for enzymatic oxidation of glucose and a reporting cell where the cathodic ECL reaction occurred between luminophore and co-reactant. The bipolar electrode bridges both cells, enabling signal transduction without electrical wiring (Figure 1-14). This setup not only allowed for wireless electrochemical coupling between analyte recognition and ECL generation, but also produced highly sensitive and rapid responses suitable for real-time glucose monitoring. This electrically triggered, optically readable signal reduces both system complexity and power requirements, positioning BPE-ECL as a highly promising solution for point-of-care testing.

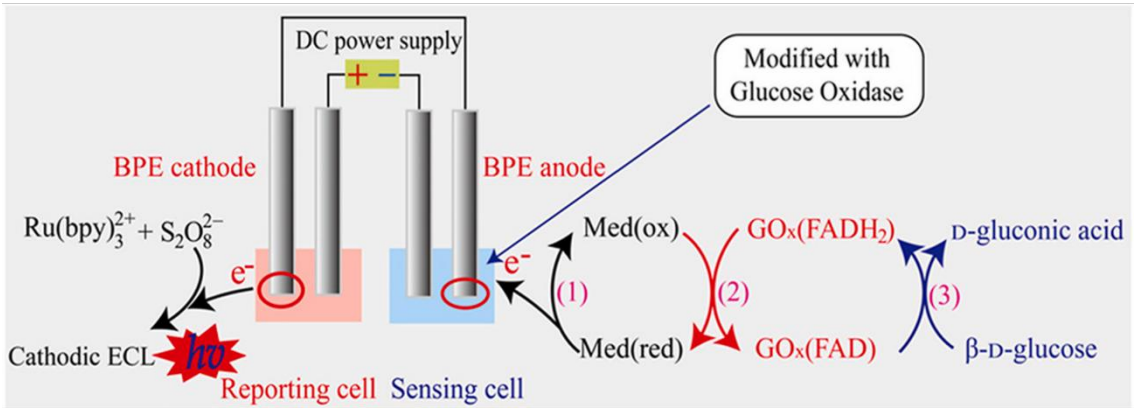

Figure 1-14 Configuration and sensing mechanism of a cathodic ECL glucose biosensor in a closed BPE system. Adapted from Ref. [48].

Another important advantage of BPE-ECL systems lies in the unique signal amplification mechanism. In this context, analyte recognition typically occurs at the non-emitting end of the bipolar electrode, which influences the current flow through the BPE and thereby changes the ECL intensity at the emission end. This process converts subtle molecular interactions into strong, easily detectable light emission, enabling high sensitivity toward trace molecules or chemical reactions at trace levels. The ECL emission also depends on the nature of the luminophore, the material and/or (micro)structure of the bipolar electrodes. To further enhance this signal transduction efficiency, recent studies have explored several strategies for the amplification of ECL signals. For instance, Ganjali's group employed MXene as bipolar electrode material due to its high conductivity and large redox-active surface area.[49] The anodic pole of the bipolar electrode was functionalized with a tyrosine kinase-like orphan receptor 1 (ROR1) antibody and used in an immunoassay employing the ROR1 antibody-modified Ag triangle. The functionalized bipolar electrodes enable ultrasensitive detection of proteins and amplify ECL signals in response to immunobinding events, achieving an ultrawide dynamic range and high accuracy using minimal sample volume via three dimensional (3D) printed microchannels. In addition to changing the material of the bipolar electrode, tuning the conductivity of the electrode by reducing $HAuCl_4$ to Au nanoparticles at the cathodic pole can also enhance the ECL response of the bipolar system[50].

BPE-ECL systems are particularly well-suited for multiplexed detection and high-throughput arrays.[51-53] Multiple bipolar electrodes can be placed within the same electrolyte solution under an external electric field and activated simultaneously. This configuration allows for the simultaneous analysis of multiple targets or samples with a single system, significantly improving detection efficiency and throughput. Hsueh et al. developed an advanced BPE array design that supports multiplexed detection and chemical imaging.[54] Their system integrated 9×10 matrices of microfabricated BPEs in a closed bipolar cell, where tuning the area ratio A_c/A_a and the driving voltage enabled control over ECL sensitivity and linear range. The devices can be used for imaging H_2O_2, provide time-lapse images for the diffusion and dilution of H_2O_2, as well as multiplexed deoxyribonucleic acid (DNA) detection.

Furthermore, by integrating microbeads, microelectrodes, or light-emitting diodes (LED), complex luminescent arrays can be integrated in a single device.[55] These arrays support advanced functions such as spatial resolution[56], color-based discrimination[57, 58], and multi-channel readout[59]. This flexible and scalable architecture makes BPE-ECL a promising tool for

clinical diagnostics, biomarker screening, and food or environmental monitoring, especially in applications requiring a parallel analysis of multiple parameters. Wang's group developed a sensor array based on a multichannel bipolar system for detecting various analytes such as H_2O_2, ascorbic acid, TPA, glucose, and blood sugar, with a single device.[59] After electrodepositing a thin Pt film on the cathodes, the stability of the proposed system was significantly improved. In another study, the reporting function was replaced by a LED. With this design, they constructed a BPE array enabling the quick and high-throughput determination of various electroactive substances with naked eyes.[60] Advances in microfabrication have further expanded the resolution and versatility of BPE-ECL arrays. Li and co-workers utilized a focused ion beam approach to fabricate bipolar nanoelectrode arrays (BPnEAs) for high-resolution electrochemical sensing applications (Figure 1-15).[61] The array design allowed for flexible integration of different electrode materials (e.g., Pt, carbon, Pt/C), making it suitable for comparative electrocatalytic analysis and localized sensing. The spatially patterned nanoelectrodes were combined with $Ru(bpy)_3^{2+}$/2-(dibutylamino)ethanol (DBAE) ECL chemistry, enabling submicron-scale optical readout within high-viscosity media.

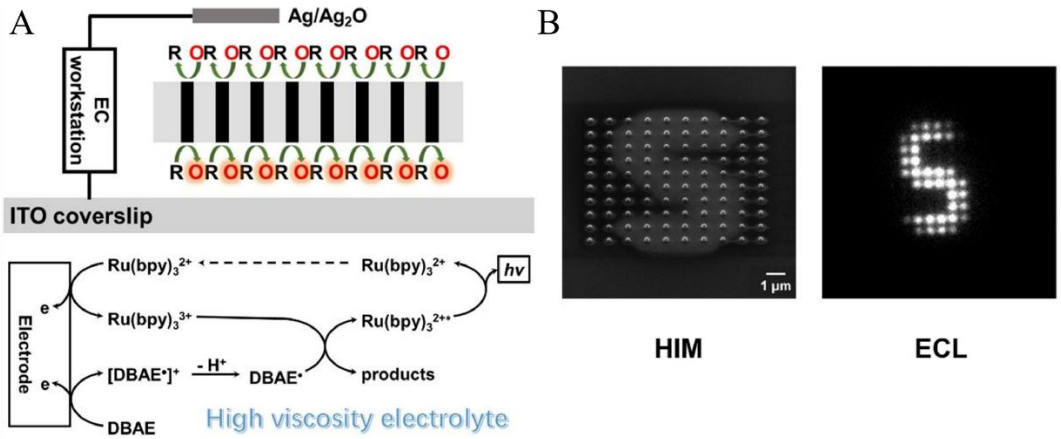

Figure 1-15 (A) Scheme of a bipolar nanoelectrode array-electrochemiluminescent (BPnEA-ECL) sensing device for spatially resolved readout via individual nanoelectrodes in the array (top) and the ECL mechanism of the $[Ru(bpy)_3]^{2+}$/DBAE system (bottom). (B) Helium ion microscopy micrographs of the Pt/C hybrid BPnEA (left) and ECL images detected using the BPnEA-ECL sensor based on a Pt/C hybrid nanoelectrode array with an "S" shape during the application of an increasing voltage (right). Adapt from Ref. [61].

1.2.3 Synthesis of gradient materials

The intrinsic potential gradient along the length of the bipolar electrode under the influence of an electric field is a unique advantage of bipolar electrochemistry, which offers a powerful and unconventional strategy for the construction of material gradients. Such gradients may involve variations in composition, morphology, thickness, or functionality, which can change either continuously or discretely along a given direction. In a classical open BPE system, the polarization potential is highest at both extremities of the object and gradually decreases toward the center. This spatial gradient of interfacial potential enables the simultaneous activation of different electrochemical reactions at different locations along the electrode surface.

The most direct application of this phenomenon is the electrochemical deposition of metals where material is deposited at the cathodic pole of the bipolar electrode in a position-dependent way. For example, Bouffier and co-workers placed an Au plate in a bipolar cell filled with a solution containing a mixture of $CuSO_4$, $NiSO_4$, and $ZnSO_4$, and then applied an electric field.[62]

A series of mixed metal electrodes with different gradients were generated based on the difference in redox potential between the different metal ions. Such a compositional variation directly modifies the optical and electronic properties of the electrode's surface.

In addition to simple metal deposition, this strategy also can be adapted to the synthesis of more complex compounds. It has been shown that gold rods immersed in $Cd^{2+}/S_2O_3^{2-}$ electrolytes under BPE conditions develop a visible gradient of CdS deposition.[63] The deposited material varies from Cd-rich CdS near the cathodic end to S-rich films near the central area, reflecting the gradient in driving force for the redox reactions. Optical images and Auger electron spectroscopy confirmed the chemical variation along the electrode, and the corresponding differences in optical absorption and photoluminescence illustrate the varying functionality along the compositional gradient.

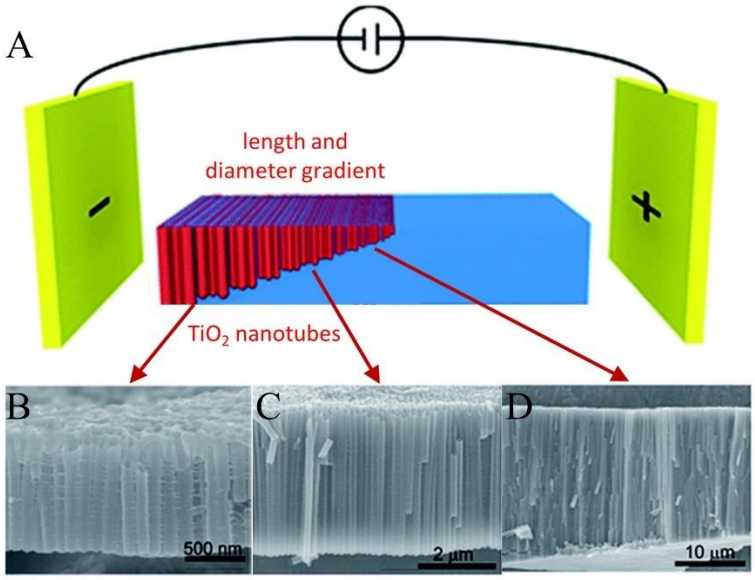

Figure 1-16 (A) Scheme of the formation of a gradient of TiO_2 nanotubes at the anodic pole of a Ti foil acting as a bipolar electrode in the presence of an electric field. (B, C, D) SEM images of TiO_2 nanotubes showing different lengths and diameters at different points. Adapted from Ref. [64].

While deposition dominates many BPE studies, corrosion processes also provide a powerful route to generate gradient materials, particularly through selective oxidation. In this case, the anodic pole of the bipolar electrode undergoes potential-dependent oxidative reactions that may lead to the formation of metal oxides, dissolution of material, or compositional changes at the electrode surface.[65-67]

Loget and co-workers demonstrated that titanium foils subjected to bipolar anodization in fluoride-containing electrolytes produce a gradient array of TiO_2 nanotubes[64] (Figure 1-16). The diameter, length, and wall thickness of the TiO_2 nanotubes changes continuously along the anodic pole of the Ti foil. The electrochemical oxidation rate depends on the value of the local overpotential, which is inherently defined by the geometry of the bipolar electrode and the intensity of the applied electric field. Such TiO_2 gradients are particularly valuable for the study of photoelectrochemical devices, as structure–function relationships can be evaluated in a single experiment.

Another compelling example is the oxidation of Cu foils with bipolar electrochemistry. It was found that a series of distinct oxide bands, including Cu_2O, CuO, and $Cu(OH)_2$, forms at different

positions along the anodic side of the Cu foil.[68] These bands exhibit both chemical and morphological variations, attributed to local differences in electric field strength, reaction kinetics, and solution pH. Such patterns are not only visually striking, but also create possibilities for designing spatially patterned oxide surfaces for catalysis or sensor applications.

The evolution of corrosion volume, quantity, depth, and shape of corrosion pits with different applied potentials can be assessed on a single bipolar electrode. Zhou et al. employed ferritic stainless-steel as the bipolar electrode to study the anodic corrosion process in phosphate-buffered electrolytes, revealing a pitting corrosion gradient where the corrosion volume and area of the stainless-steel surface changed gradually along the length of the object (Figure 1-17). These gradient oxide layers altered the magnetic and electronic properties of the surface, with potential applications in the development of corrosion-resistant coatings.[69]

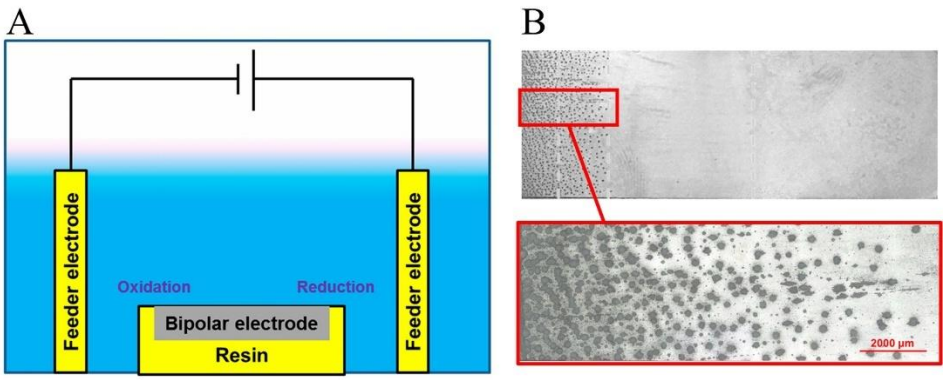

Figure 1-17 (A) Schematic diagram of the bipolar electrochemistry setup for corrosion testing. (B) The surface appearance of the 50 mm long bipolar electrode after 30 min corrosion and the magnified image of the pitting corrosion region on the bipolar electrode. Adapted from Ref. [69].

Anodic corrosion, often considered harmful in traditional systems, becomes a valuable fabrication tool in the frame of BPE. By exploiting the local electrochemical environment, it is possible to create intentionally patterned and functional surfaces through controlled dissolution or oxide formation.

Beyond simple deposition and corrosion, BPE also facilitates the implementation of more complex gradient generating processes, including spatially controlled doping, polymerization, and chemical functionalization. For instance, in conjugated polymers such as poly(3-methylthiophene) (P3MT), it has been demonstrated that bipolar electrochemical doping can induce a color and conductivity gradient across the polymer film. Under the influence of an applied electric field, the oxidation level of the polymer changes with position, leading to a visual gradient from red (neutral) to blue (doped) (Figure 1-18). Similar results were also observed on a PEDOT film with a drastic change in color from deep blue to rather transparent on its anodic side. Also a multicolored gradient was observed on the PANI film after applying an electric field. These results confirm the successful preparation of gradient-doped polymer films.[70]

Gradient polymer brush architectures have also been generated through surface-initiated polymerizations under BPE control. Inagi et al. fabricated 3D gradient poly(N-isopropylacrylamide) (NIPAM) brushes via electrochemically mediated atom transfer radical polymerization using bipolar electrochemistry. In this system, the polymerization of NIPAM started at one end of the bipolar electrode, while the polymerization rate varies at different positions, resulting in a brush

length gradient on a glassy carbon substrate. 3D laser scanning microscopy confirmed that the film thickness increases gradually toward the cathode end of the bipolar electrode. This thickness gradient is related to the ratio of [Cu^{2+}/Cu^{+}] along the substrate, so the width and length of polymer brushes is controllable by adjusting the experimental conditions.[70]

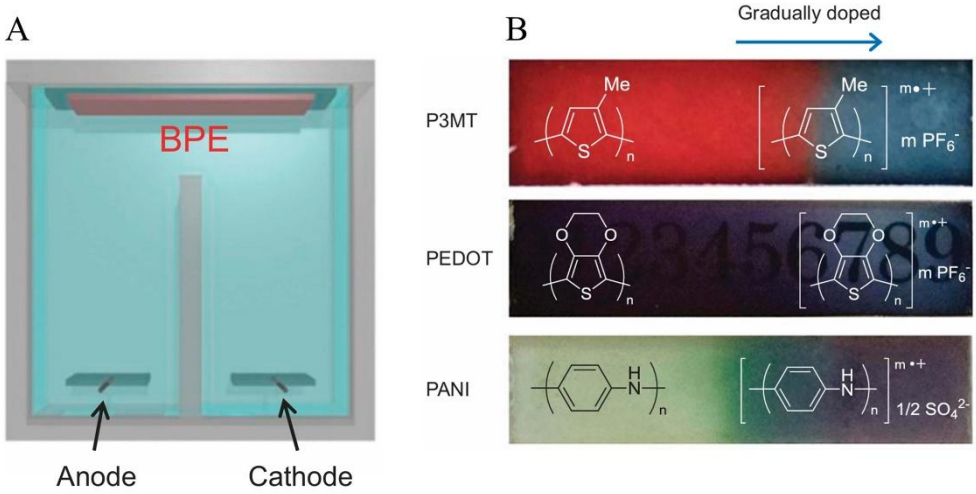

Figure 1-18 (A) Schematic illustration of a U-type electrolytic cell containing a pair of driving electrodes and a BPE covered with a conducting polymer film. (B) Photographs of P3MT, PEDOT, and PANI films gradually doped by BPE. Adapted from Ref. [70].

These advanced approaches underscore the versatility of BPE beyond traditional deposition or etching. The wireless nature of BPE simplifies device fabrication and, more importantly, enables the realization of complex structures that are challenging or completely impossible using conventional electrochemical methods.

1.2.4 Bipolar electrochemistry driven motion

As discussed above, bipolar electrochemistry can benefit from the intrinsic spatial separation of redox reactions to break the symmetry of objects and produce a variety of Janus particles. Such asymmetric particles have found broad applications in the field of self-propelled swimmers/motors.[71-73]

In this context, bipolar electrochemistry is employed to create Janus structures/particles with chemical or physical asymmetry. By tailoring the electrolyte composition, precursor materials, and deposition parameters, different materials such as platinum, gold, and silver can be deposited on one end or a specific area of the particle.[74] These asymmetrically functionalized particles then can act as self-propelled motors when placed in appropriate fuel solutions.

Depending on the surface composition and environmental conditions, different propulsion mechanisms can be activated, such as bubble propulsion, electrophoretic propulsion, etc. The most common propulsion mechanism is the bubble propulsion, where bubbles are generated at one end of the particle, propelling it forward through recoil. Kuhn and co-workers synthesized a series of Pt-functionalized carbon nanotubes via bipolar electrochemistry for the generation of microswimmers.[75] In a diluted aqueous H_2O_2 solution, the Pt-catalyzed decomposition of H_2O_2 generates oxygen bubbles at one end of the CNT, which sets it in motion. Moreover, the type of motion can be switched from linear to circular by tuning the position of the Pt cluster (Figures 1-19 A and B).

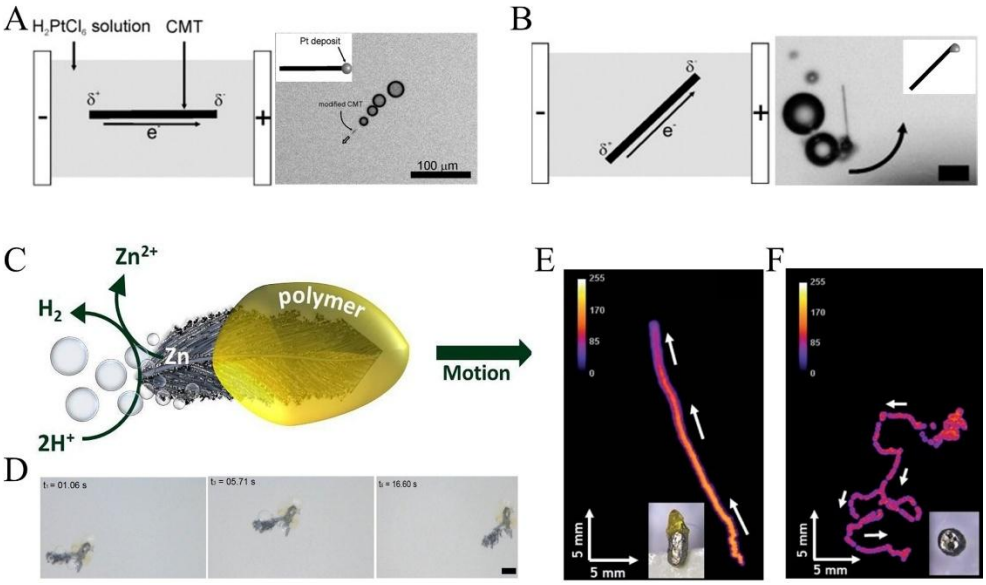

Figure 1-19 Examples of using bipolar electrochemistry for generating swimmers. Schematic illustration of Pt deposition on a CNT (A) when it is parallel to the electric field at the beginning of the electrodeposition process and the linear motion photograph of the obtained Pt-CNT microswimmer, (B) when the CNT is not parallel to the electric field at the beginning of the electrodeposition process and the resulting counter clockwise rotation of the microswimmer, scale bar 10 µm. Adapted from Ref. [75]. (C) Propulsion mechanism of a Zn dendrite modified with polymer deposit and (D) time-dependent motion of a Zn/polymer dendrite in 0.5 M H_2SO_4 solution. Scale bar: 200 µm. Adapted from Ref. [76]. Tracks of the maximum light intensity of (E) polymer-modified and (F) unmodified Mg swimmers moving at the surface of a 1 mM $Ru(bpy)_3(PF_6)_2$, 20 mM $K_2S_2O_8$, and 20 mM H_2SO_4 in H_2O/acetonitrile (1/1) solution. Inset: optical pictures of the particles. Adapted from Ref. [77].

Beyond propulsion in H_2O_2 solution, Fattah et al. developed a self-propelling microswimmer based on the self-corrosion of zinc, where asymmetry was created via indirect bipolar electrodeposition of an electrophoretic paint layer.[76] This approach enabled localized polymer deposition on one side of the Zn dendrites, resulting in an asymmetric object that could autonomously generate hydrogen gas in acidic media without the need for external fuels like H_2O_2 (Figure 1-19C). The localized gas evolution at the uncoated zinc surface induced a directional thrust, propelling the particle forward in a controlled manner (Figure 1-19D).

Building on this concept, Salinas and co-workers reported chemiluminescent Janus microswimmers. Mg particles were first shaped via bipolar electromilling and then asymmetrically modified with a polymer layer by indirect BPE.[77] When placed in a solution containing $Ru(bpy)_3^{2+}$ and $S_2O_8^{2-}$, these particles exhibited autonomous motion via bubble propulsion driven by the spontaneous redox reactions occurring on the Mg. Notably, this motion was accompanied by light emission arising from an interfacial chemiluminescence (CL) process triggered at the unmodified section of the particle. The degree of asymmetry, precisely controlled during the deposition process, dictated the trajectory of the swimmer, with the unmodified particle showing random motion and the asymmetrically modified particle exhibiting highly linear motion (Figures 1-19E and F).

In addition to generating asymmetric, self-propelled particles, bipolar electrochemistry can also serve as a direct driving mechanism for the motion of the bipolar electrodes.[14] When conductive objects are placed in a uniform electric field, the polarization leads to asymmetric redox reactions at opposing ends, typically oxidation at the anodic pole and reduction at the cathodic pole, resulting in gas evolution, or the generation of local concentration changes, especially pH gradients around the object.

These gradients generate electrophoretic forces, which can induce propulsion of the object. In this case, the bipolar object itself is both the reaction site and the moving body, eliminating the need for external fuels or pre-patterned structures. For instance, a Zn dendrite has been observed to migrate in the electric field due to the BPE-induced surface reduction and dissolution of Zn.[78] The motion direction is dictated by the asymmetry in local reaction rates and ionic fluxes around the object, and the speed can be modulated by adjusting the intensity of the electric field or the concentration of the electrolyte.

The electric field can also be employed for bubble propulsion.[79, 80] A representative example of this concept was reported by Loget and Kuhn in 2011[80]. They demonstrated that a spherical object placed in an electric field could generate directional motion due to asymmetric gas evolution at different ends (Figure 1-20A). Under a sufficiently high electric field, water oxidation will occur at the anodic pole to generate O_2 bubbles, while proton reduction at the cathodic pole produces H_2 bubbles. Since the number of moles of produced H_2 is twice that of O_2, this results in an unbalanced driving force from bubble generation between the two sides. This difference creates a net thrust that propels the object toward the anodic side, providing a simple and elegant mechanism for directional movement (Figures 1-20B and C). In a follow-up study, the same group introduced a vertical motion strategy by placing a sphere in a glass capillary and applying a vertical electric field.[81] In this configuration, the water oxidation at the anodic side of the particle is replaced by the oxidation of hydroquinone to improve the propulsion effect, while H_2 is still generated at the cathodic pole via proton reduction. The H_2 bubbles formed at the bottom created an upward buoyant force that lifts the object against gravity. By carefully tuning the field strength and capillary geometry, their achieved not only upward propulsion but also oscillatory “yo-yo” motion inside the confined space (Figure 1-20D). This anti-gravity strategy can also be combined with ECL to enable a broader range of applications.[82-86]

In addition to the two propulsion strategies mentioned above, the combination of an electric and magnetic field can also give rise to new propulsion mechanisms. Recently, Tieriekhov et al. reported a wireless magnetoelectrochemical rotor, in which rotational motion was induced by the synergistic effect of bipolar electrochemistry and the Lorentz force.[87] In this system, a conductive anchor, acting as a bipolar electrode, was positioned in the bipolar cell. Redox reactions were triggered at the two extremities of the anchor, generating a charge-compensating ionic flux along the object. When a magnetic field was applied to this system, the ionic flux experienced a Lorentz force, which induced a lateral flow of fluid and thus produced an additional driving force, causing the strip to rotate. The direction and speed of rotation could be fine-tuned by adjusting the orientation of the magnetic field, the intensity of the electric field, and the length of the bipolar electrode. (Figures 1-20E-G).

In addition to the above examples, bipolar electrochemistry can also drive objects to produce deformation and even generate regular shape oscillations. This electric field-induced deformation can be directly used for electrochemical sensing.[88-90]

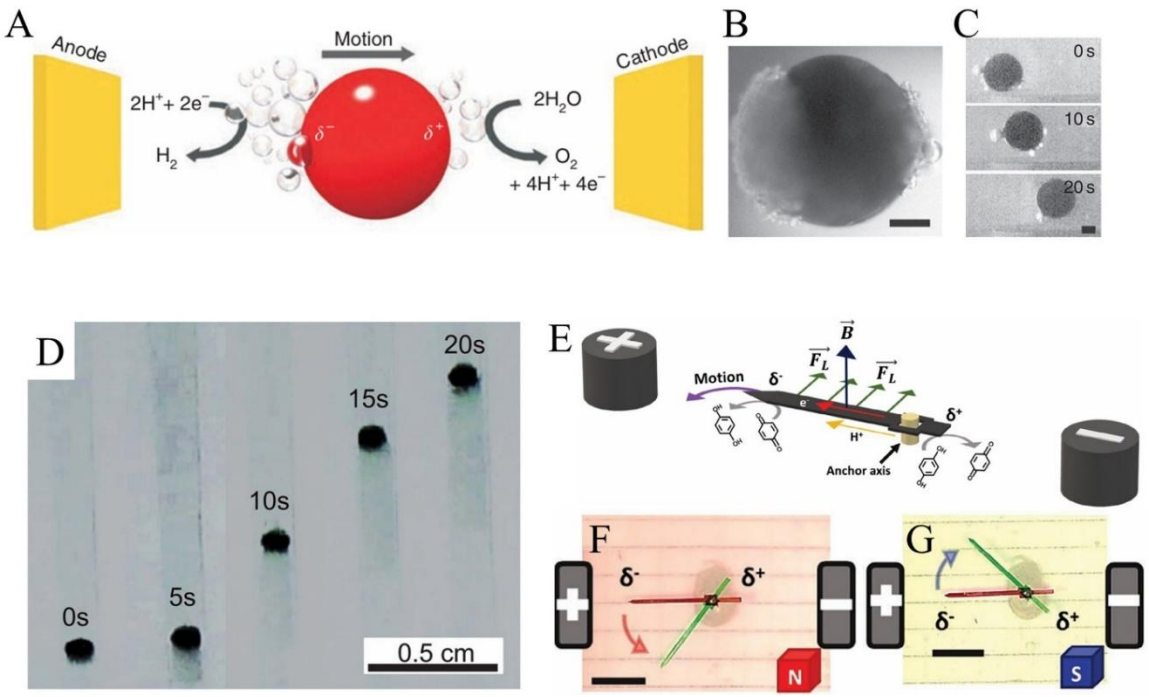

Figure 1-20 Examples of motion induced by bipolar electrochemistry. (A) Scheme of water splitting by bipolar electrochemistry. (B) Optical micrograph of a spherical object exposed to an electric field in aqueous 24 mM H_2SO_4. The left part of the bead is the cathodic pole where H_2 bubbles are produced and the right part is the anodic pole where O_2 bubbles are produced. Scale bar 250 µm. (C) Translational motion generated with a glassy carbon sphere in a microchannel exposed to an electric field in 7 mM H_2SO_4. Scale bar 100 µm. Adapted from Ref. [80]. (D) Series of optical micrographs showing the rising of a carbon bead under the influence of an electric field in a glass capillary. A cathode driving electrode was placed at the top and an anode driving electrode at the bottom of the glass capillary. Adapted from Ref. [81]. (E) Schematic illustration of the wireless induction of rotation of a carbon strip acting as a bipolar electrode positioned between two driving electrodes. The anchor axis is located at the anodic pole of the device, with a representation of the associated electrochemical reactions, the magnetic field (B) and the Lorentz force (F_L). Optical pictures of the dynamic response of the rotor under the influence of an electric field in the presence of (F) north pole up and (G) south pole up. Adapted from Ref. [87].

1.3 Motivation and aims of the thesis

Bipolar electrochemistry, as a versatile electrochemical technique, demonstrates significant potential in materials science and electrochemical analysis. The most prominent advantage of BPE is that redox reactions can be triggered at the two ends of a conducting or semiconducting object without any direct wire connection, making BPE highly attractive for applications such as asymmetric surface modification, propulsion, and wireless sensing. As illustrated above, BPE has been successfully applied to the synthesis of Janus particles, the construction of bipolar electrochemiluminescent sensors, the fabrication of gradient materials, the design of self-propelled objects, and the generation of motion.

Despite these promising developments, most current research in BPE focuses on one dimensional (1D) or 3D conducting objects, while studies on 2D materials and semiconducting materials remain scarce. In comparison with 1D and 3D materials, modifying 2D materials is more challenging because current approaches typically functionalize the entire surface, and achieving spatially precise modification remains difficult. Moreover, the applicability of BPE-driven surface modification to diverse materials is not yet fully explored, which limits its broader application in the fabrication of multifunctional or structurally complex materials. This is particularly important for applications in catalysis, sensing, and energy-related fields.

The aim of this thesis is to use BPE to explore its potential for precise and controllable surface modification of novel materials, broadening its scope from 1D or 3D to 2D systems and from conductors to semiconductors, and to evaluate its applicability for designing advanced functional materials.

In the following parts of the document, Chapter 2 introduces the precise modification of two-dimensional materials (i.e. a graphene monolayer) through BPE. This includes the design of multifunctionalized graphene and the investigation of the potential applications in various fields such as catalysis and sensing. Chapter 3 extends this approach to other types of 2D materials. In the final chapter, we introduce the BPE-based modification strategy to semiconductor materials, and investigate how these modifications influence their photocatalytic performance.

Chapter 2 Bipolar electrochemistry on graphene monolayers

2D materials have attracted a lot of attention in materials science, physics, chemistry, and energy-related fields due to their unique structures and outstanding properties.[91-94] Compared with bulk materials, 2D materials possess atomic-scale thickness, high specific surface area, and excellent electronic, thermal, and mechanical properties, giving them enormous potential in applications such as catalysis[95], energy storage[96], sensing[97, 98], and electronic devices[99]. Among the numerous 2D materials, graphene is regarded as the "thinnest material" consisting of a single layer of carbon atoms in the form of a hexagonal honeycomb of sp^2-hybridized orbitals. Since it was first discovered in 2004[100], graphene has become one of the most intensively studied materials in many fields.

As discussed in the first chapter, bipolar electrochemistry has shown unique advantages for the wireless and spatially controlled modification of various types of materials. The concept is based on localized oxidation and reduction reactions, which occur simultaneously at the two extremities of an object under the influence of an electric field. This intrinsically leads to a break of symmetry and thus gives the opportunity to generate Janus objects with a predefined architecture. Precise modification has been achieved with 1D- and 3D-based materials. Different metals, metal oxides, molecules, etc., have been successfully deposited on conducting objects (e.g., 1D nanotubes[34, 101], 3D microspheres[24, 30]), and the deposition can be precisely controlled (such as single points, rings, hemispheres) by manipulating the direction and intensity of the electric field[24, 39, 102], which allows one to fine-tune the reaction zone on a bipolar electrode. However, the application of 2D materials as bipolar electrodes remains relatively limited. The atomic-scale thickness, high conductivity, and flexibility of 2D materials make them attractive candidates for BPE-based modification. At the same time, their fragile nature makes them difficult to handle during the modification process, which brings significant challenges to achieving precise modification of 2D materials. In this context, BPE owns a unique advantage, as it enables wireless surface modification without direct physical contact with the target material.

For the modification of 2D materials via BPE, one of the most critical challenges is how to stabilize the ultrathin layers during the polarization process. Due to their atomic thickness, high surface area, and extremely soft nature, 2D materials are highly sensitive to any interference caused by the applied external electric field. As a result, they tend to rotate, fold, or drift, which severely limits the precision of the site-selective modification. To overcome this limitation, two main strategies have been reported. The first strategy is to immobilize the 2D material onto an insulating or poorly conductive substrate, such as a glass slide or a silicon wafer, before placing it into the BPE cell. Zuccaro et al. proposed a site-selective, non-contact strategy to electrochemically modify graphene edges by BPE.[103] In their approach, monolayer graphene sheets were fixed onto an insulating substrate and subjected to bipolar electrodeposition, which enabled the deposition of two different metals (Au and Cu) on opposite sides of a single 2D object. This proof-of-concept clearly demonstrated the feasibility of using BPE for spatially resolved, multi-metal modification of graphene while avoiding direct electrical connections. However, while this method allows controlled asymmetric modification, the intrinsic freedom of the 2D sheet is significantly restricted, and it becomes difficult to fully exploit its function in other fields as a freestanding object. In addition, detaching the modified 2D material from the substrate

without mechanical or structural damage remains a considerable challenge, limiting its broader applicability in fields where pristine freestanding materials are required.

The second strategy is to preserve the freestanding nature of 2D materials by placing them in a confined reaction space, such as a thin liquid film, which acts as a two-dimensional reaction layer. This method avoids direct physical anchoring and allows the sheet to behave as an independent bipolar electrode[104, 105]. For instance, Kankla et al. reported an elegant approach for achieving asymmetric deposition on graphene oxide microsheets by positioning them at the air/liquid interface of bubbles.[106] In this configuration, the thin liquid film of the bubble effectively provided a confined 2D reaction space, thereby enabling wireless site-selective modification of the sheets. Nevertheless, despite these advances, challenges still exist. In many cases, the extremely low thickness and high flexibility of 2D materials make them prone to undesired rolling, folding, or uncontrolled horizontal rotation when subjected to a strong electric field. These instabilities not only hinder reproducibility, but also limit the ability to achieve precise spatial control of the deposition process, underscoring the need for novel strategies to stabilize 2D materials during BPE modification while preserving their intrinsic freestanding character.

In this chapter, we focus on monolayer graphene as a model 2D material and investigate its behavior as a bipolar electrode. By immobilizing the graphene monolayers at the air/water interface and performing site-selective modifications, we aim to explore the possibility of fabricating multi-functional 2D materials via BPE. Furthermore, the catalytic performance of the modified graphene monolayers is evaluated to highlight their potential applications in catalysis.

2.1 Spatial precision tailoring the catalytic activity of graphene monolayers for designing Janus swimmers

In this section, we introduce a novel and straightforward strategy to achieve controlled modification of 2D materials by performing BPE at the air–water interface. As a model system, we focus on the site-selective electrodeposition of platinum on monolayer graphene using H_2PtCl_6 as a metal precursor. When the graphene sheet is positioned between two driving electrodes and subjected to a sufficiently high electric field, asymmetric polarization is induced, enabling the reduction of Pt salt at the cathodic pole once the threshold potential of the involved redox processes is exceeded. By carefully tuning the orientation of the 2D object with respect to the direction of the electric field, we aim to direct deposition toward specific locations such as corners or edges of the graphene monolayer. Moreover, by adjusting the intensity of the applied electric field, the size of the resulting Pt clusters can be precisely controlled.

Subsequently, the potential applications of the obtained hybrid 2D Janus objects are studied in terms of catalytic activity, as visualized by the site-specific decomposition of hydrogen peroxide. The resulting oxygen gas bubbles induce controlled motion, thus qualifying them as self-propelled 2D swimmers. In general, swimmers can collect different types of energy (such as chemical[107-109], magnetic[110], electrical[111], light[112, 113], and thermal energy[114, 115]) and convert them into motion even in a homogeneous environment.[116, 117] The autonomous movement of a self-propelled swimmer is typically due to asymmetric structures or reactions occurring at both extremities of Janus particles.[118] In recent years, a large variety of such Janus swimmers has been developed[119], including nanowires[120], multilayer microtubes[121], Janus spheres[122], etc.

By employing BPE for spatially controlled metal deposition on 2D materials, we expect to demonstrate its versatility for site-selective and tunable modification of 2D systems. The ability to deposit metals with such a high degree of spatial precision is anticipated to open new perspectives for the synthesis of asymmetric 2D-based hybrids, and for revealing the relationship between their structural composition and the resulting dynamic behavior.

2.1.1 Immobilization of freestanding graphene monolayers

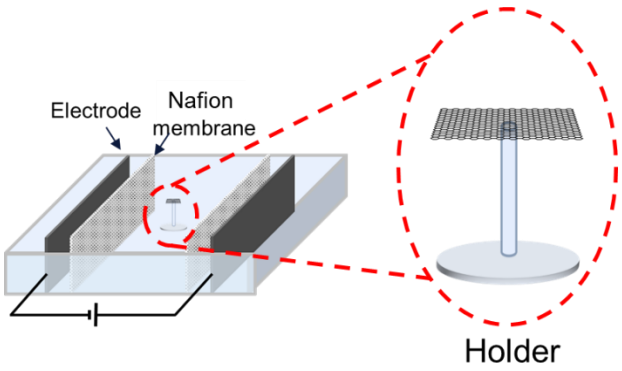

Figure 2-1 Schematic diagram of the bipolar electrochemical setup with a holder for graphene monolayers.

The graphene monolayer was prepared using a wet-transfer protocol[123, 124]. Specifically, a commercial copper-based monolayer graphene strip was immersed in 0.2 M $(NH_4)_2S_2O_8$ aqueous solution for 4 h, enabling the removal of the copper substrate by oxidative etching and thereby

releasing the freestanding graphene monolayer (the preparation procedure is described in detail in Section 2.6). After the etching process, the liberated graphene sheet was thoroughly rinsed and carefully transferred into the reaction compartment to minimize any physical damage or contamination of the prepared samples.

The configuration of the bipolar cell is illustrated in Figure 2-1. It consists of a direct current power supply connected to two driving electrodes, with two Nafion membranes placed in between. The membranes prevent convective flow generated by Joule heating when an electric field is applied, ensuring a more stable electrolyte environment during the experiment. The two driving electrodes are immersed in the electrolyte solution and participate in water electrolysis reactions, water oxidation at the driving anode and water reduction at the driving cathode. In this configuration, given the proton exchange nature of the Nafion membrane, it is reasonable to assume that protons act as the main charge carriers across the membranes. During the application of an electric field, the asymmetric generation and consumption of protons at the two driving electrodes lead to a proton concentration gradient between the two membranes. Such gradients may influence local pH conditions around the bipolar objects. However, in the present study, the duration of the experiments was very short, and fresh electrolyte solutions were employed for each deposition. Therefore, the influence of proton concentration gradients between the two Nafion membranes on the bipolar deposition is considered negligible. This system can thus be approximated as a quasi-steady state ionic transport system, in which protons are the dominant charge carriers.

Owing to its surface hydrophobicity, the graphene monolayer naturally floats at the air-water interface, where its exact position is highly sensitive to external disturbances such as air flow or minor vibrations. To enable spatially well-controlled modification of graphene monolayers via BPE, a dedicated holder was designed and introduced into the bipolar setup. This device consists of an inert column that gently stabilizes the graphene sheet when lowering the liquid level to the top of the inert column, where slight surface tension around column helps holding the graphene sheet (see zoomed image in Figure 2-1). Importantly, the support also allows precise adjustment of the orientation of the graphene monolayer with respect to the applied electric field by controlled rotation, thereby enabling reproducible and site-selective bipolar modification.

To properly place the monolayer graphene, the reaction compartment of the bipolar cell is filled with metal salt solution up to a height slightly exceeding the height of the supporting column. Then the monolayer graphene is carefully placed at the air-water interface of the metal salt solution just above the supporting column with a glass slide. Afterwards, part of the metal solution is slowly removed until the graphene sheet gets in contact with the upper end of the column. The change in surface tension around the supporting column can prevent the graphene monolayer from moving.

2.1.2 Site-selective deposition of Pt on graphene monolayers

After orienting the edge of the graphene square (~2 mm × 2 mm) at an angle of 45° with respect to the direction of the electric field (Figure 2-2A), we first studied the electrodeposition of Pt at the corner of graphene sheets. A series of such corner-modified Pt-graphene hybrid objects was synthesized with different potentials applied between the driving electrodes, and the size of the resulting metal layer was characterized by optical microscopy, SEM, and EDS mapping. According

to the principle of bipolar electrochemistry, the reduction reaction of Pt precursor and the oxidation reaction of water occur at the δ^- and δ^+ sides of the monolayer, respectively.

According to the principle of bipolar electrochemistry, the theoretical minimum voltage (V_{min}) that needs to be applied to the driving electrodes can be calculated as follows:

$$V_{min} = \frac{\Delta E^o}{d} \times L \tag{2.1}$$

where ΔE^o is the difference of the standard potentials of the two redox reactions, *d* is the length of a bipolar electrode along the direction of the electric field, and *L* is the distance of two driving electrodes. The difference in standard potentials (V vs. standard hydrogen electrode) between the reduction reaction (Eq. 2.2) and the oxidation reaction (Eq. 2.3) is 0.5 V. For a 2 mm × 2 mm graphene monolayer, the length of the diagonal is about 2.8 mm, so the theoretical voltage difference between the two driving electrodes should be above 5.4 V to trigger electrochemical reactions at the corners of the monolayer.

At room temperature (25 °C) and atmospheric pressure (1 atm), the redox reactions occurring at the two sides of the bipolar electrode can be expressed as follows:

Reduction side:

$$PtCl_6^{2-} + 4e^- \leftrightharpoons Pt + 6Cl^- \qquad E_1 = +0.73\,V - \frac{0.0592}{4} log\left(\frac{[Cl^-]^6}{[PtCl_6^{2-}]}\right) \tag{2.2}$$

Oxidation side:

$$2H_2O \leftrightharpoons O_2 + 4H^+ + 4e^- \qquad E_2 = +1.23\,V - 0.0592\,pH \tag{2.3}$$

As calculated, the standard potential difference between these two redox reactions is 0.5 V, which corresponds to a theoretical applied voltage difference of approximately 5.4 V between the two driving electrodes (the distance between the two driving electrodes is 3 cm). However, this value is derived only from thermodynamic considerations and does not account for kinetic limitations such as sluggish electron transfer or mass-transport limitations. In practice, such effects introduce significant overpotentials, and consequently, the threshold voltage required to trigger the redox processes is substantially higher than the theoretical value.

Figure 2-2A shows the schematic illustration of the corner deposition of Pt on a graphene monolayer, when a driving force of 14 V was applied between the electrodes, platinum deposition was first observed at the most cathodically polarized site, namely the corner (δ^-) of the graphene monolayer. Because the applied potential was only just sufficient to overcome the kinetic barriers, the resulting deposition was highly localized, confined to an extremely small region at the corner. Under these conditions, the amount of Pt clusters deposited was too small to be reliably detected by optical microscopy (Figure 2-2B). Additionally, no visible hydrogen bubble formation was observed under these conditions. This can be attributed to the potential difference between water reduction and water oxidation is much larger than that between Pt salt reduction and water oxidation, making proton reduction thermodynamically less favorable.

To provide definite evidence of the Pt deposition, the graphene monolayer was subsequently characterized using SEM. The SEM images in Figure 2-2C revealed distinct Pt deposition located precisely at the targeted corner of the graphene sheet. This observation was further

corroborated by EDS mapping (Figure 2-2D), which confirmed the elemental signature of Pt in the same region. Together, these results demonstrate the feasibility of employing BPE for the selective deposition of metals on 2D materials.

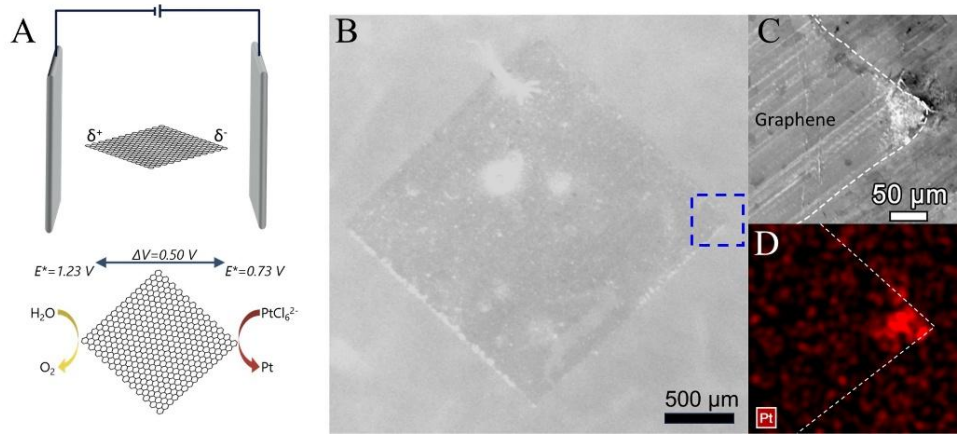

Figure 2-2 Bipolar electrodeposition of Pt at the corner of a graphene monolayer sheet. (A) Schematic illustration of the corner deposition of Pt on a graphene monolayer. (B) Optical photograph of the Pt-graphene, the modified corner is marked with blue dashed lines. (C) SEM image of the Pt modified corner of graphene. (D) EDS map of the Pt-modified corner. The shape of the graphene is outlined with a white dashed line. The size of the graphene sheet is 2 mm × 2 mm. The distance between the driving electrodes is 3 cm and the deposition time is 2 min.

After establishing the feasibility of localized deposition at the corner of a graphene monolayer, we next investigated whether the deposition site could be shifted from the corner to the edge of the sheet. Following the same principle of orientation control, the edge of the graphene was aligned perpendicular to the direction of the electric field (Figure 2-3A). Under these conditions, platinum was selectively generated along the edge rather than at the corner, illustrating that the deposit position can be tuned simply by adjusting the alignment of the 2D object with respect to the electric field.

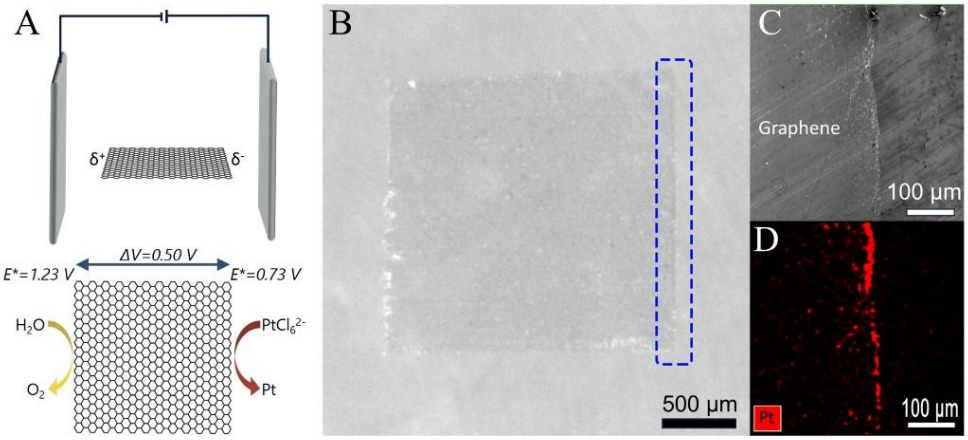

Figure 2-3 Bipolar electrodeposition of Pt at the edge of a graphene monolayer sheet. (A) Schematic illustration of the edge deposition of Pt on a graphene monolayer. (B) Optical photograph of the Pt-graphene, the modified edge is marked with blue dashed lines. (C) SEM image of the Pt modified edge of graphene. (D) EDS map of the Pt modified edge. The size of the graphene sheet is 2 mm × 2 mm. The distance between the driving electrodes is 3 cm and the deposition time is 2 min.

In contrast to the corner modification, where the deposit was confined to a single point and undetectable by optical microscopy, the edge-modified graphene exhibited a tiny gray trace, visible along the targeted edge in the optical images (Figure 2-3B). This subtle contrast is attributed to the accumulation of Pt deposits. To verify the nature of this modification, SEM was performed. The SEM result revealed continuous decoration of the graphene edge with Pt clusters

(Figure 2-3C). The elemental composition of these deposits was confirmed by EDS mapping, which showed a clear Pt signal localized exclusively along the modified edge (Figure 2-3D). These results confirm that BPE not only enables corner-selective deposition but also allows precise and controllable edge-selective functionalization of graphene monolayers.

Taken together, these two preliminary results provide direct evidence that BPE enables site-selective modification of 2D materials. By simply adjusting the orientation of the graphene monolayer, deposition can be induced at the corners or along the edges, highlighting the high spatial control that can be achieved with this strategy. Unlike conventional electrodeposition, which typically requires a direct electrical connection and often results in uniform coverage of the entire surface of a 2D material, the bipolar approach allows the reaction to be confined to a specific area without any direct connection. This not only reduces experimental complexity, but also preserves the integrity of the 2D material after modification, allowing it to be transferred to any substrate for applications.

2.1.3 Precision deposition of Pt on graphene monolayers

The above results highlight the unique capability of BPE to achieve site-selective functionalization of 2D materials. Precise spatial control over surface modification is crucial, as it enables the rational design of multifunctional 2D materials with locally tunable properties. To further evaluate the potential of this strategy, we conducted a series of control experiments, aiming to explore the detailed deposition behavior of Pt on graphene monolayers under varying driving forces and metal salt concentration.

As shown in Figure 2-4A, when a potential difference of 14 V was applied between the driving electrodes, Pt deposition first appeared at the most cathodically polarized corner of the graphene monolayer, visible as a dark gray region. Upon increasing the applied potential to 20 V and 25 V (Figures 2-4B and C), the area occupied by the deposit gradually expanded from the corner toward the central part of the sheet, which was also clearly confirmed by the corresponding EDS images. It is worth noting that, when an even higher voltage of 40 V is applied, the modified region continues to expand, but the Pt does not fill the entire corner of the graphene, and a strip-like deposition is observed (Figure 2-4D), which is consistent with previous results obtained with spherical particles. This phenomenon can be rationally explained by considering the kinetics of ion transport under strong electric fields. [39] When a voltage is applied to driving electrodes in a bipolar system, metal ions in the electrolyte solution migrate towards the driving electrode due to the presence of the electric field. Despite the use of anion-blocking Nafion membranes, a negatively charged metal complex still experiences the electric field, especially in the absence of additional supporting electrolyte, as it is the case for the majority of bipolar electrodeposition experiments. Therefore, $PtCl_6^{2-}$, migrates towards the anodic driving electrode. Once the $PtCl_6^{2-}$ ions reach a position where the polarization potential is sufficient to reduce them, (as indicated by the dashed line in Figure 2-4D), Pt is deposited at this position. In other word, those anions are reduced before they can reach the tip of the δ^- side. At the same time, $PtCl_6^{2-}$ ions, initially present at or close to the tip of the graphene sheet, will move away from the tip and migrate in direction of the anodic driving electrode. Therefore, the concentration of $PtCl_6^{2-}$ between the dashed line and the tip is relatively low, resulting in a strip of Pt deposition on graphene. Although the presence of the Nafion membrane reduces the current through the electrolyte, this phenomenon still can be observed when a higher voltage is applied. In addition, another reason

for this pattern may be attributed to the water reduction reactions at the tip of the δ^- side, where the polarization potential is now sufficiently high to reduce water and generate hydrogen gas bubbles at this high voltage. These bubbles then partially occupy the most polarized reaction sites, which results in less Pt at the tip compared to other regions, leading to the observed strip-like morphology.

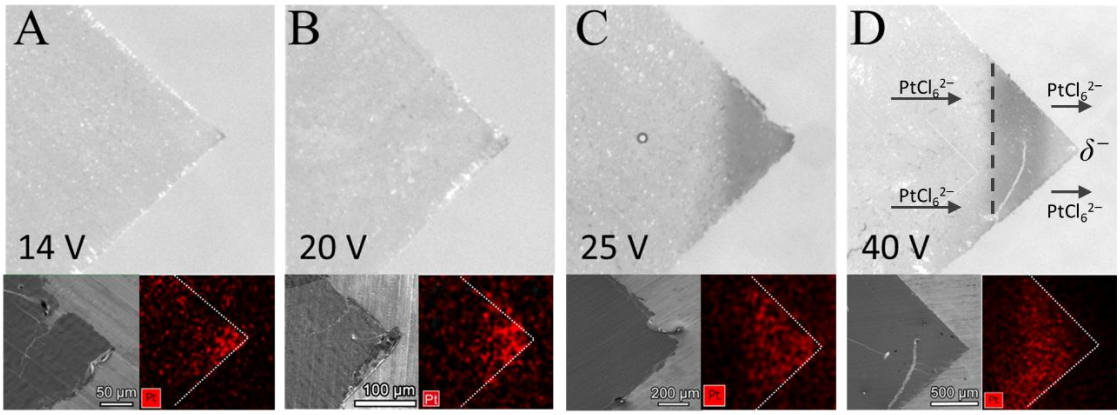

Figure 2-4 Optical micrographs, SEM images, and EDS maps of Pt-graphene Janus particles after single corner deposition, performed with different potentials applied to the driving electrodes. (A) 14 V. (B) 20 V. (C) 25 V. (D) 40 V. The insets show a zoom of the corner region and the corresponding EDS maps. The size of the graphene sheet is 2 mm × 2 mm. The distance between the driving electrodes is 3 cm and the deposition time is 2 min.

As chemical vapor deposition (CVD)-grown graphene is a polycrystalline material, one might expect that metal nucleation could also occur preferentially at grain boundaries or other structural defects. However, polarization is only strong enough at the extremities of the graphene layer, and therefore, we never observed Pt deposition at locations other than the edges or corners.

To further investigate the influence of precursor concentration on the deposition behavior, we also explored the influence of the H_2PtCl_6 concentration on Pt deposition at a given potential of 20 V. As shown in Figure 2-5 and the corresponding insets, when the concentration of H_2PtCl_6 increased from 0.2 to 6 mM, distinct changes in the deposit became apparent. At a salt concentration as low as 0.2 mM, almost no Pt deposit could be detected by optical microscopy (Figure 2-5A). Nevertheless, EDS measurements revealed clear Pt signals, confirming successful deposition (Figure 2-5C). However, this characterization approach requires fixing the modified graphene monolayer onto a conductive substrate, making it impossible to recover the intact sample after analysis. To overcome this limitation and verify the presence of Pt at the intended deposition sites without damaging the sample, we transferred the modified graphene sheets onto the air-water interface of an aqueous H_2O_2 solution. Since Pt catalyzes the decomposition of H_2O_2 into oxygen and water, the appearance of oxygen bubbles at the Pt-modified location provides direct evidence of Pt deposition (Figure 2-5B).

At a Pt salt concentration of 2 mM, the optical micrograph did not show obvious changes at the modified corner, but in H_2O_2 solution, a large amount of oxygen bubbles were clearly observed at the modified corner, confirming the success of Pt deposition (Figures 2-5D and E). When the Pt salt concentration was further increased to 6 mM, a clear dark dot was observed at the modified corner in the optical micrograph, which can be attributed to substantial Pt accumulation (Figure 2-5G). Similarly, dense bubble formation at the corresponding location in H_2O_2 solution

further validated this observation (Figure 2-5H). In addition, all samples in this group of experiments were characterized by SEM and EDS, corroborating that H_2O_2 bubble tests can serve as a reliable method to identify Pt-modified regions on graphene (Figures 2-5C, F, I). Therefore, in the following experiments, we used H_2O_2 solution to verify the deposition of Pt. These results demonstrate not only once again that Pt deposition on monolayer graphene can be achieved by BPE, but that the features of the deposits can be fine-tuned by changing the electric field strength and the metal precursor concentration.

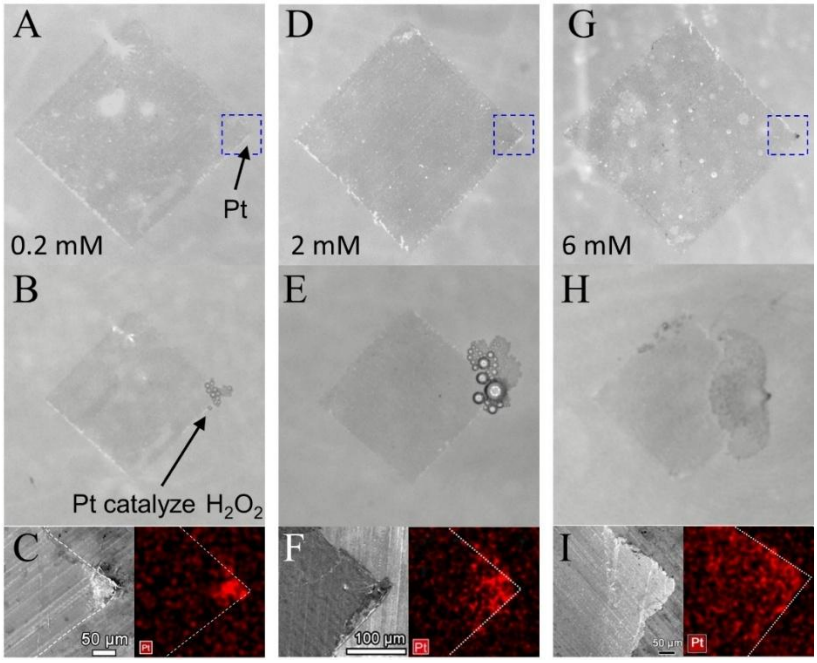

Figure 2-5 Pt-graphene Janus particles (~ 2 mm × 2 mm) after single corner deposition at the same voltage (20 V), but with varying H_2PtCl_6 concentrations. The distance between the driving electrodes is 3 cm. Deposition time is 2 min. (A, D, G) Optical micrographs of Pt-graphene in water. (B, E, H) Optical micrographs of Pt-graphene in 5% v/v H_2O_2 (5% w/v sodium dodecyl sulfate (SDS)) aqueous solution, the Pt modified corner can catalyze H_2O_2 to generate oxygen bubbles. (C, F, I) SEM images, and EDS maps of Pt-graphene after single corner deposition. The shape of graphene is outlined with white dashed line.

In addition, a small amount of SDS (5% w/v) was added to the H_2O_2 solution to facilitate bubble formation around the graphene sheet and reduce the size of the generated bubbles. Without SDS, large bubbles tend to form, which could damage the structure of the graphene monolayers.

After confirming that it is possible to deposit Pt on a single corner under suitable conditions, we applied this concept to produce more advanced Pt-graphene Janus structures, which are absolutely impossible to generate with any other physicochemical approach. This can be achieved by sequentially changing the orientation of the graphene sheet with respect to the electric field lines. The first row of Figure 2-6 shows a schematic diagram of the locations where Pt is deposited on graphene. For the smallest polarization potential, the Pt deposit is too small to be observed under the optical microscope; thus, the modified area is highlighted with dashed blue lines (middle row of Figure 2-6). The presence of Pt at particular sites is based on its catalytic activity for H_2O_2 decomposition. For the single-corner-modified graphene, bubbles appear only at one location. To accomplish Pt deposition on two corners, the monolayer is rotated clockwise by 90° after the first deposition and a second metal deposition is performed (Figure 2-6B). By executing another 90° clockwise rotation, we can successfully modify three corners (Figure 2-6C). Following the same philosophy, if the edge of the graphene sheet is oriented perpendicular to

the electric field lines, then metallic Pt was generated exclusively at the edge (Figure 2-6D). Obviously, the decoration of two edges can be achieved by a 90° rotation after the first deposition (Figure 2-6E). In all of these cases, the formation of oxygen bubbles transduces the presence of the metal deposits at the desired positions on the graphene monolayer.

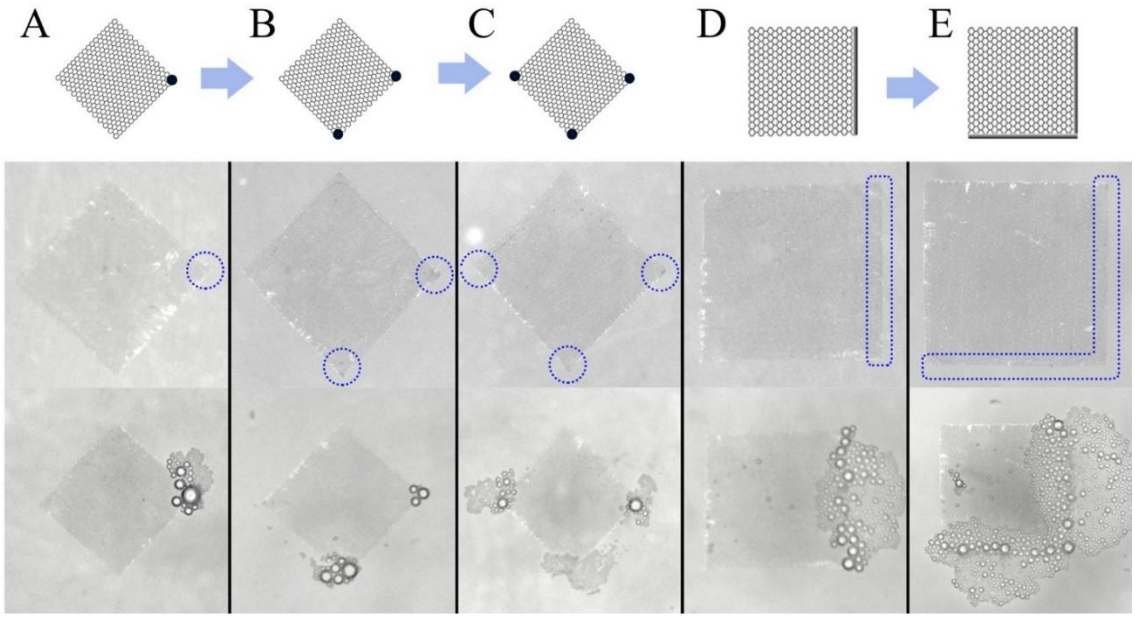

Figure 2-6 Schematic (upper row), optical micrographs in water (middle row), and corresponding images in 5% v/v H_2O_2 (5% w/v SDS) aqueous solution (bottom row) of Pt-graphene Janus particles (~ 2 mm × 2 mm). (A) Single corner. (B) Two corners. (C) Three corners. (D) Single edge. (E) Two edges. The modified corner(s) or edge(s) is marked with a blue dashed line. For the corner deposition, the polarization potential was 14 V, whereas for the edge deposition it was 16.5 V with a deposition time of 2 min and the concentration of H_2PtCl_6 is 2 mM in both cases.

The above series of results demonstrates that BPE provides an effective strategy for achieving precise metal deposition on 2D materials. Both the deposition area and the specific location of Pt on graphene monolayers can be fine-tuned by controlling the applied potential, precursor concentration, and the orientation of the sheet with respect to the electric field. This high degree of spatial control enables the selective modification of individual corners, edges, or multiple predefined sites, thereby allowing the fabrication of advanced Janus-type architectures that cannot be realized by conventional physicochemical approaches such as sputtering or CVD.

2.1.4 Dynamic behavior of Pt-graphene monolayers

After demonstrating the precise spatial control of Pt deposition, we next explored the localized catalytic activity of the deposited Pt clusters to achieve controllable bubble generation and systematically investigate the performance of the resulting Pt-graphene hybrid as self-propelled swimmers at the air-water interface. In this configuration, hydrogen peroxide was employed as the chemical fuel, while the Pt clusters acted as a catalyst to decompose H_2O_2 into oxygen and water.[125-127] The continuous release of O_2 bubbles provided the driving force required to propel the graphene sheets (Figure 2-7A).

In the first set of experiments, Pt was deposited at a single corner of a 1 mm × 1 mm graphene sheet. The modified sheet was then transferred to the air-water interface of an aqueous H_2O_2 solution to evaluate whether the catalytic decomposition of H_2O_2 could generate sufficient propulsive force to move the graphene monolayer. As shown in the optical microscopy images

(Figures 2-7B and C), a distinct dark dot appeared at the modified corner after deposition, corresponding to the presence of Pt clusters. When immersed in an H_2O_2 solution, this asymmetric catalytic site triggered localized bubble formation, which in turn induced rotational motion of the graphene monolayer, as captured in the time-lapse image sequence of Figure 2-7D. Although the graphene sheet exhibited a continuous rotational displacement, it is important to note that in this initial configuration, the direction of rotation was neither controllable nor predictable, with clockwise and anticlockwise trajectories occurring randomly.

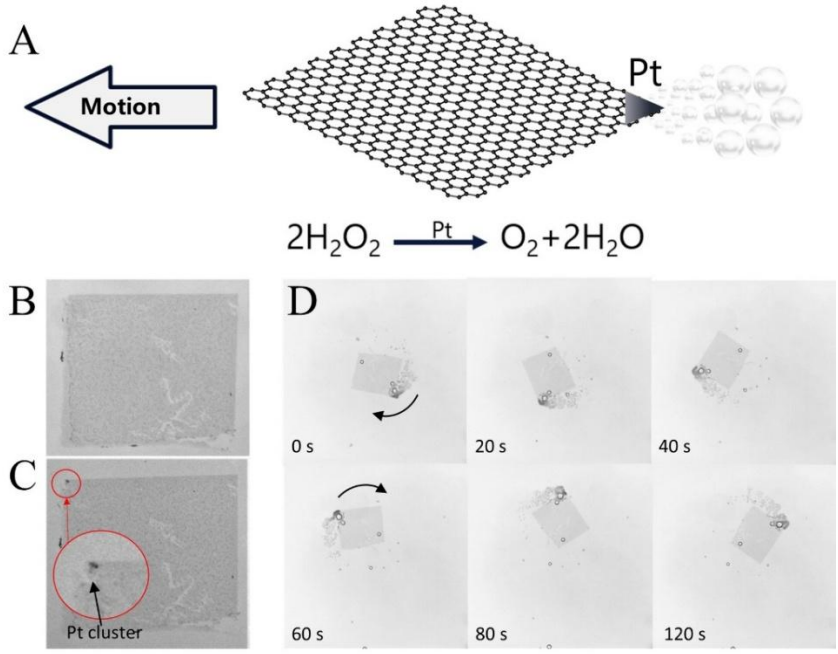

Figure 2-7 (A) Propulsion mechanism of the 2D Pt-graphene Janus swimmer. Optical micrographs of a graphene monolayer (~ 1 mm × 1 mm) (B) before and (C) after Pt deposition. The insets show a zoom of the corner modified with a Pt cluster. (D) Time-lapse images of the Pt-graphene swimmer in 5% v/v H_2O_2 (5% w/v SDS) aqueous solution.

Here the presence of SDS reduces the surface tension of the solution, facilitating the formation and detachment of oxygen bubbles, thus promoting the propulsion of the Pt-swimmer.[128] Moreover, SDS plays a significant role in the behavior of the Pt-graphene swimmers. Since the local surface tension of the oxygen bubbles is lower than the surrounding solution, a surface tension gradient forms around the bubbles. According to the Marangoni effect, liquid flows from regions of higher surface tension to the bubbles.[129] The resulting flow accelerates the movement and dispersion of the generated oxygen bubbles, which in turn enhances the propulsion of the Pt-graphene swimmer. This mechanism contributes to a more stable motion of the Pt-graphene swimmer, improving its overall dynamic behavior and ensuring smoother, continuous propulsion.

Building on these initial observations, we next investigated the key factors that govern the motion behavior of Pt-graphene swimmers, with the aim of systematically optimizing the deposition strategy to achieve more controllable and efficient propulsion. One of the most fundamental parameters is the concentration of the chemical fuel, as it directly dictates the rate of bubble generation at the catalytic sites. Therefore, we first examined the influence of H_2O_2 concentration on the oxygen bubble production using graphene monolayers decorated with Pt at a single corner.

To monitor bubble formation for different fuel conditions, sequential photographs of the swimmers were taken every 30 s after immersion in H_2O_2 solutions of varying concentrations (1%, 3%, and 5% v/v). As shown in Figure 2-8A, at the lowest concentration of 1%, oxygen generation was extremely slow, and only a single bubble nucleated at the catalytic corner after a prolonged period. When the concentration was increased to 3% (Figure 2-8B), the frequency and density of bubble formation increased substantially, resulting in greater gas evolution. At 5% H_2O_2 (Figure 2-8C), bubble generation was even more pronounced, with a high density of bubbles continuously released from the Pt modified site. These results clearly demonstrate that, for a constant amount of deposited Pt catalyst, the oxygen bubble production rate is positively correlated with the H_2O_2 fuel concentration. Consequently, the choice of fuel concentration plays an important role in tuning the driving force and therefore enhances the propulsion efficiency of Pt-graphene swimmer.

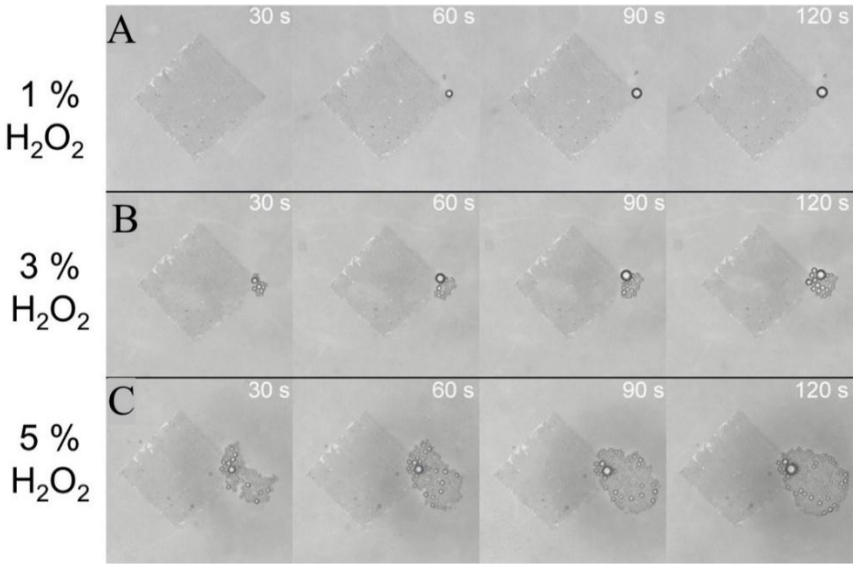

Figure 2-8 Time-laps images of a Pt-graphene Janus particle (~ 2 mm × 2 mm) in (A) 1%, (B) 3%, and (C) 5% v/v H_2O_2 (5% w/v SDS) aqueous solution. The object is obtained under an electric field of 6.67 V/cm in 0.2 mM H_2PtCl_6 solution and the deposition time is 2 min.

Next, the speed of the Pt–graphene swimmer was evaluated as a function of the lateral size of the graphene monolayer, since the balance between driving force and hydrodynamic drag is expected to strongly depend on the dimensions of the swimmer. For this purpose, square Pt-decorated graphene sheets of 1 mm × 1 mm, 2 mm × 2 mm, and 5 mm × 5 mm were prepared and tested under identical fuel concentrations.

As shown in Figure 2-9, the velocity of the Pt–graphene swimmers gradually decreased with increasing sheet size. This trend can be rationalized by considering the interplay between the propulsion force and the resistance at the air-water interface. Smaller graphene monolayers, with their lower mass and reduced contact area with the liquid surface, experience less hydrodynamic drag and therefore move more rapidly when propelled by the same catalytic bubble generation. In contrast, larger graphene sheets move more slowly because their higher mass increases inertia, and their larger contact area with the aqueous surface leads to stronger viscous resistance.

These results highlight the importance of size selection in the design of 2D catalytic swimmers. Based on this analysis, an intermediate size of 2 mm × 2 mm was chosen as the representative

model system for subsequent experiments, as it provides a balance between stability and measurable propulsion, while still allowing for clear observation of both dynamic and catalytic behavior.

Subsequently, we examined the effect of Pt loading amount on the propulsion performance of the graphene swimmers. In this set of experiments, the lateral size of the graphene sheets was kept constant (2 mm × 2 mm) in order to isolate the influence of the catalytic loading. The amount of deposited Pt was systematically tuned by varying the applied voltage during the electrodeposition process, while maintaining a constant concentration of H_2PtCl_6 precursor solution. As expected, applying higher voltages resulted in a larger deposition area on the graphene monolayer, thereby increasing the overall Pt coverage and loading amount.

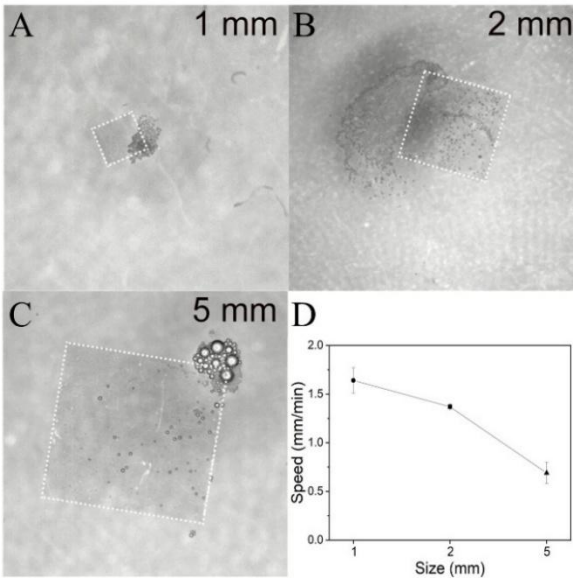

Figure 2-9 Optical micrographs of Pt-graphene Janus swimmers of different sizes with single corner deposition, along with the corresponding gas formation in the same H_2O_2 aqueous solution. (A) 1 mm × 1 mm. (B) 2 mm × 2 mm. (C) 5 mm × 5 mm. (D) The measured speed of the modified corner of each swimmer as a function of the characteristic sheet size.

The impact of this parameter on catalytic activity was immediately apparent. As shown in Figure 2-10A-C, the density of O_2 bubbles released from the Pt-graphene swimmers increased significantly with the increase of Pt loading amount. This phenomenon is because the bubble production directly determines the magnitude of the driving force. This enhancement in bubble generation translated into a significant improvement in motion performance. To quantify this effect, the velocities of three Pt-graphene swimmers prepared at 14 V, 20 V, and 25 V were measured (Figure 2-10D). The recorded speeds were 9.6, 18, and 42 mm/min, respectively, demonstrating a clear and nearly linear correlation between the applied voltage and the propulsion velocity.

This result provides evidence that the speed of the Pt-graphene swimmer is directly proportional to the catalytic activity of the deposited Pt. In other words, the efficiency of bubble-driven propulsion is critically governed by the number and distribution of active catalytic sites. This observation underscores the importance of precisely controlling the loading and spatial arrangement of Pt clusters in order to optimize the performance of graphene-based swimmers.

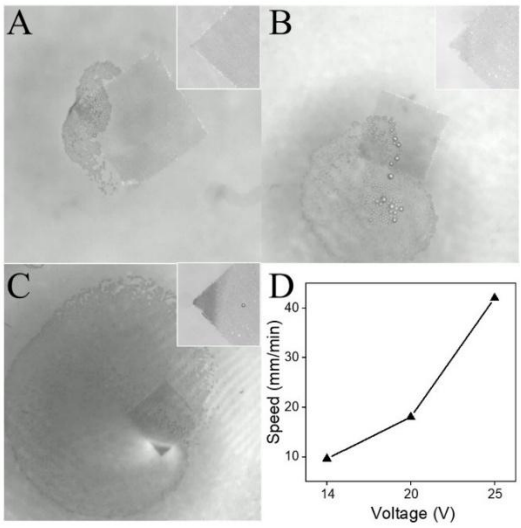

Figure 2-10 Optical micrographs of Pt-graphene Janus swimmers obtained with different voltages with single corner deposition and the related gas formation in the same aqueous H_2O_2 solution. The insets show a zoom of the Pt modified corner. (A) 14 V. (B) 20 V. (C) 25 V. (D) The measured speed of the modified corner of each swimmer as a function of applied modification voltage.

The above results reveal that the dynamic behavior of Pt-graphene swimmers can be effectively tuned by varying the deposition parameters. Specifically, their dynamics is governed by factors such as H_2O_2 concentration, Pt loading amount, and the size of the graphene sheet. Increased Pt loadings lead to a proportional increase in bubble generation and propulsion speed. These results demonstrate the correlation between experimental parameters and dynamic performance, providing guidelines for optimizing the swimmer design. Next, we aimed to achieve more precise control over the dynamic behavior of Pt-graphene swimmers.

2.1.5 Highly controlled dynamic behavior of Pt-graphene monolayers

First, we investigated the impact of oxygen flux on the dynamic behavior at the air-water interface. Initially, the motion of Pt-graphene swimmers modified at either one or two edges was examined. Their trajectories are shown in Figure 2-11. In both cases, overall near-linear motion is observed due to the rather homogeneous bubble evolution along the edges. Even more predictable motion can be achieved when using graphene monolayers modified by single point electrodeposition at the corners rather than along the entire edge (vide supra). By precisely controlling the amount of each deposited Pt cluster, it is possible to fine-tune bubble formation and thus to create on purpose an asymmetric driving force (Figure 2-12A), allowing the Janus swimmers to steer in a given direction (i.e., clockwise/anticlockwise rotation).

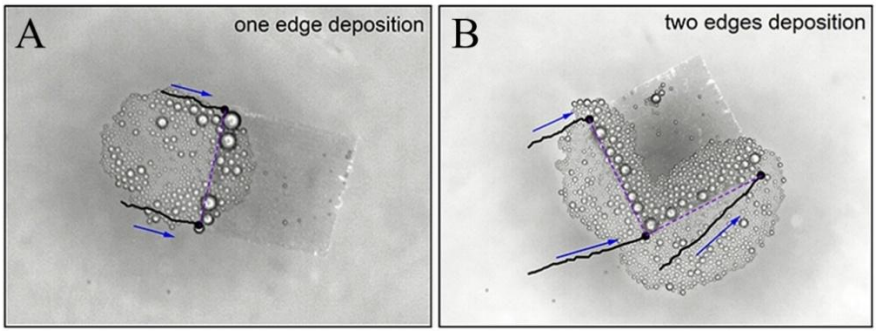

Figure 2-11 The motion trajectory (black lines) of Pt-graphene Janus swimmers with one or two edges modified.

To confirm this hypothesis, Pt deposition was carried out at two neighboring corners of a graphene monolayer with different deposition times (5 min at one corner and 10 min at the other). As expected, this resulted in Pt catalysts of different amounts at two distinct corners of the swimmer. The amount of Pt determines the magnitude of the driving force. As shown in Figure 2-12A, the direction of the individual driving force at each corner is oriented in a diagonal way from the corner toward the center of the graphene sheet with two respective components (F_{1a}, F_{1b} and F_{2a}, F_{2b}). Consequently, the corner with 10 min of Pt deposition will generate a higher overall driving force (F_1) in the fuel solution than the corner which was modified for only 5 min (F_2). Figure 2-12B and C show the resulting trajectories of these swimmers. The globally asymmetric driving force between the two corners will move the swimmer in a clockwise direction or anticlockwise for the opposite configuration. In Figures 2-12B and C, the trajectory of the corner with the bigger Pt deposit was tracked, and motion was observed for at least 20 min. This indicates that the dynamics of the Pt-graphene hybrid can be perfectly fine-tuned by precise control of the loading and position of the Pt catalyst, using BPE as a wireless electrochemical technique.

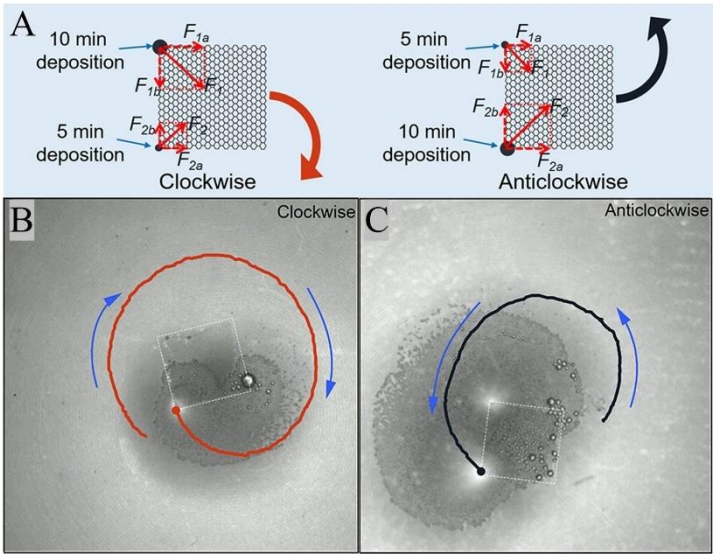

Figure 2-12 (A) Schematic illustration of clockwise and anticlockwise motion control of Pt-graphene Janus swimmers by tailoring the amount of the Pt clusters (black spots, bigger spot represents more Pt clusters) deposited at individual corners; Trajectory plots of two Pt-graphene Janus swimmers (~ 2 mm × 2 mm) moving in a 5% v/v H_2O_2 (5% w/v SDS) solution. (B) Clockwise motion. (C) Anticlockwise motion.

2.1.6 Conclusion

In conclusion of this first section, we have successfully generated Pt deposits on graphene monolayers with an unprecedented control in terms of amount, occupied surface area, and most importantly, position. Such a degree of fine-tuning can only be achieved via bipolar electrochemistry and allow us to spatially define the catalytic activity of such hybrid materials. This can be directly illustrated by the localized decomposition of H_2O_2, leading to a well-controlled evolution of oxygen bubbles. The latter serves as the driving force for inducing motion, which, in turn, can be precisely steered by modifying the deposition time and location, as well as the metal precursor concentration and the potential applied during the deposition process. Utilizing single-layer graphene over multilayer graphene potentially provides several benefits. Single-layer graphene possesses a unique 2D structure and a set of distinct physicochemical

properties, such as a high surface area per weight, exceptional thermal and electrical conductivity, and mechanical strength. These features make it an ideal candidate for applications in catalysis and energy storage. Furthermore, the transparency of single-layer graphene could prove advantages in light-related applications such as optoelectronics, photocatalysis, and light-driven swimmers. Importantly, fine-tuning such structures by the deposition of diverse metals or semiconductors could lead to significant advancements in these different fields. Although the present proof-of-concept study demonstrates the precise deposition of solely Pt on single-layer graphene, it is worth noting that both platinum and graphene can be replaced with other conducting or semiconducting materials, offering a versatile platform for creating tailored nanostructures by using BPE. Most importantly, this kind of object can also be post-modified with functional groups to obtain more complex asymmetric designer particles, allowing triggering with multiple external stimuli, e.g., light or magnetic fields. This can be interesting for completely different applications, far beyond the 2D self-propelled swimmers shown here, such as photocatalytic water splitting, environmental remediation, and molecular recognition or delivery.

2.2 Synthesis of multi-functional graphene monolayers via bipolar electrochemistry

The previous section demonstrated that Pt-modified graphene possesses tunable catalytic behavior. However, the catalytic functionality introduced by a single-component modification remains limited. To further understand the structure-function relationship, it is essential to explore the co-modification of graphene with multiple components. Such multicomponent systems not only introduce multifunctionality, but might also give rise to synergistic effects between the different components. Currently, the controlled multi-functional modification of graphene remains largely unexplored. Traditional approaches to modifying graphene mainly focus on its integration with other materials into composites, or through the modification of its entire surface with metals or organic molecules.[130-134] However, these strategies are not well adapted to achieve site-selective modification of the surface of a single graphene layer, and also encounter important challenges when deposition of several types of materials is required. Modifying graphene with multiple chemical species would significantly enhance its functionality and application potential[135], allowing for the elaboration of hybrid structures that combine the unique properties of monolayer graphene with those of metals and polymers for example. This should enable the development of versatile, high-performance materials capable of addressing complex challenges in areas such as sensing, catalysis, energy storage, and biomedical applications. Hence, there exists a strong need to develop appropriate methodologies for the preparation of multifunctional graphene. In this section, BPE is presented as a straightforward concept for the multiple functionalization of graphene monolayers. As already discussed, BPE in general allows the electrochemical modification of conducting/ semiconducting objects in a controllable way, without direct physical contact with a power supply.[7, 136, 137] In this way, asymmetric functionalization can be readily achieved for various types of substrates.[138-140]

Based on the principles of BPE, two complementary approaches can be identified: direct and indirect bipolar deposition. Direct bipolar electrodeposition is based on the reduction of metal ions directly at the interface between the bipolar electrode and the solution. This strategy has been extensively applied for the modification of objects with different shapes.[6, 102, 141] In contrast, indirect bipolar electrodeposition does not involve direct redox reactions of a precursor at the bipolar electrode/solution interface. Instead, precursors react chemically with species that are electrogenerated in situ at the bipolar object.[142, 143] Representative examples include pH-dependent precipitation or polymerization reactions, triggered by water electrolysis at the extremities of the bipolar electrode. Water electrolysis induces localized pH gradients- pH increases near the cathodic end (due to OH^- generation/H^+ consumption) and decreases near the anodic end (due to H^+ generation/OH^- consumption), thereby enabling spatially controlled reactions.[18, 76]

BPE systems based on these two methods has been extensively studied and precise control over the immobilization of different materials on the same object have been achieved, such as the modification of glassy carbon spheres with a variety of metals at specific locations[38], as well as the deposition of different metals and polymers at the ends of 1D carbon nanotubes[34]. In this context, site-selective deposition of Pt clusters on graphene monolayers has been achieved by controlling the electric field, the deposition time, and platinum salt concentration.[144] However,

multi-functionalization of 2D objects, in particular with a larger spectrum of materials such as different metals and polymers, remains underdeveloped.

To address the need for multi-functional 2D materials, this section uses proof-of-principle experiments to explore the targeted modification of graphene monolayers with various materials at the air-water interface. The bipolar electrochemical approach enables precise customization of graphene properties by selectively adding different materials to specific areas, not possible with any other type of electrochemical or physicochemical concepts. On the one hand, various metals, or compounds, can be generated at the corners and/or edges of graphene monolayers with direct bipolar electrodeposition, and on the other hand, polymers, in the form of EP, can be immobilized at predetermined positions on the graphene monolayer through indirect bipolar electrodeposition. In addition, by co-immobilizing potassium ferricyanide inside the porous polymer, the resulting hybrid metal-polymer graphene monolayer shows interesting catalytic features, illustrated by dynamic CL at the air-water interface as a model system for the controlled release of active compounds.

2.2.1 Multi-metal modification of graphene monolayers

Graphene monolayers with a size of about 2 mm × 2 mm were prepared via a wet-transfer method (see details in Section 2.6). In the BPE experiment, a graphene sheet was placed between the two driving electrodes and fixed at the air/water interface by a fixing device (see Figure 2-1). Generally, for bipolar metal deposition, water oxidation is the process occurring at the anodic pole (see equation 2.3). The cathodic pole is the site where metal ions undergo reduction:

$$M^{n+} + ne^- \leftrightharpoons M^0 \qquad E_x = E° + \frac{0.0592}{n} log[M^{n+}] \tag{2.4}$$

where *y* stands for the standard potential value of metal ions. In theory, ΔV must be higher than the standard potential difference (E_2-E_x) so that metal can be deposited on the bipolar object. Figure 2-13 illustrates the procedure for depositing different metals at the corners of a graphene sheet. For the deposition of the first metal (M_1), the cell is filled with the corresponding metal salt solution, and graphene is positioned as shown in the left part of Figure 2-13. In this case, M_1 will deposit at the cathodic side when a sufficiently high electric field is applied between the two driving electrodes. After depositing M_1, the cell is filled with another metal (M_2) salt solution, and the graphene monolayer is rotated by 90°, followed by application of an appropriate electric field to reduce M_2 ions. These steps can be repeated to deposit additional metal spots.

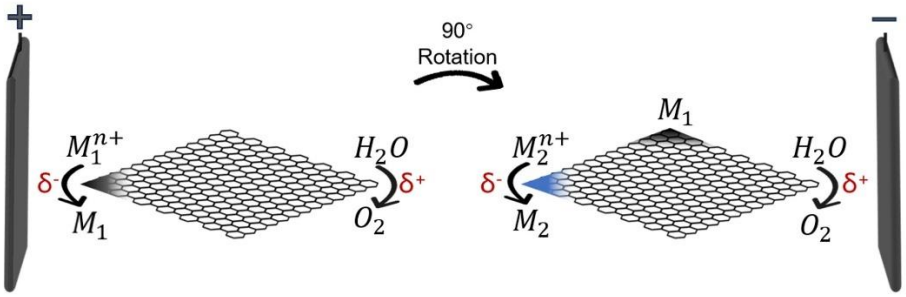

Figure 2-13 Illustration of the multi-metal modification on a graphene monolayer.

To avoid spontaneous chemical replacement reactions between deposited metals and metal salt precursors, electrodeposition should be carried out in a specific order, taking into account their

respective reactivity, from inert to more active. For example, M_1 should be more noble than M_2. In this section, Au, Pt, Pd, and Cu were chosen to sequentially modify the four corners of the graphene monolayer.

The standard potentials in aqueous solution used in this section are as follows:

$$PtCl_6^{2-} + 4e^- \leftrightharpoons Pt + 6Cl^- \qquad E_1 = +0.73\,V - \frac{0.0592}{4} log\left(\frac{[Cl^-]^6}{[PtCl_6^{2-}]}\right) \tag{2.2}$$

$$AuCl_4^- + 3e^- \leftrightharpoons Au + 4Cl^- \qquad E_3 = +0.99\,V - \frac{0.0592}{3} log\left(\frac{[Cl^-]^4}{[AuCl_4^-]}\right) \tag{2.5}$$

$$Pd^{2+} + 2e^- \leftrightharpoons Pd \qquad E_4 = +0.92\,V - \frac{0.0592}{2} log\left(\frac{1}{[Pd^{2+}]}\right) \tag{2.6}$$

$$Cu^{2+} + 2e^- \leftrightharpoons Cu \qquad E_5 = +0.34\,V - \frac{0.0592}{2} log\left(\frac{1}{[Cu^{2+}]}\right) \tag{2.7}$$

Figure 2-14A shows the schematic diagram of a graphene sheet modified with four metals. An electric field of 2 V/cm was applied for Au deposition at the first corner of the graphene. Then Pt, Pd, and Cu were deposited with electric fields of 3 V/cm, 2.3 V/cm, and 3.6 V/cm, respectively. These applied electric fields are higher than the theoretical values, due to the potential drop in the solution and the overpotentials of the reactions. Figure 2-14B shows an optical photograph of the modified graphene monolayer. A color change can be clearly observed in every corner, originating from metal deposition. It is worth noting that the size of the deposit can be fine-tuned by adjusting the electric field, as previously demonstrated in Section 2.1. Figures 2-14B, C, E, and F show the EDS mapping of Au, Pt, Pd, and Cu for each corner, respectively. These results indicate that a graphene monolayer can be modified with different metals and this modification can be precisely controlled by adjusting the experimental conditions.

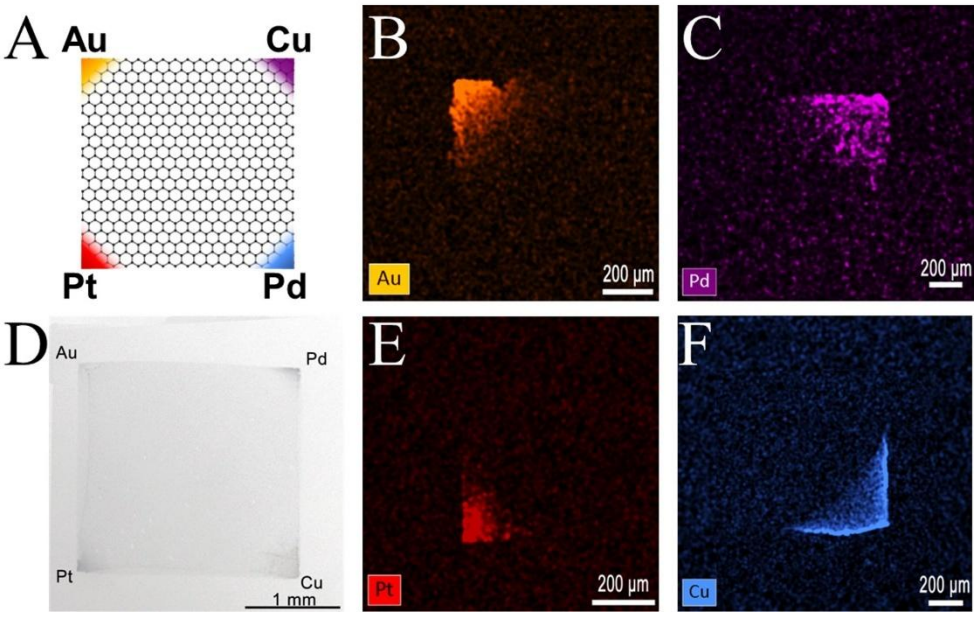

Figure 2-14 (A) Schematic diagram and (D) micrograph of a multiple corner modified graphene monolayer. (B, C, E, F) EDS mapping of the corresponding corners of a multi-metal modified graphene monolayer.

To demonstrate the versatility of our approach, we also performed edge deposition of different metals on the graphene monolayer. The procedure of edge deposition is similar to that for corner deposition, except that the graphene sheet is placed with the edges parallel to the driving electrodes and requires a slightly higher electric field than the corner deposition. The electric field values for edge deposition of Au, Pt, Pd, and Cu are 2.4 V/cm, 3.8 V/cm, 2.8 V/cm, and 5.2 V/cm, respectively. Figure 2-15A shows the schematic diagram and Figure 2-15D displays the optical photograph of an edge-modified graphene sheet. Figures 2-15B, C, E, and F show the corresponding EDS mapping of Au, Pt, Pd, and Cu, respectively. The EDS signal is only observed at the modified edge, with no signal detected in other areas, indicating highly site-selective metal deposition.

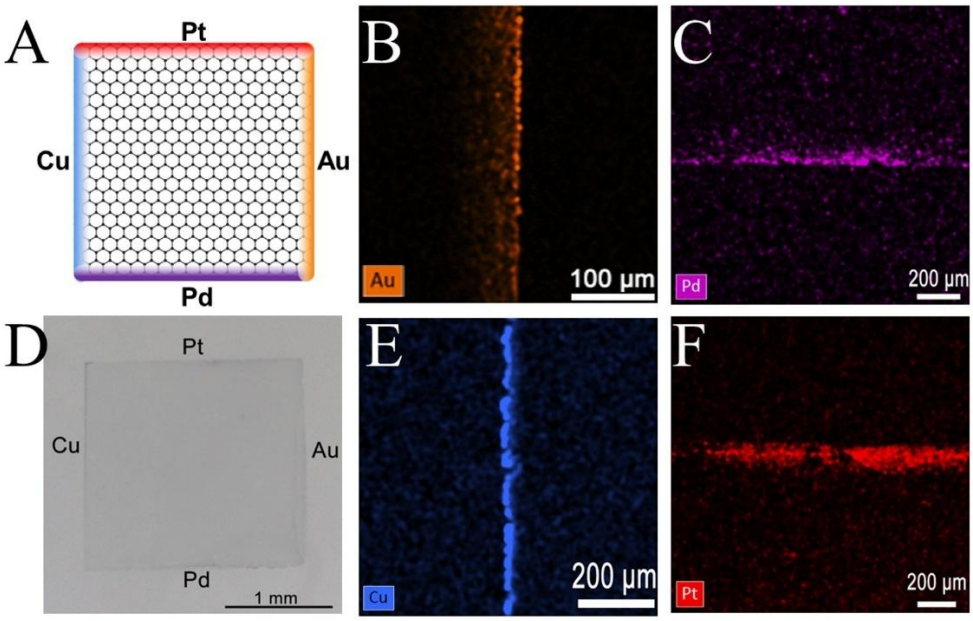

Figure 2-15 (A) Schematic diagram and (D) micrograph of a multiple edge modified graphene monolayer. (B, C, E, F) EDS mapping of an edge-modified graphene monolayer.

The corner and edge deposition results demonstrate that multi-metal modification can be achieved on graphene in a straightforward way. In addition, a metal gradient is observed from the center to the border. For instance, in Figure 2-15B, the edge exhibits the highest EDS intensity and the signal decreases gradually toward the center due to the variation of the polarization potential along the bipolar electrode. The extreme end of the bipolar electrode experiences the highest potential, enabling faster reduction of Au ions.

Both corner and edge decoration with different metals not only validate the versatility of this approach, but also highlight its potential for creating heterogeneous surfaces with spatially resolved features. Moreover, the range of bipolar electrochemical modification is not limited to simple metal reduction. Beyond metal deposition, this strategy can be extended to integrate more complex materials, enabling the fabrication of multi-functional graphene-based objects. Therefore, in the following section, we will explore such advanced functionalization, focusing on combining graphene with more complex materials to provide additional structural, electronic or catalytic features.

2.2.2 Multi-functionalized graphene monolayers and their applications

2.2.2.1 Indirect deposition of Prussian blue on a graphene monolayer

Prussian Blue (PB), with the formula $Fe^{III}_4[Fe^{II}(CN)_6]_3$, is a classical coordination compound that has attracted continuous interest owing to its versatile properties and broad range of applications.[145-147] Historically used as a pigment[148], PB has recently found important applications in analytical chemistry[149-151]. Moreover, PB efficiently catalyzes luminol CL, a phenomenon arising from the relaxation of chemically generated excited states accompanied by photon emission.[152] CL provides a highly sensitive analytical readout, and PB has been extensively employed to enhance CL-based detection schemes in both chemical and biological fields.

Given these characteristics, asymmetric modification of 2D materials such as graphene with PB layers is particularly attractive. Integrating PB with graphene not only enables the design of multifunctional surfaces for biosensing and analytical applications, but also facilitates the synthesis of hybrid Janus systems in which CL serves as an optical reporter for monitoring processes such as motion trajectories of autonomous microswimmers and molecular detection. In this section, we present the indirect deposition of PB on graphene monolayers via BPE and investigate the structural and functional properties of the resulting hybrid materials.

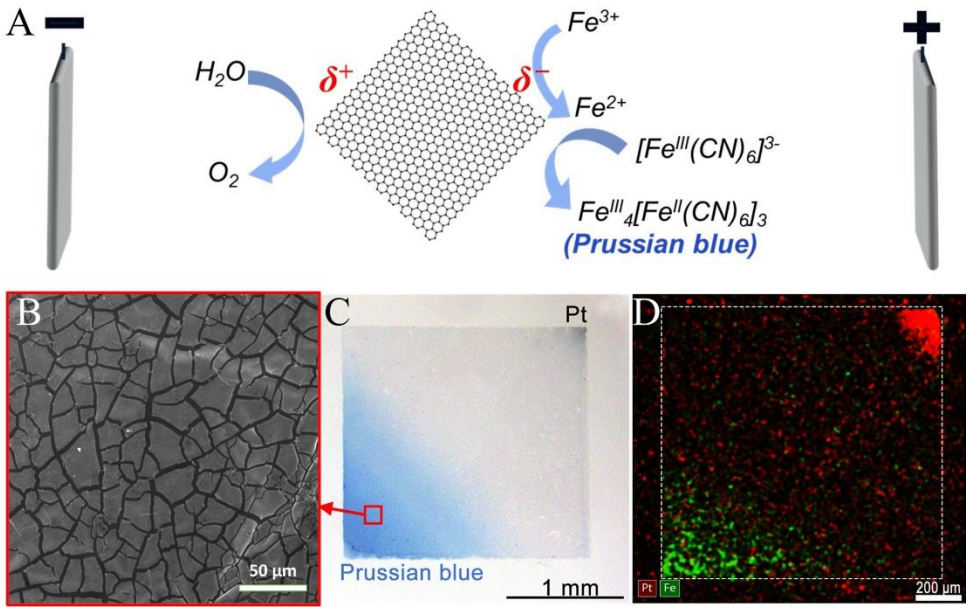

Figure 2-16 (A) Mechanism of indirect bipolar electrodeposition of Prussian blue. (B) SEM image of the deposited Prussian blue. (C) Micrograph of a graphene monolayer modified with Prussian blue and Pt. (D) EDS mapping of the Prussian blue and Pt co-modified graphene monolayer. The shape of the graphene monolayer is outlined with dashed line.

The principle of bipolar electrochemical deposition of Prussian Blue relies on localized redox processes occurring at the poles of the graphene monolayer when it is polarized by an external electric field (Figure 2-16A). At the cathodic pole of the bipolar electrode, Fe^{3+} ions in solution are reduced to Fe^{2+} according to:

$$Fe^{3+} + e^- \leftrightharpoons Fe^{2+} \qquad E_5 = +0.77\,V - 0.0592 log\left(\frac{[Fe^{2+}]}{[Fe^{3+}]}\right) \tag{2.8}$$

Meanwhile, hexacyanoferrate ions $[Fe(CN)_6]^{3-}$ are present in the bulk solution. The freshly generated Fe^{2+} ions immediately react with $[Fe(CN)_6]^{3-}$ to form insoluble Prussian Blue, $Fe^{III}_4[Fe^{II}(CN)_6]_3$, which selectively precipitates on the surface of the graphene around the cathodic pole:

$$4Fe^{2+} + 3[Fe^{III}(CN)_6]^{3-} \leftrightharpoons Fe^{III}{}_4[Fe^{II}(CN)_6]_3 \downarrow \quad (2.9)$$

This indirect deposition mechanism is crucial because the graphene itself does not directly work as a classical electrode. Instead, the potential drop across the solution under the influence of the applied electric field generates sufficiently high local cathodic polarization at one extremity of the graphene sheet to drive Fe^{3+} reduction, thereby enabling localized formation of PB. As a result, PB can be deposited in a highly site-selective manner on a graphene monolayer without any external electrical connection.

Figure 2-16C displays an optical image of a graphene monolayer after bipolar deposition, where a distinct blue-colored Prussian blue can be clearly observed at one corner of the sheet, while the opposite corner is decorated with Pt. The deposition of Pt is designed to combine the bubble-propelled motion with the catalytic functionality of Prussian blue, enabling the integration of propulsion and CL on a single graphene sheet. This asymmetric modification highlights the ability of BPE to integrate two different functional materials onto a single graphene monolayer. Figures 2-16B and D present the SEM image of the PB-modified region and the corresponding EDS maps of the Pt-graphene-PB hybrid, respectively. These results confirm the successful site-selective deposition of PB and Pt at opposite poles of the graphene monolayer.

To further explore the functional properties of the graphene-PB hybrid, we investigated its activity in catalyzing luminol CL. Prussian blue is well known for its electrocatalytic behavior, particularly in mediating electron transfer processes, and it can effectively promote the oxidation of luminol in the presence of hydrogen peroxide. When the graphene-PB composite was introduced into a luminol/H_2O_2 solution, a distinct blue CL emission was observed at the PB-modified corner of the graphene monolayer (Figure 2-17). The emission originates from the catalytic effect of PB, which accelerates the oxidation of luminol by H_2O_2 and leads to the formation of an amino phthalate dianion in an excited state, which emits light when returning to the ground state.

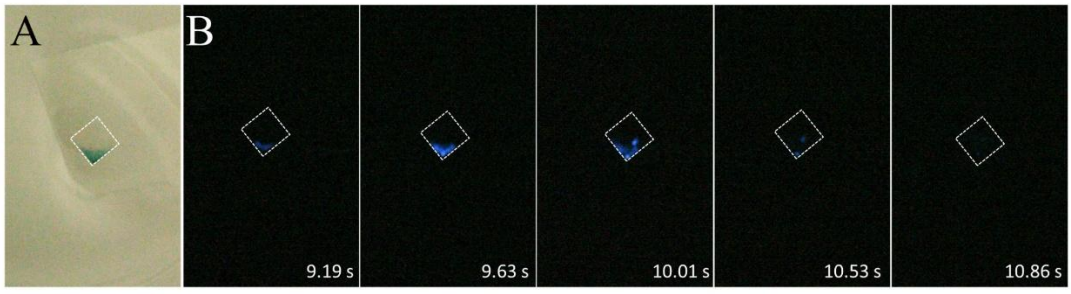

Figure 2-17 (A) Optical photograph of the Prussian blue modified graphene monolayer (~ 2 mm × 2 mm). (B) Time-laps images of chemiluminescence of the Prussian blue modified graphene monolayer. The graphene is outlined with dashed lines.

However, it is important to emphasize that the observed CL enhancement comes with a degradation of the PB layer. Once the PB layer is consumed, light emission rapidly weakens. In our experiments, we found that the CL lifetime is extremely short, with emission disappearing less than 1 second after initiation. In this case, the emission is too short to observe the

simultaneous bubble-driven motion. Although this transient behavior can produce a strong initial CL signal, it limits the long-term use of Pt-graphene-PB as a CL swimmer.

Based on these results, we realized that the transient nature of PB-induced CL limits its practical application in dynamic light emission. To overcome this limitation and achieve more sustainable and controllable light emission, we subsequently explored an alternative strategy aimed at achieving dynamic CL behavior.

2.2.2.2 Indirect deposition of electrophoretic paints on graphene monolayer

Electrophoretic paints are commonly used for anticorrosion coatings, and has recently attracted growing attention in diverse fields such as biosensors[153, 154], Janus objects[77], and as immobilization matrices for functional components[7]. To further highlight the versatility of our bipolar electrochemical strategy, an anodic EP (Resydrol AY498w/35WA) was employed to modify graphene sheets via indirect bipolar electrodeposition.

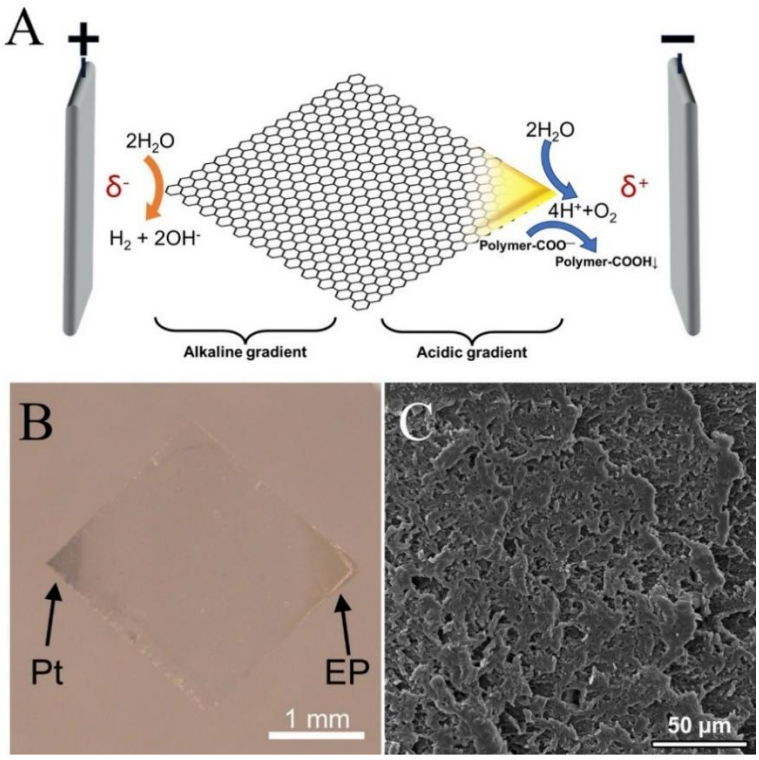

Figure 2-18 (A) Schematic diagram of indirect bipolar electrodeposition of an anodic electrophoretic paint. (B) Micrograph of a Pt-graphene-EP monolayer. (C) SEM image of the electrodeposited porous EP.

As illustrated in Figure 2-18A, during the bipolar polarization process, water oxidation occurs selectively at the anodic pole of the graphene sheet, leading to the local generation of protons and a decrease in pH. This localized acidification plays an important role in triggering EP deposition, because the precursor of EP consists of negatively charged polymer micelles stabilized by deprotonated carboxylate groups. Under acidic conditions, protonation of these carboxyl groups decreases the electrostatic stabilization of the micelles, thereby lowering their solubility in water and inducing polymer precipitation.[155] Therefore, EP is selectively deposited at the anodic extremity of the graphene sheet. This pH-mediated process enables spatially confined EP immobilization on graphene in a completely contactless manner, thereby demonstrating the efficiency of indirect bipolar electrochemistry for the site-selective modification of 2D materials.

As shown in Figure 2-18B, a graphene sheet decorated with Pt at one corner (appearing as a dark grey domain on the left) can be simultaneously modified with EP at the opposite corner (visible as a light-yellow region on the right), yielding a Pt-graphene-EP Janus hybrid. The coexistence of a metallic area and a polymer domain within a single 2D material is particularly remarkable, as it provides both catalytic functionality (from Pt) and chemical versatility (from EP) in a spatially separated yet synergistic manner. Importantly, due to the continuous evolution of oxygen bubbles during the deposition process[18], the EP layer develops a porous morphology (Figure 2-18C). Such a porous structure not only increases the effective surface area but also facilitates the incorporation and co-immobilization of other functional species, such as enzymes, nanoparticles, or biomolecules. These results demonstrate that BPE can go beyond simple metal deposition, offering a facile pathway for integrating soft matter onto 2D materials.

To facilitate the visualization of the deposited polymer, EP was used to co-immobilize $K_3Fe(CN)_6$, acting as a co-reactant for luminol-based CL.[156] Ferricyanide-induced CL of luminol (3-aminophthalhydrazide) has been widely explored[157], based on the oxidation of luminol to 3-aminophthalate. In addition, we modified the opposite corner of the graphene monolayer with Pt (Figure 2-18B), so the sheet can also act simultaneously as an autonomous 2D swimmer when H_2O_2 is present as a fuel[73, 107]. Figure 2-19A illustrates the architecture and mechanism of the combined CL-swimmer. Pt is first deposited at one corner of graphene, then the obtained Pt-graphene is exposed to a mixture comprising $K_3Fe(CN)_6$ and a diluted electrophoretic paint solution. Next, water oxidation is triggered by BPE at the anodic side, resulting in a local pH decrease when an electric field of 5.7 V/cm is applied. Consequently, the paint precipitates at the anodic corner, and $K_3Fe(CN)_6$ molecules are co-immobilized inside the porous structure of EP.

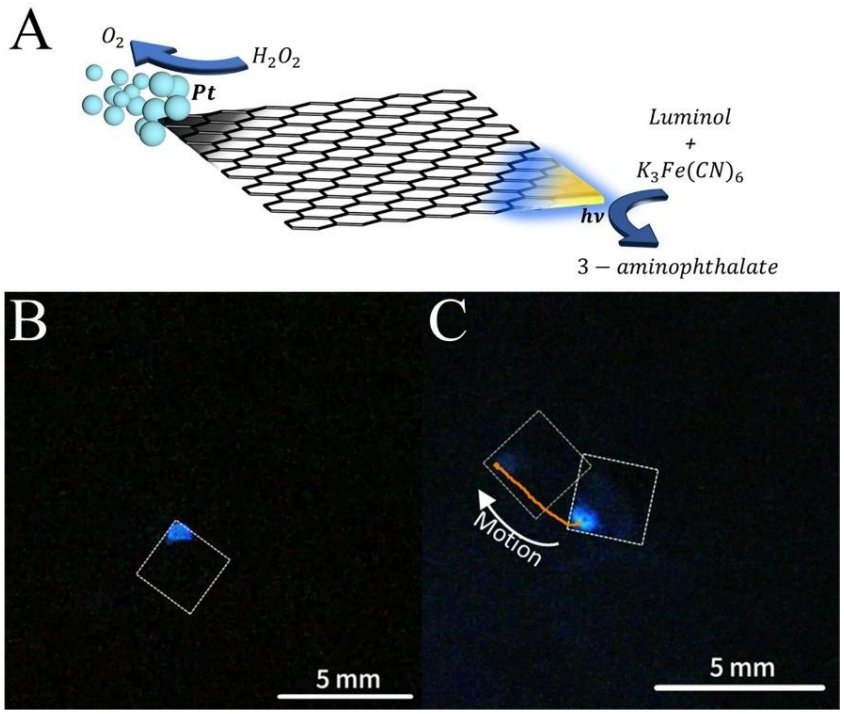

Figure 2-19 (A) Illustration of the mechanism underlying the Pt-graphene-EP chemiluminescent swimmer. (B) Chemiluminescence picture of Pt-graphene-EP in 20 mM luminol and 0.1 M NaOH solution. (C) Chemiluminescence time-laps photograph of Pt graphene-EP in 20 mM luminol, 0.1 M NaOH, 3 wt. % SDS, and 5 % (V/V) H_2O_2 solution.

To further investigate both the CL properties and the dynamic behavior of the Pt-graphene–EP composite, the sample was transferred to the air/water interface of a 20 mM luminol solution. The CL emission was recorded using a digital camera, and Figure 2-19B shows a representative photograph of the freely floating Pt-graphene–EP sheet in complete darkness. For clarity, the contour of the sheet is outlined with dashed lines. Notably, intense blue CL was observed exclusively at the EP-modified corner, which originates from the reaction of luminol with ferricyanide ($K_3Fe(CN)_6$) released from the polymeric EP domain. As the oxidation reaction proceeds, ferricyanide is gradually consumed, leading to a steady decrease in the CL intensity over time until the signal eventually vanishes. This experiment highlights that the EP-functionalized region serves as a localized reservoir of redox-active species, thereby enabling light emission from predefined positions on the graphene sheet.

To simultaneously probe motion, a separate experiment was carried out by placing another Pt-graphene-EP sheet on the surface of a solution containing 20 mM luminol, 3 wt.% SDS, and 5% (v/v) H_2O_2. In this system, the Pt domain catalyzes the decomposition of H_2O_2 to generate O_2 bubbles, which provide the driving force for propulsion. The addition of SDS plays a critical role by lowering surface tension, thus promoting efficient bubble formation and facilitating their detachment from the surface, which in turn enhances propulsion efficiency. Figure 2-19C presents two superimposed photographs, where the trajectory of the swimmer can be clearly tracked by the path of the diminishing blue CL spot. The progressive decrease in CL intensity during motion directly reflects the consumption of ferricyanide in the EP domain, which simultaneously provides a convenient optical marker for real-time tracking of the swimmer's displacement. This result shows clear difference with respect to graphene modified with PB and Pt, where the rapid consumption of PB leads only to a short-time CL signal. In comparison, the introduction of EP significantly prolongs CL, while simultaneously enabling clearly observable propulsion.

Although the CL lifetime under these conditions is limited to approximately 30 s due to ferricyanide depletion, the bubble-driven propulsion continues well beyond the luminescence period, confirming that the catalytic activity of Pt and the dynamic behavior of the composite are not restricted by the luminol/ferricyanide system. This proof-of-concept experiment demonstrates a unique coupling of catalytic motion and chemiluminescent signaling within a single graphene-based hybrid, opening exciting perspectives for the design of multifunctional micromotors that can self-report their activity through light emission while simultaneously performing mechanical tasks.

These results illustrate the multifunctional character of the modified graphene monolayer. The concept reported here is obviously not limited to graphene and can be easily extended to other 2D materials in the future, ranging from conductors to semiconductors, such as transition metal dichalcogenides or hexagonal boron nitride, to name just a few. This concept also provides the opportunity to create multifunctional 2D materials with enhanced properties for diverse applications like photocatalysis and electrocatalysis.

2.2.3 Conclusion

In this section, we demonstrated the possibility of synthesizing a hybrid 2D material based on a graphene monolayer using BPE with three key achievements. First, we achieved precise site-selective deposition of Au, Pt, Pd, and Cu on specific edges and corners of the monolayer. Second, we extended this concept to the indirect deposition of PB, a coordination compound with well-known redox activity. The PB-modified graphene monolayer exhibited catalytic activity toward luminol CL, with localized blue emission observed at the PB domains. Although the emission lifetime is short due to the rapid consumption of PB, this result demonstrates that BPE can be employed not only for metal deposition, but also for the integration of functional coordination-based materials onto 2D substrates. Third, we managed to co-deposit Pt and an electrophoretic paint at different locations of a single graphene sheet. The resulting multi-functionality is illustrated in a proof-of-principle experiment by the autonomous motion of the graphene layer, powered by the continuous release of oxygen bubbles generated from Pt-accelerated H_2O_2 decomposition, coupled with simultaneous light emission. The latter is possible due to the immobilization of $K_3Fe(CN)_6$ in the porous polymer deposit, reacting with luminol to generate spatially localized CL. The versatility of the presented approach, difficult or impossible to achieve with other methods, allows envisioning its use as a promising strategy for the elaboration of other multi-functional 2D materials which might be employed in various fields, such as analysis, (photo)catalysis, depollution, and delivery of active compounds.

2.3 Enzyme-modified graphene monolayers for the direct transformation of biochemical energy into motion

With the rapid consumption of global energy and growing environmental problems, the development of sustainable energy conversion technologies has become one of the central focuses of scientific research.[158-161] Energy conversion strategies based on biological systems have attracted extensive attention due to their environmental compatibility and renewability.[162] For instance, some microbes or enzymes, capable of converting biomass into commodity chemicals or fuels, demonstrate significant potential for generating green and clean energy.[163-165] Biofuel cell devices rely on the coupling of two spontaneous enzymatic redox reactions, fuelled by renewable biomolecules.[166-170] However, like many electrochemical processes, biofuel cells face inherent mass transport limitations. Fuel consumption at the electrode surface leads to the gradual growth of a diffusion layer, which hinders substrate supply, slows down the biocatalytic reaction, and ultimately reduces current output and power.

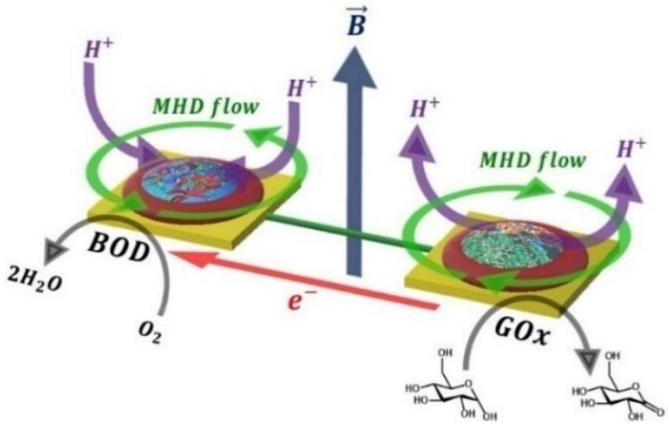

Figure 2-20 Illustration of the formation of the macro-MHD flow (green arrow) on the surface of the coupled GOx anode and BOD cathode composing the biofuel cell. Adapt from Ref. [171].

A strategy to overcome these limitations is the synergy between electric and magnetic fields. When a magnetic field is applied orthogonal to an electric or ionic current, a Lorentz force acts on the moving charges, thereby inducing an ionic magnetohydrodynamic (MHD) flow.[172-176] This well-established concept has been employed in electrocatalysis[177, 178], microfluidics[179, 180], and the design of dynamic electrochemical systems[181, 182]. In bioelectrocatalysis, magnetic fields parallel to the electrode surface have been shown to enhance the performance of enzyme-modified electrodes by inducing macro-MHD vortices[183, 184], but such improvements typically require high-intensity fields. Interestingly, imposing the magnetic field perpendicular to the electrode surface provides an alternative solution. As the ionic current at the edges of the electrode is not parallel to the magnetic field, a significant Lorentz force is generated on ionic currents near the electrode edges.[185] This results in localized macro-MHD flow along the electrode borders, effectively thinning the diffusion layer and accelerating substrate transport (Figure 2-20). The constant renewal of electroactive species near the enzyme-modified electrodes enhances Faradaic currents and thus substantially improves the efficiency of biochemical-to-electrical or biochemical-to-mechanical energy conversion.[186] These concepts not only address fundamental mass transport limitations in biofuel cells, but also open promising opportunities for developing enzymatic objects which are coupled with an external magnetic field to boost the dynamic performance.

Such a strategy can be extended to enzyme-powered micro-/nanoswimmers[187], where enzymes themselves act as the driving engines. Those enzymatic objects can convert chemical energy directly into mechanical energy, and have become a new direction in the field of energy conversion due to the use of bio-sourced fuel. Such enzymatically powered systems typically undergo redox or hydrolysis reactions, catalyzed by single or multiple enzymes (such as bilirubin oxidase (BOD)[188], glucose oxidase (Gox)[189] or urease[190], generating local ion concentration gradients and self-electrophoresis to drive autonomous movement. Compared with traditional chemical and bubble propulsion systems, enzymatic swimmers offer distinct advantages. Their fuels (such as glucose, oxygen or urea) are widely available and of natural origin, while the reaction products are environmentally friendly.[191-193] These advantages make them compatible with the requirements of sustainable energy conversion devices. Thus, the development and optimization of such devices is an ongoing challenge in current research, whether it concerns their design, the improvement of their speed or a better directional control. In addition to the often reported micro- and nanoswimmers[194, 195], macroscale enzymatic swimmers have also been studied, using *e.g.* conductive substrates such as carbon fibers[187, 196], or polypyrrole films[197], modified with enzymes, leading to interesting self-propulsion behavior.

In this general context, 2D materials offer significant potential for developing enzymatic swimmer systems due to their excellent mechanical properties, high intrinsic conductivity, and atomic thickness. To achieve directed motion, the symmetry of such materials needs to be broken and one straightforward approach, among many others, is based on bipolar electrochemistry. As discussed earlier, this versatile technique can be employed to deposit with high spatial control various metals and polymer composites at specific sites of monolayer graphene, and it therefore can be advantageously used for designing novel graphene-based bioelectrochemical swimmers

In this section, we developed an enzymatic graphene swimmer by generating first ultrathin gold layers at both extremities of a piece of monolayer graphene via bipolar electrodeposition. Then, glucose oxidase and bilirubin oxidase were immobilized on these oppositely located Au-modified areas. These bi-enzymatic hybrid 2D objects exhibit intriguing dynamic features in the presence of glucose and oxygen. Most importantly, we show for the first time that by applying an external magnetic field, their behavior can be precisely controlled, allowing well-defined rotational motion, combined with an improved energy conversion efficiency.

2.3.1 Fabrication of enzymatic Au-graphene

The graphene monolayer sheets were prepared as previously via a standard wet-transfer method, which allows the transfer of large-area, continuous graphene monolayer from the growth substrate to the desired air/water interface. To enable subsequent enzyme immobilization, Au layers were deposited selectively at both extremities of the graphene sheets using bipolar electrodeposition. As illustrated in Figure 2-21, the graphene monolayer was first positioned at the air/water interface of an aqueous Au-salt solution placed between two driving electrodes. After applying a sufficiently high electric field across the solution, localized polarization occurred at the extremities of the graphene sheet, and Au reduction was induced at the cathodically polarized pole, resulting in the formation of a thin Au layer. Subsequently, the graphene sheet was rotated by 180°, and the same procedure was repeated to deposit Au on the opposite extremity, thereby achieving symmetric dual-end modification.

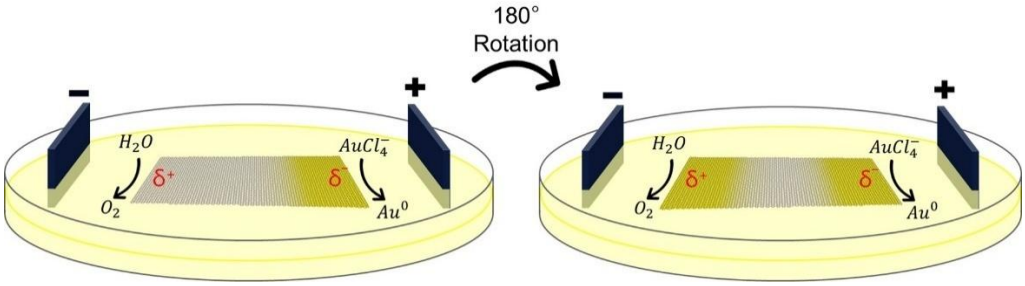

Figure 2-21 Illustration of Au deposition at the two extremities of a graphene sheet by bipolar electrochemistry.

The successful selective deposition was verified by optical microscopy and elemental analysis. As shown in Figure 2-22A, the Au-modified ends of the graphene monolayer exhibited a distinct color contrast compared to the pristine central region, which remained optically transparent, indicating that deposition was confined to the sheet's extremities. Figures 2-22B and C present the corresponding EDS mappings, clearly confirming the presence of Au exclusively at the two extremities of the sheet. These results highlight the spatial precision of bipolar electrodeposition for achieving site-selective metal modification of delicate 2D materials.

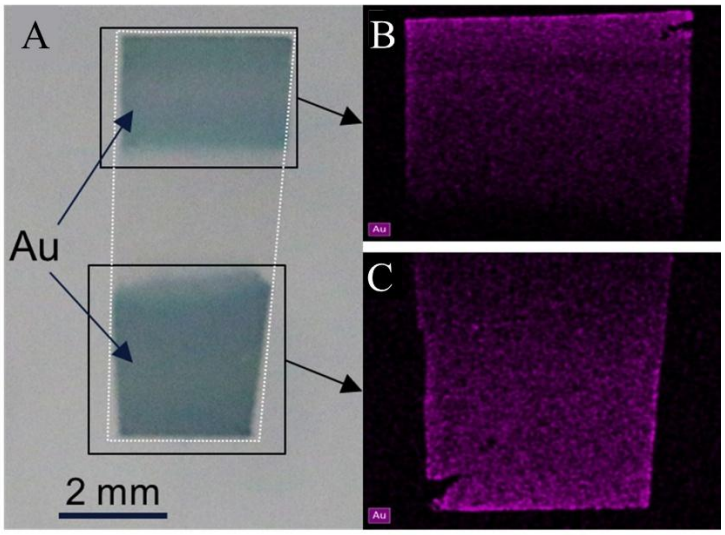

Figure 2-22 (A) Optical image of Au modified graphene monolayer sheet via bipolar electrochemistry. The outline of graphene is marked with dashed line. (B, C) EDS mapping of Au modified area on graphene sheet.

The deposition of a thin gold layer onto the graphene surface is favorable for this enzymatic device. Due to the atomically flat and hydrophobic nature of graphene, direct immobilization of enzymes often results in a poor interfacial contact, leading to inefficient electron transfer and unstable enzyme attachment. In control experiments using enzyme-modified pure graphene without gold deposition, the motion was difficult to observe and the enzyme layer easily detached during the experiments. In contrast, gold deposition significantly increases the surface roughness of graphene, providing a larger surface area which is more favorable to immobilize the enzyme layer. This roughened interface also enhances the mechanical stability of the enzyme layer and promotes the contact between the enzymes and graphene, thereby facilitating electron transfer and sustaining catalytic activity. As a result, the gold-modified graphene enables stable enzyme loading and efficient propulsion behavior, which is difficult to achieve with bare graphene.

2.3.2 Dynamic behavior of the enzymatic graphene swimmer

The enzymatic graphene swimmers were prepared by immobilizing two enzymes (Gox and BOD) at opposite extremities of an Au-modified graphene sheet using Os-based redox polymer hydrogels[198, 199]. The enzyme-hydrogel mixtures were site-specifically loaded onto the Au-modified areas *via* drop-casting. Typically, the Au-graphene sheets were transferred onto the surface of solidified agarose gel for immobilization. Then, an anodic hydrogel was deposited onto one Au-modified extremity and a cathodic hydrogel onto the other by drop-casting.

In the presence of both glucose and oxygen, the spatially separated enzymatic reactions establish a short-circuited biofuel cell. Gox catalyzes the oxidation of glucose at the anodic side, generating electrons (e^-, red arrow in Figure 2-23A) that travel through the graphene monolayer to drive the oxygen reduction reaction mediated by BOD at the cathodic side. Simultaneously, glucose oxidation at the anodic side continuously generates protons, while the oxygen reduction at the cathode consumes protons. Consequently, protons are asymmetrically distributed along the graphene layer and develop a local electric field. This self-generated field causes an electroosmotic fluid flow by proton migration within the electric double layer of the swimmer. This induces a force (F_E, orange arrow, Figure 2-23A) that propels the graphene swimmer opposite to the proton flux. To validate this self-electrophoresis mechanism, the dynamic behavior of the enzymatic graphene swimmer was systematically investigated under varying conditions. The first control experiment was carried out in an oxygen-free solution. In this case, no electron transfer is possible, and no significant motion is observed apart from a small random drift. In the next set of experiments, an oxygen-saturated 0.1 M phosphate buffer solution (pH 7.0), maintained at 37 °C in a water bath and containing 20 mM glucose as fuel, was employed. As illustrated by the trajectory displayed in Figure 2-23B, the graphene swimmer exhibits linear propulsion toward the Gox-modified edge, with an average speed of 2.7 cm s^{-1}.

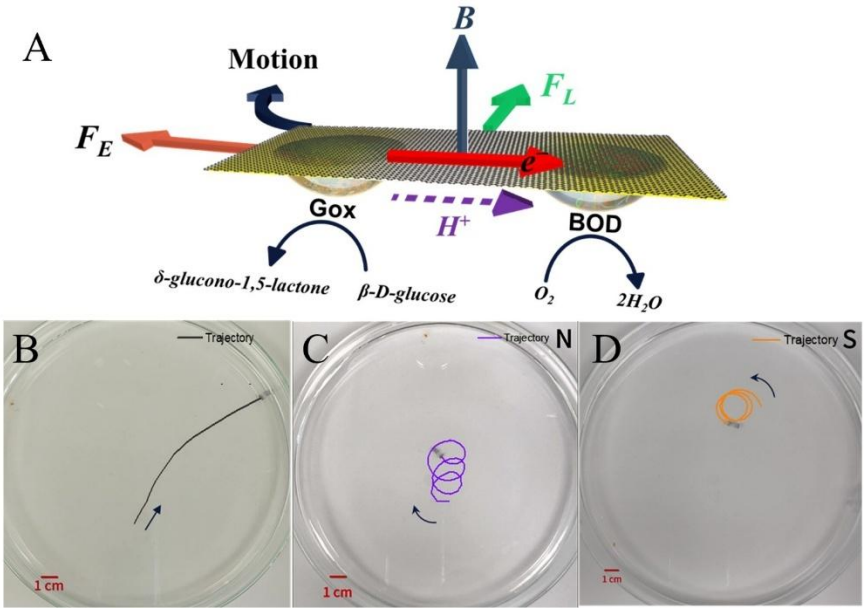

Figure 2-23 (A) Illustration of the mechanism of the enzymatic graphene swimmer. (B) Trajectory of an enzymatic graphene swimmer (BOD: Gox = 1: 1) moving at the air/water interface in the absence of magnetic field. (C) Trajectory of an enzymatic graphene swimmer (BOD: Gox = 1: 1) moving at the air/water interface in the presence of a N pole up magnetic field. (D) Trajectory of an enzymatic graphene swimmer (BOD: Gox = 1: 1) moving at the air/water interface in the presence of a S pole up magnetic field. The fuel solution consists of 0.1 M phosphate buffered saline (PBS) and 20 mM glucose solution with pH 7, 37 °C, and O_2 saturated.

Most interestingly, when an external magnetic field (Figure 2-23A, blue arrow) is imposed on this system, the induced Lorentz force (F_L, green arrow in Figure 2-23A), in synergy with F_E, results in a complete change of the swimmer's trajectory, despite the absence of magnetic elements in its architecture. Specifically, the swimmer's trajectory changes from linear to rotational motion upon application of an external magnetic field. This behavior originates from the interaction between the ion flow generated by the short-circuited enzymatic fuel cell and the external magnetic field.

The mechanism can be explained as follows: first, in the presence of their respective fuels, glucose oxidation at the Gox side and oxygen reduction at the BOD side proceed spontaneously. Owing to the spatial separation of the two enzymes on the graphene sheet, these redox reactions induce a directional flux of ions (mainly protons) from the Gox-modified area toward the BOD-modified area. As a result, a continuous ionic flow is generated in the surrounding electrolyte from Gox to BOD. Second, when an external magnetic field is applied perpendicular to this ion flux, the moving ions experience a Lorentz force, which gives rise to a MHD flow in the electrolyte. This MHD flow produces locally around each enzyme-modified area, where the ionic current interacts with the external magnetic field. As indicated in Figure 2-20, the induced MHD flow circulates anticlockwise around BOD, while a clockwise circulation is generated around the Gox-modified part. These two oppositely rotating vortices do not cancel out each other, instead, their combination generates a lateral fluid flow between the two enzyme layers. This lateral flow combined with the electrophoretic propulsion force generates a torque and ultimately leads to a transition from linear to rotational motion.[186]

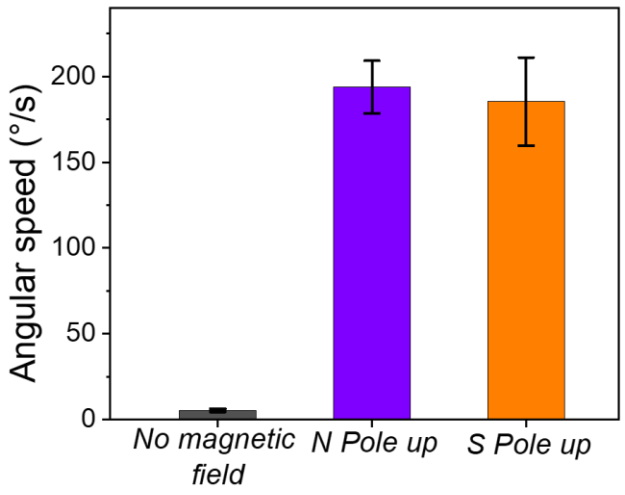

Figure 2-24 Angular speed of enzymatic graphene swimmers without magnetic field (dark column), with N pole up (purple column), and with S pole up (orange column).

To better characterize this behavior, we analyzed in more detail the generated circular motion during the first 5 seconds. With the north pole facing up (Figure 2-23C), a clockwise rotation is observed with an average speed of 2.6 cm s^{-1}. In contrast, with the south pole up (Figure 2-23D), an anticlockwise rotation with an average speed of 2.7 cm s^{-1} is recorded. Importantly, reversing the magnetic field direction changes the direction of the Lorentz force while leaving the enzymatic reaction pathway unchanged, directly confirming that the observed rotational motion

is governed by the MHD flow rather than magnetic interactions with the swimmer itself. Notably, the linear component of the motion is always directed toward the Gox-modified extremity.

To provide a more quantitative analysis of the influence of the magnetic field on the dynamic behavior of the swimmers, the angular displacement and angular speed under different conditions (no external magnetic field, north pole up, and south pole up) were analyzed. Figure 2-24 compares the initial angular speed of the three experiments after placing the swimmer at the air/solution interface. In the absence of the external magnetic field, it exhibits only a neglectable angular speed, due to either a drift or a slight asymmetry in the shape of the graphene sheet. When the magnetic field is applied, the angular speed is 193° s^{-1} and 185° s^{-1} for the north pole and south pole-up configuration, respectively.

The linear and angular speeds of the graphene swimmer not only depend on the magnetic field, but are also directly correlated with the efficiency of both redox reactions involving Gox and BOD, respectively. A critical parameter influencing the efficiency of the redox reactions is the enzyme loading. All the above discussed experiments were conducted with the same enzyme loading ratio (BOD: Gox = 1: 1). However, the speed of the enzymatic graphene swimmer may be limited by the conversion of oxygen, due to its low solubility, and the associated consumption of protons by BOD. To address this aspect, the loading ratio of BOD and Gox was changed to 2: 1. This enhanced BOD loading enables a faster consumption of the protons and electrons generated by Gox. Consequently, swimmers with a doubled BOD loading exhibit an average speed of 3.7 cm s^{-1}, a 1.4 times enhancement compared to the loading ratio of 1: 1 under otherwise identical conditions (Figure 2-25A).

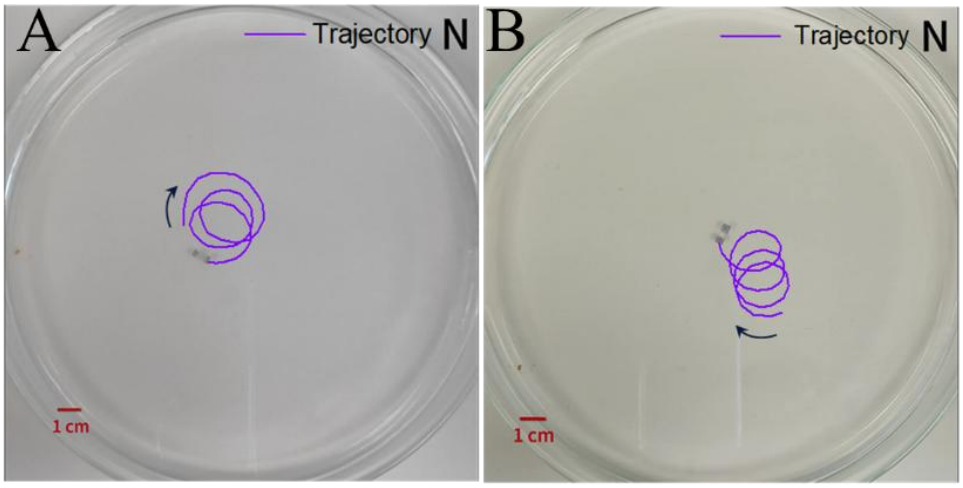

Figure 2-25 (A) Trajectory of an enzymatic graphene swimmer (BOD: Gox = 2: 1) moving at the air/water interface of a 0.1 M PBS, 20 mM glucose, pH 7, 37 °C, and an O_2 saturated solution in the presence of a N pole up magnetic field. (B) Trajectory of an enzymatic graphene swimmer (BOD: Gox = 2: 1) moving at the air/water interface of a 0.1 M PBS, 40 mM glucose, pH 5, 37 °C, and O_2 saturated solution in the presence of a S pole up magnetic field.

To further enhance the speed of the graphene swimmers, the composition of the fuel solution can also be optimized. Based on swimmers with the BOD: Gox = 2: 1 loading, the glucose concentration has been increased from 20 mM to 40 mM, and the solution pH was adjusted to 5. Under these conditions, the swimmer shows a significantly improved average linear speed of 4.8 cm s^{-1} (see Figure 2-25B). Obviously, the higher glucose concentration can provide more

substrate and thus promote the catalytic activity of Gox, but more importantly, a pH of 5 is close to the optimal pH of Gox and BOD, which enhances the activity of both enzymes, thus strengthening the proton gradient and the resulting electrophoretic force. The mass of the swimmer is also an important parameter to achieve high speed. The weight of a graphene swimmer is around 30 μg, which represents a unique advantage of using a graphene monolayer as a support.

Optimization of the enzyme loading represents an effective strategy to improve propulsion performance and thus we further investigated in more detail the motion and angular speed as a function of this parameter. Figure 2-26 illustrates the effects of the magnetic field and varying enzyme loadings. First, in the case of the same loading of BOD and Gox (black and green curves in Figure 2-26A), the speed of both swimmers gradually decreases and the magnetic field doesn't seem to have a major impact on the linear speed component, except for the very beginning of the experiment. This is because the presence of an external magnetic field also generates MHD flow around the two enzyme spots. This convection accelerates the reactions and thus the energy conversion efficiency. An enhanced linear speed is observed at short times in the presence of the magnetic field with the north pole facing up (Figure 2-26A), and a similar increase is detected for the south pole-up configuration (not shown). This improvement can be attributed to the generation of local MHD flow, which facilitates the transport of substrate molecules toward both enzyme spots in the early moments of the experiment when the swimmer starts to move. Once swimmer motion is established, this additional MHD-related mass transport no longer has a significant impact on the overall reaction rate and thus the speed. In strong contrast to this, the angular speed component (black and green curves in Figure 2-26B) is very sensitive to the presence of the magnetic field. In the absence of the magnetic field, the angular speed is close to zero with minor fluctuations. However, when the magnetic field is applied, the angular speed is significantly higher. Nevertheless, the angular speed tends to decrease gradually over time, which is consistent with the trend of the linear motion. Two factors might be responsible for this behavior: (1) initially, the redox polymer contains dissolved oxygen, so when the swimmer is placed at the air/solution interface, the enzymes encapsulated in the redox polymer will consume both the stored oxygen and oxygen from the solution. This simultaneous consumption of oxygen, provided from two sources, results in a temporarily higher speed. After the oxygen, locally stored in the hydrogel, is consumed, oxygen from the solution needs to penetrate the gel to reach the enzyme, and this transport limitation leads to a gradual decrease of linear and angular speed. (2) The swimmers move at an initially quite high speed and this creates rather important shear forces which gradually remove parts of the enzyme-containing hydrogel as it is facing downwards and is therefore directly exposed to the strong local hydrodynamics. Thus, less and less fuel can be converted per time, inducing a decrease in speed. Unfortunately, this decrease of activity prevents using the same swimmer several times. However, we have studied multiple independent swimmers and observed a very similar dynamic behavior, indicating a good reproducibility of the protocols. Related to this aspect, improvements of the lifetime might be achieved by protecting the enzyme layers with membranes.

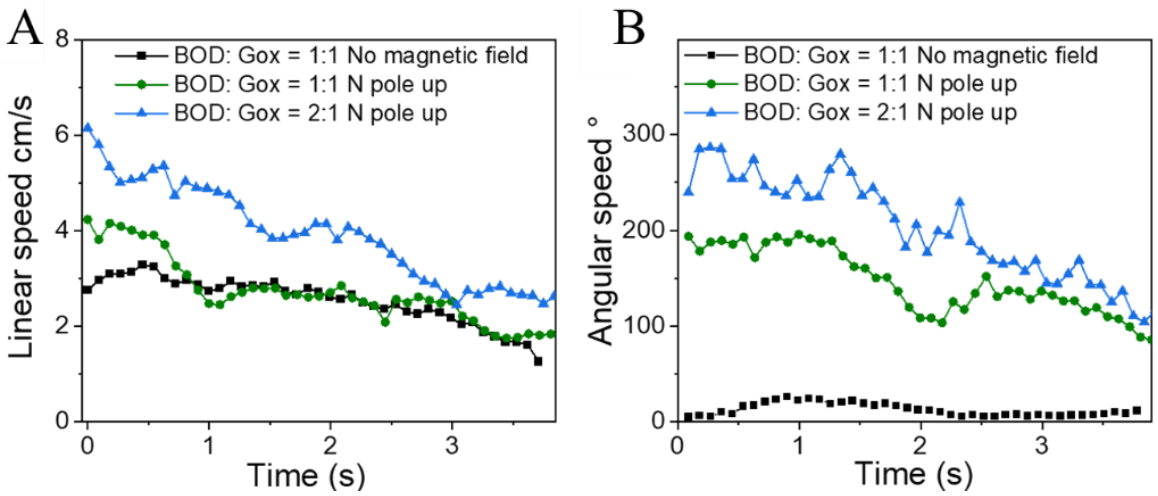

Figure 2-26 (A) Linear speed and (B) angular speed profiles of enzymatic graphene swimmers with different enzyme loading ratio in 0.1 M PBS and 20 mM glucose solution with pH 7, 37°C, O_2 saturated solution under N pole up magnetic field.

When the BOD loading is doubled with respect to the amount of immobilized Gox, linear and angular speed show a considerable increase (blue curves in Figure 2-26). This indicates that oxygen conversion is the rate limiting process and directly impacts the propulsion efficiency (*vide supra*). Also, in this case the speed decreases as a function of time, and it is reasonable to assume that this is due to a gradual stripping of the redox hydrogel exposed to strong hydrodynamic forces.

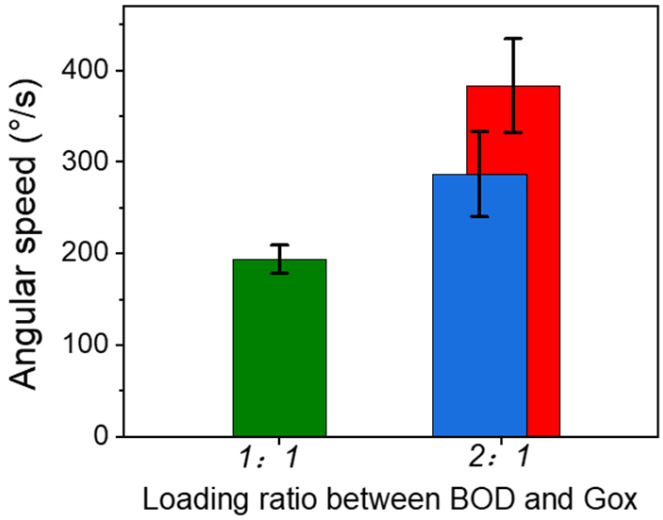

Figure 2-27 Angular speed of enzymatic graphene swimmers in the presence of N pole up with different loading ratios of BOD and Gox, glucose concentrations, and pH. (Purple column: BOD: Gox = 1: 1, 20 mM glucose, pH 7. Blue column: BOD: Gox = 2: 1, 20 mM glucose, pH 7. Red column: BOD: Gox = 2: 1, 40 mM glucose, pH 5.)

Besides the linear speed component, the average angular speed of the enzymatic graphene swimmers is also affected by the enzyme loading and the composition of the fuel solution. Figure 2-27 compares swimmers with different enzyme loading ratios and after fuel solution optimization. The green bar represents the initial condition (BOD: Gox = 1: 1) with an average angular speed of 193° s^{-1}. Doubling the BOD loading (blue bar, BOD: Gox = 2: 1) improves the average angular speed to 286° s^{-1}, while further fuel solution optimization (red bar, 40 mM glucose, pH 5) allows achieving a remarkable average angular speed of 383° s^{-1}, representing a

100% enhancement compared to the initial condition. The increased BOD loading and the optimization of the composition of the fuel solution amplify both, the proton flux between the two enzyme patches and the electron flow through the graphene sheet. This leads to an enhanced F_E and, most importantly, in the presence of the external magnetic field, also to an increase in F_L.

2.3.3 Electrochemical analysis of the enzymatic graphene biofuel cell

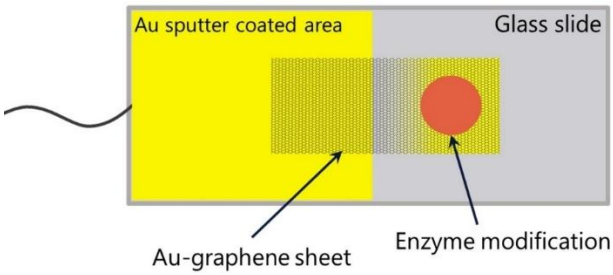

Figure 2-28 Design of the enzymatic graphene biofuel cell electrodes for classic electrochemical measurements.

To estimate the power output of such a device, electrochemical measurements were performed using a conventional biofuel cell with an analogous configuration (Figure 2-28). Typically, one bioanode and one biocathode were positioned at the bottom of a petri dish with the enzyme layers facing up. The distance between the two electrodes was around 1 cm. A rectangular FeNdB magnet was placed below the petri dish to generate a vertical magnetic field. The current measurements were carried out using an electrometer. The electrodes were then connected to an ammeter, and the electrolyte solution was added gently. The voltage measurements were performed by following the same protocol, but the electrodes were connected to a voltmeter.

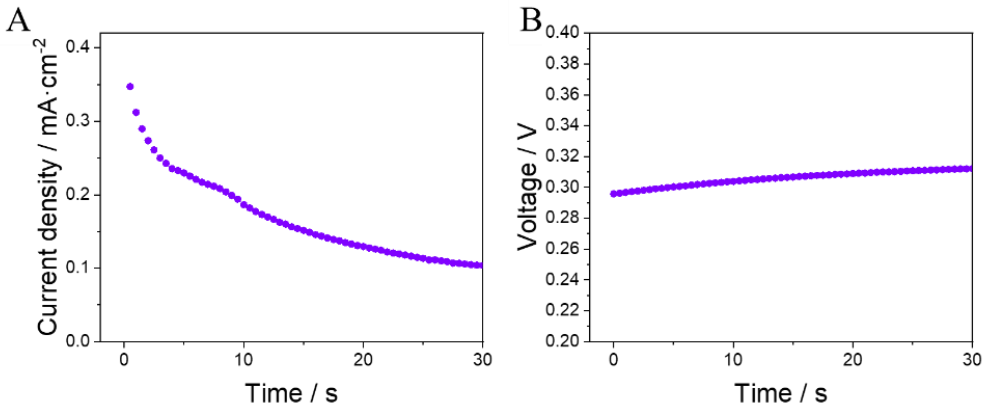

Figure 2-29 (A) Current density transient and (B) potential transient recorded with a classic biofuel cell set-up using electrodes illustrated in Figure 2-27 (BOD/Gox = 2:1) in an O_2 saturated 0.1 M PBS and 40 mM glucose solution at pH 5 and 37°C, with the north pole up configuration. The loading amounts of cathodic and anodic hydrogels are 2 µl and 1 µl, respectively.

The results reveal that the maximum current density flowing between the bioanode and the biocathode reaches approximately 0.35 mA cm^{-2}, with a corresponding open-circuit potential difference of 0.32 V. From these values, the initial maximum power density was calculated to be about 0.11 mW cm^{-2}. As illustrated in Figure 2-29, the power output is not constant, but decreases progressively with time, eventually stabilizing at a lower yet steady-state value. This decline can be attributed to mass transport limitations and the gradual consumption of enzymatic substrates, which lead to a diminished bioelectrocatalytic activity.

Interestingly, the temporal profile of the electrical power output correlates well with the dynamic behavior of the enzyme-modified graphene swimmers (Figure 2-30). At the beginning of the experiment, when the power density is at its maximum, the swimmers exhibit the highest propulsion speed. As the current output decreases due to substrate depletion and diffusion layer thickening, the swimmers gradually slow down until a quasi-stationary velocity is reached, in line with the stabilized power density of the biofuel cell. This agreement between electrochemical measurements and swimmer performance provides strong evidence that the motion of the enzymatic graphene sheets is indeed powered by bioelectrocatalytic processes and reflects the intrinsic energy conversion efficiency of the underlying biofuel cell mechanism.

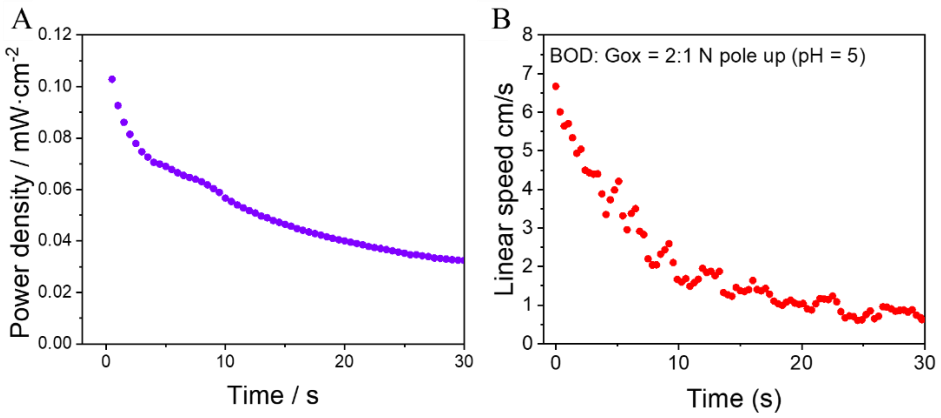

Figure 2-30 (A) Power density transient recorded with a graphene-based biofuel cell (BOD/Gox = 2:1) and (B) evolution of the linear speed component of a graphene swimmer in an O_2 saturated 0.1 M PBS and 40 mM glucose solution at pH 5 and 37°C, with the north pole up configuration. The loading amounts of cathodic and anodic hydrogels are 2 µl and 1 µl, respectively.

2.3.4 Energy conversion from electrical to mechanical energy

Next, in order to estimate how much of the electrical energy produced by the biofuel cell device is converted into mechanical energy, we compared the electrochemical power output with the mechanical power associated with the motion of the enzyme-modified graphene swimmers.

The first part is the calculation of electrochemical power output generated by a single biofuel cell.

The energy conversion efficiency from electricity energy (E_{elec}) to mechanical energy was estimated as follows:

$$E_{elec} = UIt \tag{2.10}$$

where *U (0.32 V)* is the voltage, and *I (6.8 µA)* is the maximum current of the biofuel cell, leading to a calculated E_{elec} of 2.17 *µJ*.

The second part is the calculation of mechanical energy recorded from the enzymatic swimmer.

The mechanical energy mainly involves the kinetic energy (E_k) observed on the swimmer and the energy to fight against resistance between the swimmer and solution. E_k can be calculated with the following equation:

$$E_k = \frac{1}{2}mv^2 \tag{2.11}$$

where *m* (3×10^{-8} *kg)* is mass and *v* (0.06 ms^{-1}) is the speed of the enzymatic graphene swimmer, leading to a calculated E_k of 5.4×10^{-5} *µJ*.

The enzymatic swimmer is composed of enzyme-hydrogel blocks and graphene sheet, where the enzyme-hydrogel blocks are fully immersed in the solution and the graphene sheet floats at the air–liquid interface. Thus, the resistance encountered by the swimmer during motion can be divided into two parts: the drag force between enzyme-hydrogel blocks ($F_{hydrogels}$) and the surrounding liquid, and the friction between graphene sheet and solution. To estimate the interaction between the enzyme-hydrogel and the solution, it is first necessary to calculate the Reynolds number in order to determine the appropriate model.

$$R_e = \frac{\rho v d}{\mu} \tag{2.12}$$

where ρ (*1000 kg m^{-3}*) is the density of the fluid, v (*0.06 m s^{-1}*) is the speed, d (*1.5×10^{-3} m*) is the diameter of hydrogel block, and μ (*1×10^{-3} kg m^{-1}s^{-1}*) is the dynamic viscosity of the fluid. The calculated R_e is 90, so the drag force of enzymes-hydrogel blocks can be calculated using the Stoke's drag equation when considering the enzyme-hydrogel blocks as a hemisphere. Since the two hydrogel blocks are spatially separated, it is reasonable to assume that there is no hydrodynamic interference between them under low Reynolds number. Therefore, the drag forces generated by each hydrogel block can be considered independently.

$$F_{hydrogels} = 3\pi\mu r v \times 2 \tag{2.13}$$

$$E_{hydrogels} = F_{hydrogels} \times vt \tag{2.14}$$

where μ (*1×10^{-3} kg m^{-1} s^{-1}*) is the dynamic viscosity of the fluid, r (*7.5×10^{-4} m*) is the radius of hydrogel block, v (*0.06 m/s*) is the speed, and t (*1 s*) is the time. The calculated $E_{hydrogels}$ is *5.1×10^{-2} μJ*.

Taking into account these values, the final energy conversion efficiency (η *%*) can be calculated as follows:

$$\eta = \frac{E_k + E_{hydrogels}}{E_{elec}} \times 100\% \approx 2.4\% \tag{2.15}$$

However, the actual mechanical energy recovered from electrical energy is higher than the estimated value, as the friction between graphene and solution at the air-liquid interface remains complex and difficult to quantify.

2.3.5 Conclusion

In conclusion, an enzymatic swimmer has been successfully developed through controlled immobilization of two enzymes on a graphene monolayer. The spatial separation of Gox/BOD patches enables the generation of a proton gradient, triggering autonomous motion with an extremely high speed, reaching up to 6 cm s^{-1} after optimization. Most importantly, for the first time we show that the trajectory and speed of such an enzymatic swimmer can be controlled and enhanced by an external magnetic field, allowing for an optimized energy transfer efficiency. This is also made possible, because graphene, as a typical 2D material, offers distinct advantages, including excellent conductivity, flexibility and a high surface area per weight. These proof-of-concept results bridge energy conversion with macroscopic robotics, providing an interesting alternative for biomimetic soft robotic design and targeted delivery applications.

2.4 Bipolar Electrochemistry-Driven Rotation of Light-Emitting Graphene Monolayers

As previously explained, BPE is a promising wireless strategy to induce motion in conducting objects without direct electrical connection. When a sufficiently high electric field is applied between the driving electrodes, a potential difference is generated along a conducting object, which drives asymmetric redox reactions at its extremities[7, 14]. This asymmetry generates localized electrophoretic forces or bubble generation that can induce displacement of the bipolar electrode[78-81, 85]. Such BPE-driven motion has already been exploited for translational and vertical motion of spherical beads. Importantly, compared with motion induced by structural or chemical asymmetry, BPE provides a highly tunable method of controlling both the localization and intensity of the driving forces simply by adjusting the applied electric field, thereby opening the way to more complicated dynamic behaviors.

Recently, an enhanced propulsion mechanism under magnetic fields has emerged as an attractive alternative for generating well-controlled motion.[87, 110, 200] This concept relies on the synergy between the principles of BPE[8, 201] and fundamental aspects of electromagnetism[172, 202]. In brief, when a sufficiently high polarization potential difference is induced between the extremities of a conducting object, polarization occurs at its two ends. If the polarization exceeds the thermodynamic threshold associated with the electrochemical processes involved, oxidation and reduction take place at opposite ends of the object.[181, 182, 203] These redox events create an internal flow of electrons within the bipolar electrode, which is balanced by an accompanying ionic current in the surrounding electrolyte to maintain electroneutrality. In the presence of a magnetic field oriented perpendicular to the BPE surface, the ionic current is subjected to a Lorentz force that is orthogonal to both the current and the field. When combined with an eccentric anchor point, this electromagnetic effect produces a predictable clockwise or anticlockwise rotational motion, with the direction being determined by the orientation of the magnetic field.

Moreover, this wireless mechanism has been demonstrated to asymmetrically trigger ECL at objects of different sizes.[29, 47, 105, 204, 205] Such BPE-driven dynamic behavior can thus be further expanded by coupling it with ECL, offering broader functionality. The asymmetric redox reactions at the anodic and cathodic poles of the bipolar electrode can simultaneously drive ECL processes, leading to localized light emission precisely at the polarized extremities. In this configuration, motion and light generation become intrinsically coupled: the displacement of the polarized object enhances the mass transport of electroactive species, while the emitted light serves as a real-time, highly sensitive optical readout of the redox activity.

The integration of BPE with external magnetic fields therefore makes it possible to combine two powerful concepts, motion and light emission, within a single object. BPE provides the localized redox reactions necessary for generating ECL directly on the object, while the magnetic field transforms the associated ionic flux into controllable rotational motion via Lorentz forces. In this way, even non-magnetic 2D materials such as graphene can be engineered into light-emitting rotors, where optical signals not only confirm the presence of redox activity, but also act as tracers of rotational dynamics. This dual functionality, achieved without ferromagnetic

components[206, 207], paves the way for multifunctional, wireless, and precisely controllable dynamic electrochemical analysis systems.

2.4.1 Design of 2D light-emitting magnetoelectrochemical rotor

In this section, we present a magnetic-field-enhanced electrophoretic propulsion mechanism to design a wireless light-emitting magnetoelectrochemical rotor. Graphene monolayers were selected as 2D bipolar electrodes owing to their excellent transparency and high conductivity, properties that are particularly advantageous for optical imaging of light emission. Their superior stability and mechanical strength further support their use in ECL systems under external electric fields. The light-emitting dynamic device was designed by coupling the oxidation of the $[Ru(bpy)_3]^{2+}$/TPA ECL system with water reduction reactions (Figure 2-31A). These processes generate a charge-compensating ionic flux along the 2D graphene bipolar electrode. In the presence of a magnetic field oriented orthogonally to the device, the ionic currents experience a Lorentz force, which produces an additional torque on the object (Figure 2-31B). Under these conditions, the graphene exhibits predictable clockwise or anticlockwise rotation, with the direction determined by the orientation of the external magnetic field. Furthermore, because both ECL intensity and angular velocity are directly linked to the kinetics of the electrochemical reactions, a clear correlation between the optical and mechanical performance of the rotor and the applied electric field was obtained. Finally, the interplay between the global electric field orientation and the magnetic field direction enables controlled full rotational displacements that can be monitored by ECL emission. This rotation generates additional hydrodynamic flow and reduces mass-transport limitations, which are often critical bottlenecks in heterogeneous redox processes. In the present case, the synergy between BPE and the magnetic field effectively improves the mass transport in the ECL reaction, as evidenced by the significant increase in emission intensity.

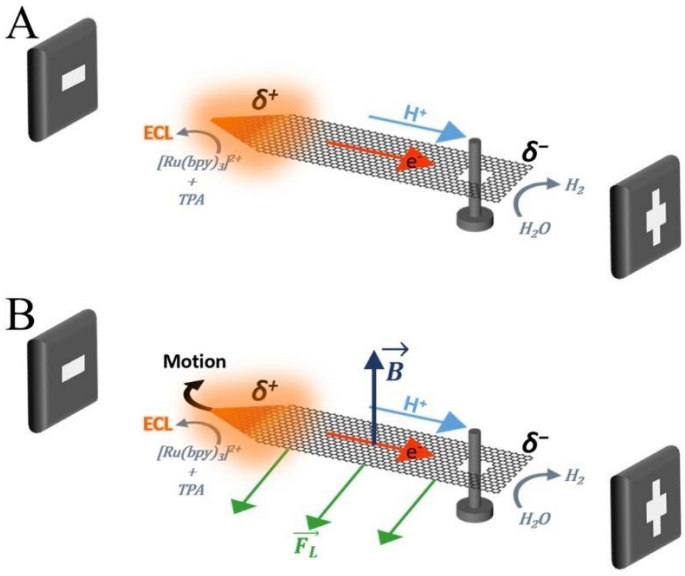

Figure 2-31 Illustration of the wireless light-emitting electromagnetic graphene monolayer rotor in (A) the absence and (B) the presence of an external magnetic field orthogonal to the surface of the BPE, with a representation of the associated electrochemical reactions, the driving electrodes, the ECL emission, the anodically and cathodically polarized extremities (δ^+ and δ^-, respectively), the electric and charge-compensating ionic currents ($\vec{J}$), in this case protons moving from the anode to the cathode of the BPE, the magnetic field ($\vec{B}$) and the resulting horizontal Lorentz force ($\vec{F_L}$).

As described above, the light-emitting magnetoelectrochemical rotor was constructed by exploiting the synergy between ECL reactions and the magnetic-field-enhanced electrophoretic mechanism. The dynamic and optical behavior of an arrow-shaped 2D graphene monolayer (l = 1 cm), acting as a bipolar electrode, was investigated at the air/water interface of a 5 mM PBS solution (pH 7.4) containing 2 mM $[Ru(bpy)_3]^{2+}$ and 50 mM TPA. To induce the magnetohydrodynamic effect, the bipolar cell was positioned at the center of a rectangular FeNdB magnet (B ≈ 200 mT, surface area ≈ 98 cm^2), with either the north or south pole oriented upward. Unless otherwise specified, these conditions were employed for all measurements. Upon application of a sufficiently strong electric field between the driving electrodes, asymmetric polarization of the graphene monolayer occurred, driving oxidation of the luminophore/co-reactant pair and concomitant water reduction. These coupled reactions resulted in photon emission in the red spectral region (~620 nm) (Figure 2-31A). In addition, these redox reactions generate an electron flow from the anodic to the cathodic pole of the graphene, accompanied by a charge-compensating ion flux ($\vec{J}$). Rotational displacement arises only when two additional asymmetries are introduced: (i) the presence of an external magnetic field oriented orthogonally to the BPE and (ii) the off-centered positioning of an anchor along the device (Figure 2-31B). The first asymmetry originates from the Lorentz force exerted on the charge-compensating ion flux generated by the electrochemical reactions (Equation 2.16), where protons migrate from the anode toward the cathode of the BPE.

$$\overrightarrow{F_L} = \vec{J} \times \vec{B} \tag{2.16}$$

This Lorentz force, orthogonal to $\vec{J}$ and $\vec{B}$, is accompanied by a flux of liquid, that in turn pushes the device in the opposite direction (Figure 2-31B). The asymmetric position of the anchor directly impacts the magnitude of the torque force ($\vec{\tau}$), since when the anchor is closer to the extremity of the device, the length of the lever arm (r) of the system increases, and consequently $\vec{\tau}$ varies according to Equation (2.17).

$$\vec{\tau} = r\overrightarrow{F_L} \sin\theta \tag{2.17}$$

Hence, the anchor axis was placed at the cathodic end of the BPE, whereas the anodic extremity, where ECL takes place, is free to rotate (Figure 2-31B). It is important to highlight that an additional macroscopic magnetohydrodynamic (macro-MHD) vortex is generated due to the induction of a Lorentz force on the electrolyte charges that migrate between the driving electrodes. However, it has been demonstrated that the impact of such a macro-MHD vortex on the rotation of the BPE is neglectable as long as the device is sufficiently polarized.

2.4.2 ECL emission and the propulsion of a graphene monolayer rotor

To verify the synergy between the optical and dynamic behavior of graphene monolayers under the action of BPE, we first investigated ECL emission and rotor propulsion under a constant electric field of 4 V cm^{-1}. Under these conditions, and in the absence of the magnetic field, a static ECL emission could be observed at one extremity of the graphene rotor, specifically at the anodic tip (Figure 2-32A, top). However, when a magnetic field was applied perpendicular to the BPE cell, predictable clockwise or anticlockwise rotation was observed (Figure 2-32A, middle and bottom). According to the right-hand rule, when the north pole of the magnet was facing upward, a clockwise light-emitting rotation was generated, while orienting the south pole upward

resulted in an anticlockwise rotation. It is worth noting that the use of a homogeneous magnetic field did not produce any additional motion of the graphene in the absence of BPE, confirming that the dynamic displacement originates from the synergy between bipolar electrochemistry and magnetic induction.[208]

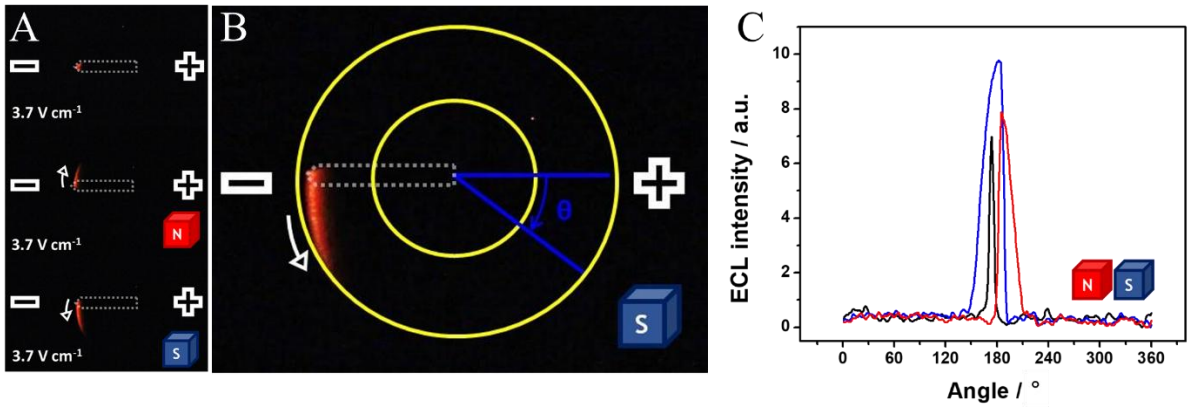

Figure 2-32 (A) Top view optical pictures of the ECL emission obtained during the dynamic response of a 1 cm long graphene monolayer rotor moving at the air/water interface of a 5 mM PBS (pH 7.4), 2 mM $[Ru(bpy)_3]^{2+}$, 50 mM TPA solution at a constant applied electric field (4 V cm^{-1}), in the absence (upper picture) and presence of a magnetic field (middle and bottom pictures, the orientation of the magnetic field is indicated in the figure). Scale bar 0.5 cm. (B) Optical picture of the ECL emission obtained during the dynamic response of a 1 cm long graphene 2D-rotor moving at the air/water interface of a 5 mM PBS (pH 7.4), 2 mM $[Ru(bpy)_3]^{2+}$, 50 mM TPA solution at a constant applied electric field (4.0 V cm^{-1}) in the presence of a magnetic field (south pole up). The angle ϑ is used for the azimuthal description and ϑ = 0° is defined as parallel to the electric field and passing through the center of the BPE. The dashed grey line indicates the initial position of the BPE. The yellow circles define the region of interest where the azimuthal analysis was carried out. (C) Azimuthal ECL profile as a function of the angle of rotation in the absence (black line) and presence of an external magnetic field with the north or south pole facing upwards (red and blue lines, respectively).

To quantitatively analyze the correlation between the optical and dynamic features of the light-emitting magnetoelectrochemical 2D rotor, the angular displacement was estimated by tracking the ECL emission. For this purpose, an azimuthal analysis of the ECL-emitting region was performed, corresponding to the arc section between two concentric circles (Figure 2-32B).[205] In this analysis, θ = 0° was defined as the direction parallel to the electric field at the cathodic extremity of the BPE (i.e., orthogonal to the driving electrode axis), and the ECL emission was extracted anticlockwise as a function of angular displacement. Unless otherwise indicated, this type of analysis was applied to all measurements. As shown in Figure 2-32C, in the absence of magnetic field, the ECL intensity profile remained centered at θ ≈ 180° for the entire duration of the experiment (t = 5 s, black line). In contrast, upon applying a magnetic field with either the north or south pole oriented upward, the ECL emission shifted toward angles higher or lower than 180°, respectively (red and blue lines), accompanied by a nearly fourfold increase in light intensity. This remarkable enhancement of ECL emission can be attributed to the effective coupling between 2D motion[182] and forced convection generated by the MHD flow near the graphene surface.[186] In practice, the convection promotes rapid local mixing of reactants, significantly accelerating the transformation of redox-active species.[209]

The azimuthal analysis provides an angular distribution map of the emitted light, thereby offering a detailed optical visualization of the polarization potential difference (ΔV) across the BPE as a function of angular displacement. According to the principles of BPE, the maximum ΔV is generated when the main axis of the BPE is aligned parallel to the applied electric field (θ = 0°).

However, as the object rotates, the polarization potential difference decreases with θ (Equation 2.18).

$$\Delta V = \varepsilon l \cos\theta \tag{2.18}$$

Since ΔV is directly linked to the kinetics of the electrochemical reactions, its variation strongly influences the ECL intensity. This correlation can be examined by plotting both the angular ECL contour and the theoretical polarization potential (ΔV_{theo}) as a function of the rotation angle (Figure 2-33). As expected, the maximum ECL intensity is observed at 180°, corresponding to ΔV_{theo} = 4 V, while the threshold polarization potential required for the coupled redox reactions is reached at θ = 140° (ΔV_{theo} = 2.7 V). Below this angular value, the ECL emission becomes negligible (Figure 2-33). Furthermore, these angular profiles enable a straightforward evaluation of the dynamic features of the magnetoelectrochemical 2D rotor, yielding angular velocities of 9.8° s^{-1} and 11.5° s^{-1} when the magnetic field is oriented with the north and south poles face up, respectively.

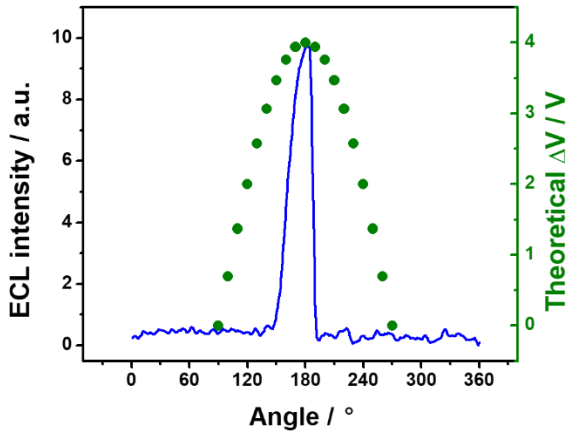

Figure 2-33 Azimuthal ECL profile (blue curve) and theoretical polarization potential (green curve) as a function of the angle of rotation, for a 1 cm long graphene sheet at a constant electric field (4 V cm^{-1}), in the presence of a magnetic field (south pole up).

We next investigated the influence of the arrangement of the applied electric field on the optical and dynamic behavior of the graphene monolayer rotor under an electric field of 4 V cm^{-1}. In this case, four driving electrodes were configured in a way that the applied fields were mutually orthogonal ($\varepsilon_1 \perp \varepsilon_2$), generating a diagonal global electric field (ε_{global}) in the cell (Figure 2-34). In this configuration, the polarization induced by ε_1 decays proportionally to cosθ, while that induced by ε_2 increases with sinθ. Consequently, the overall polarization potential of the BPE can be described by Equation (2.19).

$$\Delta V = \varepsilon l(\cos\theta + \sin\theta) \tag{2.19}$$

The results demonstrate that under this dual electric configuration, more obvious clockwise and anticlockwise rotations were produced when the north or south pole of the magnet was oriented upward, respectively (Figure 2-35A). In addition, the ECL profiles revealed an extended emission area of approximately 90° in both rotational directions (Figure 2-35B). Further analysis of the relationship between ECL emission and angular displacement shows that the regions of maximum light intensity were located at degrees of 135° and 225°, for the south and north pole orientations of the magnet, respectively. This indicates that the maximum polarization potential

difference of the rotor is induced when the graphene monolayer is aligned parallel to the global electric field, i.e., at ±45° from the initial position at 180°. Moreover, compared to systems without magnetic field (Figure 2-36), this magnetoelectrochemical displacement produced a much broader light-emission profile.

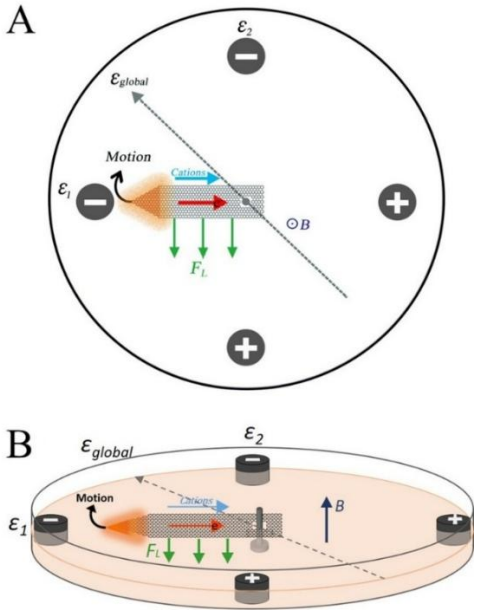

Figure 2-34 (A) Top and (B) side view of the initial position of the wireless light-emitting electromagnetic graphene 2D-rotor in a double electric field configuration with a representation of the direction of the electric and charge compensating ionic currents, the direction of individual (ε_1, ε_2) and global (ε_{global}) electric field, the ECL emission, the magnetic field ($\vec{B}$) and the resulting horizontal Lorentz force ($\vec{F_L}$).

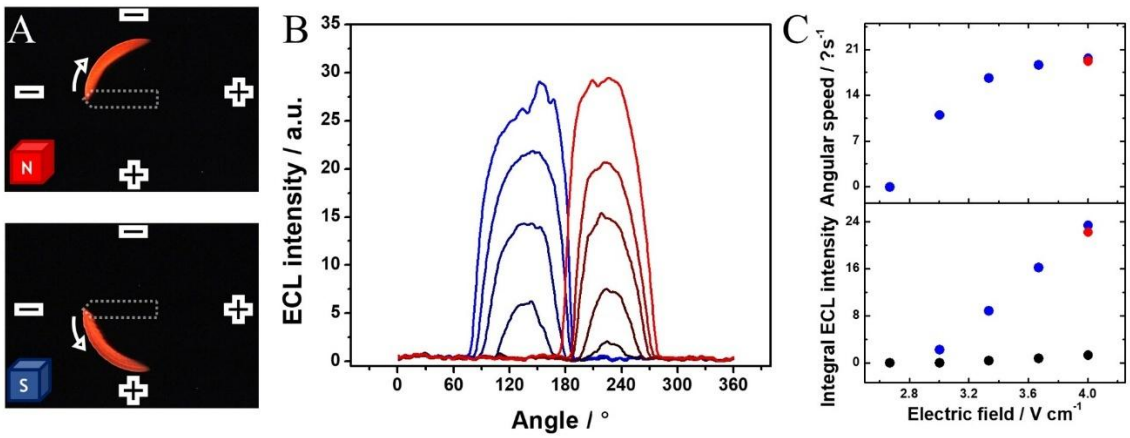

Figure 2-35 (A) Optical pictures of the ECL emission obtained during the dynamic response of a 1 cm long graphene 2D-rotor moving at the air/water interface of a 5 mM PBS (pH 7.4), 2 mM $[Ru(bpy)_3]^{2+}$, 50 mM TPA solution at a constant applied electric field (4 V cm^{-1}), as a function of the magnetic field orientation (indicated in the figure). (B) Azimuthal ECL profiles as a function of the magnetic field orientation at different applied electric fields (from 0 to 4 V cm^{-1}). (C) Angular speed (top) and integrated ECL intensity as a function of the applied electric field obtained in the presence of a magnetic field (blue dots: south pole up). The red dot refers to measurements with the north pole up, whereas the black dot relates to a measure carried out in the absence of magnetic field.

Because the induced ΔV directly effects the electrochemical reaction kinetics, and thereby affects the optical and dynamic properties of the rotor. Next, the impact of the applied electric field on device performance was evaluated. This evaluation was achieved by varying the intensity of ε in the absence and presence of an external magnetic field. First, without magnetic field, the 2D

graphene rotor displays static behavior accompanied by weak ECL emission localized near the anodic side rather than being confined exclusively to the tip of the arrow-shaped BPE (Figure 2-36), reflecting the diagonal distribution of the applied field. The angular features of the ECL emission obtained for different ε values revealed a progressive expansion of the light-emitting regions in both rotational directions (Figure 2-35B). From these data, the integrated ECL intensity and angular velocity were extracted as a function of the electric field (Figure 2-35C). The results show that the angular velocity reached the maximum of about 20° s^{-1} for electric field values higher than 3.4 V cm^{-1}, while a linear correlation between integrated ECL intensity and ε was observed in the range of 2.7-4 V cm^{-1}. These findings indicate that above 3.4 V cm^{-1}, magnetoelectrochemical rotation becomes limited, most likely due to the presence of a macro MHD flow between the driving electrodes, which counteracts the rotor's motion. Nevertheless, compared to systems without magnetic fields, the presence of a magnetic field resulted in an order-of-magnitude enhancement of ECL intensity (blue vs. black data points in Figure 2-35C, bottom). Furthermore, no significant variation of either angular velocity or ECL intensity was observed as a function of magnetic field orientation, indicating the absence of any spin-polarization effects associated with the coupling between the interfacial electrochemical reactions and the external magnetic field (blue and red points in Figure 2-35C).[210]

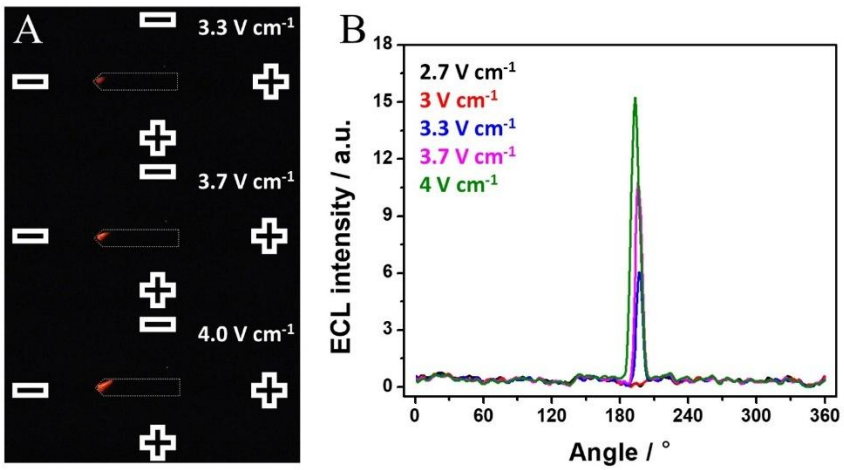

Figure 2-36 (A) Optical pictures of the ECL emission obtained during the dynamic response of a 1 cm long graphene 2D-rotor moving at the air/water interface of a 5 mM PBS (pH 7.4), 2 mM $[Ru(bpy)_3]^{2+}$, 50 mM TPA solution at different applied electric fields (indicated in the figure), in the absence of an external magnetic field. (B) Azimuthal ECL profile as a function of the angle in the absence of an external magnetic field.

Based on the findings above, we can conclude that the dual electric field configuration combined with magnetic field enabled a significant enhancement of both the optical and dynamic performance of the graphene monolayer light-emitting rotors. The cooperative effect of orthogonal electric fields and Lorentz-force-driven ion flux not only broadened the angular range of ECL emission but also amplified the overall light intensity, while simultaneously increasing the angular velocity of the rotors.

Next, we implemented a strategy to induce a complete 360° rotation of the graphene monolayer light-emitting rotor. By carefully controlling the orientation of the applied electric fields relative to the external magnetic field, a full rotational displacement can be achieved.

2.4.3 Continuous rotation of the graphene monolayer rotor

Finally, to overcome the angular limitations, dictated by the polarization potential difference, and to achieve a complete rotation, we combined the dual electric field configuration with an alternating current scheme. This strategy relies on the sequential inversion of the directions of ε_1 and ε_2 while maintaining a constant external magnetic field. As illustrated in the top left panel of Figure 2-37, the initial orientations of ε_1, ε_2, and the magnetic field generate a Lorentz force that induces anticlockwise rotation of the rotor. Once the rotor has rotated by 90° (Figure 2-37, top right), ε_1 is inverted, enabling the rotor to accomplish a half-turn. Upon reaching 180°, when the axis of the graphene monolayer rotor is aligned with ε_1, the direction of ε_2 is inverted (Figure 2-37, bottom right). The full 360° rotation is then completed by restoring both ε_1 and ε_2 to their original orientations (Figure 2-37, bottom left).

In this alternating current configuration, the arrow-shaped graphene rotor maintains its polarity throughout the cycle: the anchor consistently acts as the cathodic site, while the arrow-head extremity remains anodic. This ensures that the continuous displacement is driven by a globally rotating electric field, which effectively guides the motion without interruption. It is also important to note that the trajectory depends on the orientation of the external magnetic field: with the north pole facing upward, the device rotates anticlockwise, whereas with the south pole oriented upward, a mirror-image clockwise trajectory is induced. This cooperative mechanism thus provides a reliable method to induce full rotation of light-emitting 2D rotors by coupling BPE polarization with magnetic-field-driven ion flux.

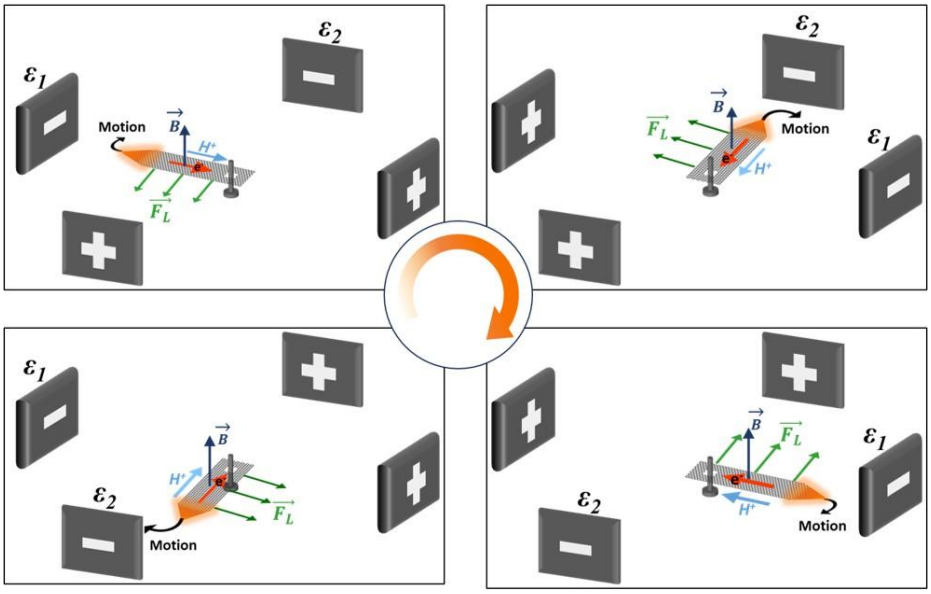

Figure 2-37 Illustration of the wireless light-emitting electromagnetic graphene 2D-rotor in an alternating double electric field configuration with a representation of the direction of the electric and charge compensating ionic currents ($\vec{J}$), in this case protons moving from the anode to the cathode of the BPE, the electric field (ε_1, ε_2), the ECL emission, the magnetic field ($\vec{B}$) and the resulting horizontal Lorentz force ($\vec{F_L}$).

We also investigated the optical and dynamic behavior of the 2D bipolar electrode by applying an electric field of 4 V cm^{-1} in the presence of a magnetic field, using the alternating double electric field scheme described above (Figure 2-37). Under these conditions, a continuous light-emitting rotation was generated, with clockwise or anticlockwise trajectories depending on the orientation of the magnetic field (Figure 2-38A). The ECL intensity profile as a function of angular

displacement revealed an oscillatory pattern, with maxima at approximately 55°, 150°, 240°, and 330°, and minima at around 8°, 98°, 196°, and 276° (Figure 2-38B). Since ε_{global} changes direction periodically, the ECL emission provides a direct optical mapping of the angular dependence of the polarization potential difference. The observed maxima and minima correspond to orientations where the graphene monolayer is parallel or orthogonal to ε_{global}, representing conditions of highest and lowest polarization potential difference, respectively. The light-emitting readout also facilitated an evaluation of the angular speed, yielding values of 13.72 ± 0.26° s^{-1} and 14.4 ± 0.32° s^{-1} for north and south pole up orientations, respectively (Figure 2-38B).

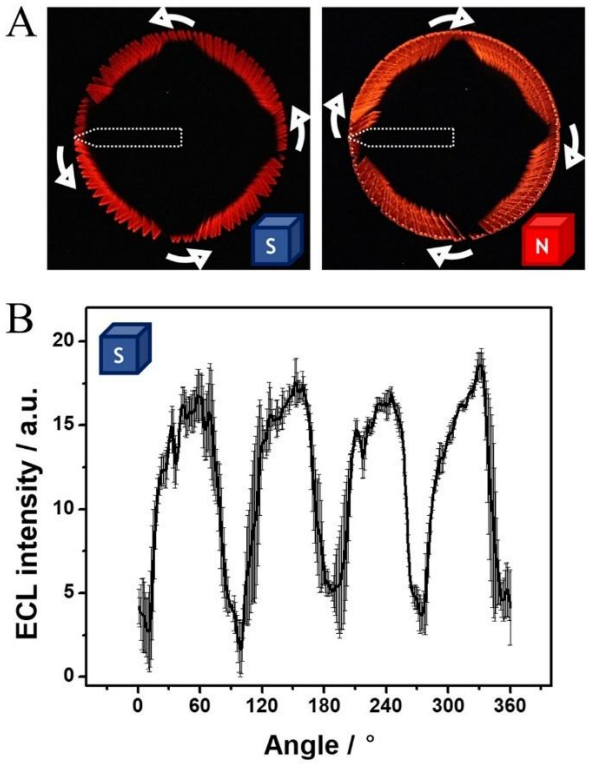

Figure 2-38 (A) Optical pictures of the ECL emission recorded during the dynamic response of a 1 cm long graphene 2D-rotor moving at the air/water interface of a 5 mM PBS (pH 7.4), 2 mM $[Ru(bpy)_3]^{2+}$, 50 mM TPA solution under the influence of an alternating double electric field configuration (4 V cm^{-1}), as a function of the magnetic field orientation (indicated in the figure). (B) Azimuthal ECL profile as a function of the angle in the presence of an external magnetic field (south pole up).

Beyond enabling precise correlation between optical signal and rotation dynamics, these results also emphasize that such a finely controlled behavior can only be achieved through bipolar electrochemistry. The asymmetric polarization along the graphene monolayer by the applied electric field not only drives rotational motion via Lorentz-force-assisted ionic flux, but also simultaneously triggers localized ECL emission at the anodic extremity. This multi-functionality, combining movement and optical signal, highlights the unique capability of BPE to couple motion with light generation within a single object. In this way, the 2D light-emitting rotor not only overcomes mass transport limitations by enhancing local convection, but also provides a real-time optical detection. Such a synergy between electrochemically induced motion and ECL-based visualization offers a promising strategy for designing multifunctional systems.[211]

2.4.4 Conclusion

In conclusion, we developed a light-emitting magnetoelectrochemical 2D rotor based on the synergy between BPE and magnetic field. In this system, the applied electric fields induce asymmetric polarization of a graphene monolayer, which simultaneously drives localized ECL reactions and generates ionic fluxes that, under the influence of an external magnetic field, translate into controlled rotational motion. The optical and dynamic properties of the device were evaluated by azimuthal angular analysis, revealing a direct correlation between the applied electric field, the ECL intensity, and the angular speed. This correlation originates from the BPE-driven rotation, which enhances interfacial mass transport and thereby increases the efficiency of ECL. Notably, the cooperation between BPE and magnetic field produced a significant enhancement of ECL emission due to dynamic local mixing of the electrolyte. Furthermore, the strategy of using a double electric field configuration, enabled an increase in the rotation amplitude, as reflected in the more uniform distribution of ECL emission along the trajectory of the rotor. These results highlight that BPE not only enables wireless and site-selective activation of redox reactions, but also provides a powerful method to couple motion with light generation, most importantly without the need of ferromagnetic components or complex alternating magnetic fields. Overall, the synergy between BPE and magnetic field establishes a versatile strategy for the design of multifunctional 2D systems, offering new perspectives for sensing, optical mapping, and electrochemically driven dynamic devices requiring precise motion control.

2.5 Experimental section

2.5.1 Preparation of graphene monolayers

The monolayer graphene on Cu foils was purchased from Graphenea®. Graphene was prepared via a wet-transfer method. As shown in Figure 2-39 the graphene/Cu foil was carefully cut into pieces of desired size and then transferred to a 0.2 M $(NH_4)_2S_2O_8$ aqueous solution for 4 h. The bare graphene monolayer can be obtained after all the Cu was dissolved. A glass slide was slowly positioned under the piece of graphene to scoop it carefully out of the solution and transfer it to water to wash away the residual $(NH_4)_2S_2O_8$. The washing step was repeated three times with fresh water. Figure 2-40 shows the optical photograph of a piece of graphene monolayer on Cu foil and a prepared pure graphene monolayer.

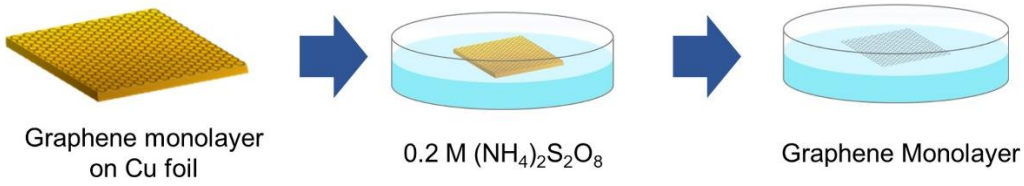

Figure 2-39 Preparation procedure of graphene monolayer.

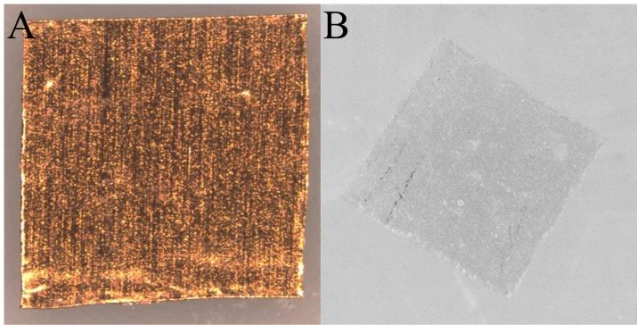

Figure 2-40 Optical photograph of a piece of (A) graphene monolayer on Cu foil and (B) pure graphene monolayer. The size of this sample is 2 mm × 2 mm.

2.5.2 Fabrication of Pt-graphene-EP and luminol CL

2.5.2.1 Fabrication of Pt-graphene

For the fabrication of Pt-graphene, the cell was filled with H_2PtCl_6 solution up to a height slightly exceeding the height of the capillary holder (see the holder in Figure 2-1). Then the graphene monolayer is carefully placed between the two membranes in the bipolar setup just above the holder with the help of a glass slide. Afterwards, the H_2PtCl_6 solution is gradually removed until the graphene sheet gets in contact with the upper end of the holder, in order to stabilize the position of the monolayer graphene. Subsequently, a given potential was applied to the driving electrodes to trigger the Pt electrodeposition at one extremity of the graphene. The obtained Pt-graphene objects were kept in DI water after washing.

2.5.2.2 Fabrication of Pt-graphene-EP

The asymmetric metal deposition on graphene monolayers was carried out with a home-made cell, the distance between the two driving electrodes was 2.5 cm and the graphene layer was immobilized on a capillary (Holder illustrated in Figure 2-1). The cell was filled with metal salt

solution and the potential was applied with a direct current (DC) power supply (AL 942, elc). The anodic electrophoretic paint deposition on the graphene monolayer was carried out with the same cell as in Figure 2-1, but the distance between the two electrodes was 3.5 cm. The anodic electrophoretic paint was diluted 10 times with water and $K_4Fe(CN)_6$ was added for preparing a 50 mM $K_4Fe(CN)_6$ paint mixture. After modification, the obtained Janus graphene monolayers were washed several times with water.

2.5.2.3 Luminol CL

The obtained Pt-graphene-EP monolayers were stored in a 50 mM $K_4Fe(CN)_6$ solution to prevent the immobilized molecules from leaking out of the EP. The CL solution contains 20 mM luminol, 0.1 M NaOH, and eventually 3 wt.% SDS, and 5 % (V/V) H_2O_2. The Pt-graphene-EP monolayer was placed at the air-water interface of the solution and the dynamic behavior was recorded with a digital camera (Canon EOS C200, Objective Canon Macro Lens 100 mm 1:2.8). All images and videos were processed with ImageJ software.

2.5.3 Enzymatic graphene swimmer

2.5.3.1 Synthesis of Au-graphene

The graphene monolayers on Cu foil were cut into small strips (about 3 mm × 8 mm). Then, the strips were processed following the same protocol as in previous work to obtain graphene monolayer sheets. A graphene sheet is placed at the air-water interface of a 2 mM Au salt solution and an electric field of 2.5 V/cm is applied to the solution for 2 minutes with a DC power supply (AL 942, elc). After the deposition of Au at one extremity, the graphene sheet is rotated by 180°, followed by the application of the same electric field for the same duration to deposit Au on the opposite extremity. The obtained Au-graphene sheets were transferred to pure water to remove residual metal salt.

2.5.3.2 Modification of Au-graphene

The anodic hydrogel and the cathodic hydrogel are prepared as follows:

Anodic hydrogel:

PAA-PVI-[Os(4,4'-dimethyl-2,2'-bipyridine)$_2$Cl]$^{+/2+}$ (10 mg/ml in water, 2.33 µl), purified GOX *A ni* (8.354 mg/ml in water, 1.78 µl) and PEGDGE (2 mg/ml in water, 2.12 µl) were mixed in a microtube. This anodic hydrogel was composed of 55 wt % polymer, 35 wt % enzyme and 10 wt % cross-linker.

Cathodic hydrogel:

PAA-PVI-[Os(4,4'-dichloro-2,2'-bipyridine)$_2$Cl]$^{+/2+}$ (10 mg/ml in water, 2.65 µl), purified BOD *B p* (5 mg/ml in water, 2.54 µl) and PEGDGE (2 mg/ml in water, 1.57 µl) were mixed in a microtube. This cathodic hydrogel was composed of 62.57 wt % polymer, 30 wt % enzyme and 7.43 wt % cross-linker.

The obtained Au-graphene sheets were transferred onto the surface of a solidified agarose gel for immobilizing them. Then a certain amount of anodic hydrogel was deposited onto one Au-modified extremity and cathodic hydrogel was deposited onto the other Au modified extremity by drop-casting onto the Au-graphene sheet. The modification area on graphene is about 0.018 cm^2. The enzyme hydrogel modified Au-graphene sheets were kept in the fridge (4 °C) to stabilize the enzyme layers.

For the loading ratio of BOD: Gox = 1: 1, 1 µl of cathodic hydrogel and 1 µl of anodic hydrogel were deposited, achieving a total loading of 350 µg/cm^2 and 380 µg/cm^2 respectively. For the loading ratio of BOD: Gox = 2: 1, 2 µl of cathodic hydrogel and 1 µl of anodic hydrogel were deposited, achieving a total loading of 700 µg/cm^2 and 380 µg/cm^2 respectively. Based on the known deposition volume, solid content, and deposition area, the thickness of the dried enzyme-hydrogel layer was estimated to be in the range of about 15-20 µm.

2.5.3.3 Dynamic behavior of enzymatic graphene swimmers

First, the enzyme-modified graphene sheets were kept at room temperature for 30 min to activate the enzymes. This procedure allows the immobilized enzymes to recover their catalytic activity after the modification and drying processes at low temperature, which ensures stable and reproducible performance during subsequent experiments. Then, the samples were transferred to the air/water interface of a 0.1 M phosphate buffer solution. Second, the enzyme-graphene hybrid was put into a mixture of ethanol and water (ethanol: water = 1: 1), and was allowed to sink at the bottom of the solution. Third, the graphene was carefully flipped with tweezers in the ethanol-water mixture. Finally, the flipped swimmer (enzyme layer facing down) was transferred back to the phosphate buffer solution for use. The motion experiments have been carried out in a glass petri dish filled with fuel solution. The fuel solution, consisting of 0.1 M phosphate buffer (pH 7) and glucose, is maintained at 37°C before use, with oxygen continuously bubbled through it to ensure saturation. Once prepared, the fuel solution is added to the petri dish. The flipped graphene swimmer is then carefully transferred to the air-water interface of the fuel solution, and its dynamic behavior is recorded using a digital camera (CANON EOS 70D). For adding an external magnetic field, a rectangular FeNdB magnet (B ≈ 200 mT, A = 98 cm^2) is placed below the petri dish to provide a vertical magnetic field.
The reaction at the anodic side catalyzed by Gox is:

$$\beta\text{-}D\text{-}glucose \rightarrow \delta\text{-}glucono\text{-}1{,}5\text{-}lactone + 2H^+ + 2e^- \qquad (2.20)$$

The reaction at the cathodic side catalyzed by BOD is:

$$O_2 + 4H^+ + 4e^- \rightarrow 2H_2O \qquad (2.21)$$

2.5.3.4 Preparation of biofuel electrodes

Biofuel electrodes for electrochemical measurements were prepared as follows: As shown in Figure 2-28, the biofuel electrode was prepared on a glass slide substrate with a size of 1 cm x 2.5 cm. First, to improve its conductivity, half of the surface of the glass slide was coated with a thin gold layer by sputter coating (5 min,35 mA). Then the prepared Au-graphene sheet was transferred from the water-air interface to the glass slide, partially covering the gold-coated area to connect the Au-graphene sheet. A metal wire was then connected to the thin gold layer with silver glue and covered with silicone glue to avoid short circuit.

For the deposition of enzymes, a certain amount of enzyme-hydrogel mixture was deposited by drop-casting onto the graphene sheet. The bioanode electrodes are modified with anodic hydrogel and the biocathode electrodes are modified with cathodic hydrogel. The enzyme-hydrogel modified area is ~1.8 mm^2 and not connected to the gold sputtered area. This is followed by an 18-hour low-temperature (4 °C) drying period to stabilize the enzyme layers.

2.5.3.5 Electrochemical measurements of an enzymatic graphene biofuel cell

Before electrochemical measurements, the prepared biofuel electrodes were placed at room temperature for 30 min to activate the enzymes. Then bioanode and biocathode were immobilized at the bottom of a petri dish with enzyme layers facing up. The distance between the two electrodes is around 1 cm. A rectangular FeNdB magnet (B $\approx$ 200 mT, A = 98 cm2) was placed below the petri dish in order to produce a vertical magnetic field. The current measurements were carried out by using a Keithley electrometer/high resistance meter connected to a computer. The immobilized bioanode and biocathode were connected to the ammeter, then the electrolyte solution was added gently. The voltage measurements were conducted with same protocol but connected to a voltmeter. All the electrochemical measurements were carried out in 0.1 M PBS and 40 mM glucose solution at pH 5 and 37°C, with the north pole up configuration.

2.5.4 ECL graphene monolayer rotor

After the TPA addition, the pH of the PBS solution was adjusted to 7.4 with concentrated H_2SO_4 solution. Single-layer graphene (Atomic force microscopy (AFM) thickness < 1 nm) was purchased from Graphenea® and prepared via a wet transfer method. Potentiodynamic measurements were performed using a three-electrode cell composed of transparent graphene (3.14 mm^2), supported on glass, acting as the working electrode, a Pt mesh and a Ag wire as the counter and pseudo reference electrodes, respectively. An Autolab (ECO Chemie BV type 2) potentiostat connected to a computer was used for these measurements. The bipolar electrochemical experiments were carried out by placing the arrow-shaped graphene single-layer, acting as BPE, between an array of four graphite driving electrodes. In the bipolar cell the driving electrodes were positioned at a distance of 7.5 cm and a rectangular FeNdB magnet (B = 200 mT, area = 98 cm^2) was placed below the bipolar cell. The electric field in the cell was controlled by a commercial power supply (EA Elektro-Automatik, EA-PS 5080-10A) coupled to a voltage amplifier (A800DI FLC Electronics). ECL emission was monitored by using a CCD camera (Canon EOS 70D, Objective Canon Macro Lens, 100 mm, 1:2.8). Images and videos (AVI encoding, ISO 6400) were processed with FIJI software and finally converted to MP4 format. Each video can be considered as an accumulation of frames resulting in a stack projection.

2.6 Conclusion of Chapter 2

In this chapter, we have demonstrated that BPE provides a powerful and versatile method for designing multifunctional 2D systems based on graphene monolayers. Across four different subtopics, we illustrated how to use BPE to fabricate multifunctional object with catalytic nature, and couple localized redox electrochemical reactions with dynamic behavior and ECL emission.

First, we showed that BPE enables precise site-selective deposition of metals on graphene, where both the amount and the location of Pt clusters could be precisely tuned. This fine control of Pt deposition was directly translated into bubble-driven motion of the graphene sheet, highlighting the ability of BPE to synthesize swimmers with controlled motion.

Second, we extended this approach beyond metals by integrating functional coordination compounds, exemplified by Prussian blue, onto graphene monolayers. The resulting hybrids exhibited localized CL activity, proving that BPE can incorporate not only metallic but also coordination-based functional materials into 2D architectures. Moreover, we further demonstrated the multi-component features by co-depositing Pt and electrophoretic paint at distinct locations of a single graphene sheet, coupling catalytic bubble propulsion with simultaneous light emission, and thus achieving truly multifunctional 2D objects.

Third, by immobilizing enzymes on graphene monolayers, we designed enzymatic swimmers that convert biochemical energy into motion. Importantly, we demonstrated for the first time that their dynamic behavior can be tuned and optimized by applying an external magnetic field and by varying the loading ratio of enzymes, bridging enzymatic catalysis with macroscopic robotics.

Finally, we combined BPE with magnetic-field assistance to propose a 2D light-emitting magnetoelectrochemical rotor, where asymmetric polarization drives localized ECL emission while Lorentz forces induce controllable rotation. This cooperative mechanism led to a direct correlation between applied electric fields, light intensity, and angular velocity, with enhanced mass transport and optical signal due to local convection.

Taken together, these studies highlight the unique advantages of BPE for the wireless, site-specific activation of redox reactions in 2D materials. By enabling the integration of metals, coordination compounds, polymers, and enzymes, BPE provides a generalizable method to build multifunctional 2D systems in which motion, catalysis, and optical signaling are intrinsically coupled. This strategy also opens promising perspectives for applications in sensing, photocatalysis, energy conversion, and environmental remediation.

Chapter 3 Bipolar electrodeposition on alternative 2D material

Building on the results presented in Chapter 2, where the feasibility of using bipolar electrochemistry to achieve highly controlled modification of graphene monolayers was systematically demonstrated, we next explore the broader applicability of this approach to other 2D materials. Even though graphene served as an ideal proof-of-concept material due to its high conductivity, mechanical stability, and optical transparency, which allowed us to correlate site-selective modification with dynamic behavior and optical readouts, the landscape of 2D materials extends far beyond graphene, such as transition metal dichalcogenides, hexagonal boron nitride, MXene, and layered oxides, each of which possesses distinctive electronic, catalytic, and interfacial properties.[212-214] Testing BPE on these alternative 2D materials is therefore crucial to evaluate the generality of the method, uncover possible material-dependent limitations, and identify new opportunities for designing multifunctional 2D hybrids.

In this chapter, we expand our investigation to MXene, aiming to determine whether the principles established for graphene can be successfully transferred to other 2D materials.

3.1 Introduction to MXene

Since their discovery in 2011, MXenes have rapidly emerged as one of the most promising families of 2D materials.[215] MXenes are typically synthesized through the selective etching of the A layers from their parent MAX phases, where M represents an early transition metal, A is a group IIIA or IVA element (e.g., Al, Si), and X represents carbon and/or nitrogen. The resulting compounds have the general formula $M_{n+1}X_nT_x$, in which T_x corresponds to surface terminations such as -OH, -O, and -F introduced during the etching process.[216-218] This structural diversity, combined with rich surface chemistry, imparts MXene with tunable physicochemical properties different from other 2D materials, making them attractive for both fundamental studies and catalytic applications.

Compared with graphene, MXenes offer unique advantages as well. They combine metallic conductivity with hydrophilicity arising from their surface functional groups.[219-223] This unusual combination enables efficient charge transfer in aqueous environments and makes MXene highly suitable for electrochemical applications such as energy storage, catalysis, and sensing. Furthermore, their layered nature enables exfoliation into few-layer or even single-layer nanosheets,[224, 225] which can form colloidal dispersions and be processed into films, coatings, or composite architectures. Such structural versatility facilitates their integration into diverse material platforms.

A particularly important advantage of MXene is its abundant surface properties.[226, 227] During synthesis, the removal of the A layer not only enhances dispersibility in polar solvents but also provides a large number of chemically active sites.[228, 229] These sites can be exploited to design the electronic structure, tune interlayer spacing, and modulate catalytic performance. As a result, MXenes have attracted significant interest across many fields. In energy storage, they have been demonstrated to act as high-performance electrodes in supercapacitors[230] and batteries[231-233], exhibiting excellent reaction rate capabilities, fast ion transport, and superior cycling stability. In electrocatalysis, MXenes have been investigated for hydrogen evolution

reaction[234], oxygen reduction reaction[234], and CO_2 reduction[235], where their conductivity and abundant surface sites enable efficient activity. Beyond applications in electrochemistry, MXenes exhibit promising photothermal and photonic properties for biomedical applications, such as photothermal therapy, drug delivery, and bioimaging.[236-238] Their flexibility and processability also make them attractive for flexible electronics and electromagnetic interference shielding.

Despite these advances, several challenges hinder the broader development of MXene. Chief among them are stability issues and the difficulty of scalable production. Another key limitation lies in the selective modification of surface sites.[239] Owing to their mixed terminations (-O, -OH, -F), MXene surfaces are heterogeneous, which complicates precise functional control.[240-242] Achieving site-selective functionalization is therefore of critical importance, as it would allow for fine-tuning of electronic structure, catalytic performance, ion intercalation, and interfacial interactions. However, such a modification is challenging due to the strong bonding of existing terminations, the dynamic nature of MXene surfaces, and their tendency to oxidize under chemical treatment. Overcoming these barriers would not only deepen the understanding of structure–property relationships, but also unlock advanced functionalities for MXene-based systems in catalysis, energy storage, electronics, and biomedicine.

In this chapter, we address this challenge by selecting a MXene material, Ti_3C_2, and exploring its asymmetric modification via BPE. By utilizing the wireless and site-selective nature of BPE, we aim to explore the spatially controlled functionalization of MXene sheets, thereby extending the concepts developed for graphene in the previous chapter to a broader class of 2D materials.

3.2 Modification of MXene via bipolar electrochemistry

For the experimental demonstration of asymmetric modification, we selected Ti_3C_2 MXene microsheets as the representative objects. The sheets were obtained by selectively etching the Al layers from Ti_3AlC_2 MAX precursors, followed by exfoliation into few-layer flakes (Figure 3-1).[243] The resulting MXene structures exhibit a typical layered morphology with lateral sizes ranging from a few micrometers up to tens of micrometers, while maintaining thicknesses in the nanometer range.

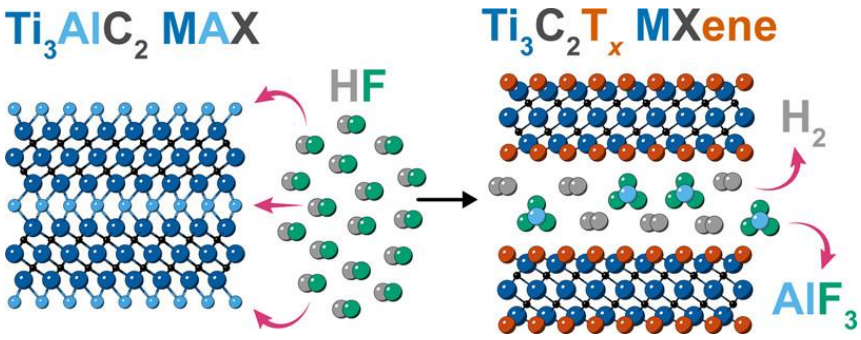

Figure 3-1 Schematic of the Ti_3AlC_2 MAX etching reaction using hydrofluoric acid, which produces hydrogen gas and aluminum fluoride. Adapt from Ref. [243].

The morphology and surface features of the as-prepared MXene were first characterized by SEM. As shown in Figure 3-2A, the MXene sheets display a relatively flat and layered structure with well-defined edges, consistent with single- or few-layer thickness.

To complement SEM, AFM was employed to determine the thickness and surface topography of individual MXene sheets. Representative AFM images (Figures 3-2B and C) reveal a thickness of the Ti_3C_2 sheets around 3.7 nm, corresponding to single- or few-layer Ti_3C_2 microsheets. The height profiles extracted across the sheets further confirm their ultrathin nature and provide direct evidence of the structural integrity of the MXene monolayers. The combination of SEM and AFM results thus indicate that the MXene used in this study consists of well-defined 2D sheets, which serve as a suitable candidate for subsequent bipolar electrochemical modification.

In Chapter 2, the graphene sheets employed in our experiments had lateral dimensions down to approximately 1 mm. This is the smallest size that we can prepare manually, and which still allows us to stabilize the sheets during bipolar modification using a fixing device, which effectively prevented undesired rotation or drifting during the electrodeposition process. In contrast, moving to micrometer-scale objects is more challenging. For such dimensions, individual particles can no longer be manipulated and anchored with macroscopic tools, and their low mass combined with high surface area makes them highly prone to undergo undesired motion in the presence of an applied electric field. Therefore, alternative strategies must be adapted to stabilize and control micrometer-scale MXene particles during BPE, ensuring both reproducibility of the modification and its structural integrity.

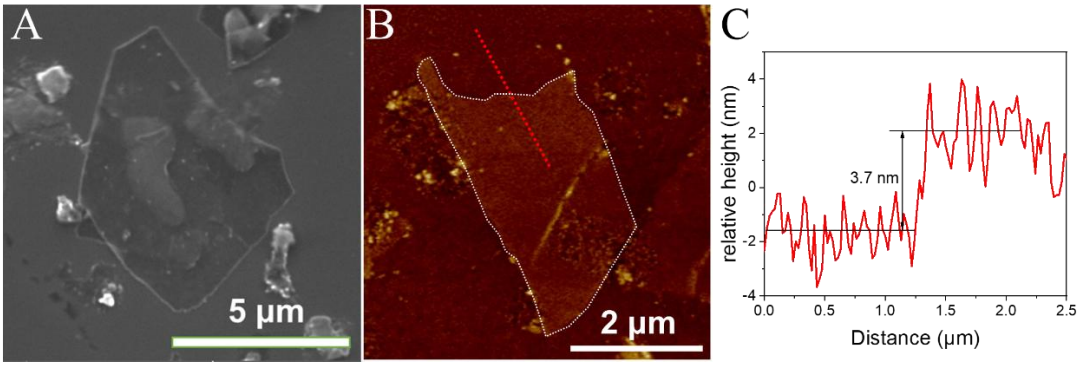

Figure 3-2 (A) SEM and (B) AFM iamge of the pure MXene microsheets. The shape of a MXene sheet is outlined in the AFM image. (C) The height profile of MXene layer extracted from the AFM data (red dashed-line in B).

Up to now, several approaches have been reported to stabilize microscale particles during bipolar electrochemical modification. The first commonly employed method is the capillary-assisted system[244], a method allows the use of objects with a high aspect ratio, where the elongated geometry helps to minimize uncontrolled rotation or drift in the electric field. However, this requirement is clearly not satisfied for the present study, as the MXene sheets investigated here are thin layers with relatively low aspect ratios.

The second strategy involves increasing the viscosity of the electrolyte to suppress particle mobility during deposition.[24] To explore this approach, we performed a preliminary test by dispersing Ti_3C_2 microsheets in an agarose gel. However, the results revealed that the surface of the MXene microsheets are noticeably roughened after the experiment, indicating the oxidation of the Ti_3C_2.[245-247] This undesired oxidation is most likely caused by the heating step required to dissolve and remove the agarose gel during the cleaning process. The increased temperature appears to accelerate the oxidation of Ti_3C_2, thereby compromising the integrity of Ti_3C_2.

Apart from the above-mentioned strategies, two alternative methods have recently been proposed to overcome the instability of micrometer-scale 2D objects during BPE.[104] One approach is based on the use of a quasi-2D reaction layer, where the nanosheets are dispersed in an ultrathin aqueous film confined between the two driving electrodes. This system provides a homogeneous environment while minimizing random rotation of the 2D particles. By tuning the applied potential and exposure time, reduced graphene oxide with controlled conductivity and dispersibility was obtained. Importantly, the freestanding 2D reaction layer avoids the drawbacks of highly viscous gels-such as incomplete dispersibility of particles and difficulty of post-processing-while still ensuring sufficient stabilization of the 2D objects during polarization.

Another strategy employs a 3D air-liquid interfacial foam as the reaction medium.[106] In this system, graphene oxide microsheets are fixed in the thin liquid layer constituting the walls of surfactant-stabilized bubbles, which provide a confined 2D reaction space within the 3D foam. Adsorption in the bubble shell restricts the mobility and rotation of the microsheets, ensuring also their alignment with the electric field. Under the influence of an applied potential, this configuration enables highly site-selective bipolar deposition of metal clusters, for example the asymmetric decoration of graphene oxide with Au at one extremity. Compared with bulk systems, the 3D foam-based structure prevents rotation and aggregation while enabling a uniform distribution of the electric field inside the bubble walls, thereby greatly improving the efficiency and selectivity of the deposition process.

However, these methods require the addition of surfactants to the electrolyte to lower the surface tension and stabilize the thin liquid film or the foam structure. While this strategy is effective for graphene oxide, it presents a serious drawback when applied to more sensitive 2D materials such as Ti_3C_2. The abundant surface-active sites of Ti_3C_2 (-O, -OH, -F) are highly sensitive, in particular, surfactant molecules may react with Ti_3C_2 and accelerate the oxidation process of Ti_3C_2, leading to changes in conductivity and integrity. This problem limits the direct transfer of surfactant-based stabilization strategies to MXene systems.

In this context, we adopt a simple strategy in bulk aqueous solution for a first attempt of bipolar electrodeposition, for which no additional chemicals are used to modify the Ti_3C_2 microsheets.

3.2.1 In bulk solution

In the first set of validation experiments, we directly mixed the MXene suspension with a metal salt solution and carried out bipolar electrodeposition immediately after mixing. To minimize undesired particle motion, the electric field was applied only for a few seconds. Under such short-pulse conditions, the exposure time is too short for significant convective flow or reorientation of the flakes to occur. As a result, the MXene microsheets remain approximately in their initial orientation. This short-pulse conditions allowed us to preliminarily test whether asymmetric polarization of MXene could be achieved with BPE.

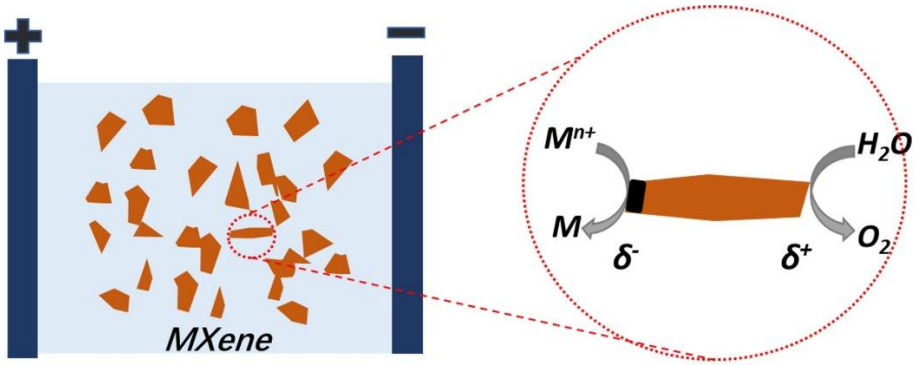

Figure 3-3 Schematic diagram of asymmetric metal deposition on MXene microsheets in bulk solution via bipolar electrochemistry.

The experiments were conducted using a custom-made bipolar electrochemical cell, designed to avoid direct contact between the target materials and the driving electrodes. The setup consists of three compartments separated by proton-exchange membranes[24]. The two side compartments contain the driving electrodes, while the middle compartment serves as the reaction chamber. As illustrated in Figure 3-3, a mixture of MXene flakes and the selected metal salt precursor was introduced into the reaction compartment, and after allowing the solution to stabilize for a few seconds, a sufficient voltage was applied across the driving electrodes to induce polarization. As a result, the metal reduction occurs selectively at one extremity of the MXene sheets.

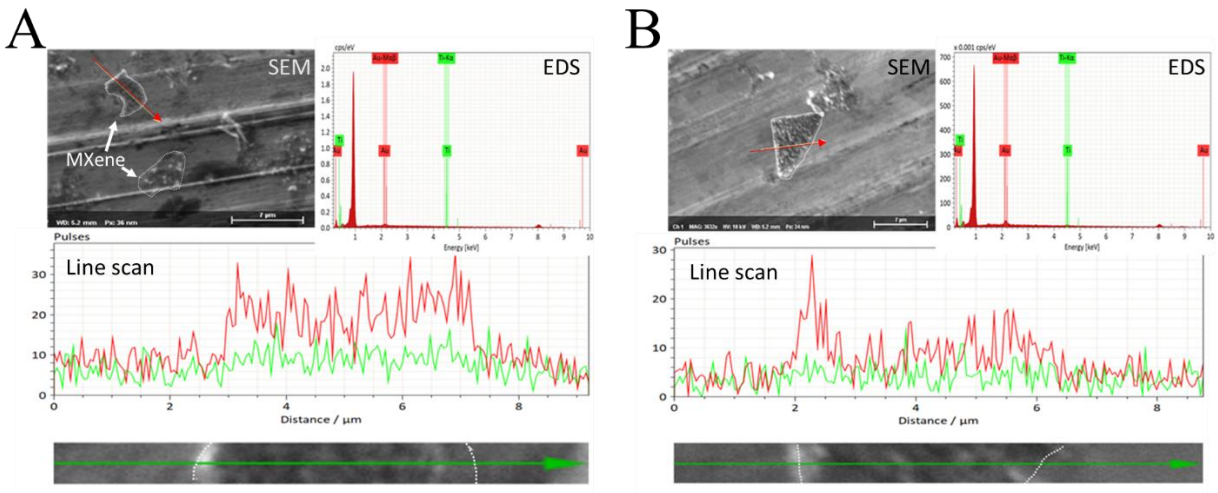

Figure 3-4 SEM images, EDS images, and EDS line scan profiles of the MXene microsheets (A) without electric field and (B) under the influence of an electric field of 500 V/cm for 5 s in a 2 mM $HAuCl_4$ solution. The scale bar in SEM image is 7 µm. The red line and green lines in the EDS line scan represent Au and Ti, respectively.

In a control experiment, Ti_3C_2 microsheets were mixed with an aqueous Au salt solution for a few seconds to evaluate the result in the absence of an applied voltage. As shown in Figure 3-4A, the surface of the Ti_3C_2 microsheets appears rougher compared to pristine Ti_3C_2 in Figure 3-2A. To identify the composition of these clusters, EDS analysis was performed. The EDS result reveal that those clusters are composed of Au, confirmed also by the corresponding EDS line-scan profiles. This result seems impossible at first glance, because theoretically, in the absence of an external electric field or reducing agents, metal ions cannot undergo spontaneous reduction. However, this phenomenon is likely due to the presence of abundant unsaturated reactive sites generated during the etching process of Ti_3C_2, which possess an intrinsic reducing power and are able to convert Au ions into metallic Au.

For comparison, an electric field was applied for 5 s to a freshly prepared mixture of Ti_3C_2 microsheet and Au salt solution under otherwise identical conditions. The line scan, presented in Figure 3-4B, shows that Au deposition was in this case more localized at the edge of the microsheet, consistent with asymmetric deposition by BPE. Nevertheless, spontaneous self-reduction of Au was still observed on the MXene surface, indicating that the intrinsic reductive nature of Ti_3C_2 cannot be fully suppressed under these experimental conditions.

These preliminary results demonstrate that BPE can indeed induce site-selective modification of MXene surfaces, but the spontaneous reduction of metal ions on Ti_3C_2 microsheets does not allow the preparation of perfectly shaped MXene-based Janus particles.

3.2.2 Optimization

In the following set of experiments, we aimed to explore strategies to minimize the spontaneous surface reduction on MXene. First, we measured the zeta potential of Ti_3C_2 suspensions at different pH values to assess how surface charge influences the reductive tendency of the microsheets. As shown in Figure 3-5, the zeta potential of the suspension was approximately -17.9 mV at pH ≈ 6, -9.3 mV at pH ≈ 4, and +7.2 mV at pH ≈ 2. These results are in good agreement with literature, which suggests that a more negative zeta potential correlates with a stronger reducing capability of colloidal particles.[248] Accordingly, when MXene is dispersed without pH adjustment (e.g., near neutral conditions), it spontaneously reduces metal ions in solution, leading to the formation of metal clusters on its surface even in the absence of electric field or reducing agents.

To mitigate this spontaneous reduction, it is therefore necessary to adjust the pH of the electrolyte to values where the surface charge of MXene is less negative or even positive. Based on the data in Figure 3-5, the zero-zeta potential point of the Ti_3C_2 suspension can be approximately estimated at around pH 3. Under this condition, the electrostatic driving force for electron transfer from MXene to metal ions is minimized, which in principle should suppress spontaneous reduction and allow more controlled metal deposition under bipolar electrochemical conditions. This method of tuning the electrolyte environment before BPE experiments ensures that the site-selective metal modification of MXene is driven mainly by electric field rather than uncontrolled spontaneous reduction at the surface.

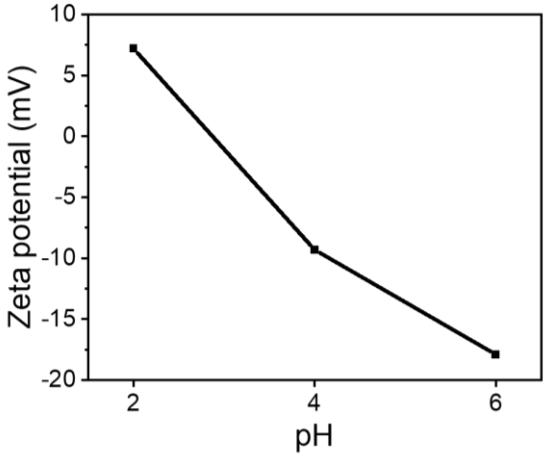

Figure 3-5 Zeta potential of the MXene solution as a function of pH.

Based on the above results, we further tested mixtures of Ti_3C_2 and metal salt solutions to experimentally validate the proposed mechanism. A metal precursor solution of 2 mM tetrachloroauric acid ($HAuCl_4$) were prepared. To avoid introducing additional ionic species, the pH of these solutions was adjusted using HCl for the gold salt. Four different pH values were studied (6, 4, 3, and 2). The solutions were then mixed with Ti_3C_2 microsheet suspensions for several seconds, immediately followed by centrifugation to collect the resulting samples, which were subsequently characterized by SEM.

As shown in Figure 3-6, at pH = 6, the surface of Ti_3C_2 microsheets was covered with numerous Au clusters, indicating a strong spontaneous reduction capability under near-neutral conditions. This observation is consistent with the results obtained in Figure 3-4A. When the pH was gradually decreased to 4 and 3, the amount of Au clusters on the Ti_3C_2 surface decreased significantly. At pH = 2, almost no Au clusters were observed on the microsheets, confirming that Ti_3C_2 loses its intrinsic reducing ability when the suspension is adjusted to a pH below the point of zero-zeta potential (~3), where the zeta potential becomes positive. It should be noted that the speciation and redox properties of $HAuCl_4$ are also pH-dependent, which may contribute to the less pronounced deposition observed under acidic conditions.[249]

These encouraging results provide direct experimental evidence that adjusting the electrolyte to acidic conditions (pH < 3) effectively suppresses the spontaneous reduction of metal ions on Ti_3C_2 surfaces. These findings establish a favorable condition for subsequent bipolar electrochemical deposition, where metal modification should be driven primarily by the generated polarization potential difference rather than uncontrolled self-reduction.

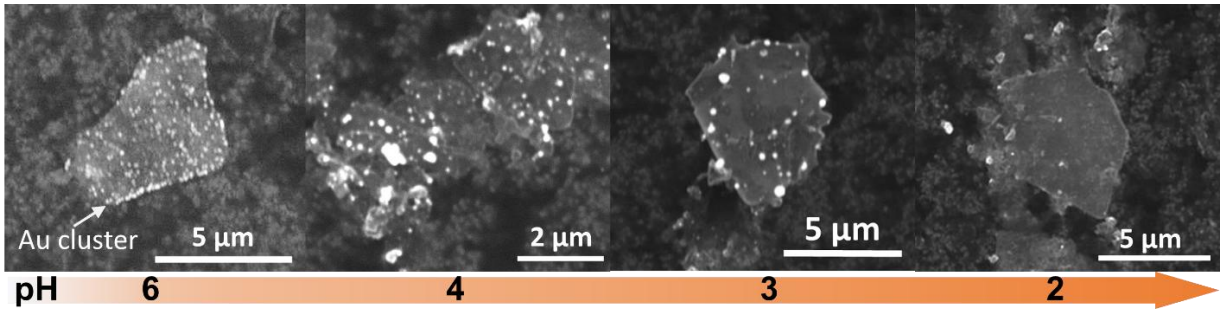

Figure 3-6 SEM images of MXene microsheets mixed with $HAuCl_4$ solution of different pH values.

Next, we carried out asymmetric gold deposition in an electrolyte adjusted to pH = 2 under optimized conditions. The experiment was performed in an ice-water bath to stabilize the temperature, while an electric field of 500 V/cm was applied for 5 s. For such short deposition time, Joule heating does not significantly increase the temperature of the reaction compartment, thereby minimizing the oxidation of the Ti_3C_2 microsheets.

As shown in Figures 3-7A and B, Au clusters were formed preferentially on one side of the Ti_3C_2 microsheets, displaying a characteristic dendritic morphology. Elemental analysis based-on EDS mapping confirmed that these deposits consist of Au. However, some small Au clusters could still be observed at non-polarized regions of the Ti_3C_2 surface. This is most likely due to undesired rotation or displacement of the sheets within the bulk solution, which prevents polarization at a fixed position during the metal deposition.

Nevertheless, these results clearly demonstrate that the spontaneous reduction induced by Ti_3C_2 can be effectively suppressed by controlling the electrolyte composition. Although the mechanism is not yet fully understood, these findings still confirm that BPE-driven asymmetric deposition is achievable on Ti_3C_2. At the same time, the undesired deposition outside of the polarized zone illustrates the limit of a bulk-solution system. To achieve the synthesis of truly Janus-type Ti_3C_2-based particles, an alternative strategy is required to further stabilize the orientation of the microsheets and to restrict polarization-induced reactions exclusively to predetermined sites.

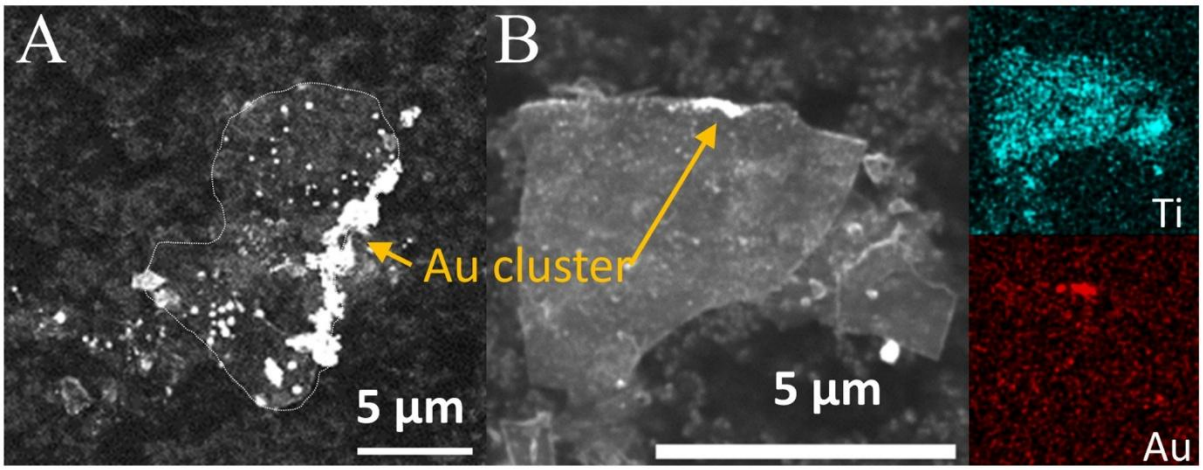

Figure 3-7 (A) SEM image of a MXene microsheet with Au clusters deposited only at one edge. The shape of the MXene microsheet is outlined with white dashed-line. (B) SEM and EDS mapping images of a Au-modified MXene microparticle.

3.2.3 On a glass substrate

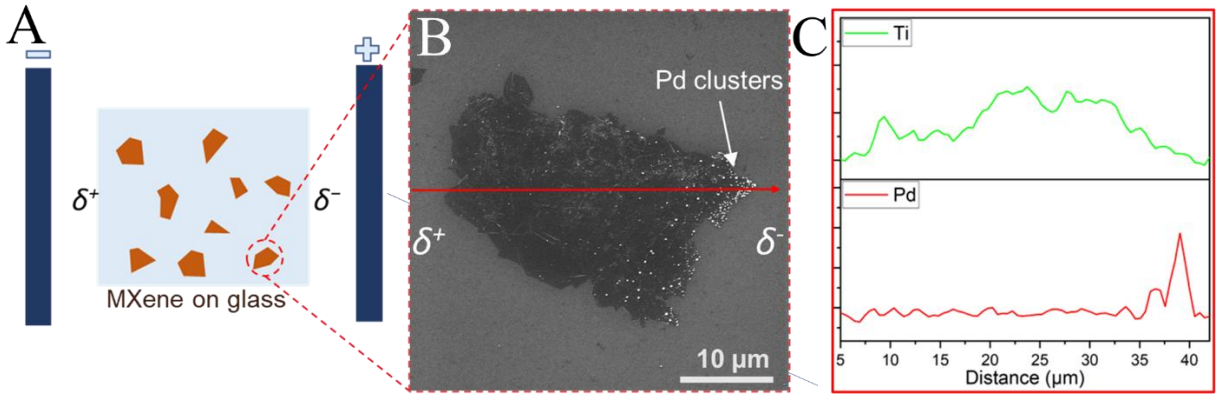

Figure 3-8 (A) Scheme of the asymmetric metal deposition on MXene microparticles via bipolar electrochemistry. The MXene microsheets are dispersed on a glass slide by drop-casting. (B) SEM image of a MXene microsheet asymmetric modified with Pd clusters. The applied electric field is 500 V/cm and deposition time is 5 s. (C) EDS line scan of the MXene microsheet, corresponding to the red line in (B).

To overcome the limitations of the bulk-solution experiments, where uncontrolled motion of Ti_3C_2 flakes led to partial loss of deposition selectivity, we next explored an alternative strategy by immobilizing MXene microsheets on a solid support. In this configuration, Ti_3C_2 nanosheets were uniformly dispersed onto an insulating glass substrate via drop-casting before bipolar electrochemical modification (Figure 3-8A). The glass support provided a mechanically stable substrate that effectively suppressed undesired rotation or aggregation of individual sheets

during deposition. At the same time, the electrical insulation of the substrate ensured that the applied field was exclusively applied to the suspended Ti_3C_2 microsheets, keeping the wireless feature of BPE.

Here, palladium sulfate was chosen as the metal precursor to further evaluate the use of MXene materials for the deposition of different metals. First, a glass substrate more or less uniformly decorated with Ti_3C_2 microsheets was immersed in a 2 mM $PdSO_4$ solution adjusted to pH = 2. An electric field of 500 V/cm was applied and kept for 5 s, after which the glass slide was removed and rinsed with deionized water. The short exposure time minimized direct contact between Ti_3C_2 and Pd^{2+} ions, thereby decreasing the probability of spontaneous reduction on the MXene surface.

As shown in the SEM image of Figure 3-8B, a Ti_3C_2 microsheet with a lateral length of approximately 14.6 µm was characterized after Pd deposition. The theoretical calculation confirmed that under the influence of an electric field of 500 V/cm, the polarization potential difference across this microsheet should be sufficient to trigger the reduction of Pd^{2+} ions. Consistent with the expected asymmetric polarization, many Pd clusters were observed at the δ^- side of the microsheet, while no Pd deposits could be observed on the δ^+ side. To provide a more quantitative evidence, EDS line-scan analysis was carried out across the Ti_3C_2 microsheet. The Ti signal was present throughout the entire microsheet, and as expected, a sharp Pd peak was detected at the δ^- extremity. These results provide clear evidence that BPE enables site-selective deposition of Pd on Ti_3C_2 microsheets and demonstrates that BPE can be generalized for different metal precursors.

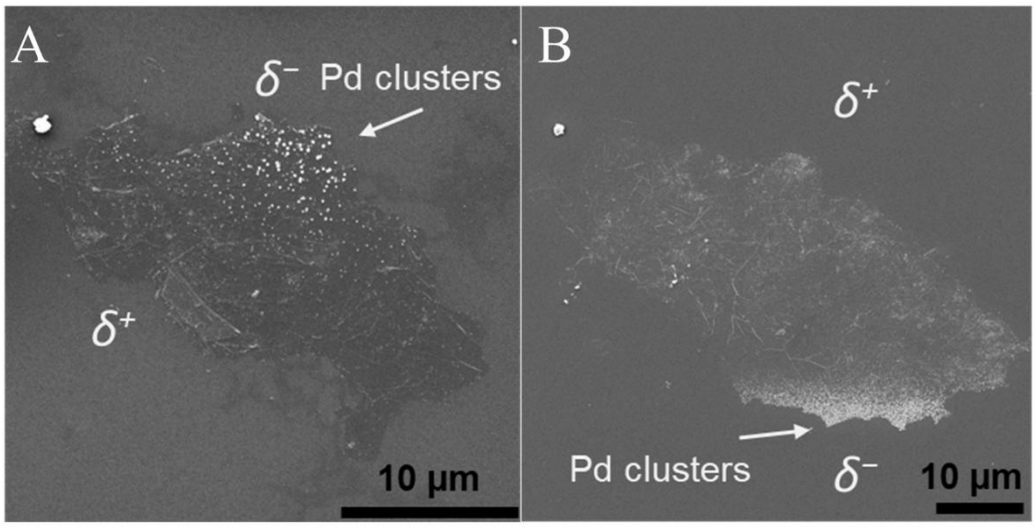

Figure 3-9 SEM image of a MXene microsheets asymmetrically modified with Pd clusters for different electric fields. (A) 500 V/cm for 10 s. (B) 660 V/cm for 10 s.

To further examine the effect of deposition parameters, the polarization time was increased from 5 s to 10 s while maintaining the same electric field intensity. SEM characterization again revealed asymmetric deposition, with Pd clusters localized mainly at the δ^- side of the Ti_3C_2 microsheets. Compared with the shorter deposition time, however, the amount of Pd clusters was significantly increased, and the deposits became more clearly visible extending from the edge toward the center area of the Ti_3C_2 microsheets (Figure 3-9A). In theory, the spatial extention of the polarized region is only determined by the intensity of electric field, but a longer deposition time allows for

more metal accumulation, making deposition visible even in areas with weaker polarization. Nevertheless, even after 10 s, the δ^+ side reveals no Pd clusters deposition, confirming that the change of deposition time does not affect the location of the polarization.

We next increased the electric field intensity to 660 V/cm in order to evaluate whether a stronger electric field could affect the deposition. Interestingly, despite the enhanced driving force, Pd clusters were once again only observed at the δ^- extremity of the Ti_3C_2 microsheets (Figure 3-9B), while the δ^+ side remains without modification. These results demonstrate that the asymmetric deposition behavior is remarkably stable for both extended deposition time and increased electric field intensity. Together, these findings highlight the tunable and predictable nature of BPE-driven modification, where experimental parameters such as deposition time and electric field intensity primarily affect the density and extension of the metal deposits.

3.3 Conclusion

In this chapter, we demonstrated the applicability of bipolar electrochemistry to 2D Ti_3C_2 MXene microsheets, extending the concept beyond graphene monolayers. Due to the sensitive nature of the surface, Ti_3C_2 shows strong spontaneous reduction even without the application of an electric field, leading to undesired metal deposition randomly on its surface. By correlating zeta potential with surface reactivity, we identified that adjusting the electrolyte to acidic conditions effectively suppresses spontaneous reduction, enabling controlled BPE-driven site-selective modification. Under optimized conditions, asymmetric deposition of Au and Pd clusters was achieved, with deposits localized on the cathodically polarized side of MXene microsheets. Substrate immobilization further enhanced the reliability of the BPE modification, maintaining high spatial selectivity even for longer deposition times or higher electric field intensities.

Overall, these findings establish that BPE can be applied to other 2D materials as an effective method for asymmetric modification. These proof-of-concept results broaden the scope of BPE beyond graphene and open up new opportunities for designing other multifunctional 2D-based materials for catalysis, energy conversion, and sensing applications.

Chapter 4 Bipolar electrodeposition on TiO_2 microspheres for environmental applications

In this chapter, we extend the scope of BPE from conducting materials to semiconducting material, aiming to explore how this wireless and site-selective strategy can be applied to the precise modification of photoactive substrates. Unlike metals or highly conductive carbides, semiconductors present additional challenges for BPE due to their intrinsic lower conductivity. At the same time, their unique band gap structure and stability offer opportunities to explore the influence of asymmetric modification on photocatalytic performance.

4.1 Introduction to semiconductor photocatalyst

With the increasing demand for sustainable energy and the urgent need to mitigate environmental pollution, the development of highly efficient and low-cost photocatalytic materials has become a central focus in materials science and environmental chemistry.[250, 251] Photocatalysts are particularly attractive because they directly utilize solar energy, the most abundant, clean, and renewable energy source, to drive chemical reactions, thereby offering environmentally friendly solutions for hydrogen production, solar fuel generation, and pollutant degradation.[252, 253]

Among the wide variety of semiconductor-based photocatalysts, titanium dioxide (TiO_2) stands out as one of the most widely studied materials.[254-257] TiO_2 possesses multiple advantages, such as excellent chemical stability, environmental compatibility, earth abundance, low cost, and remarkable photocatalytic activity. These features have made TiO_2 a versatile material in fields ranging from hydrogen evolution and solar fuel cells to wastewater treatment and decomposition of organic pollutants.[258-261] However, the photocatalytic performance of pristine TiO_2 remains limited. The main drawback is the low separation efficiency and rapid recombination of photogenerated electron–hole pairs,[262] which significantly decreases the quantum yield and restricts the practical application of TiO_2 in energy and environmental fields.

To overcome these limitations, extensive efforts have been devoted to promoting the charge separation for improving the photocatalytic performance of TiO_2. Those strategies include surface modification approaches[263, 264], compositional design[265, 266], and heterojunction construction[267, 268]. Among them, the deposition of metal particles on the surface of photocatalysts has been shown to be particularly effective, so called cocatalyst deposition.[269-271] Noble metals such as Pt and Pd can act as electron sinks due to their work function value, thereby capturing photogenerated electrons, promoting charge migration and suppressing recombination.[271-273]

Nevertheless, conventional deposition techniques such as photoreduction or chemical reduction generally led to a random distribution of metal particles across the entire surface of the photocatalyst. This random distribution of cocatalyst causes disordered charge migration pathways and increases the possibility of electron–hole recombination during the random migration process[274-276] (Figure 4-1A), thereby reducing the overall catalytic efficiency. In contrast, site-selective modification with metal cocatalysts offers the opportunity to direct charge migration.[277-280] By controlling the deposit location, photogenerated charges can be

guided along a preferred pathway, for example the electrons will mainly migrate to the modified area (Figure 4-1B), resulting in more efficient separation and improved photocatalytic performance.[281, 282] Such spatially engineered photocatalysts not only enhance efficiency, but also provide opportunities to design systems with customized functionality.

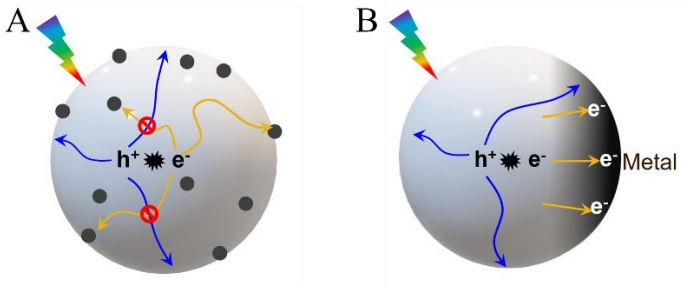

Figure 4-1 Schematic diagram of the migration of photogenerated carriers when metal clusters are deposited (A) randomly on the entire surface or (B) partially on the surface of a semiconductor particle.

However, achieving precise and reproducible spatial modification of TiO_2 with metal cocatalysts remains a considerable challenge. Current conventional strategies often involve complex steps and lack precise control over the modification. Therefore, addressing this limitation is crucial for advancing photocatalyst design and enlarging the potential applications of photocatalytic systems for energy conversion and environmental remediation. In this context, bipolar electrochemistry is introduced to achieve such spatial modification of semiconducting materials.

4.2 Bipolar electrodeposition on semiconducting materials

As discussed in Chapter 1, Janus particles have been extensively synthesized using conductive materials via BPE. In such cases, the conductivity of the material is much higher than that of the electrolyte, and once the applied electric field exceeds the associated threshold potentials, redox reactions can be readily induced at the two extremities of the object. This allows redox processes to take place without the need for direct electrical contact, making conductive systems ideal for conventional BPE-driven modification.

However, extending this concept to semiconducting materials introduces new challenges. Unlike metals or graphene, semiconductors cannot sustain sufficient current flow under electric field alone, which makes it impossible to induce polarization and trigger redox reactions. To realize the asymmetric modification on semiconductors, light-assisted bipolar electrochemistry has been developed.[26, 27, 283] In this approach, an external electric field is combined with UV or visible light to generate electron–hole pairs in the bulk of semiconductor. The applied electric field then spatially separates these photogenerated charge carriers, driving electrons and holes to opposite ends of the object, where they participate in reduction and oxidation reactions, respectively. This synergy of photoexcitation of the semiconductor and BPE providing an electric field thus enables the site-selective modification of semiconducting materials.

The concept was first demonstrated by Ongaro et al., who successfully employed light-assisted BPE to fabricate Janus particles from semiconductor materials.[25] In their study, TiO_2 nanofibers were suspended in an electrolyte containing a gold salt, and an external electric field was applied simultaneously with UV irradiation. Under these conditions, electron–hole pairs generated by TiO_2 were separated by the electric field, where electrons accumulated at one extremity while

holes were driven to the opposite side of the fibers. Consequently, gold ions in solution were selectively reduced at the electrons accumulating extremity, leading to site-selective deposition of Au clusters and the formation of Janus structures. This work represents the first successful demonstration of light-assisted BPE with semiconductors, and provides compelling evidence that directional charge migration induced by the synergy of light and electric field that can be used for asymmetric functionalization.

In this chapter, we address this challenge by applying BPE to TiO_2 microspheres as a model semiconductor system. By studying the asymmetric polarization of TiO_2 under the influence of an electric field, we aim to achieve controlled deposition of metal cocatalysts at specific locations on the microspheres. This approach allows us not only to investigate the feasibility of applying BPE to semiconductors, but also to systematically evaluate how such spatially defined modifications affect photocatalytic performance. In particular, we investigate whether asymmetric decoration of TiO_2 with noble metals can enhance charge separation, suppress recombination, and ultimately improve photocatalytic degradation processes relevant to environmental applications.

4.3 Modification of TiO_2 microspheres

In this study, core-shell TiO_2 microspheres were selected as semiconductor bipolar electrodes, in which the core consists of SiO_2 and the shell is composed of a uniformly coated TiO_2 layer.[284-286] Figure 4-2 shows the SEM image of the as-prepared microspheres, which exhibit a uniform size distribution with an average particle diameter of approximately 1.3 µm. Such a uniform size distribution is an advantage for investigating the precision bipolar electrodeposition and for systematically evaluating the resulting surface modifications.

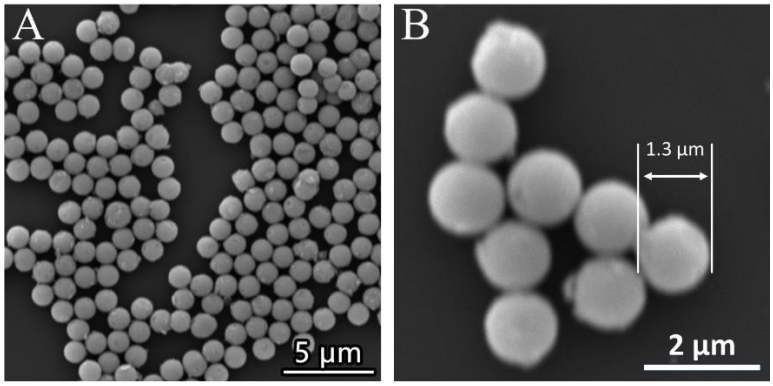

Figure 4-2 SEM images of TiO_2 microspheres before modification under different magnification.

In addition to size uniformity, achieving the precise surface modification requires also an effective strategy to immobilize these microscale spherical particles during the experiment. As reported in previous studies, the gel-assisted method has proven effective for stabilizing micro-scale spherical particles to prevent undesired rotation or movement during the application of the electric field. Following this approach, the TiO_2 microspheres were dispersed in an agarose gel containing metal salt. In this way, the gel environment enables both mechanical stabilization and ionic conductivity, thus allowing asymmetric metal deposition on the TiO_2 microspheres.

Figure 4-3 illustrates the configuration of the bipolar electrochemistry cell and a schematic representation of the light-assisted bipolar electrodeposition process on TiO_2 microspheres. The

electrochemical cell was divided into three compartments, separated by two proton-exchange membranes, which prevented direct contact between the target objects and the driving electrodes, while maintaining conductivity across the system. A light source was positioned directly above the central reaction compartment to provide continuous illumination, and two driving electrodes connected to a DC power supply were placed in the two other compartments to provide the external electric field. To suppress random rotation and uncontrolled migration of TiO_2 microspheres during deposition, the reaction compartment was filled with an agarose gel containing TiO_2 microspheres and the metal precursor solution.

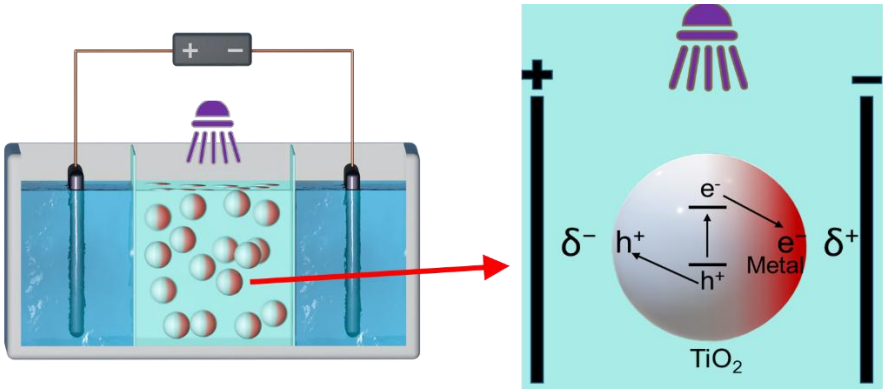

Figure 4-3 Schematic diagram of light-assisted bipolar electrodeposition set-up. The zoom image shows the postulated migration direction of photogenerated electrons and holes in a semiconductor particle under the synergistic effect of electric field and light.

Under a suitable light excitation, electrons in TiO_2 are transferred from the valence band to the conduction band, leading to the generation of electron–hole pairs. In the absence of an applied field, these charge carriers typically migrate randomly to surface-active sites, where they either participate in redox reactions or recombine rapidly with each other, resulting in a homogenous surface deposition or low photocatalytic efficiency. However, once an electric field is applied to the electrolyte, asymmetric polarization of the TiO_2 microspheres occurs: one hemisphere becomes positively polarized (δ^+), while the opposite side becomes negatively polarized (δ^-). This polarization generates an internal electric field across each microsphere, which, under certain conditions related to the crystal structure of the semiconductor, can drive photogenerated electrons to the δ^+ side and holes to the δ^- side.[287] This synergy of light irradiation and electric field application enables spatial separation of electrons and holes within individual TiO_2 microspheres, effectively decreasing the probability of recombination while directing redox reactions to specific hemispheres. In some cases, metal ions in the electrolyte are thus reduced preferentially on the δ^+ side, while oxidation reactions occur on the δ^- side. Compared to classic BPE, this is at first sight somewhat counterintuitive and the precise reasons for this inversion seem to be related to crystallographic parameters which are currently under investigation. Such a precise spatial control of charge carrier migration and reactivity is only achievable through BPE.

In BPE, microscale objects generally require extremely high voltages to trigger the redox reactions.[24] The theoretically necessary electric field can be estimated by Equation 1.2. For instance, in the case of Pd deposition on a 1.3 µm conductive particle, the calculated threshold electric field can be as high as 2.4 kV/cm. Providing such a strong electric field not only demands specialized equipment, but also leads to large energy consumption, which severely limits practical applicability.

In contrast, when dealing with semiconducting materials such as TiO_2, the situation is different. Here, the applied electric field is no longer the dominant factor for driving redox reactions. Instead, the energy for reducing metal ions originates from the light excitation, which generates electron–hole pairs in the semiconductor.[288] The role of the external electric field is to spatially separate these photogenerated electrons and holes to opposite sides of the TiO_2 microsphere. In this way, the synergy between electric field and light enables site-selective deposition of metal cocatalyst on the semiconductor.

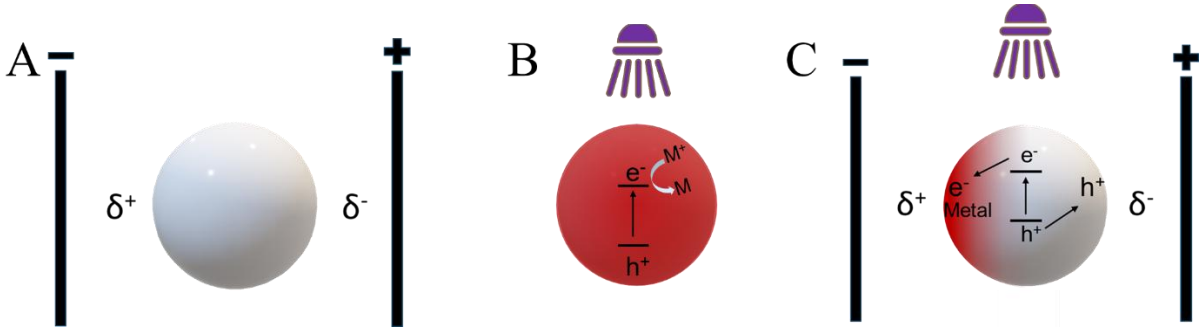

Figure 4-4 Schematic diagram of the deposition on the photocatalyst surface under different experimental conditions. (A) Under only electric field. (B) Under exposure to only light. (C) Under irradiation and simultaneous presence of an electric field.

Based on this principle, three possible results can be expected under different experimental conditions (Figure 4-4). First, when only an electric field is applied without illumination, TiO_2 microspheres behave essentially as insulators, and no metal deposition occurs (Figure 4-4A). Second, under light irradiation alone, corresponding to conventional photodeposition, metal ions are reduced across the entire surface of the TiO_2 microspheres, leading to a random distribution of deposits (Figure 4-4B). Finally, with the synergy of light and electric field, photogenerated electrons are driven to one side of the TiO_2 microsphere, resulting in site-selective asymmetric metal deposition (Figure 4-4C).

4.3.1 Control experiments

To validate the above considerations, a group of control experiments was first performed using TiO_2 microspheres and Pd salt solutions. These experiments were designed to study the individual contributions of light and electric field.

Figure 4-5A shows the SEM image and Figures 4-5B and C shows the corresponding EDS mapping images. As expected, no Pd deposition was observed on the surface of the TiO_2 microspheres, and the EDS analysis revealed no Pd signal. This confirms that, in the absence of light excitation, TiO_2 behaves as an insulator, and it is impossible to trigger the redox reactions required for metal deposition. This result provides clear evidence that light irradiation is a necessary condition for activating TiO_2. In the next set of experiments, we therefore investigated the presence of light irradiation alone, corresponding to conventional photoreduction conditions.

In this case, the TiO_2 microspheres exhibited clear photodeposition behavior (Figure 4-6). To ensure that the generated Pd clusters could be clearly visualized, a relatively long illumination time of 30 s was used. After 30 s of UV exposure in agarose gel, SEM characterization (Figure 4-6A) reveals that there are numerous Pd clusters randomly distributed across the entire surface of the TiO_2 microspheres. The corresponding EDS mapping (Figures 4-6B and C) confirmed a uniform Pd signal, further verifying the photodeposition of Pd on TiO_2.

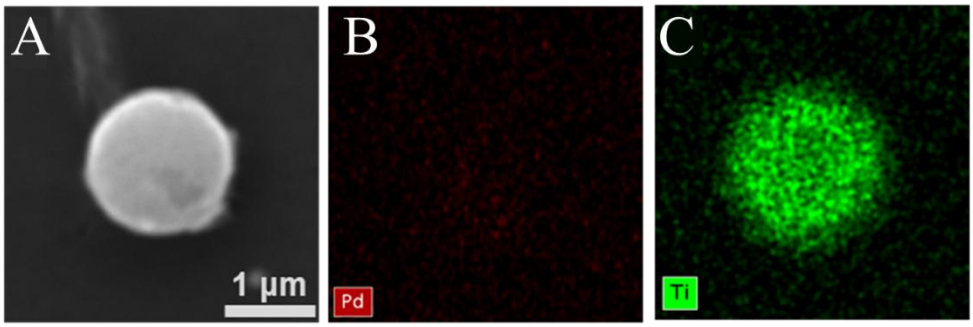

Figure 4-5 (A) SEM image and corresponding (B, C) EDS mapping images of TiO_2 modification under with only the electric field. The applied electric field is 200 V/cm and the deposition time is 10 s.

This can be explained by the photocatalytic mechanism of TiO_2. Under light excitation, electron-hole pairs are generated in the semiconductor. The photogenerated electrons migrate randomly to the surface of the microspheres, where they reduce Pd^{2+} ions to metallic Pd^0 clusters. Meanwhile, the photogenerated holes either participate in water oxidation reactions at the TiO_2-electrolyte interface or undergo recombination with electrons. The random migration of charge carriers results in a non-selective deposition of Pd across the entire TiO_2 surface. These results demonstrate that while light irradiation alone is sufficient to induce metal deposition on TiO_2, the resulting coverage is uniform and uncontrolled. Therefore, to achieve site-selective deposition, an additional driving force is required to spatially separate electrons and holes.

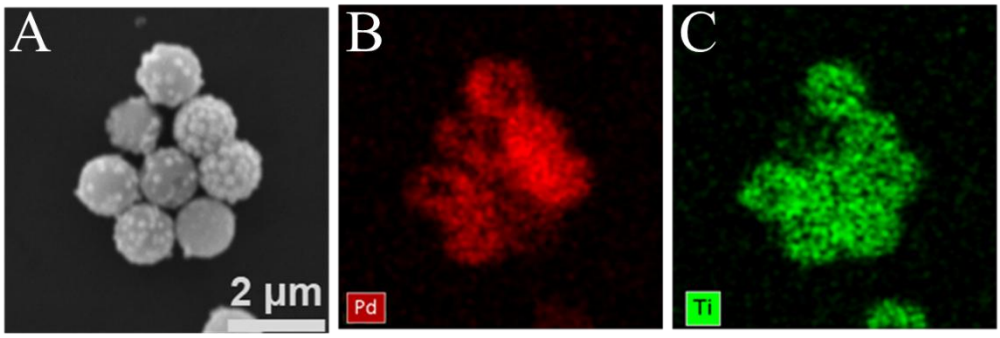

Figure 4-6 (A) SEM corresponding (B, C) EDS mapping images of TiO2 modification under the synergy of electric field and light. The applied electric field is 200 V/cm and the irradiation time is 30 s.

4.3.2 Synergy of electric field and light

The above control experiments clearly demonstrate that site-selective modification of TiO_2 cannot be achieved under light irradiation or electric field alone. Light irradiation alone induces random photodeposition over the entire microsphere surface, while the application of only an electric field leaves TiO_2 inactive due to its semiconducting nature. These observations confirm that an additional cooperative mechanism is required to direct the spatial localization of metal deposits. We therefore investigated Pd deposition on TiO_2 microspheres under the synergy of an external electric field and light irradiation. As shown in Figures 4-7A-D, SEM and EDS mapping images reveal that Pd clusters were asymmetrically deposited, with the Pd localized predominantly at one side of the TiO_2 microsphere, while the opposite hemisphere shows no Pd signal. The EDS spectra further confirm the elemental composition, with distinct peaks corresponding to O (0.5 eV), Pd (2.8 eV), and Ti (4.5 eV), validating the successful reduction of Pd^{2+} ions to metallic Pd clusters.

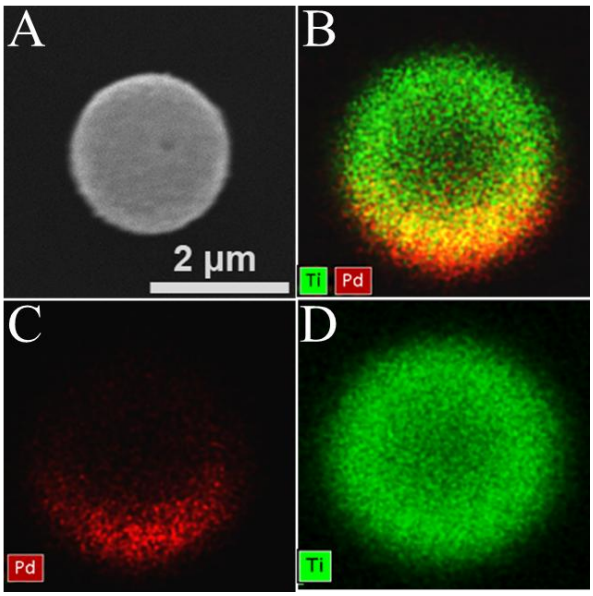

Figure 4-7 (A) SEM and corresponding (B, C, D) EDS mapping images of TiO_2 modified under the influence of light and electric field. The applied electric field is 200 V/cm and the deposition time is 10 s.

This asymmetric deposition provides direct evidence of the effective spatial separation of photogenerated charge carriers under the combined influence of light and an electric field. The external field establishes a directional potential gradient across the microsphere, which guides electrons and holes toward opposite hemispheres.

4.3.3 Precision control of light-assisted bipolar electrodeposition

In order to systematically regulate the Pd deposition on TiO_2 microspheres, a series of experiments were carried out with different electric field intensities and deposition durations. Figure 4-8A displays the morphology and element distribution of Janus Pd-TiO_2 particles synthesized with an electric field of 200 V/cm. The Pd clusters covered nearly half of the surface of the sphere, with a signal intensity gradually decreasing from one extremity toward the opposite extremity. This deposit gradient looks similar to the one obtained with classical bipolar electrodeposition on conducting objects, but apparently occurs at the opposite side in the specific case of this kind of objects (*vide supra*). The hypothesis is that, along the direction of the electric field, the potential difference across the TiO_2 microsphere reaches a maximum between the two extremities and gradually decreases toward the center. As a result, the δ^+ extremity possesses the strongest attractive force for photogenerated electrons which decreases towards the center. This leads to the observed gradient deposition of Pd clusters on the microsphere surface. Thus, it seems possible to tune the area occupied by the deposit by modulating the electric field.

Figures 4-8B and C present Janus Pd-TiO_2 microspheres generated with different electric field intensities. When increasing the electric field to 300 V/cm, the Pd deposition area became more localized toward the polarized extremity (Figure 4-8B). When further increasing the electric field to 400 V/cm, Pd clusters were only observed in a small area (Figure 4-8C), indicating that a stronger electric field more efficiently drives and confines the photogenerated electrons to a small area at the particle's extremity, where they participate in the metal reduction reaction.

These results highlight the critical role of electric field intensity in tuning the deposit area on the surface of semiconductors.

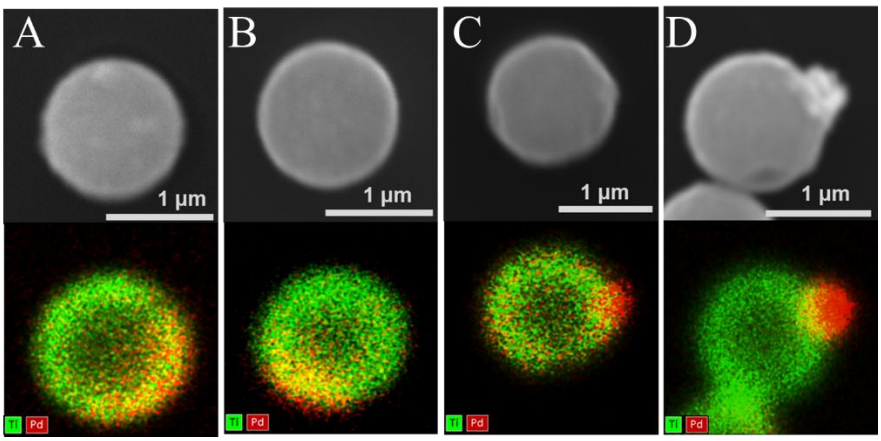

Figure 4-8 SEM and corresponding EDS mapping images of Janus Pd-TiO_2 microspheres synthesized with different electric fields and varying irradiation times, (A) 200 V/cm for 10 s, (B) 300 V/cm for 10 s, (C) 400 V/cm for 10 s, (D) 400 V/cm for 60 s.

Next, the influence of the deposition time was further investigated at 400 V/cm by extending the effective deposition time from 10 s to 60 s. To avoid melting of the agarose gel caused by Joule heating and to minimize the inhomogeneous ion distribution resulting from migration, a pulsed deposition strategy was employed. Specifically, the 60 s deposition process was divided into six 10 s deposition cycles, each followed by a 10 s application of a reversed electric field without illumination. Compared to the 10 s deposition (Figure 4-8C), the 60 s deposition results in significantly enlarged Pd clusters (Figure 4-8D), as confirmed by the EDS analysis. This time-dependent growth emphasizes the ability to precisely control cluster size through tuning deposition time while preserving spatial selectivity.

These results emphasize the critical role of electric field intensity and deposition time in regulating asymmetric metal deposition on semiconductor microspheres, offering a versatile approach to fine-tune the spatial distribution and the size of catalytically active areas.

4.3.4 Deposition of different metals

To further demonstrate the versatility of this approach, we next attempted the asymmetric deposition of other metals on TiO_2 microspheres. As shown in Figure 4-9, both Ag and Cu were successfully deposited in a site-selective way, the deposited clusters are mainly localized on one side of the TiO_2 microspheres. SEM images clearly reveal the asymmetric distribution of the metallic domains, while the corresponding EDS mapping confirmed the presence of Ag and Cu signals restricted to the polarized position.

These results provide strong evidence that the light-assisted bipolar electrochemical strategy is not limited to noble metals such as Pd, but is also compatible with a broader range of metal ions. The ability to achieve asymmetric deposition of Ag, a metal with well-known plasmonic and catalytic properties, and Cu, a low-cost and earth-abundant metal, highlights the general validity of the approach. Importantly, this compatibility with different metals suggests that the concept can be adapted to fabricate a variety of TiO_2-metal Janus structures, enabling applications ranging from enhanced photocatalysis to environmental remediation and even plasmon-driven energy conversion.

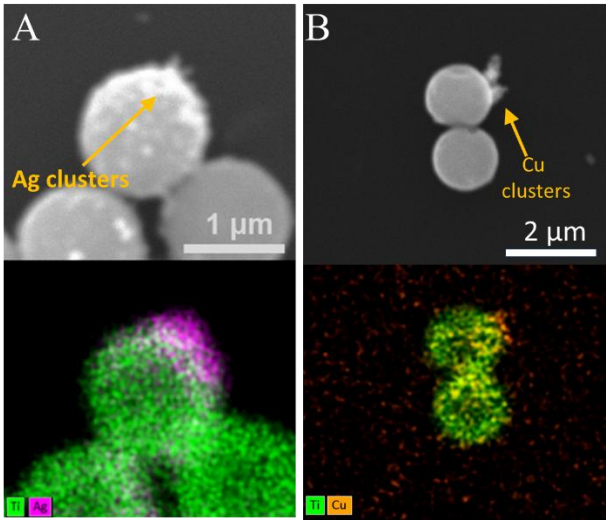

Figure 4-9 SEM and corresponding EDS mapping image of Janus Ag-TiO_2 microspheres and Janus Cu-TiO_2 microspheres, synthesized with an electric field of 200 V/cm for 5 s.

4.4 Application in photocatalysis

After having demonstrated the successful site-selective deposition of metal clusters on TiO_2 microspheres, we next investigated how this spatially controlled modification influences their photocatalytic performance. Theoretically, the asymmetric deposition of Pd cocatalysts on TiO_2 is expected to enhance photocatalytic efficiency by promoting charge separation and suppressing recombination. To validate this hypothesis, photocatalytic degradation experiments were performed using rhodamine B (RhB) as a model organic pollutant.

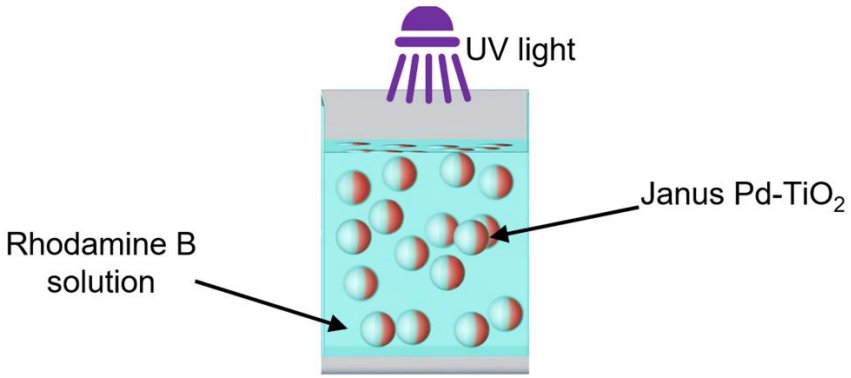

Figure 4-10 Schematic diagram of the set-up for the degradation of RhB using Janus Pd-TiO_2 particles as photocatalyst.

Figure 4-10 shows the schematic of the experimental setup for photocatalytic degradation. A suspension of Pd-TiO_2 particles containing RhB was poured into a glass reactor positioned directly under a UV light source. To avoid thermal effects that could influence the photocatalytic process, the reactor was placed in a water bath, maintaining the experiment at a constant temperature of 20 °C. Then the suspension was continuously irradiated with UV light. At regular intervals of 10 minutes, part of the solution was taken out from the reactor and analyzed by UV–vis absorption spectroscopy. After that, the analyzed solution was returned to the vessel to maintain a constant solution volume throughout the experiment. This procedure allowed us to monitor in real time the progressive degradation of RhB and to directly compare the catalytic activity of modified TiO_2 with pure TiO_2.

4.4.1 Photodegradation performance of RhB

The photocatalytic performance of a material is generally evaluated through a combination of activity and stability tests, which together provide a comprehensive assessment of its practical applicability. In this study, the catalytic activity of the samples was quantified by monitoring the change in absorbance of RhB at its characteristic wavelength, and the corresponding degradation efficiency was calculated from the absorbance decay over time. To further assess the robustness of the catalyst, recycling experiments were conducted with the same sample over multiple degradation cycles, thereby providing insight into the long-term stability and reusability of the Janus Pd-TiO_2 photocatalyst.

4.4.1.1 The influence of modification on performance

Figure 4-11A shows the time-dependent UV-vis spectra of the RhB solution in the presence of Janus Pd-TiO_2 photocatalysts synthesized with an applied electric field of 200 V/cm. All photocatalytic degradation experiments were carried out using a photocatalyst concentration of 0.05 mg/mL, and no external stirring was applied during the degradation process. Before the irradiation with light, the suspension was stirred in the dark for 30 min to establish an adsorption-desorption equilibrium. However, no noticeable decrease in the RhB absorption intensity was observed after this dark adsorption step, which can be attributed to the relatively low photocatalyst amount used in this study. The characteristic absorption band of RhB at ~550 nm gradually decreased with irradiation time, confirming the progressive degradation of the dye molecules.[289, 290] The almost complete disappearance of this absorption peak within 30 minutes clearly indicates the high photocatalytic efficiency of the Janus Pd-TiO_2 system.

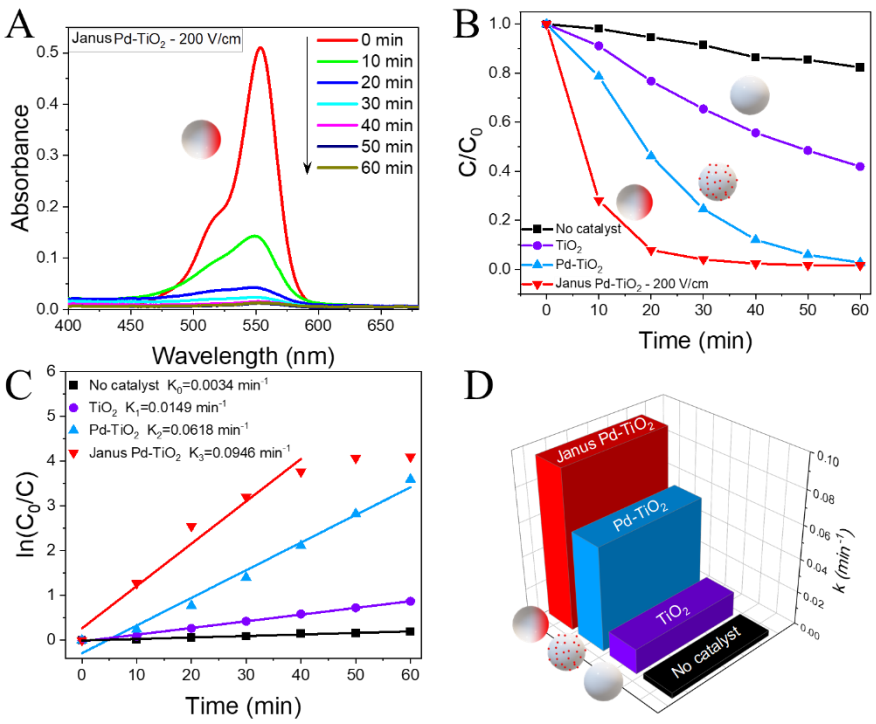

Figure 4-11 (A) UV-vis absorption spectra of a 5 ppm RhB solution during the photodegradation experiment with Janus Pd-TiO_2 photocatalyst microspheres (synthesized with 200 V/cm under irradiation with light for 10 s) at different irradiation times. (B) Photodegradation activity of RhB vs light irradiation time with different photocatalysts. (C) Photodegradation kinetics and (D) comparison of rate constants for the photodegradation of RhB for different samples.

A comparison of the photocatalytic degradation performance of differently structured samples is summarized in Figure 4-11B. Under UV irradiation for 60 minutes without any catalyst, the degradation rate (C/C_o) reached only 18%, attributable to the direct photolysis of RhB under the impact of high-energy light.[291] Pure TiO_2 exhibited moderate activity, achieving 58% degradation after 60 minutes, reflecting the intrinsic limitations of TiO_2 due to electron–hole recombination. When Pd was randomly photodeposited across the entire TiO_2 surface, the degradation significantly increased to 97% for the same duration, demonstrating that the presence of Pd clusters is indeed beneficial for suppressing recombination and facilitating charge transfer. Remarkably, the Janus Pd-TiO_2 photocatalysts, with site-selective deposition of Pd clusters, achieved ~96% degradation in only 30 minutes, almost twice as fast as the randomly deposited counterpart. This notable difference emphasizes the importance of spatial charge separation in enhancing photocatalytic activity.

To further quantify the enhancement, the degradation kinetics were analyzed using a pseudo-first-order model, and the corresponding rate constants (*k*) were calculated (Figures 4-11C and D). Since the degradation rate of Janus Pd-TiO_2 photocatalyst reached 98% in 40 minutes, we only calculated the rate constant of the first 40 minutes for this sample. The Janus Pd-TiO_2 photocatalyst exhibited a rate constant of 0.0946 min^{-1}, which represents a ~630% enhancement compared to pure TiO_2 and a ~150% increase compared to randomly Pd-deposited TiO_2.

These comparisons are made under the hypothesis that the same loading amount of Pd was obtained, as identical irradiation times were applied during the deposition process. While the exact Pd loading was not quantified, it is reasonable to assume that same deposition time correlates with the loading amount. Therefore, we conclude that the excellent performance of Janus Pd-TiO_2 is mainly due to the asymmetric distribution of Pd.

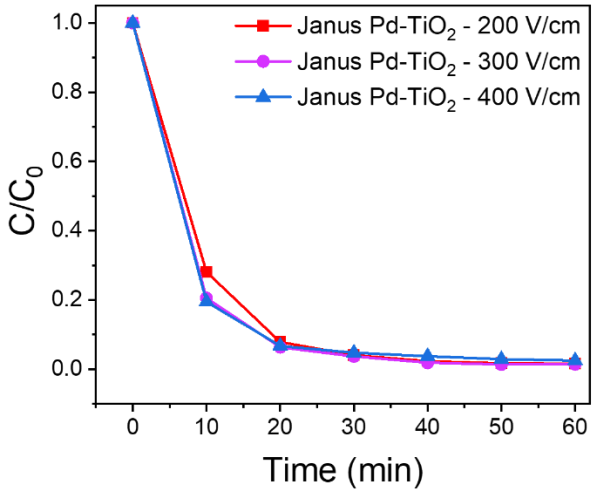

Figure 4-12 Photodegradation activity of RhB vs light irradiation time with Janus Pd-TiO_2 microspheres synthesized at 200 V/cm, 300 V/cm, and 400 V/cm with a deposition time of 10 s.

One key reason for such an enhanced photocatalytic performance of Janus Pd-TiO_2 is the asymmetric modification of Pd on the surface of TiO_2 microspheres. This configuration creates a heterojunction at the Pd-TiO_2 interface. Since TiO_2 is an n-type semiconductor and Pd possesses a higher work function[292, 293], photogenerated electrons in the conduction band preferentially migrate toward the Pd-modified area. This effect significantly reduces

recombination between electrons and holes through spatial separation, improving the charge carrier's lifetime and thus the efficiency of the photodegradation process. To investigate the influence of Pd coverage on the photocatalytic activity of Janus Pd-TiO_2 particles, photodegradation experiments with catalyst particles synthesized at different electric fields of 200, 300, and 400 V/cm were performed. The comparable degradation profiles shown in Figure 4-12 suggest that the asymmetric spatial distribution of Pd is the dominating factor governing the performance, and not necessarily the size of the modified area. Even very localized Pd clusters, such as for the Janus Pd-TiO_2 particles synthesized at 400 V/cm, can effectively facilitate charge separation.

4.4.1.2 Stability

To further test the stability of the Janus Pd-TiO_2 photocatalysts, recycling experiments were performed using RhB as a model pollutant. After each cycle of photodegradation, the suspension was centrifuged to recover the photocatalyst, washed with deionized water, and then re-dispersed in a fresh RhB solution for the next cycle. As shown in Figure 4-13, no significant decrease in photocatalytic activity was observed over three consecutive degradation cycles. The degradation efficiency remained above 95% in each run, indicating that both the Pd clusters and the Janus structure of the TiO_2 microspheres remained stable under repeated use. These results demonstrated the durability of the Janus photocatalyst, suggesting that the spatially controlled deposition strategy not only enhances photocatalytic efficiency, but also endows the material with excellent stability, an essential precondition for environmental applications.

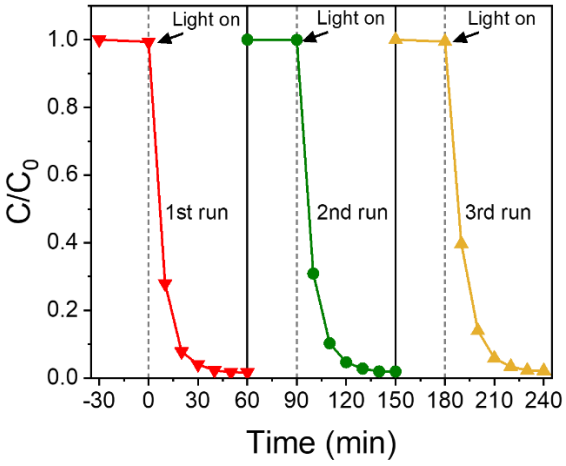

Figure 4-13 Photocatalytic stability test of Janus Pd-TiO_2 microspheres (synthesized under 200 V/cm and irradiated for 10 s.

4.4.2 Mechanism of the enhanced performance

The mechanism of the enhanced photocatalytic performance can be attributed to the spatially selective deposition of Pd clusters, which induces a more ordered migration of photogenerated charge carriers. First, as illustrated in Figure 4-14A, under UV illumination, electron-hole pairs are generated in the TiO_2 microspheres (Equation 4.1). In the Janus structure, photogenerated electrons preferentially migrate to the Pd-modified area, where they are trapped by Pd clusters and subsequently participate in the degradation of RhB molecules. Specifically, the photogenerated holes react with water molecules to generate hydroxyl radicals (·OH) and protons (Equation 4.2), while the photogenerated electrons react with dissolved oxygen to generate superoxide radicals ($\cdot O_2^-$) (Equation 4.3). The generated $\cdot O_2^-$ radicals can be protonated

to form hydroperoxyl radicals (HO_2·), which then produce H_2O_2 (Equations 4.4). The H_2O_2 molecules can be reduced by electrons to generate additional ·OH (Equations 4.5). Consequently, these reactive species synergistically contribute to the degradation of RhB (Equation 4.6).[294-297]

$$TiO_2 + hv \rightarrow h^+ + e^- \quad (4.1)$$

$$H_2O + h^+ \rightarrow \cdot OH + H^+ \quad (4.2)$$

$$e^- + O_2 \rightarrow \cdot O_2^- \quad (4.3)$$

$$2 \cdot O_2^- + 2H^+ \rightarrow 2HO_2 \cdot \rightarrow H_2O_2 + O_2 \quad (4.4)$$

$$H_2O_2 + e^- \rightarrow \cdot OH + OH^- \quad (4.5)$$

$$RhB + (\cdot OH, \cdot O_2^- \; or \; h^+) \rightarrow Intermediate\ products \rightarrow H_2O + CO_2 \quad (4.6)$$

This design greatly reduces the probability of recombination between electrons and holes by maintaining their spatial separation across the microsphere. As a result, both electrons and holes are more effectively utilized in the photocatalytic degradation process.

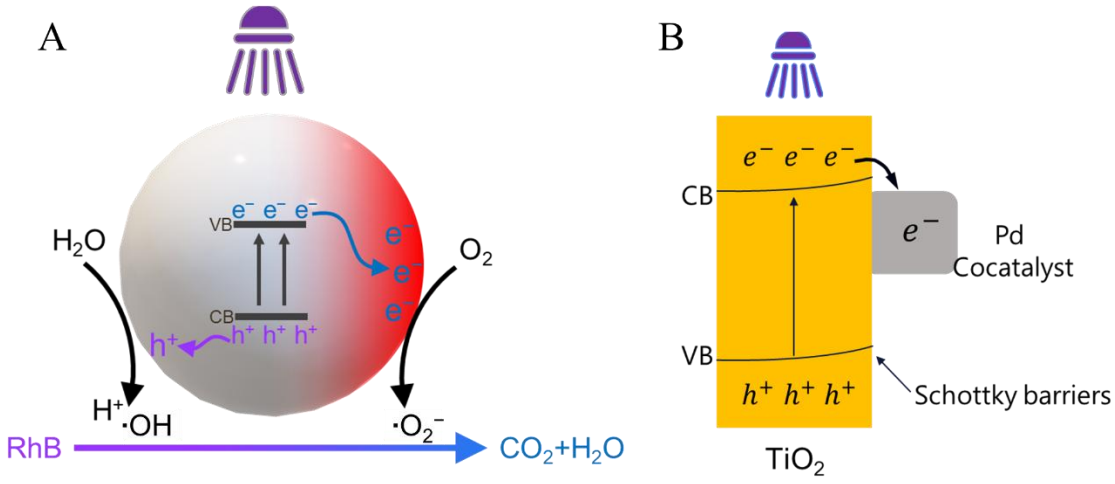

Figure 4-14 (A) Schematic diagram of the photodegradation mechanism of RhB by Janus Pd-TiO_2 photocatalyst. (B) Schematic illustration of the energy band structure and charge transfer pathways of the Pd-TiO_2 photocatalyst under irradiation.

Second, the enhanced photocatalytic performance of Janus Pd-TiO_2 can be attributed to the role of Pd as an efficient electron donor arising from its high work function relative to TiO_2. As shown in Figure 4-14B, under light irradiation, electron-hole pairs are generated in TiO_2, with electrons promoted from the valence band (VB) to the conduction band (CB). Due to the formation of a Schottky junction at the Pd-TiO_2 interface, electrons in the CB of TiO_2 will transfer to the Pd cocatalyst and participate RhB decomposition there. As a consequence, Pd does not directly participate in catalytic reactions, but acts as an electron sink that efficiently captures photogenerated electrons, thereby prolonging charge carrier lifetime. Thus, other metals, such as Pt or Au might lead to a similar increase in photocatalytic efficiency, as long as they can also generate such a Schottky junction. Meanwhile, the photogenerated holes remain in the VB of TiO_2 and participate in oxidation reactions, such as the formation of reactive oxygen species.

Third, we propose another reason for the significantly enhanced photocatalytic performance of Janus Pd-TiO_2 microspheres. It is based on their light-induced self-propulsion in the RhB solution, resulting in a “swimming” photocatalyst. Under illumination, the photogenerated electrons

migrate to the Pd modified area, where they participate in the reduction of dissolved oxygen accompanied by H^+ consumption. Meanwhile, photogenerated holes oxidize water to produce ·OH and H^+. This asymmetric generation and consumption of protons establishes an H^+ gradient around the Janus Pd-TiO_2 particle, giving rise to a self-electrophoretic propulsion phenomenon (Figure 4-15A).[298]

Consequently, the Janus Pd-TiO_2 particle exhibits an autonomous movement with a velocity of 1.8 µm/s, which enables fluid mixing and enhances mass transport of the target RhB molecules toward the photocatalyst surface. Figure 4-15B shows the motion trajectory of a Janus Pd-TiO_2 particle in the RhB solution. In contrast, no propulsion was observed for the unmodified TiO_2 microspheres and the Pd-modified TiO_2 samples uniformly coated with Pd under illumination without electric field (not shown), confirming that the asymmetric Janus configuration is essential for the light-induced motion. Before turning on the UV light, no motion was observed. However, distinct autonomous movement is observed when the light is switched on. This motion stops immediately when the light is switched off again, indicating that it is most likely not a thermophoretic motion. This self-propulsion of Janus Pd-TiO_2 microspheres introduces a dynamic aspect to photocatalysis and offers a novel approach to optimizing photocatalytic systems.

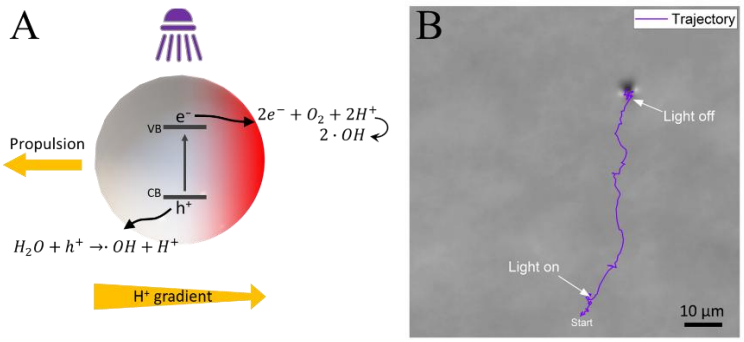

Figure 4-15 (A) Schematic diagrams of the propulsion mechanism of the Janus Pd-TiO_2 swimmer. (B) Trajectory of a Janus Pd-TiO_2 microsphere in RhB solution with light on and light off.

4.5 Interferometric scattering microscopy of modified TiO_2

To further investigate the catalytic behavior of individual Janus Pd-TiO_2 particles, we employed interferometric scattering (iSCAT) microscopy. iSCAT microscopy is an optical technique that detects weak scattering signals from nanoscale objects by interfering them with a reference field, typically the reflection of the illumination beam from a substrate.[299, 300] The resulting intensity encodes changes in the object's polarizability, which is directly linked to its refractive index and dielectric environment. This makes iSCAT highly sensitive to dynamic processes such as molecular adsorption, catalytic reactions, or local chemical fluctuations, without requiring fluorescent labels or invasive probes. Because the technique relies on interference rather than absolute scattering intensity, it achieves nanometer-scale sensitivity to changes in the optical path length and can track extremely small refractive-index variations in real time.

To quantify temporal changes, we applied a differential rolling average (DRA) analysis: a median of several hundred frames before a given time point is divided by the median of several hundred frames after it. This approach suppresses static background signals from the substrate and highlights only relative variations in scattering contrast, which can be interpreted as local dielectric fluctuations around the particle. The effective temporal resolution (~2 s in this study)

is set by the number of frames included in each rolling window, providing a balance between sensitivity and time resolution.

This methodology is particularly relevant here because Pd-TiO_2 particles immobilized on a substrate cannot be characterized through motility as in classical microswimmer studies. Instead, iSCAT provides a label-free, in situ probe of catalytic activity, revealing how product generation and release manifest as nanoscale refractive-index changes around each particle during hydrogen peroxide decomposition under illumination. By combining continuous 785 nm imaging with intermittent 450 nm photoactivation, we were able to resolve both stochastic local fluctuations and oriented bursts of activity associated with the Janus configuration, offering direct optical signatures of catalytic behavior that are otherwise inaccessible.

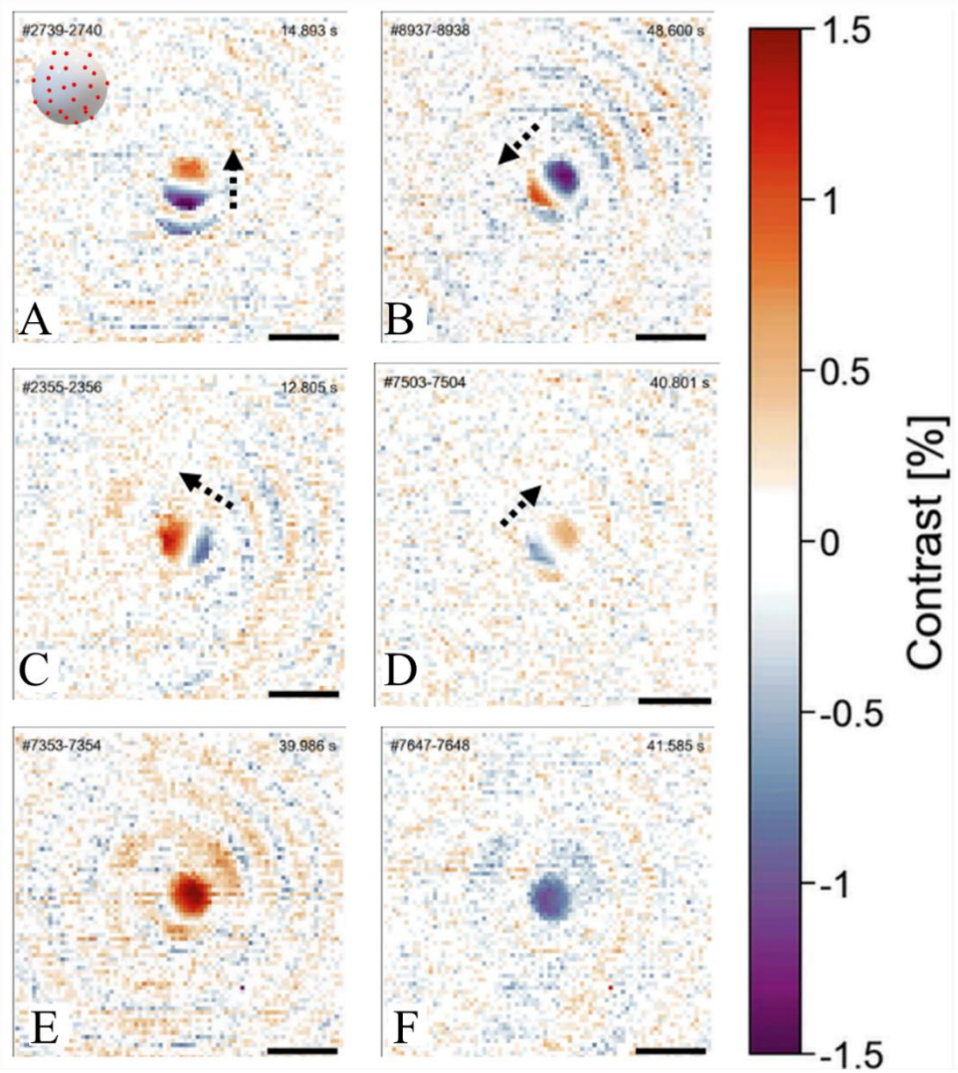

Figure 4-16 iSCAT/DRA contrast maps of immobilized TiO_2 particles with homogeneous Pd coverage. Representative frames (A-F) show relative scattering contrast changes at different times under catalytic turnover in 3% H_2O_2 and SDS. Colours encode relative contrast variations (–1.5% to +1.5%): red corresponds to a relative increase in scattering, blue to a relative decrease. Arrows mark transient dipolar features. While some particles display dipole-like contrast changes with alternating red/blue lobes (A-D), others show almost monopolar behavior, appearing either predominantly red (E) or predominantly blue (F). Scale bars: 2 µm.

For TiO_2 particles with homogeneous Pd coverage, iSCAT revealed dynamic contrast signatures without any fixed orientation. In most cases (Figures 4-16A-D), the particles displayed transient red–blue dipolar lobes. These correspond to partial, localized product generation, where catalytic turnover produces refractive-index changes confined to one side of the particle. The

lobes rapidly flip or drift, consistent with stochastic, isotropic catalytic activity where reaction products and intermediates diffuse in random directions. This behavior dominated the videos and suggests that most events involve only limited product release that dissipates quickly.

Occasionally, the contrast extended across the entire particle (Figures 4-16E and F). In these instances, the particle first appeared completely red, indicating a surge of product generation sufficient to increase the refractive index globally around the particle. This was typically followed by a completely blue state, as the accumulated products dissipated or detached, leaving the surrounding region with relatively lower scattering contrast. Such global swings were rare compared to the more common dipolar fluctuations but highlight episodes of stronger, collective catalytic bursts.

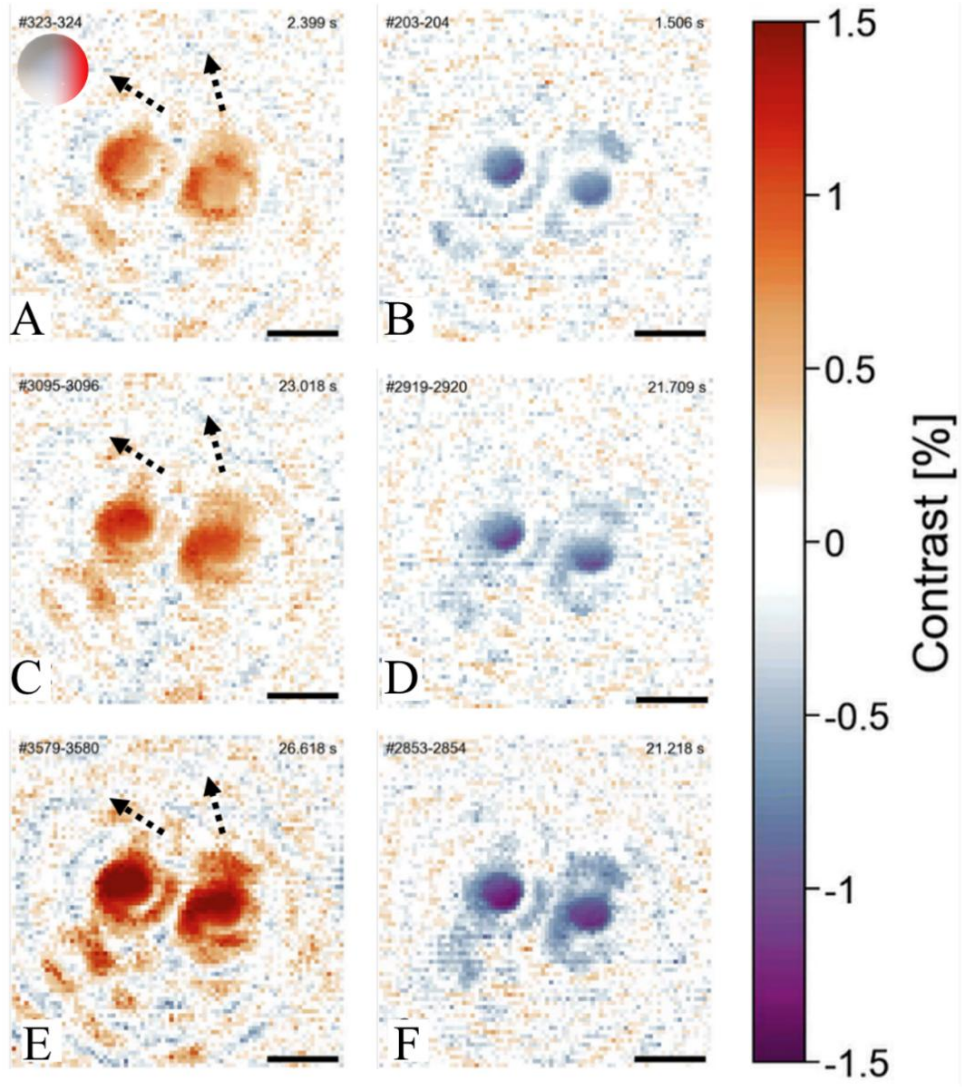

Figure 4-17 iSCAT/DRA contrast maps of immobilized Janus Pd-TiO_2 particles. Representative frames (A-F) show alternating states of strong red and strong blue contrast around two neighbouring Janus particles. Colours encode relative contrast variations (–1.5% to +1.5%): red indicates an increase, and blue a decrease, in scattering relative to the preceding frames. The arrows mark transient orientation of the red–blue dipoles. The particles consistently exhibit global red states, reflecting bursts of product generation, followed by global blue states as products are rapidly released. In contrast to homogeneously coated particles, the Janus configuration imparts a preferred orientation, visible as directional contrast lobes.

Because the catalytic activity in these homogeneously coated particles is isotropic and non-persistent in direction, it does not establish stable chemical gradients or fluid flows. As a result, free particles of this type would lack effective propulsion, instead showing only random fluctuations in their environment without sustained motion.

In contrast to these homogeneously coated particles, the Janus Pd-TiO_2 particles displayed a distinct contrast behavior compared to homogeneously coated one. As shown in Figures 4-17A-F, the particles alternated between uniformly red states and uniformly blue states. The red phases correspond to intense catalytic activity, where a large amount of product accumulates within a short time, increasing the refractive index around the particle. This is rapidly followed by blue phases, consistent with a fast release or diffusion of the accumulated products, leaving the surrounding medium depleted relative to the reference frames.

In addition to these red–blue cycles, the contrast patterns frequently exhibited a directional dipolar character (arrows in Figures 4-17A, C, E). This reflects the inherent asymmetry of the Janus structure, where catalytic activity is localized predominantly on the Pd hemisphere. The resulting orientation bias is directly linked to the mechanism of motion in free-swimming Janus particles: asymmetric product release establishes chemical gradients and fluid flow that drive propulsion. In the immobilized state studied here, this manifests as oriented scattering contrast; in suspension, the same effect translates into persistent directional motion.

These findings further confirmed that breaking the symmetry of particle not only alters the spatial distribution of catalytic activity, but also introduces directional chemical gradients that underpin the propulsion behavior of Janus photocatalysts in suspension.

4.6 Experimental section

Synthesis of Janus Metal/TiO_2:

First, 0.5 g of agarose (low gelling temperature, Sigma Aldrich) was dissolved in 50 mL of water at 60 ℃ to prepare the agarose solution. Then 5 mg of TiO_2 powder and 10 mg of $PdSO_4$ (>99.9%, Sigma Aldrich) were added to the agarose solution. 1 mL of the obtained mixture was transferred into the reaction compartment of a customized bipolar electrochemical cell and the electrode compartments were filled with 1 mM NH_4Cl (99.99%, Sigma Aldrich). The cell was positioned in an ice bath for at least 5 min to solidify the agarose mixture and an electric field and light (HAMAMATSU-LC8, 62 mW/cm^2, ⩽400 nm, same below) were simultaneously applied to the agarose mixture for a given time. Subsequently, the mixture was heated to 60 ℃ and centrifuged to separate the Janus Pd/ TiO_2 particles from the gel. For the control experiments in Figures 4-5 and 4-6, the same procedure was performed except the light and electric field were removed, respectively.

Photocatalytic performance evaluation of Janus Pd-TiO_2:

The photodecomposition experiments were conducted in a glass cell, filled with a solution containing a mixture of RhB (5 ppm) and TiO_2 photocatalyst (0.05 mg/mL). This suspension was stirred for 30 min in the dark to achieve an adsorption-desorption equilibrium before light irradiation. Then the cell was placed under the light source. The RhB solution was extracted every 10 min for centrifugation and UV-vis spectroscopy. After the measurement, the tested RhB solution was returned to the centrifuge tube and used to re-disperse the photocatalyst by

sonication, after which the suspension was poured back into the cell to continue the photodegradation experiment. This procedure ensured that the amount of photocatalyst remained constant throughout the experiment. For the recycling test, the TiO_2 microspheres were centrifuged after every cycle and re-dispersed in fresh RhB solution for the next cycle.

To convert the absorbance data into concentration, an absorbance–concentration calibration curve was prepared. First, a series of standard RhB solutions with different concentrations were prepared and their UV-vis absorption spectra were tested. Then, the absorbances at the maximum absorption wavelength (~550 nm) were recorded. Finally, a calibration curve was constructed by plotting absorbance versus concentration, and a regression equation was obtained (Equation 4.7).

$$A = 9.79C + 0.007 \tag{4.7}$$

where A is the absorbance and C is the concentration. The absorbance of RhB solutions could then be substituted into this equation to calculate their concentration.

Light-induced motion of Janus Pd-TiO_2:

The light-controlled propulsion experiments were conducted in a poly(methyl methacrylate) cell (5 mm in diameter and 1 mm in depth) fixed on a glass slide. 20 µL of suspension containing RhB solution and Janus Pd-TiO_2 particles were added to the cell and covered by a quartz cover glass. Then the suspension was irradiated by a light source (≤400 nm) for generating motion. The video was recorded by a microscope (LEICA DM6000) equipped with a EMCCD Camera (HAMAMATSU, C9100-13).

Interferometric scattering microscopy:

Janus Pd-TiO_2 particles were prepared following established protocols. For microscopy, a small amount of the particle suspension was drop-cast onto a clean glass coverslip, dried under ambient conditions, and subsequently overlaid with an aqueous solution of 3% (v/v) H_2O_2 containing 0.5% sodium dodecyl sulfate. The sample chamber was sealed with a spacer to minimize evaporation during imaging.

iSCAT microscopy was performed using a 785 nm continuous-wave laser for illumination at an intensity of 10-13 W cm^{-2}. Scattered light from the particles interfered with the reflected reference field at the glass–solution interface and was collected onto a CMOS camera. To activate the photocatalytic response of TiO_2, a 450 nm laser was coupled into the optical path. Image sequences were recorded continuously and processed using a DRA analysis. For each frame, the median of ~100-200 preceding frames was divided by the median of ~100-200 subsequent frames, yielding relative contrast maps with an effective temporal resolution of 10 ms. Variations in scattering contrast were interpreted as signatures of catalytic turnover and associated changes in the local dielectric environment around individual immobilized Janus particles.

4.7 Conclusion

In conclusion, we have demonstrated the precise site-selective modification of TiO_2 microspheres with metal clusters by using light-assisted BPE. This strategy is based on the synergy of light and electric field to separate photogenerated electrons and holes and drive them to opposite extremities, enabling the synthesis of Janus Pd-TiO_2 hybrid photocatalysts with well-defined

spatial asymmetry. Although the precise position of the metal clusters on the semiconducting particles may depend on factors such as crystal structure, we have demonstrated that the Pd deposition area can be fine-tuned by adjusting the experimental parameters such as electric field intensity and light irradiation duration, allowing the elaboration of diverse surface morphologies from half-sphere coatings to isolated metal islands. The Janus Pd-TiO_2 photocatalysts exhibited a significant improvement in photocatalytic RhB degradation, an over 5-fold enhancement compared to bare TiO_2. This spatially precise modification strategy can be extended to other metals and semiconducting materials for the generation of advanced multifunctional photocatalysts, with promising applications in environmental remediation.

Chapter 5 Conclusion and perspectives

5.1 Conclusions

This thesis systematically explores the concept and applicability of BPE as a powerful and versatile strategy for the wireless, site-selective modification of different materials, ranging from conducting 2D graphene monolayers, to transition-metal carbides (MXene) and semiconducting TiO_2 microspheres. Across those chapters, we demonstrated how to adapt BPE to different types of materials, and how the asymmetric modification influences their catalytic, optical, and dynamic behavior, paving the way for the synthesis of novel multifunctional materials.

Chapter 1 introduces the fundamental principles of BPE and its various applications in materials science, analysis, and motion generation. This includes the synthesis of Janus particles, the further development of original bipolar electrochemiluminescent systems, the fabrication of gradient materials, and the induction of motion in microscopic and macroscopic objects. This highlights the wireless and site-selective modification feature of BPE, laying the foundation for its application in different fields.

In Chapter 2, we demonstrated that graphene monolayer is an ideal model 2D material to reveal the full potential of BPE for constructing multifunctional 2D hybrids. Through precise site-selective metal deposition, we achieved controllable Pt loading that directly translates into bubble-driven swimmers with tunable trajectories. Beyond metals, Prussian Blue was combined with graphene monolayers as a coordination compound to achieve localized CL. Additionally, Pt and electrophoretic paint were co-deposited at the opposite corners of a graphene monolayer to create multifunctional 2D hybrids, which are capable of simultaneous catalytic propulsion and light emission. We further expanded the concept to enzyme-modified graphene swimmers, for which enzymatic reactions power autonomous motion that can be optimized by an external magnetic field. Finally, BPE was coupled with a magnetic field to design a light-emitting 2D graphene rotor, where asymmetric electrochemical reactions trigger localized ECL emission while the induced Lorentz force triggers controlled rotational dynamics. These proof-of-concept studies confirmed the unique advantage of BPE for integrating metals, coordination compounds, polymers, and biomolecules into multifunctional graphene-based systems in which motion, catalysis, and optical signaling are coupled.

In Chapter 3, we extended the use of BPE beyond graphene monolayers to other 2D materials, namely Ti_3C_2 MXene as a model compound. Due to its sensitive surface nature, Ti_3C_2 exhibited spontaneous reduction of metal ions even without the application of an electric field, leading to undesired deposition on its surface. By correlating surface charge with zeta potential, we demonstrated that spontaneous surface reduction can be effectively suppressed in acidic electrolytes. Under optimized conditions, site-selective deposition of Au clusters was realized. Moreover, the selectivity and the controllability of BPE modification was further improved by immobilizing MXene microsheets on glass substrates, even for extended deposition times or higher electric fields. These results illustrate the utility of BPE for site-selective functionalization of other types of 2D materials, even very sensitive materials like Ti_3C_2.

In Chapter 4, we shifted our focus from conductive 2D materials to semiconductor materials, and light-assisted BPE was introduced as a strategy to overcome the conductivity issues of semiconductors. TiO_2 microspheres were employed as model objects. By combining UV irradiation with an electric field, photogenerated electrons and holes were spatially separated to opposite hemispheres, enabling the synthesis of Janus Pd–TiO_2 photocatalyst particles. The Pd deposition morphology could be fine-tuned by controlling the electric field intensity and the deposition time, ranging from half-sphere coated modification to localized metallic dots. The resulting Janus Pd-TiO_2 photocatalysts exhibited markedly enhanced photocatalytic activity, leading to a more than five-fold higher RhB degradation efficiency compared to pure TiO_2. The study revealed two possible key contributions to this enhancement: (i) spatially separated charge migration toward Pd-modified and unmodified hemispheres, and (ii) light-driven self-propulsion of Janus particles, which promote dynamic mixing and enhanced mass transfer. These findings make light-assisted BPE a generalizable approach for designing advanced multifunctional photocatalysts with potential applications in environmental remediation and solar energy conversion.

In summary, this thesis demonstrates that bipolar electrochemistry is a general and powerful method for precise, wireless, and asymmetric modification of materials across different dimensions and types: conductors, carbides, and semiconductors. By coupling redox chemistry with dynamic behavior and optical readouts, BPE enables the creation of advanced multifunctional materials that integrate motion, catalysis, and sensing within a single object. These results not only broaden the applicability spectrum of BPE to diverse materials, but also demonstrate how precise modification can influence catalytic performance. This thesis provides new insights for future applications in energy conversion, environmental remediation, photocatalysis, sensing, and soft robotics.

5.2 Perspectives

The work presented in this thesis illustrates the importance of BPE as a general and versatile method for the asymmetric modification of diverse materials, ranging from 2D conducting materials (graphene, MXene) to semiconducting materials (TiO_2). The discussed proof-of-concept studies provide convincing evidence of the power of BPE, and also opens various perspective for further exploration.

5.2.1 Perspective for the precise modification of microscale 2D objects

This thesis has demonstrated that at the macro scale and in the context of BPE, 2D materials can be precisely and selectively modified. However, at the micro scale, achieving the same level of precise control over deposition still remains an open challenge. A critical precondition for the successful site-selective modification with BPE is the immobilization of the target object, since uncontrolled rotation or drift strongly influences spatial selectivity.

For microscale 2D materials, two possible strategies can be employed. The first approach is the use of an ultrathin 2D reaction layer instead of suspending the particles in bulk electrolyte, where they are prone to random rotation and motion. Specifically, a thin electrolyte layer can be spread across a flat and hydrophilic insulating substrate, such as glass or oxidized silicon. Compared with bubble-supported thin films, substrate-supported water films exhibit much greater mechanical stability and reproducibility. In this configuration, 2D materials deposited or dispersed in the thin film remain in a quasi-2D environment, physically restricted from uncontrolled displacement while still fully exposed to the electric field and ionic species. The reduced thickness of the electrolyte not only minimizes convective phenomena, but also provides a more uniform electric field across the object, which is highly advantageous for achieving precise, site-selective modification with 2D microparticles.

The second approach is based on immobilizing the 2D sheets on flexible supporting substrates, similar to the strategy presented in Section 2.3, where monolayer graphene was stabilized on a flat agarose gel surface. For microscale systems, a similar procedure could be applied: dilute suspensions of 2D materials can be dispersed on the surface of solidified agarose gel and stabilized in a high-humidity environment. This treatment generates a soft contact between the sheets and the gel surface. After modification, the objects could be gently released simply by rehydrating the agarose block to minimize damaging of the 2D structures. Such immobilization strategies hold promise for extending BPE-based modification to various other 2D materials.

Besides developing new immobilization methods, future work can also focus on tailoring the geometry of the target object. With the advancement of photolithography and micro/nano-printing technologies, highly precise patterned materials with well-defined geometry can be fabricated now. BPE can be applied to these patterned materials to achieve nanoscale or microscale spatial modification, which enables localized deposition and functionalization at predefined areas. This approach could allow the creation of multifunctional systems in which different areas perform distinct catalytic, optical, or sensing functions. Therefore, the integration of patterned materials with BPE holds great potential for the fabrication of on-chip electrochemical devices and microreactor arrays.

In preliminary experiments, we have already demonstrated that asymmetric modification can be achieved on patterned graphene sheets supported on silicon substrates (Figure 5-1). Future work will focus on understanding how the pattern geometry affects local polarization and physicochemical properties of such patterned systems.

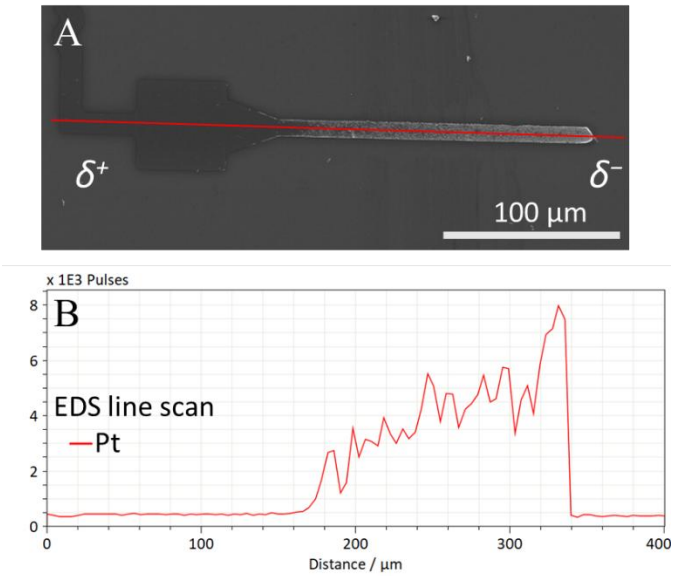

Figure 5-1 (A) SEM image and (B) EDS line scan of a Pt modified patterned graphene sheet. An electric field of 30 V/cm is applied for 30 s.

5.2.2 Perspective for the synthesis of multifunctional photocatalysts

Another promising direction is the use of light-assisted bipolar electrochemistry for multifunctional modification of semiconductor materials. The current work has focused on single-metal deposition, but future studies could integrate dual cocatalyst systems on a single semiconductor particle. For example, simultaneously depositing RuO_2 as a hole sink on one side and Pt as an electron sink on the other would establish a synergistic configuration. In such a system, photogenerated electrons and holes would be guided to spatially separated areas to carry out the respective redox processes. This dual-cocatalyst design could further optimize charge separation efficiency and photocatalytic performance. It also offers new opportunities to synthesize highly efficient photocatalysts for energy-related fields like solar fuel generation or CO_2 reduction.

In summary, future efforts should focus on (i) extending precise site-selective BPE modification to microscale 2D materials through innovative immobilization strategies, and (ii) broadening the scope of light-assisted BPE to achieve multifunctional cocatalyst deposition of semiconductors. These perspectives may provide promising routes for the application of BPE-modified multifunctional materials, not only in areas such as energy conversion and environmental remediation, but also for example to generate particles with chiro-optical properties.

Publications

[1] R. Gao, M. Beladi-Mousavi, G. Salinas, P. Garrigue, L. Zhang, A. Kuhn, Spatial Precision Tailoring the Catalytic Activity of Graphene Monolayers for Designing Janus Swimmers, Nano Letters 2023, 23, 17, 8180–8185.

[2] R. Gao, M. Beladi-Mousavi, G. Salinas, L. Zhang, A. Kuhn, Synthesis of Multi-Functional Graphene Monolayers via Bipolar Electrochemistry, ChemPhysChem, 2024, 25, 16, e202400257.

[3] R. Gao, S. Bichon, S. Gounel, G. Salinas, L. Zhang, N. Mano, A. Kuhn, Magnetic field-enhanced transformation of biochemical energy into motion of enzyme-modified graphene monolayers, Chemical Communications., 2025,61, 14410-14413.

[4] L. R Arias-Aranda, R. Gao, L. Zhang, A. Kuhn, N. Sojic, L. Bouffier, G. Salinas, Magnetoelectrochemical Rotation of Light Emitting Graphene Monolayers, Small, 2025, DOI: 10.1002/smll.202500778.

[5] R. Gao, M. Beladi-Mousavi, F. Gröbmeyer, L. Zhang, A. Kuhn, Bipolar Electrodeposition on TiO_2 Microspheres for Environmental Applications, in preparation.

References

[1] A. J. Hale, E. Thorpe, Ed. *The Applications of Electrolysis in Chemical Industry*, 1 ed. Longmans, Green and Co., 1918.

[2] J. R. Backhurst, J. M. Coulson, F. Goodridge, R. E. Plimley, and M. Fleischmann, "A Preliminary Investigation of Fluidized Bed Electrodes," *Journal of The Electrochemical Society,* vol. 116, no. 11, pp. 1600-1607, 1969.

[3] F. Goodridge, C. J. H. King, and A. R. Wright, "The behaviour of bipolar packed-bed electrodes," *Electrochimica Acta,* vol. 22, no. 4, pp. 347-352, 1977.

[4] F. Goodridge, C. J. H. King, and A. R. Wright, "Performance studies on a bipolar fluidised bed electrode," *Electrochimica Acta,* vol. 22, no. 10, pp. 1087-1091, 1977.

[5] M. Fleischmann, J. Ghoroghchian, and S. Pons, "Electrochemical behavior of dispersions of spherical ultramicroelectrodes. 1. Theoretical considerations," *The Journal of Physical Chemistry,* vol. 89, no. 25, pp. 5530-5536, 1985.

[6] N. Karimian, P. Hashemi, A. Afkhami, and H. Bagheri, "The principles of bipolar electrochemistry and its electroanalysis applications," *Current Opinion in Electrochemistry,* vol. 17, pp. 30-37, 2019.

[7] S. E. Fosdick, K. N. Knust, K. Scida, and R. M. Crooks, "Bipolar electrochemistry," *Angewandte Chemie International Edition,* vol. 52, no. 40, pp. 10438-10456, 2013.

[8] L. Koefoed, S. U. Pedersen, and K. Daasbjerg, "Bipolar electrochemistry—A wireless approach for electrode reactions," *Current Opinion in Electrochemistry,* vol. 2, no. 1, pp. 13-17, 2017.

[9] L. Bouffier, D. Zigah, N. Sojic, and A. Kuhn, "Recent Advances in Bipolar Electrochemistry," in *Electroanalytical Chemistry*, 2017, pp. 1-92.

[10] G. Loget and A. Kuhn, "Shaping and exploring the micro- and nanoworld using bipolar electrochemistry," *Analytical and Bioanalytical Chemistry,* vol. 400, no. 6, pp. 1691-1704, 2011.

[11] N. Shida, Y. Zhou, and S. Inagi, "Bipolar Electrochemistry: A Powerful Tool for Electrifying Functional Material Synthesis," *Accounts of Chemical Research,* vol. 52, no. 9, pp. 2598-2608, 2019.

[12] G. Salinas, S. Arnaboldi, L. Bouffier, and A. Kuhn, "Recent Advances in Bipolar Electrochemistry with Conducting Polymers," *ChemElectroChem,* vol. 9, no. 1, p. e202101234, 2021.

[13] K. L. Rahn and R. K. Anand, "Recent Advancements in Bipolar Electrochemical Methods of Analysis," *Analytical Chemistry,* vol. 93, no. 1, pp. 103-123, 2021.

[14] G. Loget, D. Zigah, L. Bouffier, N. Sojic, and A. Kuhn, "Bipolar electrochemistry: from materials science to motion and beyond," *Accounts of Chemical Research,* vol. 46, no. 11, pp. 2513-2523, 2013.

[15] A. J. Bard and L. R. Faulkner, *Electrochemical methods. Fundamentals and applications*, Second Edition ed. John Wiley & Sons, Inc, 2001, pp. 24-28.

[16] H. H. Girault, *Analytical and Physical Electrochemistry*. 2004.

[17] L. Bouffier, D. Zigah, N. Sojic, and A. Kuhn, "Bipolar Electrochemistry," in *Encyclopedia of Electrochemistry*, 2021, pp. 1-53.

[18] G. Loget, J. Roche, E. Gianessi, L. Bouffier, and A. Kuhn, "Indirect bipolar electrodeposition," *Journal of the American Chemical Society,* vol. 134, no. 49, pp. 20033-20036, 2012.

[19] D. Aymé-Perrot and H. H. Girault, "Bipolar plates in water electrolysis stacks: understanding basics and electrochemical aspects impacting the energy efficiency during operation," *Electrochimica Acta,* p. 148305, 2026.

[20] F. Mavre, K.-F. Chow, E. Sheridan, B.-Y. Chang, J. A. Crooks, and R. M. Crooks, "A Theoretical and Experimental Framework for Understanding Electrogenerated Chemiluminescence (ECL) Emission at Bipolar Electrodes," *Analytical Chemistry,* vol. 81, pp. 6218–6225, 2009.

[21] H. Xing, J. Li, and E. Wang, "Recent Advances in Bipolar Electrochemiluminescence for Analytical Application," *Current Analytical Chemistry,* vol. 18, no. 6, pp. 601 - 611, 2022.

[22] J. P. Guerrette, S. M. Oja, and B. Zhang, "Coupled electrochemical reactions at bipolar microelectrodes and nanoelectrodes," *Analytical Chemistry,* vol. 84, no. 3, pp. 1609-1616, 2012.

[23] J. T. Cox, J. P. Guerrette, and B. Zhang, "Steady-state voltammetry of a microelectrode in a closed bipolar cell," *Analytical Chemistry,* vol. 84, no. 20, pp. 8797-8804, 2012.

[24] G. Loget, J. Roche, and A. Kuhn, "True bulk synthesis of janus objects by bipolar electrochemistry," *Advanced Materials,* vol. 24, no. 37, pp. 5111-5116, 2012.

[25] M. Ongaro, J. Roche, A. Kuhn, and P. Ugo, "Asymmetric Modification of TiO_2 Nanofibers with Gold by Electric‐Field‐Assisted Photochemistry," *ChemElectroChem,* vol. 1, no. 12, pp. 2048-2051, 2014.

[26] K. Missaoui, G. Wantz, T. Toupance, S. Chambon, and A. Kuhn, "Targeted design of organic Janus particles for improved photocatalytic hydrogen evolution," *Chemical Science,* vol. 16, no. 24, pp. 10691-10700, 2025.

[27] A. A. Melvin, E. Lebraud, P. Garrigue, and A. Kuhn, "Light and electric field induced unusual large-scale charge separation in hybrid semiconductor objects," *Physical Chemistry Chemical Physics,* vol. 22, no. 39, pp. 22180-22184, 2020.

[28] S. Tiewcharoen, C. Warakulwit, V. Lapeyre, P. Garrigue, L. Fourier, C. Elissalde, S. Buffiere, P. Legros, M. Gayot, J. Limtrakul, and A. Kuhn, "Anisotropic Metal Deposition on TiO_2 Particles by Electric-Field-Induced Charge Separation," *Angewandte Chemie International Edition,* vol. 56, no. 38, pp. 11431-11435, 2017.

[29] A. Arora, J. C. Eijkel, W. E. Morf, and A. Manz, "A wireless electrochemiluminescence detector applied to direct and indirect detection for electrophoresis on a microfabricated glass device," *Analytical Chemistry,* vol. 73, no. 14, pp. 3282-3288, 2001.

[30] G. Loget and A. Kuhn, "Bulk synthesis of Janus objects and asymmetric patchy particles," *Journal of Materials Chemistry,* vol. 22, no. 31, pp. 15429-16146, 2012.

[31] A. Walther and A. H. Muller, "Janus particles: synthesis, self-assembly, physical properties, and applications," *Chemical Reviews,* vol. 113, no. 7, pp. 5194-5261, 2013.

[32] J. Zhang, B. A. Grzybowski, and S. Granick, "Janus Particle Synthesis, Assembly, and Application," *Langmuir,* vol. 33, no. 28, pp. 6964-6977, 2017.

[33] J.-C. Bradley and Z. Ma, "Contactless Electrodeposition of Palladium Catalysts," *Angewandte Chemie International Edition,* vol. 38, no. 11, pp. 1663-1666, 1999.

[34] G. Loget, V. Lapeyre, P. Garrigue, C. Warakulwit, J. Limtrakul, M.-H. Delville, and A. Kuhn, "Versatile Procedure for Synthesis of Janus-Type Carbon Tubes," *Chemistry of Materials,* vol. 23, no. 10, pp. 2595-2599, 2011.

[35] O. Phuakkong, M. Sentic, H. Li, C. Warakulwit, J. Limtrakul, N. Sojic, A. Kuhn, V. Ravaine, and D. Zigah, "Wireless Synthesis and Activation of Electrochemiluminescent

Thermoresponsive Janus Objects Using Bipolar Electrochemistry," *Langmuir,* vol. 32, no. 49, pp. 12995-13002, 2016.
[36] Z. Fattah, P. Garrigue, B. Goudeau, V. Lapeyre, A. Kuhn, and L. Bouffier, "Capillary electrophoresis as a production tool for asymmetric microhybrids," *Electrophoresis,* vol. 34, no. 14, pp. 1985-1990, 2013.
[37] C. Warakulwit, T. Nguyen, J. Majimel, M. H. Delville, V. Lapeyre, P. Garrigue, V. Ravaine, J. Limtrakul, and A. Kuhn, "Dissymmetric carbon nanotubes by bipolar electrochemistry," *Nano letters,* vol. 8, no. 2, pp. 500-504, 2008.
[38] P. Chassagne, P. Garrigue, and A. Kuhn, "Bulk Electrosynthesis of Patchy Particles with Highly Controlled Asymmetric Features," *Advanced Materials,* vol. 36, no. 6, p. e2307539, 2024.
[39] J. Roche, G. Loget, D. Zigah, Z. Fattah, B. Goudeau, S. Arbault, L. Bouffier, and A. Kuhn, "Straight-forward synthesis of ringed particles," *Chemical Science,* vol. 5, no. 5, pp. 1961-1966, 2014.
[40] Y. Fu, K. Chen, B. Xie, X. Zhang, L. Zhang, A. Kuhn, and W. Yang, "Design of Janus Particles by Bipolar Electrochemistry at the Water–Organic Interface," *Chemistry of Materials,* vol. 36, no. 14, pp. 7079-7088, 2024.
[41] B. Xie, Y. Fu, Z. Wang, Y. Li, Q. Zhu, L. Zhang, W. Yang, and A. Kuhn, "One-Pot Single-Step Approach for the Controlled Synthesis of Multifunctional Microparticles," *Advanced Materials,* p. e2506777, 2025.
[42] H. Sopha, J. Rodriguez‐Pereira, V. Cicmancova, and J. M. Macak, "Wireless Anodization of Ti in Closed Bipolar Cells," *ChemElectroChem,* vol. 8, no. 20, pp. 3827-3831, 2021.
[43] M. Sepúlveda, K. Baishya, J. Rodriguez-Pereira, V. Cicmancova, L. Hromadko, and J. M. Macak, "Wireless electrochemical fabrication of tungsten oxide nanoporous layers in closed bipolar cells," *Electrochemistry Communications,* vol. 176, p. 107963, 2025.
[44] M. M. Richter, "Electrochemiluminescence," in *Optical Biosensors*, 2008, pp. 317-384.
[45] J. S. Borchers, M. J. Clark, S. B. Van Scoy, and R. K. Anand, "Array of Interdigitated Bipolar Electrodes for Selective Capture and Analysis of Melanoma Cells," *ChemElectroChem,* vol. 11, no. 4, p. e202300345, 2024.
[46] Z. Dong, Y. Chen, S. Xia, A. M. A. Alboull, A. Hussain, Y. Tian, and G. Xu, "Single-Electrode Flow Cell for Electrochemiluminescent Flow Analysis," *Analytical Chemistry,* vol. 96, no. 48, pp. 18927-18931, 2024.
[47] R. Zou, L. R. Arias-Aranda, G. Salinas, A. Kuhn, L. Bouffier, and N. Sojic, "Bipolar electrochemiluminescence: from fundamentals to emerging trends," *Chemical Communications,* vol. 61, no. 64, pp. 11896-11906, 2025.
[48] B. Wang, M. Akteruzzaman, S. Yu, M. Mehrgardi, C. Shannon, C. Jin, and S. Fan, "Fast response cathodic electrochemiluminescence sensor based on closed bipolar electrode for point-of-care blood glucose testing," *Talanta,* vol. 293, p. 128104, 2025.
[49] S. M. R. Mortazavi, M. Hosseini, G. Xu, H. Naderi-Manesh, and M. R. Ganjali, "Highly specific detection of ROR1 cancer biomarker with bipolar electrochemiluminescence," *Mikrochim Acta,* vol. 191, no. 12, p. 734, 2024.
[50] Y.-L. Wang, L.-Z. Zhao, C. Chen, S.-W. Ren, J.-T. Cao, and Y.-M. Liu, "A bipolar-electrochemiluminescence split-type immunoassay based on a cathodic amplification strategy," *Journal of Electroanalytical Chemistry,* vol. 930, p. 117153, 2023.

[51] Y. Xiao, L. Xu, and L. W. Qi, "Electrochemiluminescence bipolar electrode array for the multiplexed detection of glucose, lactate and choline based on a versatile enzymatic approach," *Talanta,* vol. 165, pp. 577-583, 2017.

[52] J. S. Borchers, C. R. Campbell, S. B. Van Scoy, M. J. Clark, and R. K. Anand, "Redox Cycling at an Array of Interdigitated Bipolar Electrodes for Enhanced Sensitivity in Biosensing**," *ChemElectroChem,* vol. 8, no. 18, pp. 3482-3491, 2021.

[53] S. E. Fosdick and R. M. Crooks, "Bipolar electrodes for rapid screening of electrocatalysts," *Journal of the American Chemical Society,* vol. 134, no. 2, pp. 863-866, 2012.

[54] A. J. Hsueh, N. A. A. Mutalib, Y. Shirato, and H. Suzuki, "Bipolar Electrode Arrays for Chemical Imaging and Multiplexed Sensing," *ACS Omega,* vol. 7, no. 23, pp. 20298-20305, 2022.

[55] G. Salinas, S. M. Beladi-Mousavi, L. Gerasimova, L. Bouffier, and A. Kuhn, "Wireless Imaging of Transient Redox Activity Based on Bipolar Light-Emitting Electrode Arrays," *Analytical Chemistry,* vol. 94, no. 41, pp. 14317-14321, 2022.

[56] Y. Ning, Y. Du, Y. Dong, and G. Jie, "Color-Potential-Resolved Nanoreactor Luminophore for Bipolar Electrode Electrochemiluminescence Biosensing and Imaging Assay of Dual DR Genes," *Analytical Chemistry,* vol. 97, no. 23, pp. 12389-12399, 2025.

[57] H. Li, Q. Cai, Z. Li, G. Jie, and H. Zhou, "A spatial-potential resolved bipolar electrode electrochemiluminescence biosensor based on polarity conversion for dual-mode detection of miRNA-122 and CEA," *Biosensors and Bioelectronics,* vol. 255, p. 116258, 2024.

[58] H. Li, Q. Cai, Y. Wang, G. Jie, and H. Zhou, "Spatial-Potential-Color-Resolved Bipolar Electrode Electrochemiluminescence Biosensor Using a $CuMoO_x$ Electrocatalyst for the Simultaneous Detection and Imaging of Tetracycline and Lincomycin," *Analytical Chemistry,* vol. 96, no. 18, pp. 7073-7081, 2024.

[59] X. Zhang, J. Li, X. Jia, D. Li, and E. Wang, "Full-featured electrochemiluminescence sensing platform based on the multichannel closed bipolar system," *Analytical Chemistry,* vol. 86, no. 11, pp. 5595-5599, 2014.

[60] X. Zhang, C. Chen, J. Yin, Y. Han, J. Li, and E. Wang, "Portable and visual electrochemical sensor based on the bipolar light emitting diode electrode," *Analytical Chemistry,* vol. 87, no. 9, pp. 4612-4616, 2015.

[61] G. Li and R. Hao, "Focused ion beam fabrication of high-resolution electrochemical-electroluminescence coupling bipolar nanoelectrode array sensors," *Sensors and Actuators Reports,* vol. 8, p. 100220, 2024.

[62] G. Tisserant, Z. Fattah, C. Ayela, J. Roche, B. Plano, D. Zigah, B. Goudeau, A. Kuhn, and L. Bouffier, "Generation of metal composition gradients by means of bipolar electrodeposition," *Electrochimica Acta,* vol. 179, pp. 276-281, 2015.

[63] S. Ramakrishnan and C. Shannon, "Display of solid-state materials using bipolar electrochemistry," *Langmuir,* vol. 26, no. 7, pp. 4602-4606, 2010.

[64] G. Loget, S. So, R. Hahn, and P. Schmuki, "Bipolar anodization enables the fabrication of controlled arrays of TiO_2 nanotube gradients," *Journal of materials Chemistry A,* vol. 2, no. 42, pp. 17740-17745, 2014.

[65] R. Shrivastava, R. Maurya, and P. K. Katiyar, "A review on bipolar electrochemistry for corrosion testing: highlighting mechanisms, applications, and future prospects," *Journal of Solid State Electrochemistry,* vol. 29, no. 2, pp. 471-511, 2024.

[66] Y. Zhou, S. Mahmood, and D. L. Engelberg, "A novel high throughput electrochemistry corrosion test method: Bipolar electrochemistry," *Current Opinion in Electrochemistry,* vol. 39, p. 101263, 2023.

[67] Y. Zhou and D. L. Engelberg, "Development of a two‐dimensional bipolar electrochemistry technique for high throughput corrosion screening," *Materials Genome Engineering Advances,* vol. 2, no. 3, p. e57, 2024.

[68] L. Fuentes-Rodríguez, E. Pujades, J. Fraxedas, A. Crespi, K. Xu, L. Abad, and N. Casañ-Pastor, "Oscillatory patterns in redox gradient materials through wireless bipolar electrochemistry. The dynamic wave-like case of copper bipolar oxidation," *Materials Chemistry Frontiers,* vol. 6, no. 16, pp. 2284-2296, 2022.

[69] Y. Zhou and D. L. Engelberg, "On the Application of Bipolar Electrochemistry to Characterise the Localised Corrosion Behaviour of Type 420 Ferritic Stainless Steel," *Metals,* vol. 10, no. 6, p. 794, 2020.

[70] S. Inagi, "Fabrication of gradient polymer surfaces using bipolar electrochemistry," *Polymer Journal,* vol. 48, no. 1, pp. 39-44, 2015.

[71] H. Wang and M. Pumera, "Fabrication of Micro/Nanoscale Motors," *Chemical Reviews,* vol. 115, no. 16, pp. 8704-8735, 2015.

[72] J. Hu, S. Zhou, Y. Sun, X. Fang, and L. Wu, "Fabrication, properties and applications of Janus particles," *Chemical Society Reviews,* vol. 41, no. 11, pp. 4356-4378, 2012.

[73] Y. Wang, R. M. Hernandez, D. J. Bartlett, Jr., J. M. Bingham, T. R. Kline, A. Sen, and T. E. Mallouk, "Bipolar electrochemical mechanism for the propulsion of catalytic nanomotors in hydrogen peroxide solutions," *Langmuir,* vol. 22, no. 25, pp. 10451-10456, 2006.

[74] G. Loget and A. Kuhn, "Electrochemical Motors," in *Discovering the Future of Molecular Sciences*, 2014, pp. 349-378.

[75] Z. Fattah, G. Loget, V. Lapeyre, P. Garrigue, C. Warakulwit, J. Limtrakul, L. Bouffier, and A. Kuhn, "Straightforward single-step generation of microswimmers by bipolar electrochemistry," *Electrochimica Acta,* vol. 56, no. 28, pp. 10562-10566, 2011.

[76] Z. A. Fattah, L. Bouffier, and A. Kuhn, "Indirect bipolar electrodeposition of polymers for the controlled design of zinc microswimmers," *Applied Materials Today,* vol. 9, pp. 259-265, 2017.

[77] G. Salinas, A. L. Dauphin, S. Voci, L. Bouffier, N. Sojic, and A. Kuhn, "Asymmetry controlled dynamic behavior of autonomous chemiluminescent Janus microswimmers," *Chemical Science,* vol. 11, no. 28, pp. 7438-7443, 2020.

[78] G. Loget and A. Kuhn, "Propulsion of microobjects by dynamic bipolar self-regeneration," *Journal of the American Chemical Society,* vol. 132, no. 45, pp. 15918-15919, 2010.

[79] J.-Z. Jiang, M.-H. Guo, F.-Z. Yao, J. Li, and J.-J. Sun, "Propulsion of copper microswimmers in folded fluid channels by bipolar electrochemistry," *RSC Advances,* vol. 7, no. 11, pp. 6297-6302, 2017.

[80] G. Loget and A. Kuhn, "Electric field-induced chemical locomotion of conducting objects," *Nature Communications,* vol. 2, p. 535, 2011.

[81] G. Loget and A. Kuhn, "Bipolar electrochemistry for cargo-lifting in fluid channels," *Lab on a Chip,* vol. 12, no. 11, pp. 1967-1971, 2012.

[82] M. Sentic, S. Arbault, B. Goudeau, D. Manojlovic, A. Kuhn, L. Bouffier, and N. Sojic, "Electrochemiluminescent swimmers for dynamic enzymatic sensing," *Chemical Communications,* vol. 50, no. 71, pp. 10202-10205, 2014.

[83] L. Bouffier, D. Zigah, C. Adam, M. Sentic, Z. Fattah, D. Manojlovic, A. Kuhn, and N. Sojic, "Lighting Up Redox Propulsion with Luminol Electrogenerated Chemiluminescence," *ChemElectroChem,* vol. 1, no. 1, pp. 95-98, 2013.

[84] A. L. Dauphin, A. Akchach, S. Voci, A. Kuhn, G. Xu, L. Bouffier, and N. Sojic, "Tracking Magnetic Rotating Objects by Bipolar Electrochemiluminescence," *The Journal of Physical Chemistry Letters,* vol. 10, no. 18, pp. 5318-5324, 2019.

[85] J. Roche, S. Carrara, J. Sanchez, J. Lannelongue, G. Loget, L. Bouffier, P. Fischer, and A. Kuhn, "Wireless powering of e-swimmers," *Scientific Reports,* vol. 4, p. 6705, 2014.

[86] M. Sentic, G. Loget, D. Manojlovic, A. Kuhn, and N. Sojic, "Light-emitting electrochemical "swimmers"," *Angewandte Chemie International Edition,* vol. 51, no. 45, pp. 11284-11288, 2012.

[87] K. Tieriekhov, N. Sojic, L. Bouffier, G. Salinas, and A. Kuhn, "Wireless Magnetoelectrochemical Induction of Rotational Motion," *Advanced Science,* vol. 11, no. 9, p. e2306635, 2024.

[88] S. Arnaboldi, "Wireless electrochemical actuation of soft materials towards chiral stimuli," *Chemical Communications,* vol. 59, no. 15, pp. 2072-2080, 2023.

[89] G. Salinas, F. Malacarne, G. Bonetti, R. Cirilli, T. Benincori, S. Arnaboldi, and A. Kuhn, "Wireless electromechanical enantio-responsive valves," *Chirality,* vol. 35, no. 2, pp. 110-117, 2023.

[90] L. Zhang, B. Gupta, B. Goudeau, N. Mano, and A. Kuhn, "Wireless Electromechanical Readout of Chemical Information," *Journal of the American Chemical Society,* vol. 140, no. 45, pp. 15501-15506, 2018.

[91] H.-P. Komsa and A. V. Krasheninnikov, "Physics and theory of defects in 2D materials: the role of reduced dimensionality," in *Defects in Two-Dimensional Materials*, 2022, pp. 7-41.

[92] F. Xia, H. Wang, D. Xiao, M. Dubey, and A. Ramasubramaniam, "Two-dimensional material nanophotonics," *Nature Photonics,* vol. 8, no. 12, pp. 899-907, 2014.

[93] A. Jayakumar, S. Mathew, S. Radoor, J. T. Kim, J.-W. Rhim, and S. Siengchin, "Recent advances in two-dimensional nanomaterials: properties, antimicrobial, and drug delivery application of nanocomposites," *Materials Today Chemistry,* vol. 30, 2023.

[94] A. S. Faisal Mahamude, K. Farhana, and W. S. Wan Harun, "Progress in graphene–sulfur–lithium-ion batteries for electric vehicles: a forward-looking evaluation," *Graphene and 2D Materials,* 2025.

[95] Y. Yang, J. Liu, D. Wu, J. Ding, and B. Xiong, "Two-dimensional pyrite supported transition metal for highly-efficient electrochemical CO_2 reduction: A theoretical screening study," *Chemical Engineering Journal,* vol. 424, 2021.

[96] X. Zhang, L. Hou, A. Ciesielski, and P. Samorì, "2D Materials Beyond Graphene for High‐Performance Energy Storage Applications," *Advanced Energy Materials,* vol. 6, no. 23, 2016.

[97] S. Radhakrishnan, M. Mathew, and C. S. Rout, "Microfluidic sensors based on two-dimensional materials for chemical and biological assessments," *Materials Advances,* vol. 3, no. 4, pp. 1874-1904, 2022.

[98] D. Tyagi, H. Wang, W. Huang, L. Hu, Y. Tang, Z. Guo, Z. Ouyang, and H. Zhang, "Recent advances in two-dimensional-material-based sensing technology toward health and environmental monitoring applications," *Nanoscale,* vol. 12, no. 6, pp. 3535-3559, 2020.

[99] T. Dutta, N. Yadav, Y. Wu, G. J. Cheng, X. Liang, S. Ramakrishna, A. Sbai, R. Gupta, A. Mondal, Z. Hongyu, and A. Yadav, "Electronic properties of 2D materials and their junctions," *Nano Materials Science,* vol. 6, no. 1, pp. 1-23, 2024.

[100] K. S. Novoselov, A. K. Geim, S. V. Morozov, D. Jiang, Y. Zhang, S. V. Dubonos, I. V. Grigorieva, and A. A. Firsov, "Electric field effect in atomically thin carbon films," *Science,* vol. 306, no. 5696, pp. 666-669, 2004.

[101] G. Loget, G. Larcade, V. Lapeyre, P. Garrigue, C. Warakulwit, J. Limtrakul, M. H. Delville, V. Ravaine, and A. Kuhn, "Single point electrodeposition of nickel for the dissymmetric decoration of carbon tubes," *Electrochimica Acta,* vol. 55, no. 27, pp. 8116-8120, 2010.

[102] M. Ketkaew, S. Assavapanumat, S. Klinyod, A. Kuhn, and C. Wattanakit, "Bifunctional Pt/Au Janus electrocatalysts for simultaneous oxidation/reduction of furfural with bipolar electrochemistry," *Chemical Communications,* vol. 58, no. 27, pp. 4312-4315, 2022.

[103] L. Zuccaro, A. Kuhn, M. Konuma, H. K. Yu, K. Kern, and K. Balasubramanian, "Selective Functionalization of Graphene Peripheries by using Bipolar Electrochemistry," *ChemElectroChem,* vol. 3, no. 3, pp. 372-377, 2015.

[104] S. M. Beladi-Mousavi, G. Salinas, N. Antonatos, V. Mazanek, P. Garrigue, Z. Sofer, and A. Kuhn, "Fine-tuning the functionality of reduced graphene oxide via bipolar electrochemistry in freestanding 2D reaction layers," *Carbon,* vol. 191, pp. 439-447, 2022.

[105] S. M. Beladi-Mousavi, G. Salinas, L. Bouffier, N. Sojic, and A. Kuhn, "Wireless electrochemical light emission in ultrathin 2D nanoconfinements," *Chemical Science,* vol. 13, no. 48, pp. 14277-14284, 2022.

[106] P. Kankla, P. Luksirikul, P. Garrigue, B. Goudeau, L. Bouffier, and A. Kuhn, "Site‐Selective Bipolar Electrodeposition of Gold Clusters on Graphene Oxide Microsheets at a 3D Air|Liquid Interface," *Advanced Materials Interfaces,* vol. 9, no. 21, p. 2200304, 2022.

[107] S. Sanchez, L. Soler, and J. Katuri, "Chemically powered micro- and nanomotors," *Angewandte Chemie International Edition,* vol. 54, no. 5, pp. 1414-1444, 2015.

[108] W. Gao, A. Pei, R. Dong, and J. Wang, "Catalytic iridium-based Janus micromotors powered by ultralow levels of chemical fuels," *Journal of the American Chemical Society,* vol. 136, no. 6, pp. 2276-2279, 2014.

[109] S. Sengupta, K. K. Dey, H. S. Muddana, T. Tabouillot, M. E. Ibele, P. J. Butler, and A. Sen, "Enzyme molecules as nanomotors," *Journal of the American Chemical Society,* vol. 135, no. 4, pp. 1406-1414, 2013.

[110] G. Salinas, K. Tieriekhov, P. Garrigue, N. Sojic, L. Bouffier, and A. Kuhn, "Lorentz Force-Driven Autonomous Janus Swimmers," *Journal of the American Chemical Society,* vol. 143, no. 32, pp. 12708-12714, 2021.

[111] D. Xu, Y. Wang, C. Liang, Y. You, S. Sanchez, and X. Ma, "Self-Propelled Micro/Nanomotors for On-Demand Biomedical Cargo Transportation," *Small,* vol. 16, no. 27, p. e1902464, 2020.

[112] M. Fernández‐Medina, M. A. Ramos‐Docampo, O. Hovorka, V. Salgueiriño, and B. Städler, "Recent Advances in Nano‐ and Micromotors," *Advanced Functional Materials,* vol. 30, no. 12, p. 1908283, 2020.

[113] R. Dong, Y. Hu, Y. Wu, W. Gao, B. Ren, Q. Wang, and Y. Cai, "Visible-Light-Driven BiOI-Based Janus Micromotor in Pure Water," *Journal of the American Chemical Society,* vol. 139, no. 5, pp. 1722-1725, 2017.

[114] J. Li, P. S. Kollipara, Y. Liu, K. Yao, Y. Liu, and Y. Zheng, "Opto-Thermocapillary Nanomotors on Solid Substrates," *ACS Nano,* vol. 16, no. 6, pp. 8820-8826, 2022.

[115] Z. Wu, T. Si, W. Gao, X. Lin, J. Wang, and Q. He, "Self‐Propulsion: Superfast Near‐Infrared Light‐Driven Polymer Multilayer Rockets," *Small,* vol. 12, no. 5, pp. 550-550, 2016.

[116] W. Wang, W. Duan, S. Ahmed, T. E. Mallouk, and A. Sen, "Small power: Autonomous nano- and micromotors propelled by self-generated gradients," *Nano Today,* vol. 8, no. 5, pp. 531-554, 2013.

[117] N. Shida and S. Inagi, "Bipolar electrochemistry in synergy with electrophoresis: electric field-driven electrosynthesis of anisotropic polymeric materials," *Chemical Communications,* vol. 56, no. 92, pp. 14327-14336, 2020.

[118] X. Zhang, Q. Fu, H. Duan, J. Song, and H. Yang, "Janus Nanoparticles: From Fabrication to (Bio)Applications," *ACS Nano,* vol. 15, no. 4, pp. 6147-6191, 2021.

[119] X. Ju, C. Chen, C. M. Oral, S. Sevim, R. Golestanian, M. Sun, N. Bouzari, X. Lin, M. Urso, J. S. Nam, Y. Cho, X. Peng, F. C. Landers, S. Yang, A. Adibi, N. Taz, R. Wittkowski, D. Ahmed, W. Wang, V. Magdanz, M. Medina-Sanchez, M. Guix, N. Bari, B. Behkam, R. Kapral, Y. Huang, J. Tang, B. Wang, K. Morozov, A. Leshansky, S. A. Abbasi, H. Choi, S. Ghosh, B. Borges Fernandes, G. Battaglia, P. Fischer, A. Ghosh, B. Jurado Sanchez, A. Escarpa, Q. Martinet, J. Palacci, E. Lauga, J. Moran, M. A. Ramos-Docampo, B. Stadler, R. S. Herrera Restrepo, G. Yossifon, J. D. Nicholas, J. Ignes-Mullol, J. Puigmarti-Luis, Y. Liu, L. D. Zarzar, C. W. t. Shields, L. Li, S. Li, X. Ma, D. H. Gracias, O. Velev, S. Sanchez, M. J. Esplandiu, J. Simmchen, A. Lobosco, S. Misra, Z. Wu, J. Li, A. Kuhn, A. Nourhani, T. Maric, Z. Xiong, A. Aghakhani, Y. Mei, Y. Tu, F. Peng, E. Diller, M. S. Sakar, A. Sen, J. Law, Y. Sun, A. Pena-Francesch, K. Villa, H. Li, D. E. Fan, K. Liang, T. J. Huang, X. Z. Chen, S. Tang, X. Zhang, J. Cui, H. Wang, W. Gao, V. Kumar Bandari, O. G. Schmidt, X. Wu, J. Guan, M. Sitti, B. J. Nelson, S. Pane, L. Zhang, H. Shahsavan, Q. He, I. D. Kim, J. Wang and M. Pumera, "Technology Roadmap of Micro/Nanorobots," *ACS Nano,* vol. 19, no. 27, pp. 24174-24334, 2025.

[120] W. Gao, K. M. Manesh, J. Hua, S. Sattayasamitsathit, and J. Wang, "Hybrid nanomotor: a catalytically/magnetically powered adaptive nanowire swimmer," *Small,* vol. 7, no. 14, pp. 2047-51, 2011.

[121] M. Bayraktaroglu, B. Jurado-Sanchez, and M. Uygun, "Peroxidase driven micromotors for dynamic bioremediation," *Journal of Hazardous Materials,* vol. 418, p. 126268, 2021.

[122] P. Sharan, Z. Xiao, V. Mancuso, W. E. Uspal, and J. Simmchen, "Upstream Rheotaxis of Catalytic Janus Spheres," *ACS Nano,* vol. 16, no. 3, pp. 4599-4608, 2022.

[123] S. Krause, E. Ploetz, J. Bohlen, P. Schuler, R. Yaadav, F. Selbach, F. Steiner, I. Kaminska, and P. Tinnefeld, "Graphene-on-Glass Preparation and Cleaning Methods Characterized by Single-Molecule DNA Origami Fluorescent Probes and Raman Spectroscopy," *ACS Nano,* vol. 15, no. 4, pp. 6430-6438, 2021.

[124] I. Kaminska, J. Bohlen, R. Yaadav, P. Schuler, M. Raab, T. Schroder, J. Zahringer, K. Zielonka, S. Krause, and P. Tinnefeld, "Graphene Energy Transfer for Single-Molecule Biophysics, Biosensing, and Super-Resolution Microscopy," *Advanced Materials,* vol. 33, no. 24, p. e2101099, 2021.

[125] R. F. Ismagilov, A. Schwartz, N. Bowden, and G. M. Whitesides, "Autonomous Movement and Self-Assembly," *Angewandte Chemie International Edition,* vol. 41, no. 4, pp. 652-654, 2002.

[126] S. Fournier-Bidoz, A. C. Arsenault, I. Manners, and G. A. Ozin, "Synthetic self-propelled nanorotors," *Chemical Communications,* no. 4, pp. 441-443, 2005.
[127] A. A. Solovev, W. Xi, D. H. Gracias, S. M. Harazim, C. Deneke, S. Sanchez, and O. G. Schmidt, "Self-propelled nanotools," *ACS Nano,* vol. 6, no. 2, pp. 1751-1756, 2012.
[128] J. Simmchen, V. Magdanz, S. Sanchez, S. Chokmaviroj, D. Ruiz-Molina, A. Baeza, and O. G. Schmidt, "Effect of surfactants on the performance of tubular and spherical micromotors – a comparative study," *RSC Adv.,* vol. 4, no. 39, pp. 20334-20340, 2014.
[129] H. Yu, Y. Wang, Z. Hou, X. Xia, H. Chen, B. Zou, and Y. Zhang, "Marangoni Effect Enabling Autonomously Miniatured Swimmers: Mechanisms, Design Strategy, and Applications," *Advanced Functional Materials,* vol. 35, no. 27, p. 2424235, 2025.
[130] G. Chakraborty, R. Padmashree, and A. Prasad, "Recent advancement of surface modification techniques of 2-D nanomaterials," *Materials Science and Engineering: B,* vol. 297, p. 116817, 2023.
[131] Z. Najafi Rad, F. Farzad, and L. Razavi, "Surface functionalization of graphene nanosheet with poly (L-histidine) and its application in drug delivery: covalent vs non-covalent approaches," *Science Reports,* vol. 12, no. 1, p. 19046, 2022.
[132] G. V. Bianco, A. Sacchetti, M. Grande, A. D'Orazio, P. Capezzuto, and G. Bruno, "Highly conductive and transparent graphene: Synergy of covalent and non-covalent co-doping," *Applied Surface Science,* vol. 564, p. 150377, 2021.
[133] B. Gwalani, X. Li, A. Nittala, W. Choi, M. Reza-E-Rabby, J. E. Atehortua, A. Bhattacharjee, M. Pole, J. Silverstein, M. Song, and K. Kappagantula, "Unprecedented electrical performance of friction-extruded copper-graphene composites," *Materials & Design,* vol. 237, p. 112555, 2024.
[134] J. A. Baimova and S. A. Shcherbinin, "Metal/Graphene Composites: A Review on the Simulation of Fabrication and Study of Mechanical Properties," *Materials,* vol. 16, no. 1, p. 202, 2022.
[135] V. Georgakilas, J. N. Tiwari, K. C. Kemp, J. A. Perman, A. B. Bourlinos, K. S. Kim, and R. Zboril, "Noncovalent Functionalization of Graphene and Graphene Oxide for Energy Materials, Biosensing, Catalytic, and Biomedical Applications," *Chemical Reviews,* vol. 116, no. 9, pp. 5464-519, 2016.
[136] L. Bouffier, S. Reculusa, V. Ravaine, and A. Kuhn, "Modulation of Wetting Gradients by Tuning the Interplay between Surface Structuration and Anisotropic Molecular Layers with Bipolar Electrochemistry," *Chemphyschem,* vol. 18, no. 19, pp. 2637-2642, 2017.
[137] A. Ismail, S. Voci, L. Descamps, A. Buhot, N. Sojic, L. Leroy, and A. Bouchet-Spinelli, "Bipolar Electrochemiluminescence Imaging: A Way to Investigate the Passivation of Silicon Surfaces," *Chemphyschem,* vol. 22, no. 11, pp. 1094-1100, 2021.
[138] H. Asoh, M. Ishino, and H. Hashimoto, "AC-Bipolar Anodization of Aluminum: Effects of Frequency on Thickness of Porous Alumina Films," *Journal of The Electrochemical Society,* vol. 165, no. 7, pp. C295-C301, 2018.
[139] H. Sopha, L. Hromadko, M. Motola, and J. M. Macak, "Fabrication of TiO_2 nanotubes on Ti spheres using bipolar electrochemistry," *Electrochemistry Communications,* vol. 111, p. 106669, 2020.
[140] Y. Koizumi, N. Shida, I. Tomita, and S. Inagi, "Bifunctional Modification of Conductive Particles by Iterative Bipolar Electrodeposition of Metals," *Chemistry Letters,* vol. 43, no. 8, pp. 1245-1247, 2014.

[141] C. Zhang, H. Zhang, J. Pi, L. Zhang, and A. Kuhn, "Bulk Electrocatalytic NADH Cofactor Regeneration with Bipolar Electrochemistry," *Angewandte Chemie International Edition,* vol. 61, no. 3, p. e202111804, 2022.
[142] Z. Qi, S. You, and N. Ren, "Wireless Electrocoagulation in Water Treatment Based on Bipolar Electrochemistry," *Electrochimica Acta,* vol. 229, pp. 96-101, 2017.
[143] K. Ino, T. Matsumoto, N. Taira, T. Kumagai, Y. Nashimoto, and H. Shiku, "Hydrogel electrodeposition based on bipolar electrochemistry," *Lab Chip,* vol. 18, no. 16, pp. 2425-2432, 2018.
[144] R. Gao, S. M. Beladi-Mousavi, G. Salinas, P. Garrigue, L. Zhang, and A. Kuhn, "Spatial Precision Tailoring the Catalytic Activity of Graphene Monolayers for Designing Janus Swimmers," *Nano letters,* vol. 23, no. 17, pp. 8180-8185, 2023.
[145] K. Itaya, T. Ataka, and S. Toshima, "Spectroelectrochemistry and electrochemical preparation method of Prussian blue modified electrodes," *Journal of the American Chemical Society,* vol. 104, no. 18, pp. 4767-4772, 2002.
[146] A. A. Karyakin, "Prussian Blue and Its Analogues: Electrochemistry and Analytical Applications," *Electroanalysis,* vol. 13, no. 10, pp. 813-819, 2001.
[147] J. A. Ibers and N. Davidson, "On the Interaction between Hexacyanatoferrate(III) Ions and (a) Hexacyanatoferrate(II) or (b) Iron(III) Ions[1a,2]," *Journal of the American Chemical Society,* vol. 73, no. 1, pp. 476-478, 2002.
[148] L. Samain, G. Silversmit, J. Sanyova, B. Vekemans, H. Salomon, B. Gilbert, F. Grandjean, G. J. Long, R. P. Hermann, L. Vincze, and D. Strivay, "Fading of modern Prussian blue pigments in linseed oil medium," *Journal of Analytical Atomic Spectrometry,* vol. 26, no. 5, pp. 930-941, 2011.
[149] A. A. Karyakin and E. E. Karyakina, "Electroanalytical applications of Prussian Blue and its analogs," *Russian Chemical Bulletin,* vol. 50, no. 10, pp. 1811-1817, 2001.
[150] P. Salazar, M. Martin, R. D. O'Neill, R. Roche, and J. L. Gonzalez-Mora, "Surfactant-promoted Prussian Blue-modified carbon electrodes: enhancement of electro-deposition step, stabilization, electrochemical properties and application to lactate microbiosensors for the neurosciences," *Colloids and Surfaces B: Biointerfaces,* vol. 92, pp. 180-189, 2012.
[151] A. A. Karyakin, E. A. Kotel'nikova, L. V. Lukachova, E. E. Karyakina, and J. Wang, "Optimal environment for glucose oxidase in perfluorosulfonated ionomer membranes: improvement of first-generation biosensors," *Analytical Chemistry,* vol. 74, no. 7, pp. 1597-1603, 2002.
[152] W. Qin, Z. Zhang, and C. Zhang, "Chemiluminescence flow sensor with immobilized reagents for the determination of iron(III)," *Mikrochimica Acta,* vol. 129, no. 1-2, pp. 97-101, 1998.
[153] M. Meininger, T. Schmitz, T. Wagner, A. Ewald, U. Gbureck, J. Groll, and C. Moseke, "Real-time measurement of protein adsorption on electrophoretically deposited hydroxyapatite coatings and magnetron sputtered metallic films using the surface acoustic wave technique," *Materials Science and Engineering: C,* vol. 61, pp. 351-354, 2016.
[154] K. Sakdaphetsiri, S. Teanphonkrang, and A. Schulte, "Cheap and Sustainable Biosensor Fabrication by Enzyme Immobilization in Commercial Polyacrylic Acid/Carbon Nanotube Films," *ACS Omega,* vol. 7, no. 23, pp. 19347-19354, 2022.

[155] C. Kurzawa, A. Hengstenberg, and W. Schuhmann, "Immobilization method for the preparation of biosensors based on pH shift-induced deposition of biomolecule-containing polymer films," *Analytical Chemistry,* vol. 74, no. 2, pp. 355-361, 2002.
[156] P. B. Shevlin and H. A. Neufeld, "Mechanism of the ferricyanide-catalyzed chemiluminescence of luminol," *The Journal of Organic Chemistry,* vol. 35, no. 7, pp. 2178-2182, 2002.
[157] X. Chen, L. L. Xing, Y. H. Tang, and G. B. Zhang, "Luminol-$K_3Fe(CN)_6$ chemiluminescence system for the determination of glipizide," *Journal of Pharmaceutical Analysis,* vol. 3, no. 2, pp. 127-131, 2013.
[158] V. K. Vaithyanathan, B. Goyette, and R. Rajagopal, "A critical review of the transformation of biomass into commodity chemicals: Prominence of pretreatments," *Environmental Challenges,* vol. 11, p. 100700, 2023.
[159] A. Hommes, H. J. Heeres, and J. Yue, "Catalytic Transformation of Biomass Derivatives to Value ‐ Added Chemicals and Fuels in Continuous Flow Microreactors," *ChemCatChem,* vol. 11, no. 19, pp. 4671-4708, 2019.
[160] A. Mellalou, W. O. Silva, M. Soutrenon, H. H. Girault, A. Outzourhit, J. Alami, and F. Ghamouss, "Biomass screening for syngas production by flash photopyrolysis," *RSC Advances,* vol. 14, no. 17, pp. 11706-11714, 2024.
[161] A. Mellalou, A. Khorssa, H. H. Girault, A. Outzourhit, and F. Ghamouss, "Laser pyrolysis of biomass: Comparing cellulose-rich and lignin-rich feedstocks for hydrogen rich-gas production," *International Journal of Hydrogen Energy,* vol. 151, p. 150131, 2025.
[162] X. Arque, T. Patino, and S. Sanchez, "Enzyme-powered micro- and nano-motors: key parameters for an application-oriented design," *Chemical Science,* vol. 13, no. 32, pp. 9128-9146, 2022.
[163] J. M. Le and K. L. Bren, "Engineered Enzymes and Bioinspired Catalysts for Energy Conversion," *ACS Energy Letters,* vol. 4, no. 9, pp. 2168-2180, 2019.
[164] C. Beans, "Microbes could convert industrial wastewater into ecofriendly products," *Proceedings of the National Academy of Sciences of the United States of America,* vol. 122, no. 2, p. e2426630122, 2025.
[165] I. Mazurenko, M. Etienne, G.-W. Kohring, F. Lapicque, and A. Walcarius, "Enzymatic bioreactor for simultaneous electrosynthesis and energy production," *Electrochimica Acta,* vol. 199, pp. 342-348, 2016.
[166] P. Bollella, I. Lee, D. Blaauw, and E. Katz, "A Microelectronic Sensor Device Powered by a Small Implantable Biofuel Cell," *Chemphyschem,* vol. 21, no. 1, pp. 120-128, 2020.
[167] P. Pinyou, V. Blay, L. M. Muresan, and T. Noguer, "Enzyme-modified electrodes for biosensors and biofuel cells," *Materials Horizons,* vol. 6, no. 7, pp. 1336-1358, 2019.
[168] M. Gamella, A. Koushanpour, and E. Katz, "Biofuel cells - Activation of micro- and macro-electronic devices," *Bioelectrochemistry,* vol. 119, pp. 33-42, 2018.
[169] A. Zebda, J. P. Alcaraz, P. Vadgama, S. Shleev, S. D. Minteer, F. Boucher, P. Cinquin, and D. K. Martin, "Challenges for successful implantation of biofuel cells," *Bioelectrochemistry,* vol. 124, pp. 57-72, 2018.
[170] A. Nasar and R. Perveen, "Applications of enzymatic biofuel cells in bioelectronic devices – A review," *International Journal of Hydrogen Energy,* vol. 44, no. 29, pp. 15287-15312, 2019.
[171] G. Salinas, T. Safarik, M. Meneghello, S. Bichon, S. Gounel, N. Mano, and A. Kuhn, "Magnetohydrodynamic Enhancement of Biofuel Cell Performance," *Chemistry,* vol. 31, no. 9, p. e202403329, 2025.

[172] W. Gao, J. Lu, S. Zhang, X. Zhang, Z. Wang, W. Qin, J. Wang, W. Zhou, H. Liu, and Y. Sang, "Suppressing Photoinduced Charge Recombination via the Lorentz Force in a Photocatalytic System," *Advanced Science,* vol. 6, no. 18, p. 1901244, 2019.
[173] S. Mutlu, O. Yasa, O. Erin, and M. Sitti, "Magnetic Resonance Imaging-Compatible Optically Powered Miniature Wireless Modular Lorentz Force Actuators," *Advanced Science,* vol. 8, no. 2, p. 2002948, 2021.
[174] I. Mogi, R. Morimoto, and R. Aogaki, "Surface chirality effects induced by magnetic fields," *Current Opinion in Electrochemistry,* vol. 7, pp. 1-6, 2018.
[175] G. Hinds, J. M. D. Coey, and M. E. G. Lyons, "Influence of magnetic forces on electrochemical mass transport," *Electrochemistry Communications,* vol. 3, no. 5, pp. 215-218, 2001.
[176] O. Lioubashevski, E. Katz, and I. Willner, "Magnetic Field Effects on Electrochemical Processes: A Theoretical Hydrodynamic Model," *The Journal of Physical Chemistry B,* vol. 108, no. 18, pp. 5778-5784, 2004.
[177] P. Vensaus, Y. Liang, J. P. Ansermet, G. Soler-Illia, and M. Lingenfelder, "Enhancement of electrocatalysis through magnetic field effects on mass transport," *Nature Communications,* vol. 15, no. 1, p. 2867, 2024.
[178] Y. Zhang, C. Liang, J. Wu, H. Liu, B. Zhang, Z. Jiang, S. Li, and P. Xu, "Recent Advances in Magnetic Field-Enhanced Electrocatalysis," *ACS Applied Energy Materials,* vol. 3, no. 11, pp. 10303-10316, 2020.
[179] M. C. Weston, M. D. Gerner, and I. Fritsch, "Magnetic fields for fluid motion," *Analytical Chemistry,* vol. 82, no. 9, pp. 3411-3418, 2010.
[180] J. C. Sikes, K. Wonner, A. Nicholson, P. Cignoni, I. Fritsch, and K. Tschulik, "Characterization of Nanoparticles in Diverse Mixtures Using Localized Surface Plasmon Resonance and Nanoparticle Tracking by Dark-Field Microscopy with Redox Magnetohydrodynamics Microfluidics," *ACS Physical Chemistry Au,* vol. 2, no. 4, pp. 289-298, 2022.
[181] G. Salinas, S. Arnaboldi, P. Garrigue, G. Bonetti, R. Cirilli, T. Benincori, and A. Kuhn, "Magnetic field-enhanced redox chemistry on-the-fly for enantioselective synthesis," *Faraday Discuss,* vol. 247, no. 0, pp. 34-44, 2023.
[182] G. Salinas, A. Kuhn, and S. Arnaboldi, "Self-Sustained Rotation of Lorentz Force-Driven Janus Systems," *The Journal of Physical Chemistry C,* vol. 127, no. 30, pp. 14704-14710, 2023.
[183] E. Katz, O. Lioubashevski, and I. Willner, "Magnetic field effects on bioelectrocatalytic reactions of surface-confined enzyme systems: enhanced performance of biofuel cells," *Journal of the American Chemical Society,* vol. 127, no. 11, pp. 3979-3988, 2005.
[184] E. Katz, O. Lioubashevski, and I. Willner, "Magnetic field effects on cytochrome c-mediated bioelectrocatalytic transformations," *Journal of the American Chemical Society,* vol. 126, no. 35, pp. 11088-92, 2004.
[185] L. M. A. Monzon and J. M. D. Coey, "Magnetic fields in electrochemistry: The Lorentz force. A mini-review," *Electrochemistry Communications,* vol. 42, pp. 38-41, 2014.
[186] G. Salinas, T. Safarik, M. Meneghello, S. Bichon, S. Gounel, N. Mano, and A. Kuhn, "Magnetohydrodynamic Enhancement of Biofuel Cell Performance," *Chemistry-A European Journal,* vol. 31, no. 9, p. e202403329, 2025.
[187] D. Pantarotto, W. R. Browne, and B. L. Feringa, "Autonomous propulsion of carbon nanotubes powered by a multienzyme ensemble," *Chemical Communications,* no. 13, pp. 1533-1535, 2008.

[188] L. K. Abdelmohsen, M. Nijemeisland, G. M. Pawar, G. J. Janssen, R. J. Nolte, J. C. van Hest, and D. A. Wilson, "Dynamic Loading and Unloading of Proteins in Polymeric Stomatocytes: Formation of an Enzyme-Loaded Supramolecular Nanomotor," *ACS Nano,* vol. 10, no. 2, pp. 2652-26560, 2016.

[189] S. Arnaboldi, G. Salinas, A. Karajic, P. Garrigue, T. Benincori, G. Bonetti, R. Cirilli, S. Bichon, S. Gounel, N. Mano, and A. Kuhn, "Direct dynamic read-out of molecular chirality with autonomous enzyme-driven swimmers," *Nature Chemistry,* vol. 13, no. 12, pp. 1241-1247, 2021.

[190] S. Tang, F. Zhang, H. Gong, F. Wei, J. Zhuang, E. Karshalev, B. Esteban-Fernandez de Avila, C. Huang, Z. Zhou, Z. Li, L. Yin, H. Dong, R. H. Fang, X. Zhang, L. Zhang, and J. Wang, "Enzyme-powered Janus platelet cell robots for active and targeted drug delivery," *Science Robotics,* vol. 5, no. 43, p. aba6137, 2020.

[191] T. Zhang, "Taking on all of the biomass for conversion," *Science,* vol. 367, no. 6484, pp. 1305-1306, 2020.

[192] H. B. Noh, M. Halappa Naveen, Y. J. Choi, E. S. Choe, and Y. B. Shim, "Implantable nonenzymatic glucose/O_2 micro film fuel cells assembled with hierarchical AuZn electrodes," *Chemical Communications,* vol. 51, no. 30, pp. 6659-6662, 2015.

[193] S. El Ichi, A. Zebda, A. Laaroussi, N. Reverdy-Bruas, D. Chaussy, M. Naceur Belgacem, P. Cinquin, and D. K. Martin, "Chitosan improves stability of carbon nanotube biocathodes for glucose biofuel cells," *Chemical Communications,* vol. 50, no. 93, pp. 14535-14538, 2014.

[194] C. Zhou, C. Gao, Z. Lin, D. Wang, Y. Li, Y. Yuan, B. Zhu, and Q. He, "Autonomous Motion of Bubble-Powered Carbonaceous Nanoflask Motors," *Langmuir,* vol. 36, no. 25, pp. 7039-7045, 2020.

[195] C. Gao, C. Zhou, Z. Lin, M. Yang, and Q. He, "Surface Wettability-Directed Propulsion of Glucose-Powered Nanoflask Motors," *ACS Nano,* vol. 13, no. 11, pp. 12758-12766, 2019.

[196] N. Mano and A. Heller, "Bioelectrochemical propulsion," *Journal of the American Chemical Society,* vol. 127, no. 33, pp. 11574-11575, 2005.

[197] S. Arnaboldi, G. Salinas, S. Bichon, S. Gounel, N. Mano, and A. Kuhn, "Bi-enzymatic chemo-mechanical feedback loop for continuous self-sustained actuation of conducting polymers," *Nature Communications,* vol. 14, no. 1, p. 6390, 2023.

[198] F. Conzuelo, N. Markovic, A. Ruff, and W. Schuhmann, "The Open Circuit Voltage in Biofuel Cells: Nernstian Shift in Pseudocapacitive Electrodes," *Angewandte Chemie International Edition,* vol. 57, no. 41, pp. 13681-13685, 2018.

[199] F. Mao, N. Mano, and A. Heller, "Long tethers binding redox centers to polymer backbones enhance electron transport in enzyme "Wiring" hydrogels," *Journal of the American Chemical Society,* vol. 125, no. 16, pp. 4951-4957, 2003.

[200] G. Salinas, C. Lozon, and A. Kuhn, "Unconventional applications of the magnetohydrodynamic effect in electrochemical systems," *Current Opinion in Electrochemistry,* vol. 38, p. 101220, 2023.

[201] L. Bouffier, D. Zigah, N. Sojic, and A. Kuhn, "Bipolar (Bio)electroanalysis," *Annual Review of Analytical Chemistry,* vol. 14, no. 1, pp. 65-86, 2021.

[202] S. Luo, K. Elouarzaki, and Z. J. Xu, "Electrochemistry in Magnetic Fields," *Angewandte Chemie International Edition,* vol. 61, no. 27, p. e202203564, 2022.

[203] H. Liu, A. Hussain, Y. T. Zholudov, D. V. Snizhko, N. Sojic, and G. Xu, "Self-Powered Electrochemiluminescence for Imaging the Corrosion of Protective Coating of Metal

and Quantitative Analysis," *Angewandte Chemie International Edition,* vol. 63, no. 45, p. e202411764, 2024.
[204] Y. Fu, B. Xie, M. Liu, S. Hou, Q. Zhu, A. Kuhn, L. Zhang, W. Yang, and N. Sojic, "Bipolar electrochemiluminescence at the water/organic interface," *Chemical Science,* vol. 15, no. 47, pp. 19907-19912, 2024.
[205] L. R. Arias-Aranda, G. Salinas, A. Kuhn, G. Xu, F. Kanoufi, L. Bouffier, and N. Sojic, "Complex electrochemiluminescence patterns shaped by hydrodynamics at a rotating bipolar electrode," *Chemical Science,* vol. 15, no. 23, pp. 8723-8730, 2024.
[206] H. Zhou, C. C. Mayorga-Martinez, S. Pane, L. Zhang, and M. Pumera, "Magnetically Driven Micro and Nanorobots," *Chemical Reviews,* vol. 121, no. 8, pp. 4999-5041, 2021.
[207] J. Tian, N. Gao, M. Wang, M. Zhou, G. Ling, and P. Zhang, "Application of Magnetic Micro/Nanomotors in Biomedicine," *ACS Applied Nano Materials,* vol. 7, no. 6, pp. 5745-5760, 2024.
[208] F. Lin, C. Niu, J. Hu, Z. Wang, and J. Bao, "Graphene Diamagnetism: Levitation, transport, rotation, and orientation alignment of graphene flakes in a magnetic field," *IEEE Nanotechnology Magazine,* vol. 14, no. 1, pp. 14-22, 2020.
[209] M. Shao, L. Yan, H. Pan, I. Ivanov, and B. Hu, "Giant magnetic field effects on electroluminescence in electrochemical cells," *Advanced Materials,* vol. 23, no. 19, pp. 2216-2220, 2011.
[210] F. Tassinari, D. Amsallem, B. P. Bloom, Y. Lu, A. Bedi, D. H. Waldeck, O. Gidron, and R. Naaman, "Spin-Dependent Enantioselective Electropolymerization," *The Journal of Physical Chemistry C,* vol. 124, no. 38, pp. 20974-20980, 2020.
[211] C. Li, S. Zhou, J. Chen, and X. Jiang, "Fluorescence Imaging of Inflammation with Optical Probes," *Chemical & Biomedical Imaging,* vol. 1, no. 6, pp. 495-508, 2023.
[212] Z. Xu, X. Ding, S. Li, F. Huang, B. Wang, S. Wang, X. Zhang, F. Liu, and H. Zhang, "Oxidation-Resistant MXene-Based Melamine Foam with Ultralow-Percolation Thresholds for Electromagnetic-Infrared Compatible Shielding," *ACS Applied Materials & Interfaces,* vol. 14, no. 35, pp. 40396-40407, 2022.
[213] T. Agarkar, V. K. Nair, S. Tripathy, V. Chawla, S. Ghosh, and A. Kumar, "Oxygen vacancy modulated MnO_2 bi-electrode system for attomole-level pathogen nucleic acid sequence detection," *Electrochimica Acta,* vol. 407, p. 139876, 2022.
[214] Y. Li, Q. Zhu, M. Xu, B. Zang, Y. Wang, and B. Xu, "Cu‐Modified $Ti_3C_2Cl_2$ MXene with Zincophilic and Hydrophobic Characteristics as a Protective Coating for Highly Stable Zn Anode," *Advanced Functional Materials,* vol. 33, no. 18, p. 2213416, 2023.
[215] M. Naguib, M. Kurtoglu, V. Presser, J. Lu, J. Niu, M. Heon, L. Hultman, Y. Gogotsi, and M. W. Barsoum, "Two-dimensional nanocrystals produced by exfoliation of Ti_3AlC_2," *Advanced Materials,* vol. 23, no. 37, pp. 4248-4253, 2011.
[216] A. VahidMohammadi, J. Rosen, and Y. Gogotsi, "The world of two-dimensional carbides and nitrides (MXenes)," *Science,* vol. 372, no. 6547, p. eabf1581, 2021.
[217] Y. Gogotsi, *MXenes: From Discovery to Applications of Two-Dimensional Metal Carbides and Nitrides*. Jenny Stanford Publishing, 2023.
[218] Q. Zhao, Q. Zhu, Y. Liu, and B. Xu, "Status and Prospects of MXene‐Based Lithium–Sulfur Batteries," *Advanced Functional Materials,* vol. 31, no. 21, 2021.
[219] P. Zhang, Y. Peng, Q. Zhu, R. A. Soomro, N. Sun, and B. Xu, "3D Foam‐Based MXene Architectures: Structural and Electrolytic Engineering for Advanced Potassium‐Ion Storage," *Energy & Environmental Materials,* vol. 7, no. 4, p. e12379, 2022.

[220] P. Zhang, J. Li, D. Yang, R. A. Soomro, and B. Xu, "Flexible Carbon Dots‐Intercalated MXene Film Electrode with Outstanding Volumetric Performance for Supercapacitors," *Advanced Functional Materials,* vol. 33, no. 1, p. 2209918, 2022.

[221] P. Zhang, Q. Zhu, Y. Wei, and B. Xu, "Achieving stable and fast potassium storage of Sb_2S_3@MXene anode via interfacial bonding and electrolyte chemistry," *Chemical Engineering Journal,* vol. 451, p. 138891, 2023.

[222] S. Chen, S. F. Tan, H. Singh, L. Liu, M. Etienne, and P. S. Lee, "Functionalized MXene Films with Substantially Improved Low-Voltage Actuation," *Advanced Materials,* vol. 36, no. 9, p. e2307045, 2024.

[223] H. Singh, S. Chen, G. Francius, L. Liu, P. S. Lee, and M. Etienne, "Understanding In-Plane Sliding of Functionalized $Ti_3C_2T_x$ MXene by In Situ Microscale Analysis of Electrochemical Actuation," *Chemistry of Materials,* vol. 36, no. 19, pp. 9575-9583, 2024.

[224] M. Alhabeb, K. Maleski, B. Anasori, P. Lelyukh, L. Clark, S. Sin, and Y. Gogotsi, "Guidelines for Synthesis and Processing of Two-Dimensional Titanium Carbide ($Ti_3C_2T_x$ MXene)," *Chemistry of Materials,* vol. 29, no. 18, pp. 7633-7644, 2017.

[225] L. Verger, V. Natu, M. Carey, and M. W. Barsoum, "MXenes: An Introduction of Their Synthesis, Select Properties, and Applications," *Trends in Chemistry,* vol. 1, no. 7, pp. 656-669, 2019.

[226] M. Khazaei, A. Mishra, N. S. Venkataramanan, A. K. Singh, and S. Yunoki, "Recent advances in MXenes: From fundamentals to applications," *Current Opinion in Solid State and Materials Science,* vol. 23, no. 3, pp. 164-178, 2019.

[227] S. Bae, Y. G. Kang, M. Khazaei, K. Ohno, Y. H. Kim, M. J. Han, K. J. Chang, and H. Raebiger, "Electronic and magnetic properties of carbide MXenes—the role of electron correlations," *Materials Today Advances,* vol. 9, p. 100118, 2021.

[228] H. Ding, Y. Li, M. Li, K. Chen, K. Liang, G. Chen, J. Lu, J. Palisaitis, P. O. A. Persson, P. Eklund, L. Hultman, S. Du, Z. Chai, Y. Gogotsi, and Q. Huang, "Chemical scissor-mediated structural editing of layered transition metal carbides," *Science,* vol. 379, no. 6637, pp. 1130-1135, 2023.

[229] K. Rajavel, T. Ke, K. Yang, and D. Lin, "Condition optimization for exfoliation of two dimensional titanium carbide ($Ti_3C_2T_x$)," *Nanotechnology,* vol. 29, no. 9, p. 095605, 2018.

[230] X. Wang, S. Lin, H. Tong, Y. Huang, P. Tong, B. Zhao, J. Dai, C. Liang, H. Wang, X. Zhu, Y. Sun, and S. Dou, "Two-dimensional V_4C_3 MXene as high performance electrode materials for supercapacitors," *Electrochimica Acta,* vol. 307, pp. 414-421, 2019.

[231] Z. Wang, K. Yu, Y. Feng, R. Qi, J. Ren, and Z. Zhu, "VO_2(p)-V_2C(MXene) Grid Structure as a Lithium Polysulfide Catalytic Host for High-Performance Li-S Battery," *ACS Appl Mater Interfaces,* vol. 11, no. 47, pp. 44282-44292, 2019.

[232] X. Zhu, Z. Cao, W. Wang, H. Li, J. Dong, S. Gao, D. Xu, L. Li, J. Shen, and M. Ye, "Superior-Performance Aqueous Zinc-Ion Batteries Based on the In Situ Growth of MnO_2 Nanosheets on V_2CT_X MXene," *ACS Nano,* vol. 15, no. 2, pp. 2971-2983, 2021.

[233] Y. Liu, Y. Jiang, Z. Hu, J. Peng, W. Lai, D. Wu, S. Zuo, J. Zhang, B. Chen, Z. Dai, Y. Yang, Y. Huang, W. Zhang, W. Zhao, W. Zhang, L. Wang, and S. Chou, "In‐Situ Electrochemically Activated Surface Vanadium Valence in V_2C MXene to Achieve High Capacity and Superior Rate Performance for Zn‐Ion Batteries," *Advanced Functional Materials,* vol. 31, no. 8, p. 2008033, 2020.

[234] Z. Wang, W. Xu, K. Yu, Y. Feng, and Z. Zhu, "2D heterogeneous vanadium compound interfacial modulation enhanced synergistic catalytic hydrogen evolution for full pH range seawater splitting," *Nanoscale,* vol. 12, no. 10, pp. 6176-6187, 2020.
[235] J. Shen, Z. Wu, C. Li, C. Zhang, A. Genest, G. Rupprechter, and L. He, "Emerging applications of MXene materials in CO_2 photocatalysis," *FlatChem,* vol. 28, 2021.
[236] H. Huang, C. Dong, W. Feng, Y. Wang, B. Huang, and Y. Chen, "Biomedical engineering of two-dimensional MXenes," *Advanced Drug Delivery Reviews,* vol. 184, p. 114178, 2022.
[237] A. Koyappayil, S. G. Chavan, Y. G. Roh, and M. H. Lee, "Advances of MXenes; Perspectives on Biomedical Research," *Biosensors,* vol. 12, no. 7, p. 454, 2022.
[238] M. Qin, C. Merzougui, Y.-m. Su, Y.-f. Li, W.-y. Chen, and D. Huang, "Recent developments in MXene and MXene/carbon composites for use in biomedical applications," *New Carbon Materials,* vol. 38, no. 3, pp. 496-506, 2023.
[239] Y. Chae, S. J. Kim, S. Y. Cho, J. Choi, K. Maleski, B. J. Lee, H. T. Jung, Y. Gogotsi, Y. Lee, and C. W. Ahn, "An investigation into the factors governing the oxidation of two-dimensional Ti_3C_2 MXene," *Nanoscale,* vol. 11, no. 17, pp. 8387-8393, 2019.
[240] X. Bai and J. Guan, "MXenes for electrocatalysis applications: Modification and hybridization," *Chinese Journal of Catalysis,* vol. 43, no. 8, pp. 2057-2090, 2022.
[241] Y. Zhu, K. Rajouâ, S. Le Vot, O. Fontaine, P. Simon, and F. Favier, "Modifications of MXene layers for supercapacitors," *Nano Energy,* vol. 73, p. 104734, 2020.
[242] J. Zou, J. Wu, Y. Wang, F. Deng, J. Jiang, Y. Zhang, S. Liu, N. Li, H. Zhang, J. Yu, T. Zhai, and H. N. Alshareef, "Correction: Additive-mediated intercalation and surface modification of MXenes," *Chemical Society Reviews,* vol. 51, no. 8, p. 3314, 2022.
[243] M. Anayee, C. E. Shuck, M. Shekhirev, A. Goad, R. Wang, and Y. Gogotsi, "Kinetics of Ti_3AlC_2 Etching for $Ti_3C_2T_x$ MXene Synthesis," *Chemistry of Materials,* vol. 34, no. 21, pp. 9589-9600, 2022.
[244] L. Bouffier, N. Sojic, and A. Kuhn, "Capillary-assisted bipolar electrochemistry: A focused mini review," *Electrophoresis,* vol. 38, no. 21, pp. 2687-2694, 2017.
[245] S. Sunderiya, S. Suragtkhuu, S. Purevdorj, T. Ochirkhuyag, M. Bat-Erdene, P. Myagmarsereejid, A. D. Slattery, A. S. R. Bati, J. G. Shapter, D. Odkhuu, S. Davaasambuu, and M. Batmunkh, "Understanding the oxidation chemistry of Ti_3C_2T (MXene) sheets and their catalytic performances," *Journal of Energy Chemistry,* vol. 88, pp. 437-445, 2024.
[246] T. Habib, X. Zhao, S. A. Shah, Y. Chen, W. Sun, H. An, J. L. Lutkenhaus, M. Radovic, and M. J. Green, "Oxidation stability of $Ti_3C_2T_x$ MXene nanosheets in solvents and composite films," *npj 2D Materials and Applications,* vol. 3, no. 1, p. 8, 2019.
[247] M. Cao, F. Wang, L. Wang, W. Wu, W. Lv, and J. Zhu, "Room Temperature Oxidation of Ti_3C_2MXene for Supercapacitor Electrodes," *Journal of The Electrochemical Society,* vol. 164, no. 14, pp. A3933-A3942, 2017.
[248] V. Natu, M. Sokol, L. Verger, and M. W. Barsoum, "Effect of Edge Charges on Stability and Aggregation of $Ti_3C_2T_z$ MXene Colloidal Suspensions," *The Journal of Physical Chemistry C,* vol. 122, no. 48, pp. 27745-27753, 2018.
[249] S. Wang, K. Qian, X. Bi, and W. Huang, "Influence of Speciation of Aqueous $HAuCl_4$ on the Synthesis, Structure, and Property of Au Colloids," *The Journal of Physical Chemistry C,* vol. 113, no. 16, pp. 6505-6510, 2009.

[250] M. A. Hassaan, M. A. El-Nemr, M. R. Elkatory, S. Ragab, V. C. Niculescu, and A. El Nemr, "Principles of Photocatalysts and Their Different Applications: A Review," *Topics in Current Chemistry,* vol. 381, no. 6, p. 31, 2023.
[251] J. Kou, C. Lu, J. Wang, Y. Chen, Z. Xu, and R. S. Varma, "Selectivity Enhancement in Heterogeneous Photocatalytic Transformations," *Chemical Reviews,* vol. 117, no. 3, pp. 1445-1514, 2017.
[252] Y. Luo, X. Wang, F. Gao, L. Jiang, D. Wang, and H. Pan, "From Single Atom Photocatalysts to Synergistic Photocatalysts: Design Principles and Applications," *Advanced Functional Materials,* vol. 35, no. 16, p. 2418427, 2024.
[253] A. Saravanan, P. S. Kumar, S. Jeevanantham, M. Anubha, and S. Jayashree, "Degradation of toxic agrochemicals and pharmaceutical pollutants: Effective and alternative approaches toward photocatalysis," *Environmental Pollution,* vol. 298, p. 118844, 2022.
[254] S. J. Armaković, M. M. Savanović, and S. Armaković, "Titanium Dioxide as the Most Used Photocatalyst for Water Purification: An Overview," *Catalysts,* vol. 13, no. 1, p. 26, 2022.
[255] N. Rahimi, R. A. Pax, and E. M. Gray, "Review of functional titanium oxides. I: TiO_2 and its modifications," *Progress in Solid State Chemistry,* vol. 44, no. 3, pp. 86-105, 2016.
[256] R. Mutsak Ahmed and I. Hasan, "A review on properties and applications of TiO_2 and associated nanocomposite materials," *Materials Today: Proceedings,* vol. 81, pp. 1073-1078, 2023.
[257] N. Li, W. Zhang, D. Wang, G. Li, and Y. Zhao, "Synthesis and Applications of TiO_2 -based Nanostructures as Photocatalytic Materials," *Chemistry – An Asian Journal,* vol. 17, no. 23, p. e202200822, 2022.
[258] Y. Sari, P. L. Gareso, B. Armynah, and D. Tahir, "A review of TiO_2 photocatalyst for organic degradation and sustainable hydrogen energy production," *International Journal of Hydrogen Energy,* vol. 55, pp. 984-996, 2024.
[259] T. Zhang, P. Lin, N. Wei, and D. Wang, "Enhanced Photoelectrochemical Water-Splitting Property on TiO_2 Nanotubes by Surface Chemical Modification and Wettability Control," *ACS Applied Materials & Interfaces,* vol. 12, no. 17, pp. 20110-20118, 2020.
[260] L. Duan, S. Liu, X. Wang, Z. Zhang, and J. Luo, "Interfacial Crosslinking for Efficient and Stable Planar TiO_2 Perovskite Solar Cells," *Advanced Science,* vol. 11, no. 33, p. e2402796, 2024.
[261] N. Desch, A. Rheindorf, C. Fassbender, M. Sloot, and M. Lake, "Photocatalytic degradation of methylene blue by anatase TiO_2 coating," *Applied Research,* vol. 3, no. 5, 2024.
[262] W. Hu, S. Yang, and S. Yang, "Surface Modification of TiO_2 for Perovskite Solar Cells," *Trends in Chemistry,* vol. 2, no. 2, pp. 148-162, 2020.
[263] M. Sun, W. Wan, X. Zhao, C. Shao, N. Liu, M. Fan, and J. Wang, "TiO_2 Anchored Cu Single Atoms Catalysts Boost Nitrite Electroreduction to Ammonia for Water Remediation," *Advanced Functional Materials,* vol. 35, no. 27, p. 2500553, 2025.
[264] H. Wang, C. You, and Z. Tan, "Enhanced photocatalytic oxidation of SO_2 on TiO_2 surface by Na_2CO_3 modification," *Chemical Engineering Journal,* vol. 350, pp. 89-99, 2018.
[265] G. Lim, M. Irfandi, R. Nakayama, D. W. Lim, T. Ozawa, K. Kato, M. Wilde, K. Fukutani, H. Kitagawa, and M. Maesato, "Ultrahigh Concentration Hydrogen Doping into TiO_2," *Journal of the American Chemical Society,* vol. 146, no. 46, pp. 32013-32021, 2024.

[266] M. Mehdikhanloo, Z. Hagheh Kavousi, M. Ghorbanloo, A. A. Nada, H. H. El-Maghrabi, R. Hosny, F. Zahran, R. Viter, D. Bezzerga, J. Hong, B. Fraisse, F. S. Soliman, I. Iatsunskyi, E. Coy, Y. Holade, M. Saffari, and M. Bechelany, "Influence of interface defects and Zr doping on the photocatalytic activity of TiO_2 nanofibers in water splitting," *Journal of Alloys and Compounds,* vol. 1020, p. 179439, 2025.

[267] C. Xia, L. Yuan, H. Song, C. Zhang, Z. Li, Y. Zou, J. Li, T. Bao, C. Yu, and C. Liu, "Spatial Specific Janus S-Scheme Photocatalyst with Enhanced H_2O_2 Production Performance," *Small,* vol. 19, no. 29, p. e2300292, 2023.

[268] X. Cao, H. Dong, K. Zhu, Q. Qu, D. Jiang, Y. Zheng, C. Yao, B. Wang, F. F. Abdi, W. Luo, and Z. Zou, "Enhanced performance of quantum-dot-sensitized solar cells by suppressing back transfer in TiO_2/CdS faradaic junction photoelectrode," *Nano Research,* vol. 18, no. 6, p. 94907455, 2024.

[269] K. Maeda and K. Domen, "Photocatalytic Water Splitting: Recent Progress and Future Challenges," *The Journal of Physical Chemistry Letters,* vol. 1, no. 18, pp. 2655-2661, 2010.

[270] P. Chakraborty, A. Sarkar, S. T. Ahamed, A. Mondal, K. Kargupta, and D. Banerjee, "Photocatalytic Solar Hydrogen Generation by SWCNT-Supported Nickel Oxide Nanoparticles Wrapped by Polypyrrole," *ACS Applied Engineering Materials,* vol. 2, no. 8, pp. 2055-2068, 2024.

[271] Q. Liu, J. Huang, L. Wang, X. Yu, J. Sun, and H. Tang, "Unraveling the Roles of Hot Electrons and Cocatalyst toward Broad Spectrum Photocatalytic H_2 Generation of g‐C_3N_4 Nanotube," *Solar RRL,* vol. 5, no. 6, p. 2000504, 2020.

[272] S. Veziroglu, J. Shondo, T. Tjardts, T. B. Sarwar, A. Sunbul, Y. K. Mishra, F. Faupel, and O. C. Aktas, "Photocatalytic deposition of noble metals on 0D, 1D, and 2D TiO_2 structures: a review," *Nanoscale Advances,* vol. 6, no. 24, pp. 6096-6108, 2024.

[273] Q. Zhang, R. Li, Z. Li, A. Li, S. Wang, Z. Liang, S. Liao, and C. Li, "The dependence of photocatalytic activity on the selective and nonselective deposition of noble metal cocatalysts on the facets of rutile TiO_2," *Journal of Catalysis,* vol. 337, pp. 36-44, 2016.

[274] A. Li, T. Wang, X. Chang, W. Cai, P. Zhang, J. Zhang, and J. Gong, "Spatial separation of oxidation and reduction co-catalysts for efficient charge separation: Pt@TiO_2@MnO_x hollow spheres for photocatalytic reactions," *Chemical Science,* vol. 7, no. 2, pp. 890-895, 2016.

[275] R. Li, F. Zhang, D. Wang, J. Yang, M. Li, J. Zhu, X. Zhou, H. Han, and C. Li, "Spatial separation of photogenerated electrons and holes among 010 and 110 crystal facets of $BiVO_4$," *Nature Communications,* vol. 4, p. 1432, 2013.

[276] S. Obregón and G. Colón, "Improved H_2 production of Pt-TiO_2/g-C_3N_4-MnOx composites by an efficient handling of photogenerated charge pairs," *Applied Catalysis B: Environmental,* vol. 144, pp. 775-782, 2014.

[277] J. Zhang, T. Bai, H. Huang, M. H. Yu, X. Fan, Z. Chang, and X. H. Bu, "Metal-Organic-Framework-Based Photocatalysts Optimized by Spatially Separated Cocatalysts for Overall Water Splitting," *Advanced Materials,* vol. 32, no. 49, p. e2004747, 2020.

[278] D. Wang, T. Hisatomi, T. Takata, C. Pan, M. Katayama, J. Kubota, and K. Domen, "Core/Shell photocatalyst with spatially separated co-catalysts for efficient reduction and oxidation of water," *Angewandte Chemie International Edition,* vol. 52, no. 43, pp. 11252-11256, 2013.

[279] M.-Y. Qi, Y.-H. Li, F. Zhang, Z.-R. Tang, Y. Xiong, and Y.-J. Xu, "Switching Light for Site-Directed Spatial Loading of Cocatalysts onto Heterojunction Photocatalysts with Boosted Redox Catalysis," *ACS Catalysis,* vol. 10, no. 5, pp. 3194-3202, 2020.

[280] H. S. Moon, K. C. Hsiao, M. C. Wu, Y. Yun, Y. J. Hsu, and K. Yong, "Spatial Separation of Cocatalysts on Z-Scheme Organic/Inorganic Heterostructure Hollow Spheres for Enhanced Photocatalytic H(2) Evolution and In-Depth Analysis of the Charge-Transfer Mechanism," *Advanced Materials,* vol. 35, no. 4, p. e2200172, 2023.

[281] G. E. Eperon, S. D. Stranks, C. Menelaou, M. B. Johnston, L. M. Herz, and H. J. Snaith, "Formamidinium lead trihalide: a broadly tunable perovskite for efficient planar heterojunction solar cells," *Energy & Environmental Science,* vol. 7, no. 3, pp. 982-988, 2014.

[282] S. D. Stranks, G. E. Eperon, G. Grancini, C. Menelaou, M. J. Alcocer, T. Leijtens, L. M. Herz, A. Petrozza, and H. J. Snaith, "Electron-hole diffusion lengths exceeding 1 micrometer in an organometal trihalide perovskite absorber," *Science,* vol. 342, no. 6156, pp. 341-344, 2013.

[283] S. Tiewcharoen, C. Warakulwit, V. Lapeyre, P. Garrigue, L. Fourier, C. Elissalde, S. Buffiere, P. Legros, M. Gayot, J. Limtrakul, and A. Kuhn, "Anisotropic Metal Deposition on TiO(2) Particles by Electric-Field-Induced Charge Separation," *Angewandte Chemie International Edition,* vol. 56, no. 38, pp. 11431-11435, 2017.

[284] J.-W. Lee, S. Kong, W.-S. Kim, and J. Kim, "Preparation and characterization of SiO_2/TiO_2 core-shell particles with controlled shell thickness," *Materials Chemistry and Physics,* vol. 106, no. 1, pp. 39-44, 2007.

[285] T. Leshuk, S. Linley, G. Baxter, and F. Gu, "Mesoporous hollow sphere titanium dioxide photocatalysts through hydrothermal silica etching," *ACS Applied Materials & Interfaces,* vol. 4, no. 11, pp. 6062-6070, 2012.

[286] S. Linley, T. Leshuk, and F. X. Gu, "Synthesis of magnetic rattle-type nanostructures for use in water treatment," *ACS Applied Materials & Interfaces,* vol. 5, no. 7, pp. 2540-2548, 2013.

[287] A. A. Melvin, B. Gupta, K. Tieriekhov, W. Nogala, P. Garrigue, S. Reculusa, and A. Kuhn, "Wireless Dual Stimuli Actuation of Dye Sensitized Conducting Polymer Hybrids," *Advanced Functional Materials,* vol. 31, no. 22, p. 2101171, 2021.

[288] L. Zhang, N. Ding, L. Lou, K. Iwasaki, H. Wu, Y. Luo, D. Li, K. Nakata, A. Fujishima, and Q. Meng, "Localized Surface Plasmon Resonance Enhanced Photocatalytic Hydrogen Evolution via Pt@Au NRs/C_3N_4 Nanotubes under Visible‐Light Irradiation," *Advanced Functional Materials,* vol. 29, no. 3, p. 1806774, 2018.

[289] M. A. Hamza, S. A. Rizk, E. M. Ezz-Elregal, S. A. A. El-Rahman, S. K. Ramadan, and Z. M. Abou-Gamra, "Photosensitization of TiO_2 microspheres by novel Quinazoline-derivative as visible-light-harvesting antenna for enhanced Rhodamine B photodegradation," *Scientific Reports,* vol. 13, no. 1, p. 12929, 2023.

[290] S. Y. Lee, D. Kang, S. Jeong, H. T. Do, and J. H. Kim, "Photocatalytic Degradation of Rhodamine B Dye by TiO_2 and Gold Nanoparticles Supported on a Floating Porous Polydimethylsiloxane Sponge under Ultraviolet and Visible Light Irradiation," *ACS Omega,* vol. 5, no. 8, pp. 4233-4241, 2020.

[291] Y. Cui, S. M. Goldup, and S. Dunn, "Photodegradation of Rhodamine B over Ag modified ferroelectric $BaTiO_3$ under simulated solar light: pathways and mechanism," *RSC Advances,* vol. 5, no. 38, pp. 30372-30379, 2015.

[292] U. Diebold, "The surface science of titanium dioxide," *Surface Science Reports,* vol. 48, no. 5-8, pp. 53-229, 2003.
[293] I. Majeed, H. Ali, A. Idrees, A. Arif, W. Ashraf, S. Rasul, M. A. Khan, M. A. Nadeem, and M. A. Nadeem, "Understanding the role of metal supported on TiO_2 in photoreforming of oxygenates," *Energy Advances,* vol. 1, no. 11, pp. 842-867, 2022.
[294] D. Zigah, J. Rodriguez-Lopez, and A. J. Bard, "Quantification of photoelectrogenerated hydroxyl radical on TiO_2 by surface interrogation scanning electrochemical microscopy," *Physical Chemistry Chemical Physics,* vol. 14, no. 37, pp. 12764-12772, 2012.
[295] L. Cui, T. Pu, Z. Shen, S. Li, S. Kang, Q. Xia, Y. Wang, and X. Li, "A facile strategy to synthesize Pd/TiO_2 nanotube arrays with high visible light photocatalytic performance," *Research on Chemical Intermediates,* vol. 45, no. 4, pp. 2167-2177, 2019.
[296] D. Jiang, T. A. Otitoju, Y. Ouyang, N. F. Shoparwe, S. Wang, A. Zhang, and S. Li, "A Review on Metal Ions Modified TiO_2 for Photocatalytic Degradation of Organic Pollutants," *Catalysts,* vol. 11, no. 9, p. 1039, 2021.
[297] A. A. Ismail, D. W. Bahnemann, L. Robben, V. Yarovyi, and M. Wark, "Palladium Doped Porous Titania Photocatalysts: Impact of Mesoporous Order and Crystallinity," *Chemistry of Materials,* vol. 22, no. 1, pp. 108-116, 2009.
[298] C. Marschelke, A. Fery, and A. Synytska, "Janus particles: from concepts to environmentally friendly materials and sustainable applications," *Colloid and Polymer Science,* vol. 298, no. 7, pp. 841-865, 2020.
[299] M. Beladi Mousavi, F. Gröbmeyer, C. Gruber, K. Matthews, K. Shevchuk, A. Inman, J. Wang, Y. Gogotsi, and E. Cortes, "Ion Transport Dynamics in Single MXene Nanoparticles Revealed by Interferometric Scattering Microscopy," presented at the Proceedings of the MATSUS Spring 2025 Conference, 2024.
[300] R. W. Taylor and V. Sandoghdar, "Interferometric Scattering (iSCAT) Microscopy and Related Techniques," in *Label-Free Super-Resolution Microscopy*(Biological and Medical Physics, Biomedical Engineering, 2019, pp. 25-65.